Technical Physics Letters, Vol. 26, No. 7, 2000, pp. 539–540. Translated from Pis'ma v Zhurnal Tekhnicheskoĭ Fiziki, Vol. 26, No. 13, 2000, pp. 1–4.

Estimation of the Component Amplitudes in Oscillation Spectra and the Feigenbaum Constant in Solutions of the Rossler Set of Equations

V. A. Dvinskikh and S. V. Frolov

Saratov State University, Saratov, Russia

Received December 16, 1999

Abstract—A method based upon approximation of the sequence of counts by a first-order trigonometric polynomial with variable frequencies of the harmonic functions is proposed for evaluation of the parameters of components in oscillation spectra. This approach was used to estimate the parameters of bifurcational period doubling and the Feigenbaum constant in solutions of the Rossler set of equations. A possibility of decreasing the level of side components of an intense oscillation by using a difference spectrum in estimating a weak spectral component is considered. *© 2000 MAIK "Nauka/Interperiodica".*

Anishchenko [1] considered a procedure for constructing the bifurcation lines of the cycle repetition period in one of the Rossler model systems:

$$\dot{x} = -y - z, \quad \dot{y} = x + ey, \quad \dot{z} = b + xz - \mu z,$$

with the parameters $e = b = 0.2$. For $\mu = 2.5$, this system features a stable limiting cycle with a certain period T_0, while for $\mu = 2.83$ the cycle exhibits bifurcational period doubling.

As is known [2], the classical method for calculating the parameters of components of a spectrum of numerical signals is based on a discrete Fourier transformation. A disadvantage of this method is a rather low resolution. Limitation of the observation interval results in distortion of the calculated spectrum caused by the mutual influence of components. A general approach capable of reducing the level of side components consists in using various windows with the main lobe width increased in comparison to that in the rectangular window. However, this method decreases the frequency selectivity. For this reason, we have used a different method for calculating the parameters of components in oscillation spectra based upon approximation of the sequence of counts by a first-order trigonometric polynomial [3], which provides for a better frequency resolution.

Let us approximate the sequence of counts $x(n)$ ($n = 0, 1, \ldots, N-1$) for a fixed frequency factor h by an expression of the type

$$v(n) = G + S\sin(hn) + C\cos(hn),$$
$$n = 0, 1, \ldots, N-1.$$

Then, using the least squares method [4], we construct the sums

$$\sum_{n=0}^{N-1} [x(n) - v(n)]^2$$

proceeding from the condition of zero partial derivatives of v with respect to G, S, and C, followed by calculating these quantities from a system of linear algebraic equations. As a result, we obtain a component with a frequency equal or close to h, provided that this component exists in the process under consideration. Thus, the task reduces to selecting the h values providing evaluation of the parameters of components in a given quasiperiodic process. Proceeding from physical considerations, we may preset a frequency range of the expected periodic components, whereas their number P and frequencies would remain unknown. Let us subdivide this predicted frequency range into L intervals with the corresponding frequency factors h_j and the values of G_j, S_j, and C_j ($j = 1, 2, \ldots, L$), thus establishing boundaries for these intervals. Taking into account the known relationship of h_j with a period of N_j counts, we obtain

$$h_j = (2\pi/N_j), \quad j = 1, 2, \ldots, L.$$

The number of frequency intervals can be selected sufficiently large so as to provide resolving small details of the spectrum studied. Then, a modulus of the oscillation spectrum is calculated by the formula

$$M_j = \sqrt{S_j^2 + C_j^2}, \quad j = 1, 2, \ldots, L.$$

A solution to the above set of equations for $\mu = 2.8$ was obtained by the fourth-order Runge–Kutta method with a step of 0.05 for the initial conditions $x_0 = 2.8$, $y_0 = z_0 = 0$, the number of counts $N = 985$, and the frequency interval 0.0025.

1063-7850/00/2607-0539$20.00 © 2000 MAIK "Nauka/Interperiodica"

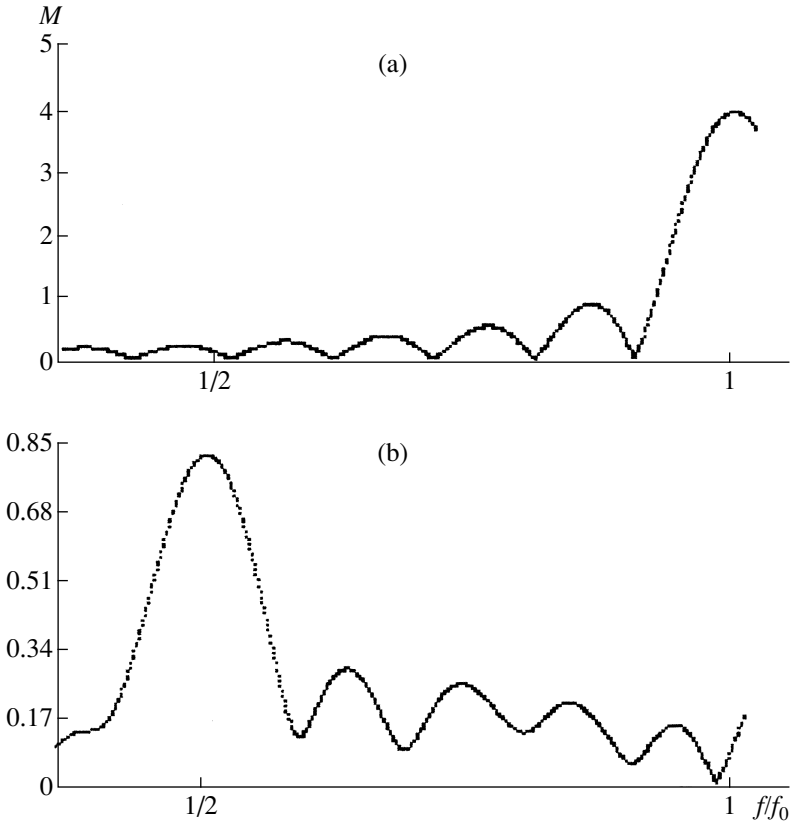

Fig. 1. Calculated oscillation spectra plotted as the amplitude modulus versus relative frequency (f_0 is the main component frequency).

The solution gave the following values of the bifurcation parameters: $\mu_2 = 2.625$, $\mu_4 = 3.837$, $\mu_8 = 4.184$, and $\mu_{16} = 4.269$. The Feigenbaum constant increased from $\delta_1 = 3.49$ to $\delta_2 = 4.08$, which is in agreement with the Feigenbaum theory. The ratio of the main oscillation component amplitude M_0 at the bifurcational period doubling boundary to the amplitude of double-period oscillations M_2 was determined as $k = 20\log\frac{M_0}{M_2}$. The M_0 value determined from data presented in the Fig. 1a is 4.244.

In order to calculate the amplitude of the double-period oscillations, we have to reduce the amplitude of the side components. For this purpose, we propose to use a subtraction procedure based on memorized parameters of the oscillation component (coefficients G_k, S_k, and C_k and the frequency factor b_k). Assuming that the influence of the double-period component on the main oscillation component is negligibly small, we may write

$$q_k = G_k + S_k\sin(b_k i) + C_k\cos(b_k i),$$
$$i = 0, 1, \ldots, N-1.$$

Then, we determine the coefficients $Z1_j$ and $Z2_j$ ($j = 1, 2, \ldots, L$) at the sine and cosine components as functions of the main oscillation. Finally, we perform sequential subtraction

$$W1_j = S_j - Z1_j,\ W2_j = C_j - Z2_j,\ j = 1, 2, \ldots, L$$

and calculate the modulus

$$MR_j = \sqrt{W1_j^2 + W2_j^2},\quad j = 1, 2, \ldots, L.$$

The results are presented in the Fig. 1b, from which it follows that $M_2 = 0.8339$. The value of $k = 14.13$ dB agrees well with the value reported in [1] ($k \approx 13$ dB).

REFERENCES

1. V. S. Anishchenko, *Complex Oscillations in Simple Systems* (Nauka, Moscow, 1990).
2. S. L. Marple, Jr., *Digital Spectral Analysis with Application* (Prentice-Hall, Englewood Cliffs, 1987; Mir, Moscow, 1990).
3. V. A. Dvinskikh, Zh. Tekh. Fiz. **62** (12), 168 (1992) [Sov. Phys. Tech. Phys. **37**, 1213 (1992)].
4. T. E. Shoup, *Applied Numerical Methods for the Microcomputer* (Prentice-Hall, Englewood Cliffs, 1984; Vysshaya Shkola, Moscow, 1990).

Translated by P. Pozdeev

Technical Physics Letters, Vol. 26, No. 7, 2000, pp. 541–543. Translated from Pis'ma v Zhurnal Tekhnicheskoĭ Fiziki, Vol. 26, No. 13, 2000, pp. 5–10.

Amorphization of the Subsurface Regions in Ion-Implanted Alloys

V. A. Ivchenko, N. N. Syutkin, and L. Yu. Kuznetsova

Institute of Electrophysics, Ural Division, Russian Academy of Sciences, Yekaterinburg, 620049 Russia

e-mail: ivchenko@ief.uran.ru

Received October 25, 1999

Abstract—The effect of partial amorphization of the subsurface regions in atomically ordered alloys upon the implantation of 20 keV positive argon ions ($D = 10^{18}$ ion/cm^2 and $j = 200$ μA/cm^2) has been established by the method of field ion microscopy. The phenomenon of partial amorphization is observed at distances not less than 90 nm from the irradiated surface of materials. © *2000 MAIK "Nauka/Interperiodica".*

An important problem in the study of radiation effects in materials science is the determination of the structural state and phase composition of thin subsurface layers of irradiated alloys. One of the most urgent tasks here is the study of the interaction between the beams of charged particles and the material within a subsurface region at a distance of ~10–100 nm from the irradiated surface.

Below, we describe the results of a high-precision investigation of changes in the real structure of surface atomic layers of alloys by the method of field ion microscopy (FIM). The method allows the subsurface volume of irradiated materials to be studied in the course of controlled removal of atoms from the surface, whereby the sample structure is analyzed during gradual (layer-by-layer) field evaporation of the surface atomic layers. By visualizing the atomically clean surface of an object at the temperature of liquid nitrogen, it is possible to obtain quantitative data on the changes in the atomic positions caused by ion implantation of positive argon ions accelerated to an energy of 20–25 keV, the atomic structure of lattice defects, their distribution over the volume, the thickness of the modified subsurface layer, etc.

We studied the interaction between an atomically ordered Cu_3Au alloy and Ar^+ ions ($E = 20$ keV, $D = 10^{18}$ ion/cm^2 and $j = 200$ μA/cm^2). The choice of the object was dictated by the main goal of our investigation—to study the effect of ion implantation on the ordered surface and subsurface layers of an alloy without additional radiation-induced structural order–disorder phase transition [1].

It is well known that atoms of each species in atomically ordered alloys occupy the sites of "their own" sublattice. Under the action of ion implantation, the atoms are displaced from their positions to distances comparable with interatomic distances. This can give rise to the formation of segregations, various lattice defects, and even separate phases, all of which can be observed comparatively easily by the method of field ion microscopy based on the contrast variation in the FIM images of the surface studied.

The blank samples of wire rods ($d = 0.2$ mm) prepared from Cu_3Au alloy of the stoichiometric composition were subjected to long-term annealing from 450 down to 200°C at a rate of 10 K/day in vacuum (10^{-2} Pa). The samples for FIM investigations were prepared from these thermally treated blanks by electrolytically polishing and had the shape of tips with a point curvature radius of 30–50 nm. The antiphase domains in the alloy were not less than 500 nm in size. Therefore, the FIM micrographs obtained from the surface of the field emitters examined prior to ion implantation showed a relatively small number of lattice defects—thermally induced antiphase boundaries. The samples selected for irradiation had atomically smooth surfaces prepared *in situ* by the field evaporation of surface atoms of the alloys (see Fig. 1a).

The implanted tip samples were mounted into the field ion microscope again, where their surface atomic layers were removed in a controlled regime with simultaneous photo or video recording of the ion images for analyzing the structural state of the bulk alloy layers. The thickness of the modified layer was usually 0.2–0.5 μm. The field ion microscope was equipped with an ion–electron converter; the cooling agent was usually liquid nitrogen ($T = 78$ K) and the imaging gas was neon.

The FIM images of the surface of ordered binary alloys exhibit highly regular ring patterns, because their contrast is provided by the atoms of only one component. Our previous FIM study of the gold–copper system [2, 3] showed that it is gold atoms that determine the visible image of the ordered alloy surface in the form of regular ring patterns similar to the micrographs of pure metals (copper atoms were not imaged on the microscope screen). A structural phase transformation

1063-7850/00/2607-0541$20.00

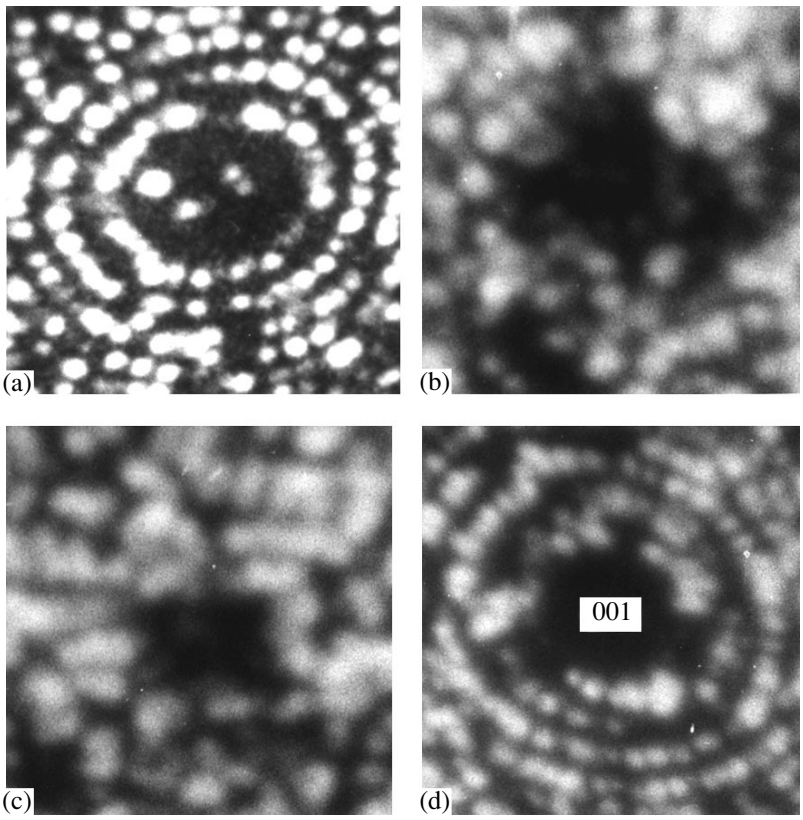

Fig. 1. Neon FIM images of the (001) Cu_3Au alloy surface showing (a) thermally ordered unirradiated alloy (V = 5 kV) and (b–d) the same alloy in the course of field evaporation of atomic layers from the irradiated sample surface: (b) 10 at. sheets (3.7 nm), V = 5.7 kV; (c) 39 at. sheets (14.5 nm), V = 5.8 kV; (d) ~650 at. sheets (243 nm), V = 11 kV.

resulted in the statistical redistribution of copper and gold atoms over the crystal lattice sites and led to the corresponding change in the ion contrast. Thus, the ion contrast of the ordered Cu_3Au alloy corresponds to the contrast from the $L1_2$ type superstructure.

Once the order–disordered phase transition has occurred (e.g., due to irradiation), the Cu_3Au alloy exhibits the ion contrast characteristic of a disordered face-centered solid solution. A disordered arrangement of atoms of the alloy components in the binary solid solution, in turn, determines the irregular ion contrast of the surface. Therefore, any change in the ion contrast caused by the surface irradiation with beams of charged particles is evidence of the effect of ion implantation on the structural state of the material. Violation of the regular ring pattern from the face surface is interpreted using the well-known theory of the geometric contrast [4], which allows identification of the regions with irradiation-induced defects. Thus, it is possible to identify the contrast from antiphase boundaries, stacking faults, dislocations, dislocation loops and pileups, segregation of atoms of one component, formation of new phase inclusions, etc. [5–8].

In the present study, only the ion beam current density was varied, the energy and the implantation dose being unchanged (E = 20 keV, $D = 10^{18}$ ion/cm^2). At j = 275 μA/cm^2, the all of the material underwent the structural phase transition, which indicated that the beam current heated the sample up to a critical temperature of the phase transition (~390°C) and that the cooling rate of the sample corresponded to the conditions of phase transition to a disordered state. Irradiation with a beam at j = 250 μA/cm^2 did not lead to phase transitions, which uniquely indicated that accelerated argon ions could not heat the sample to the critical temperature. For this reason, the structural state of the ordered Cu_3Au alloy was studied upon irradiation with j = 200 μA/cm^2, which *a priori* indicated that, during the process of ion implantation, the sample had a sufficiently low temperature.

The ion micrographs of the surface recorded upon the ion implantation (j = 200 μA/cm^2) of the ordered alloy showed evidence of a structureless (random) atomic arrangement in the subsurface layers. The observed ion contrast corresponded to the ion contrast from amorphous materials obtained upon their ultrafast cooling. On the other hand, a comparison of the ion contrast observed with the ion contrast from the thermally disordered alloy (Fig. 1a) showed that no order–

disorder phase transition occurred even in the subsurface volume (Fig. 1d).

The analysis of changes in the micrographs from the surface of the (001) face in the course of controlled removal of atoms showed (Fig. 1b–1c) that the atoms were randomly arranged on the surface. It should be noted that analysis of the subsurface volume during the field evaporation also revealed some surface regions with partial ring contrast, which additionally confirmed the absence of the order–disorder phase transition in the ion-implanted Cu_3Au alloy. On the other hand, this pattern is indicative of a partial amorphization of the subsurface layers of the irradiated alloy. This structural state was observed in the subsurface volume at distances up to 90 nm from the irradiated surface. According to [9], the projected range of the 20–25 keV argon ions in the alloy components does not exceed 15 nm, whence it became clear that the phenomenon of partial amorphization observed in the subsurface volume of the Cu_3Au alloy could not be explained by the incorporation of argon ions.

Thus, implantation of 20 keV positive argon ions ($D = 10^{18}$ ion/cm^2 and $j = 200$ μA/cm^2) into the subsurface region of the ordered Cu_3Au alloy resulted in the phenomenon of partial amorphization to a depth no less than 90 nm from the irradiated surface.

The authors are grateful to Prof. V.V. Ovchinnikov for his help in performing experiments.

The study was supported by the Russian Foundation for Basic Research (project no. 98-02-17304) and by the Ministry of Science and Technologies.

REFERENCES

1. V. A. Ivchenko, N. N. Syutkin, and A. Yu. Bunkin, J. Phys. (Paris) **49–C6**, 379 (1988).
2. V. A. Ivchenko and N. N. Syutkin, Fiz. Met. Metalloved. **61**, 575 (1986).
3. V. A. Ivchenko and N. N. Syutkin, Fiz. Tverd. Tela (Leningrad) **25**, 3049 (1983) [Sov. Phys. Solid State **25**, 1759 (1983)].
4. H. N. Southworth and B. Ralph, Philos. Mag. **21**, 23 (1970).
5. V. A. Ivchenko, N. N. Syutkin, and L. Yu. Kuznetsova, in *Abstracts of the 34th IFES Conf., Osaka, 1987, Japan*, p. 54.
6. V. A. Ivchenko and N. N. Syutkin, Fiz. Met. Metalloved. **52**, 552 (1981).
7. V. A. Ivchenko, N. N. Syutkin, and E. F. Talantsev, Fiz. Met. Metalloved. **69**, 121 (1990).
8. V. A. Ivchenko, N. N. Syutkin, and L. Yu. Kuznetsova, Fiz. Met. Metalloved. **64**, 162 (1987).
9. A. F. Burenkov, F. F. Komarov, M. A. Kumakhov, and M. M. Temkin, *Spatial Distributions of the Energy Liberated in the Atomic Collision Cascades in Solids* (Énergoatomizdat, Moscow, 1985).

Translated by L. Man

Technical Physics Letters, Vol. 26, No. 7, 2000, pp. 544–546. Translated from Pis'ma v Zhurnal Tekhnicheskoĭ Fiziki, Vol. 26, No. 13, 2000, pp. 11–16.

A Resonant-Tunneling Transit-Time Diode for the Terahertz Frequency Range Employing Transitions between Quantum States in a Double-Barrier Injector

É. A. Gel'vich, E. I. Golant, A. B. Pashkovskiĭ, and V. P. Sazonov

Istok State Research and Production Enterprise, Fryazino, Moscow oblast

Received May 11, 1999; in final form, November 19, 1999

Abstract—The possibility of considerably reducing the start-up current of a coherent resonant-tunneling transit-time diode operating in the terahertz range is demonstrated. The proposed scheme relies on resonance electron transitions in a double-barrier injector. © *2000 MAIK "Nauka/Interperiodica".*

Completely new properties can be imparted to a well-known semiconductor device, the resonant-tunneling transit-time diode (RTTTD), by harnessing the phenomenon of coherent (collisionless) electron passage through the active region: a considerable resonant increase in the diode negative differential resistance (NDR) should be expected at frequencies of about 3 THz [1].

A device proposed in [1] consists of an injector, a double-barrier (DB) heterostructure (DBH), and a transit region. The injector (e.g., based on a multibarrier heterostructure [2]) produces a flux of electrons with the energy of longitudinal motion much higher than their thermal energy and the maximum of the particle energy distribution corresponding to the position of the ground quantum-confinement level in the DBH. This flux falls on the DB structure, which mostly transmits the electrons whose energy coincides with the quantum-confinement level, the energy spread of the transmitted electrons being equal to the level width. Next, the electrons enter the transit region, for which the DBH serves as an injector. The electron interaction with the high-frequency (HF) electromagnetic field occurs primarily in the transit region, while the DB injector provides HF modulation of the electron flux. Under certain conditions, this layout enables one to obtain zero reactive components of the diode HF admittance due to compensation of the capacitive susceptance ωC (ω being the angular frequency of the applied field) by the inductive component of the electronic admittance. This effect, demonstrated by the quantum-mechanical calculation carried out in [1], is manifested at rather high current densities obtainable only in the short-pulse mode (with a pulse duration less than 100 ns); for the structures considered in [1], the working current density was $(2–4) \times 10^5$ A/cm^2.

Even higher current densities are required to advance into the frequency range above 3 THz. One of the possible ways to overcome these difficulties is to make use of the DBH not only to modulate the electron flux density and to achieve the necessary phase retardation but also to transform the electron energy directly into the HF field energy through the quantum transitions in this part of the device.

The general layout of the coherent RTTTD remains unchanged (see the inset in Fig. 2). A hot electron flux from region *1* (we do not specify how this flux is formed) falls on a DB structure of thickness *a* and, after traveling through the transit region *2* of length *l*, exits to the heavily doped contact region *3*. However, in contrast to the previous treatment, here we consider the case when the energy band positions in the diode are selected in such a way that, similarly to the station considered in [2], the hot electrons entering the DB structure would fall on one of the upper energy levels (rather

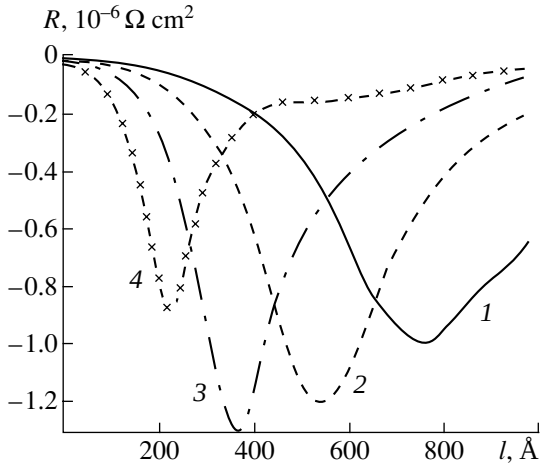

Fig. 1. Dependence of the specific resistance of a GaAs resonant-tunneling transit-time diode at 77 K on the length of the transit region. The electron density in the injector equals 10^{18} cm^{-3} and the injector relative height is $\mathscr{E}_g/\mathscr{E}_1$ = 1.0225 (*1*), 1.0200 (*2*), 1.0175 (*3*), and 1.015 (*4*).

than on the ground level) and are subsequently injected into the transit region with the longitudinal energy corresponding to this excited level. It is assumed that the energy separation between the working levels is equal to $\hbar\omega$. For the frequency range under consideration, $\hbar\omega$ is lower than the optical phonon energy; thus, the lifetime of the coherent electron state in the quantum well (QW) of the DBH can be made rather long, and the DB injector with sufficiently narrow levels can be used. The contribution of the DB injector to the active dynamic conductance of the diode, related to the quantum transitions between electron states accompanied by emission of the electromagnetic field quantum $\hbar\omega$, appears to be at least comparable to the contribution from the transit region. This modification of the electron–field interaction not only leads to significant changes in the size and parameters of the diode structure as compared to that considered in [1] but implies a considerable modification of the high-frequency characteristics of this structure as well.

To evaluate potentialities of these kinds of structures, we performed a series of calculations for the RTTTDs with quantum transitions between the first and zeroth (ground) levels in the DB injector. The goal was to find a way to increase the working frequency and to reduce the start-up current of this diode. The calculations were based on the technique previously developed for solving the Schrödinger equation with a harmonic time-dependent potential [3]. We demonstrated for the first time that, with thorough selection of the diode structure parameters (the QW width; the barrier strength; and, importantly, the position of the conduction band bottom $\mathscr{E}_g$ in the hot electron injector with respect to the middle of the first (quasi)level in the DB structure $\mathscr{E}_1$), it is possible to achieve a small-signal specific NDR at 5 THz higher than $10^{-6}\ \Omega\ \text{cm}^2$ in magnitude at current densities that can be sustained in the continuous mode of operation.

Figures 1 and 2 show the calculation results for the GaAs- and InAs-based structures, respectively. An advantage of the latter structure is the markedly lower electron effective mass. The dependences of the NDR on the length of the transit region obviously differ from those calculated for the RTTTD with the ground-level injection [1]: the NDR peak values obtained in the present study are significantly (two orders of magnitude) lower and, accordingly, the resonance curves are broader. This is related to the small magnitude of the electronic component in the DB injector conductance in the absence of quantum transitions [1]. This means that, when the reactive component of the diode admittance B (including the contribution from the transit region) vanishes at resonance, the active component G can be quite small [4]. Then, the active resistance $R = G/(B^2 + G^2)$ is very large (infinitely high in the ideal case). The DB injector with quantum transitions contributes to the active conductance, which no longer vanishes at resonance together with the reactive component, which makes it impossible to achieve giant NDR magnitudes such as in [1]. However, even with an NDR of the order of $10^{-6}\ \Omega\ \text{cm}^2$ (see Figs. 1 and 2), it is feasible, in principle, to overcome the resistance related to losses in the passive regions of an actual semiconductor structure. In addition, a significant increase in the width of the NDR resonance makes the technological allowances less stringent.

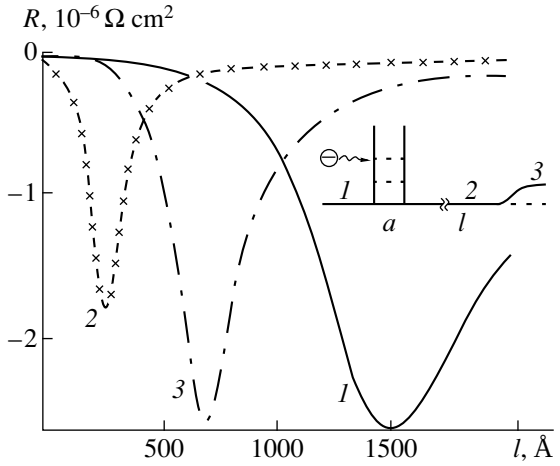

Fig. 2. Dependence of the specific resistance of an InAs resonant-tunneling transit-time diode at 77 K on the length of the transit region. The electron density in the injector equals $10^{17}\ \text{cm}^{-3}$ and the injector relative height is $\mathscr{E}_g/\mathscr{E}_1$ = 1.0100 (*1*), 1.0075 (*2*), and 1.0050 (*3*).

The calculation showed that another critical parameter, along with the length of the transit region, is the position of the conduction band bottom of the hot electron injector (which depends on the voltage applied). For the system considered in [1], the conduction band bottom should occur below the middle of the quantum-confinement level in the DBH. In the present layout, a resonant increase in the NDR can be obtained only in that case when the conduction band bottom of the injector is slightly higher than the middle of the resonant level in the DB structure. Reduction of the ratio $\mathscr{E}_g/\mathscr{E}_1$ leads to an increase in the current density. The optimum values of this ratio (i.e., those corresponding to the highest NDR possible) were found from the calculation: $\mathscr{E}_g/\mathscr{E}_1 \approx 1.02$ for the GaAs-based structure (current density, $2.0 \times 10^4\ \text{A/cm}^2$) and $\mathscr{E}_g/\mathscr{E}_1 \approx 1.0075$ for the InAs-based structure (current density, $0.2 \times 10^4\ \text{A/cm}^2$). It can be concluded from Fig. 2 that, in the case of InAs, the NDR would increase with a further slight increase in the ratio $\mathscr{E}_g/\mathscr{E}_1$ and, correspondingly, in the current density. However, the active conductance of the DB injector in this case would become higher than $0.7\omega\varepsilon\varepsilon_0$ (where ε is the permittivity). This implies that the influence of the alternating space-charge field on the quantum transitions in the DB structure has to be accounted for [5], which cannot be performed within the approximation used.

In summary, the calculation performed demonstrates that it is feasible to obtain quite a high negative differential resistance at a rather low bias current in a device comprising a double-barrier structure connected in series with the transit region coherently passed by electrons. Adding a hot-electron injector at the input and connecting in series N consecutive cells in a single crystal (a design similar to the quantum-cascade laser [2, 6]), one can increase the negative resistance N times; thus, quite promising active elements for various types of oscillators in the 5-THz range can be obtained. Note that this spectral region corresponds to significantly (about tenfold) longer waves than those obtained with quantum-cascade lasers.

This study was supported by the Russian Foundation for Basic Research (project no. 97-02-16652) and the State Interdisciplinary Program "Physics of the Solid-State Nanostructures" (project no. 97-1094).

REFERENCES

1. É. A. Gel'vich, E. I. Golant, A. B. Pashkovskiĭ, and V. P. Sazonov, Pis'ma Zh. Tekh. Fiz. **25** (10), 7 (1999) [Tech. Phys. Lett. **25**, 382 (1999)].
2. C. Sirtori, J. Faist, F. Capasso, *et al.*, Appl. Phys. Lett. **69**, 2810 (1996).
3. E. I. Golant and A. B. Pashkovskiĭ, Pis'ma Zh. Tekh. Fiz. **21** (7), 16 (1995) [Tech. Phys. Lett. **21**, 246 (1995)].
4. E. I. Golant and A. S. Tager, Élektron. Tekh., Ser. Élektronika SVCh **8** (422), 19 (1989).
5. A. B. Pashkovskiĭ, Pis'ma Zh. Éksp. Teor. Fiz. **64**, 829 (1996) [JETP Lett. **64**, 884 (1996)].
6. J. Faist, A. Tredicucci, F. Capasso, *et al.*, IEEE J. Quantum Electron. **34**, 336 (1998).

Translated by M. Skorikov

Technical Physics Letters, Vol. 26, No. 7, 2000, pp. 547–549. Translated from Pis'ma v Zhurnal Tekhnicheskoĭ Fiziki, Vol. 26, No. 13, 2000, pp. 17–22.

Vircator Generation Spectrum Controlled by an External SHF Signal

A. E. Dubinov and V. D. Selemir

Institute of Experimental Physics, Russian Federal Nuclear Center, Sarov, Russia

Received August 16, 1999; in final form, February 14, 2000

Abstract—The possibility of controlling the vircator generation spectrum by an external SHF signal is confirmed by the results of computer simulation using the method of large particles. Duration of the vircator adjustment process is evaluated. © *2000 MAIK "Nauka/Interperiodica".*

Solving the task of controlling the generation spectra of vircators—SHF devices with a virtual cathode (VC)—would open the way to the creation of frequency-adaptive phased antenna arrays [1, 2] and allow these devices to be used for amplification of the SHF signals [3, 4]. There have been only a few experiments devoted to the study of vircators controlled by external SHF signals, which did not elucidate the pattern of interactions in this system. Therefore, theoretical analysis and computer simulation have to fill the gap in our understanding of the problem.

The interaction of a vircator with an external SHF signal was theoretically studied by Sze *et al.* [5, 6], where the whole device was modeled by a single van der Paul oscillator. However, this representation seems to be oversimplified and inadequate to the real situation, where the vircator usually acts as a source of wideband SHF radiation. Therefore, a vircator as a dynamic object can be satisfactorily described only by using a large ensemble of strongly interacting oscillators.

The most appropriate approach to this description is offered by the method of large particles, which allows the dynamics of electron oscillators in the vircator interaction space to be modeled both qualitatively and quantitatively.

The purpose of this work was to study the effect of an external SHF signal on the vircator generation spectrum using a particle-in-cell (PIC) variant of the large particle simulation method. The task was solved using the well-known fully self-consistent relativistic electromagnetic KARAT code (Version 70720-xz) described in [7].

Figure 1 shows the geometry of the modeled system in the *xz* coordinates (the system is homogeneous in the *y*-axis direction) and indicates all the important dimensions. The vircator represents a two-chamber system

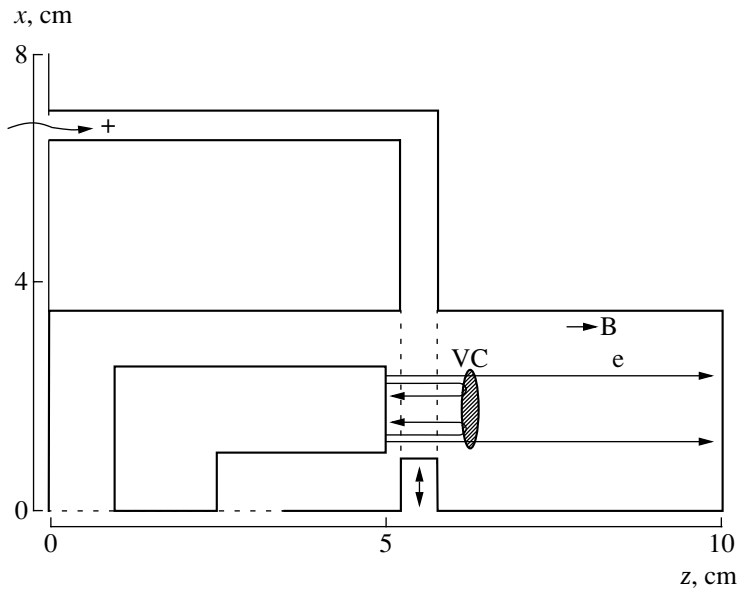

Fig. 1. Schematic diagram of a vircator with external control.

1063-7850/00/2607-0547$20.00 © 2000 MAIK "Nauka/Interperiodica"

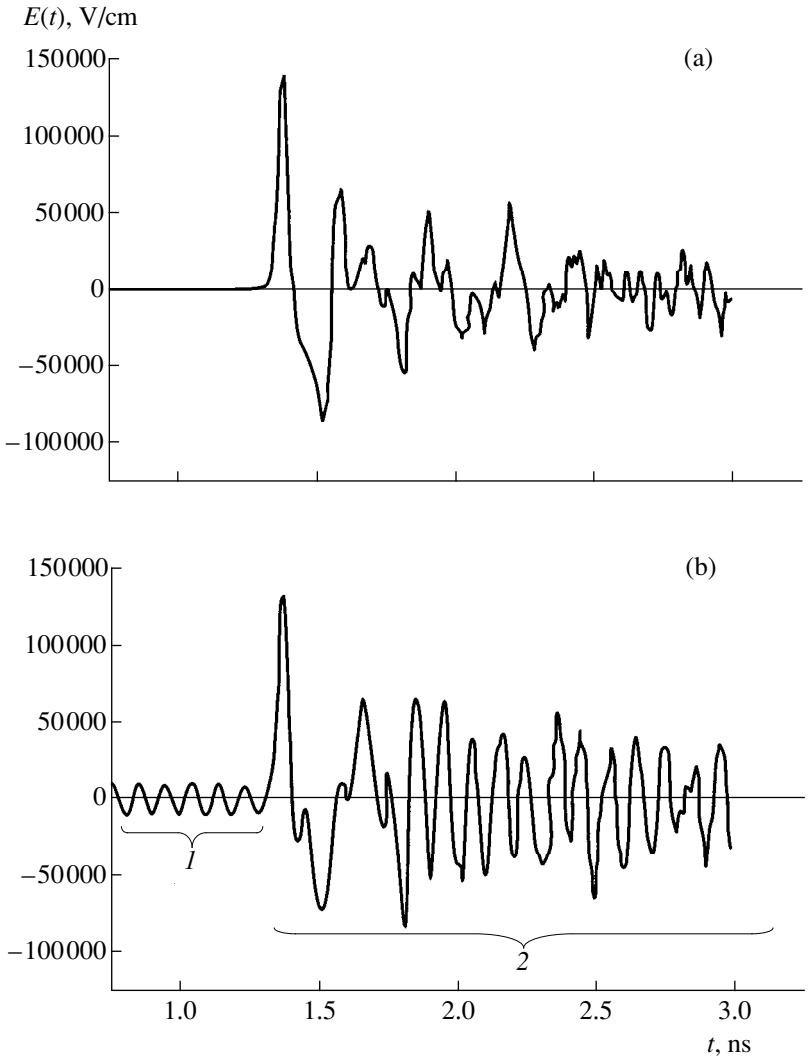

Fig. 2. Calculated oscillograms from a transducer in (a) free and (b) SHF-controlled vircator: (*1*) external signal; (*2*) generated signal.

(diode and drift compartments) separated by two anode grids. The grid gap is connected to an SHF waveguide and contains a protrusion with a controlled height, modeling the adjustment short-circuit piston. This method of introducing the external SHF signal was selected based on the results of our previous work [8], where it was suggested that the efficiency of coupling between a vircator and an external signal can be increased by supplying the signal immediately to the generation region (in this case, to the middle of a potential well formed by the real and virtual cathodes). The double-grid vircators were previously studied in [9, 10].

The SHF radiation generated by the vircator is extracted via the coupling waveguide. The SHF components of the control and generated signals were monitored with the aid of a special transducer mounted at the waveguide output (indicated by the cross in Fig. 1).

The model assumed that the system is exposed to a strong longitudinal magnetic field $B = 50$ kG. The diode and drift chamber geometries (diode gap, 3 mm; diode voltage, 120 kV) and the cathode current density (2.5 kA/cm per unit length in the y-axis direction) were selected so that the free vircator would generate a wideband radiation in the band containing 10 GHz.

The external SHF signal (TEM wave) was supplied via the waveguide and, upon reflection from the adjustment piston, formed a standing wave in the waveguide channel. The piston position was selected so that the maximum of the standing wave intensity was localized against the cathode (piston protrusion, 9 mm).

The vircator operation was as follows: a rectangle voltage pulse was applied to the cathode 1 ns after switching on the external SHF signal. This delay was necessary to ensure termination of the transient process of the standing wave formation by the time when the beam would travel into the grid gap.

The accuracy of calculations was assessed by checking for the energy conservation law in each time step. The maximum error of the energy balance did not exceed 2%.

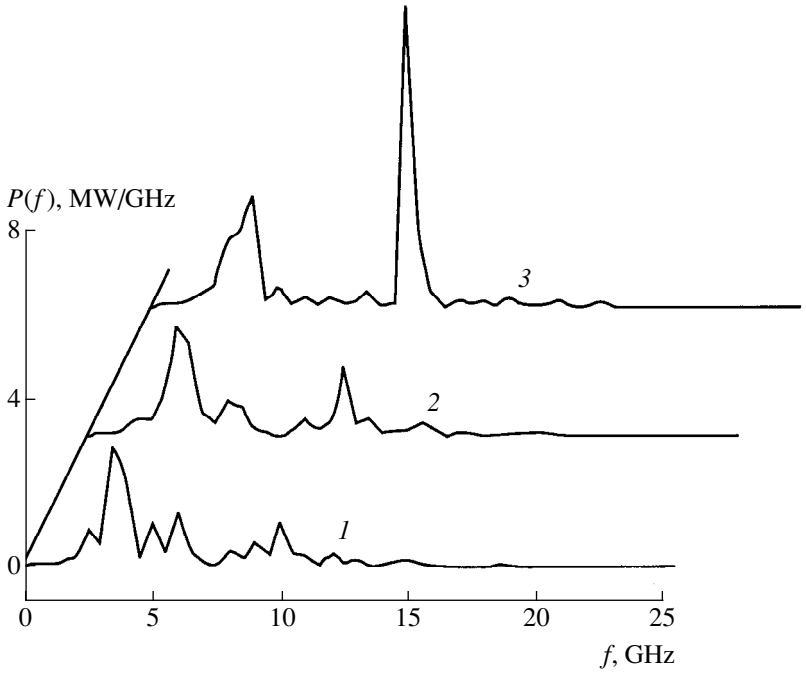

Fig. 3. SHF power spectra measured in the coupling waveguide (at the transducer position) for various values of the control SHF signal in the grid gap: (*1*) 0.1, (*2*) 1, (*3*) 10.

The calculation involved a variation of the standing wave amplitude. Figure 2 shows the calculated oscillograms of the SHF field monitored by the transducer in the presence of an external SHF signal with an amplitude of 10 kV/cm and in the absence of external signals. For comparison, it may be noted that the amplitude of accelerating field in the diode was 400 kV/cm.

Analysis of the results of model calculations showed that, in the absence of the external signal, the vircator generates a wideband random signal. In the presence of the external signal, the vircator produces a more regular signal with a narrower band and an amplitude 5–7 times that of the control signal. Application of the external signal is characterized by certain dynamics: the control and generated signals are initially almost coinciding (cf. Figs. 2a and 2b) at least over the first period of oscillations (about 0.5 ns). This provides an estimate for the duration of vircator adjustment to the external signal.

Analysis of the data presented in Fig. 2a indicates that the dynamics of frequency adjustment in response to the external SHF signal does not correspond to the van der Paul excited oscillator model [5, 6], according to which the oscillator frequency gradually shifts toward that of the control signal. In our case, the vircator almost instantaneously begins to generate at the frequency of the external SHF signal.

Figure 3 shows the spectra of signal power in the waveguide cross section where the transducer is situated. The curves were calculated for various standing wave amplitudes (between 100 and 10 kV/cm) in the grid gap. As seen, all curves display a peak at 10 GHz, which becomes dominating in the vircator spectrum generated at a large amplitude of the external SHF signal.

The authors are grateful to V.P. Tarakanov for his help in this work.

REFERENCES

1. H. Sze, D. Price, and B. Harteneck, J. Appl. Phys. **67**, 2278 (1990).
2. A. E. Dubinov and V. D. Selemir, Zarubezh. Radioélektron., No. 4, 54 (1995).
3. V. P. Grigor'ev and T. V. Koval', in *Proceedings of the All-Union Symposium on High-Current Electronics, Tomsk, 1986*, Chap. 3, p. 43.
4. V. P. Grigor'ev and T. V. Koval', Radiotekh. Élektron. (Moscow) **39**, 1185 (1994).
5. H. Sze, D. Price, B. Harteneck, and N. Cooksey, J. Appl. Phys. **68**, 3073 (1990).
6. D. Price and H. Sze, IEEE Trans. Plasma Sci. **18**, 580 (1990).
7. V. P. Tarakanov, *User's Manual for Code Karat* (Berkley Research Associate, Springfield, VA, 1992).
8. B. V. Alekhin, A. E. Dubinov, V. D. Selemir, *et al.*, RF Patent No. 2124250 (June 27, 1997), Byull. Izobret., No. 36 (1998).
9. L. M. Miner, D. E. Voss, R. A. Koslover, *et al.*, IEEE Trans. Electromagn. Compat. **34**, 229 (1992).
10. A. E. Dubinov, K. V. Mikheev, V. D. Selemir, and A. V. Sudovtsov, Izv. Vyssh. Uchebn. Zaved., Fiz., No. 6, 76 (1999).

Translated by P. Pozdeev

Technical Physics Letters, Vol. 26, No. 7, 2000, pp. 550–552. Translated from Pis'ma v Zhurnal Tekhnicheskoĭ Fiziki, Vol. 26, No. 13, 2000, pp. 23–28.

Streamer Corona Removes Styrene Vapor from Air Flow

Yu. N. Novoselov, Yu. S. Surkov, and I. E. Filatov

Institute of Electrophysics, Ural Division, Russian Academy of Sciences, Yekaterinburg, Russia

Received January 19, 2000

Abstract—Decomposition of the styrene vapor in air induced by a 60-ns pulsed streamer corona discharge was studied. Empirical relationships were obtained that allow the necessary energy consumption to be evaluated depending on the required degree of purification, the initial styrene content in air, and the nitrogen–oxygen mixture composition. On this basis, a general equation is derived that provides systematization of the experience in air purification. © *2000 MAIK "Nauka/Interperiodica".*

The production of plastics and fabrication of plastic articles is accompanied by ventilation of waste air contaminated with vapors of volatile organic compounds (VOCs). Comparatively low concentrations of these vapors hinder the use of conventional purification methods (such as, e.g., catalytic burning). A promising approach to the removal of VOCs from air is offered by methods employing treatment of the contaminated air by electron beams or discharges of various types [1, 2]. Previously [3], we demonstrated that pulsed electron beams provide effective removal of VOC at a low energy consumption but may require solving related technological problems (for example, providing protection against accompanying bremsstrahlung radiation). One of the simplest and most effective methods consists in air treatment by a pulsed discharge of the streamer corona type.

The experiments were performed with styrene—a monomer employed in the production of poly(styrene), the main polymer component of many plastics and composites. Modern technologies of poly(styrene) production minimize the monomer ejections into air but still cannot completely exclude this factor. We have used a streamer corona discharge induced by voltage pulses with an amplitude of 70–100 kV and a pulse width of 60 ns (FWHM) at a current amplitude of 100–120 A. The high-voltage pulses were obtained from a generator implementing the scheme of inductive energy storage with a semiconductor current switch analogous to that described in [4]. The discharge chamber comprised a stainless steel cylinder with an internal diameter of 120 mm and a 460-mm-long active zone. A wire electrode with a diameter of 0.5 mm was stretched along the cylinder axis, the high-voltage pulses being applied to one end of this electrode. The pulse generator design allowed polarity of the output pulses to be reversed. The pulse repetition rate was 20 Hz.

The discharge chamber was equipped with a built-in ventilator providing an air flow at a rate of 0.2 m/s. The air circulated over a closed loop with a total volume of 8×10^{-3} m^3. Thus, the system modeled a multistage gas treatment in a streamer corona discharge. In addition, averaging of the VOC concentration in the air volume improved the reproducibility of the experimental data and reduced the error of VOC concentration determination. The impurity concentration was measured before experiment and after each series of 1000 pulses. Styrene from the air samples was absorbed in a tube with adsorbent, extracted with hexane, and analyzed in a liquid chromatograph with a UV detector tuned to 208 nm. The determination error of the impurity content did not exceed 5 and 12% in the styrene concentration intervals 100–1000 and 10–100 ppm, respectively.

The experiments were performed using air modeled by a nitrogen–oxygen mixtures $N_2 : O_2 = 80 : 20$ at atmospheric pressure and room temperature with the concentration of styrene vapor varied from 100 to 600 ppm (100 to 600 styrene molecules per 10^6 molecules of the gas mixture).

The results of experiments with the artificial gas mixture modeling atmospheric air showed that a decrease in the styrene vapor concentration with increasing number of pulses (i.e., with the amount of energy dissipated in the gas phase) can be described by an exponent. This law must be apparently followed by most VOCs at low concentrations typical of real industrial gas ejects. Indeed, the probability of interactions between VOC molecules in such media is very small as compared to the probability of their contacts with different particles (e.g., molecules, atoms, and other oxygen species).

Mathematical processing of the experimental data showed that the efficiency of VOC removal from air can be characterized by the energy coefficient K determined by the least squares treatment of the experimental plots and calculated by the formula

$$\ln(C_0/C) = W/K, \quad (1)$$

where C_0 and C are the initial and current impurity concentrations, respectively, and W (J/l) is the specific energy transferred from discharge to gas.

1063-7850/00/2607-0550$20.00

Figure 1 shows the results of experiments with various initial styrene concentrations until 90% purification. Here, black circles refer to the data obtained for the negative polarity of pulsed voltage applied to the central electrode and open circles refer to the positive polarity. As seen, the process of impurity removal obeys the law expressed by equation (1), with the coefficient K independent of the polarity of applied pulsed voltage. However, the K value depends on the initial impurity concentration, which is evidence of the deviation of the K versus C_0 curve from this law at high VOC concentrations. It should be noted that the strict validity of equation (1) implies that the reaction of styrene vapor removal from air is a process of the first macrokinetic order. This is possible only provided that the concentrations of all other components of the ionized air involved in the process of VOC removal are constant (i.e., these components are in excess relative to C_0).

The relationship presented in Fig. 1 indicates that when the concentration of VOC decreases to nearly zero, the amount of energy necessary to provide for the preset purification level approaches a certain nonzero level. From the curve in Fig. 1, we may conclude that the amount of energy that has to be dissipated in the gas in order to decrease the content of styrene e times from the initial concentration below 100 ppm is about 100 J/l. This is a rather large value: application of an electron beam allows the same effect to be obtained at the expense of a lower amount (by 5–7 times) of deposited energy [3]. Although the parameter K is, to a certain extent, an individual characteristic of each setup, using these values allows us to compare different systems with respect to the efficiency of VOC removal.

The increase in the coefficient K with the initial concentration of styrene vapor C_0 (Fig. 1) can be explained by the reaction order smoothly varied from unity to zero. Eventually, the concentration of active species generated in the ionized air becomes comparable to (or less than) C_0 (i.e., it is styrene vapor that is present in excess), and we can no longer neglect variation in the amount of active species. The process of VOC removal can also be affected by the VOC decomposition products capable of competitively trapping a considerable part of active species. However, when the VOC concentration decreases to the level typical of real industrial gas ejects, the concentration of active species can always be considered as comparatively high.

The principal mechanism of styrene vapor removal from ionized air apparently consists in the vapor oxidation by active oxygen species. In order to elucidate the role of oxygen in the process of styrene removal, we have performed experiments with gas mixtures containing variable proportions of molecular oxygen O_2. The experiments were conducted with the positive polarity of voltage pulses applied to the discharge gap. The results of these experiments are presented in Fig. 2 in the form of a plot of K versus the oxygen concentration $[O_2]$. These data indicate that the coefficient K is

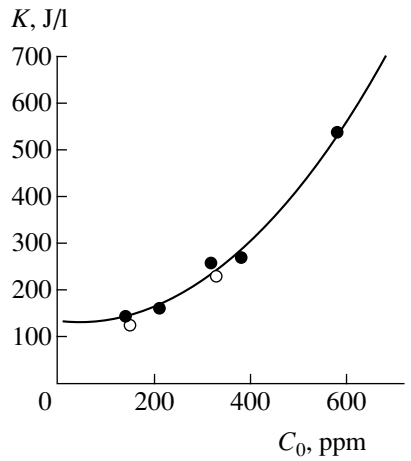

Fig. 1. The plot of energy coefficient K versus initial styrene concentration in air C_0.

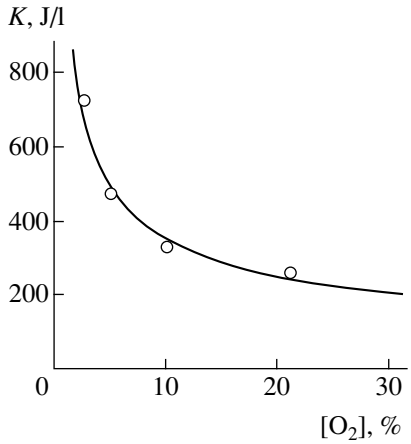

Fig. 2. The plot of energy coefficient K versus oxygen content in the mixture with nitrogen. Initial styrene concentration C_0 = 200 ppm.

proportional to the square root of the oxygen concentration: $K \sim 1.1 \times 10^3 [O_2]^{1/2}$. Then, we may present the general macrokinetic equation of the process in following form:

$$d[C]/dN = -A[C][O_2]^{1/2}, \quad (2)$$

where A is some generalized coefficient. Equation (2) indicates that, in fact, the main process of styrene removal involves atomic oxygen or ozone (the latter is also formed with participation of atomic oxygen).

Using the laws and numerical coefficients, we may predict the parameters of air purification setups for the known initial concentrations of VOC (styrene vapor), air flow rate, and preset degree of purification. For example, the efficiency of purification can be assessed using the following expressions derived from equation (1):

$$V = -P/[K\ln(1-\eta)], \quad (3)$$

$$P = -VK\ln(1-\eta). \quad (4)$$

Here, V (m^3/s) is the flow rate of the gas medium purified; P (kW/m^3) is the specific power supplied to (and dissipated in) the gas; $\eta = 1 - (C/C_0)$ is the required degree of purification, where C_0 and C are the known initial and the required final VOC concentrations, respectively. Using formulas (3) and (4), one may estimate, proceeding from the known impurity concentration and the purified gas flow rate, the necessary power transferred to the gas via the streamer discharge in order to provide for a preset degree of purification. These estimates can be used as initial data for selecting the pulse generator scheme and the gas-discharge reactor design.

Thus, we have presented the results of experimental investigation of the process of styrene vapor removal from air based on the gas treatment with a streamer corona discharge. The established laws allowed us to derive approximated expressions that can be used in predicting the parameters of gas purification systems.

REFERENCES

1. E. L. Neau, IEEE Trans. Plasma Sci. **22**, 2 (1994).
2. D. L. Kusnetsov, G. A. Mesyats, and Yu. N. Novoselov, in *Proceedings of the Conference on Novel Application of Lasers and Pulsed Power, San Jose, 1995*, pp. 142–146.
3. Yu. N. Novoselov and I. E. Filatov, Pis'ma Zh. Tekh. Fiz. **24** (16), 35 (1998) [Tech. Phys. Lett. **24**, 638 (1998)].
4. S. K. Lyubutin, G. A. Mesyats, S. N. Rukin, and B. G. Slovikovskiĭ, in *Proceedings of the 11th IEEE International Pulsed Power Conference, Baltimore, Maryland, 1997*, Vol. 2, pp. 992–998.

Translated by P. Pozdeev

Technical Physics Letters, Vol. 26, No. 7, 2000, pp. 553–556. Translated from Pis'ma v Zhurnal Tekhnicheskoĭ Fiziki, Vol. 26, No. 13, 2000, pp. 29–36.

The Velocity Autocorrelation Function of Nanoparticles in a Hard-Sphere Molecular System

V. Ya. Rudyak, G. V. Kharlamov, and A. A. Belkin

State Institute of Architecture and Civil Engineering, Novosibirsk, Russia

Received February 1, 2000

Abstract—The diffusion of nanoparticles in a dense molecular medium representing a fluid (liquid or gas) composed of hard absolutely elastic spheres was studied by the molecular dynamics method in a broad range of the medium density. It was established that relaxation of the velocity autocorrelation function of the particles is well described by a superposition of two exponents with different characteristic relaxation times. Dependence of the velocity autocorrelation function on the particle and radius and on the carrying fluid density was studied.

The so-called nanotechnologies rapidly developing in recent years have posed new, urgent problems, including the need for studying the diffusion of nanoparticles—the species with dimensions ranging from a few Ängströms to several tens of nanometers (hundreds of Ängströms). There is still no commonly accepted opinion as to what approach has to be used in describing this process. On the one hand, some researchers declared that the diffusion of nanoparticles can be described, by analogy with the usual Brownian particles, in terms of the Einstein diffusion coefficient D_E:

$$D_E = kT/M\gamma_s, \quad \gamma_s = 3\pi\eta\sigma_p/M, \tag{1}$$

where η is the medium viscosity; σ_p and M are the diameter and mass of the spherical Brownian particle, respectively; and T is the absolute temperature of the medium.

On the other hand, there were attempts to describe the diffusion of nanoparticles within the framework of the kinetic theory of gases using, as a rule, a modified Enscog's theory [1]:

$$D_k = kT/M\gamma_k, \quad \gamma_k = \frac{8n\sigma_0^2 g(\sigma_0)}{3}\sqrt{\frac{2\pi mkT}{M(M+m)}}, \tag{2}$$

where m and σ are the mass and diameter of a molecule of the carrying fluid, respectively; n is the fluid density, $\sigma_0 = (\sigma_p + \sigma)/2$; and g is the pairwise configuration distribution function of the system.

Strictly speaking, there are no sufficient grounds for describing the diffusion of nanoparticles by either of these methods. In order to elucidate the mechanisms of this process, it is necessary to study microscopic processes occurring in the vicinity of these particles. As is known, the diffusion coefficient D is related to the particle velocity autocorrelation function (VACF) χ_{vv} by the relationship

$$D = \frac{1}{3}\int_0^\infty \chi_{vv}\,dt. \tag{3}$$

Thus, an adequate description of the diffusion of nanoparticles must be preceded by studying the evolution of the corresponding VACF. The purpose on this work was to study the VACF of nanoparticles by the molecular dynamics method.

We will consider a heterogeneous system of hard spheres comprising a nanoparticle and its molecular environment. In our calculations, the ratio of diameters of the particle and molecule was varied from 1 to 4, and the ratio of their masses, from 1 to 1000. The density of medium, expressed as $\alpha = (V - V_p)/V_0$ (where $V_0 = N\sigma^3/\sqrt{2}$, V and V_p being the volumes of the molecule and the Brownian particle, respectively), was varied from 2 to 75.3.

The calculations were performed using a typical molecular dynamics algorithm [2, 3] with periodic boundary conditions. The modeled cell represented a cube containing a single nanoparticle and N molecules. The VACF was calculated by the formula

$$\chi_{vv} = \langle \mathbf{v}_p(0)\cdot\mathbf{v}_p t\rangle = \frac{1}{N_r}\sum_{i=0}^{N_r}\mathbf{v}_p(i\Delta t)\cdot\mathbf{v}_p(i\Delta t + t),$$

where $\mathbf{v}_p$ is the Brownian particle velocity and N_r is the number of realizations (in our calculations, $N_r \gtrsim 10^5$).

The results of numerical calculations were compared to the results obtained within the framework of the Einstein and Enscog theories using equations (1) and (2), respectively. The pairwise configuration functions for the particle and molecules were calculated by the formula of Mansoori *et al.* [4]. The relaxation times

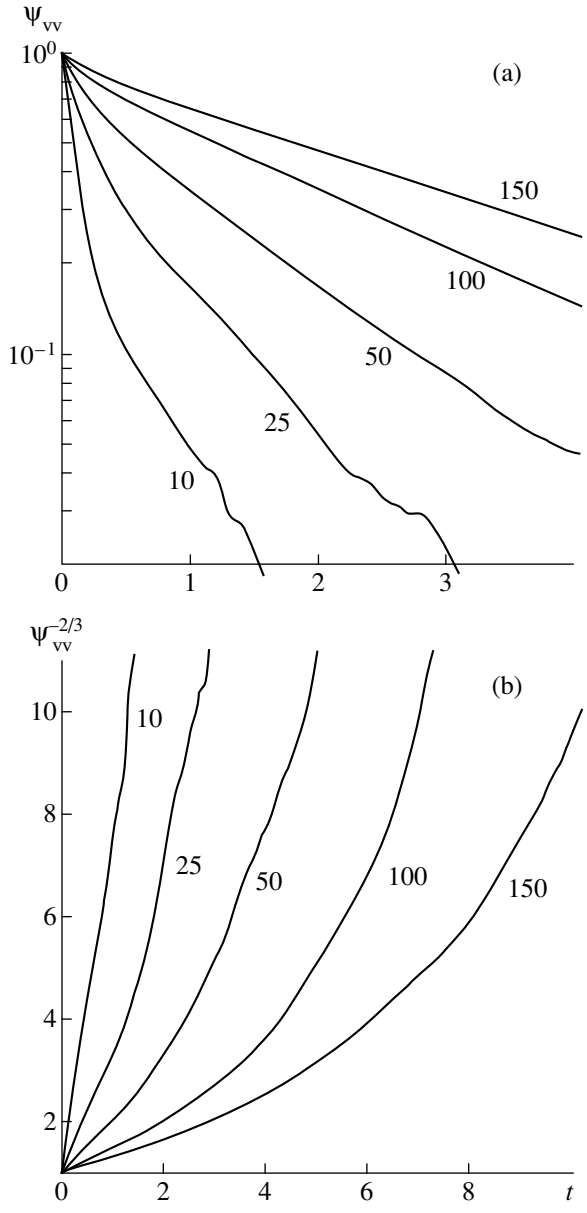

Fig. 1. Normalized velocity autocorrelation function of a nanoparticle in a molecular system of hard spheres.

were determined in all cases as $\tau = 1/\gamma$ so that the relaxation time according to the hydrodynamic theory is $\tau_E = 1/\gamma_s$ and the Enscog relaxation time is $\tau_k = 1/\gamma_k$.

The time variation of the normalized VACF ($\psi_{vv} = \chi_{vv}/\langle v_p^2 \rangle$) for nanoparticles with $\sigma_p = 4\sigma$; $\alpha = 4.8$; and $M/m = 10$, 25, 50, 100, and 150 is illustrated on a logarithmic scale in the figure (a) and in Table 1. The mean free travel time in this system is $\tau = 0.071$. In all cases, we may separate the curve into two parts exhibiting qualitatively different characters of relaxation, their relative lengths depending on the particle to molecule mass ratio. Another interesting feature of the curves is a linear character of relaxation in the second (long-term) part of VACF. Since the curves are plotted on a logarithmic scale, this fact indicates that the second VACF relaxation stage can also be approximated by an exponent. Indeed, the time evolution of the autocorrelation function in the entire range of the particle to molecule mass ratio is well described by a sum of two exponents:

$$\psi_{vv} = a_1 \exp(-t/\tau_1) + a_2 \exp(-t/\tau_2), \qquad (4)$$

where a_1, a_2, τ_1, and τ_2 are the parameters listed in Table 1. The same table compares the relaxation times calculated according to the Einstein–Langevin and Enscog theories. In all cases, the diffusion coefficient determined by formula (1) is $D_E = 1.623$.

The existence of two relaxation regions is well known both for a homogeneous system of hard spheres [5] and for a lone Brownian particle [6]. The second relaxation region is usually related to longwave hydrodynamic "tails" of perturbations caused by a correlated collective motion of molecules. According to the hydrodynamic theory [7], the asymptotic behavior of VACF at large times must obey the "3/2" law: $\chi_{vv}(t) \sim t^{-3/2}$. Although this concept has been known for a long time and is now commonly accepted, it should be emphasized that numerical experiments reliably confirmed this result only for a homogeneous molecular system (see, e.g., [3] and references therein). To the best of our knowledge, there is only one work [6] where this statement referred to a heterogeneous systems. However, the results of our previous calculations [3] indicated that the data reported in [6] were obtained with large errors and do not allow unambiguous conclusions to be made concerning the character of relaxation on the VACF "tails."

The results of our calculations of the VACF relaxation (see Fig. 1a) show that, at least for large values of the M/m ratio, the functions do not decay by the power law. The same conclusion follows from Fig. 1b showing time variation of the functions $\psi_{vv}^{-2/3}$ for the systems with various particle to molecule mass ratios (M/m = 10, 25, 50, 100, and 150). The obviously nonlinear character of the curves plotted in these coordinates indicates that, beginning with $M/m = 10$, VACF exhibit no relaxation regions described by the power law.

We have also studied dependence of the nanoparticle VACF on the medium density for a model system comprising a single particle with a mass $M = 25m$ and a diameter $\sigma_p = 4\sigma_0$ surrounded by 1712 molecules. The density of this medium had the values $\alpha = 2$, 4.8, 22.3, or 75.3. At large densities (small α values), the VACF of the particle can be described by a superposition of two exponents, one of which had a relaxation time close to the value provided by the Enscog theory. However, the contribution of longwave relaxation processes has proved to be significant as well ($a_2 = 0.29$, see Table 2, where λ is the calculated mean free path of the molecules expressed in the units of molecular

Table 1. VACF parameters and diffusion coefficients of nanoparticles calculated for various M/m ratios

M/m	a_1	τ_1	a_2	τ_2	D	τ_k	D_k	τ_E
1	0.985	0.0143	0.015	1.23	1.950	0.0147	1.103	0.0217
2	0.965	0.0241	0.035	0.69	1.769	0.0255	0.956	0.0433
3	0.93	0.0328	0.07	0.58	1.803	0.0361	0.901	0.065
5	0.87	0.0476	0.13	0.55	1.810	0.0570	0.855	0.108
10	0.79	0.087	0.21	0.69	1.616	0.109	0.818	0.217
25	0.55	0.169	0.45	0.98	1.534	0.266	0.796	0.541
50	0.38	0.263	0.62	1.59	1.495	0.526	0.788	1.08
75	0.19	0.222	0.81	1.786	1.336	0.786	0.786	1.624
100	0.14	0.200	0.86	2.169	1.299	1.047	0.784	2.166
150	0.09	0.200	0.91	3.03	1.211	1.569	0.783	3.249
1000	–	–	1.0	17.9	1.1	10.421	0.781	21.658

Table 2. VACF parameters and diffusion coefficients of nanoparticles calculated for two media of large and small density α ($\sigma_p = 4\sigma_0$, $M = 25\,m$)

α	λ	a_1	τ_1	a_2	τ_2	D	τ_E	D_E	τ_h	D_h
2	0.23	0.71	0.037	0.29	0.324	0.360	0.039	0.117	0.0736	0.221
75.3	24.0	0.98	7.726	0.02	2.523	22.83	7.246	21.73	0.860	2.580

radius). When the density drops to minimum ($\alpha = 75.3$), the nanoparticle VACF can be approximated, to within a precision of 1–2%, by a single exponent. The relaxation time sharply (more than 200 times) increases to reach $\tau = 7.726$ and coincides (to within 5%) with that provided by the Enscog theory.

We believe that a two-exponent structure of the nanoparticle VACF variation revealed by the calculation corresponds to two operative relaxation mechanisms. The first contribution reflects interactions of the nanoparticle with surrounding molecules, which are for the most part multiparticle interactions. The smaller the particle size, the more effective this mechanism. However, beginning with a certain critical level (threshold), the diffusion of a nanoparticle proceeds predominantly due to its interactions with microscopic fluctuations of a hydrodynamic field of the carrying medium. In this work, the consideration is restricted to fluctuations occurring in liquids and gases under equilibrium conditions (the case of diffusion in turbulent media falls outside the scope of our study). A trivial example is offered by the density fluctuations arising in collisions of two or several molecules.

When the fluctuations have a small characteristic size l_f ($l_f \ll \sigma_p$), their influence upon the particle evolution is very small, reducing essentially to slight variations in the frequency of particle–molecule collisions. This influence will be noticeable if the characteristic fluctuation size l_f would increase to become comparable with the particle size. The size of nanoparticles is typically of the order of a hydrodynamic scale parameter r_h, which is a physically infinitesimal quantity for the carrying medium: $l_f \gtrsim r_h$. The hydrodynamic scale varies from $r_h \sim \sqrt{\sigma L}$ (in liquids) to $r_h \sim \sqrt{\lambda L}$ (in rarefied gases) [8]. The corresponding fluctuation relaxation time τ_f must be of the order of the time of "interaction" between the disperse particle and fluctuation. This quantity is determined by the following relationships:

$$\tau_f \sim l_f / v_p \sim \sqrt{\sigma L}/v_p \sim \sqrt{\sigma L}/c\sqrt{m/M}, \qquad (5)$$

where c is the thermal velocity of molecules in the carrying medium.

The ratio of the relaxation time according to the Enscog theory to the above fluctuation relaxation time is

$$\frac{\tau_k}{\tau_f} \sim \frac{c\sqrt{m/M}}{cn\sigma_p^2(m/M)\sqrt{\sigma L}} \sim \frac{1}{\epsilon}\left(\frac{\sigma}{\sigma_p}\right)^2\sqrt{\frac{\sigma M}{Lm}},$$

where ϵ is the van der Waals parameter of the carrying fluid. For $\alpha = 4.8$ and $M = 100m$, as can be readily checked, the τ_f and τ_k differ by one order of magnitude, which is in agreement with the values obtained in the numerical calculations (Table 1). Thus, the nanoparti-

cle VACF shape of the type (4) established in our calculations appears as quite reasonable.

From the standpoint of statistics, the smaller the scale of microscopic fluctuations, the greater the probability of their existence in the system studied. Microfluctuations of the order $l_f \gtrsim r_h$ are rather typical. Moreover, it was demonstrated [8] that consistent determination of the hydrodynamic variables and formulation of the corresponding transfer equations inevitably leads to the hydrodynamic equations including these fluctuations.

The work was supported by the Russian Foundation for Basic Research, project nos. 98-01-00719 and 96-15-96310.

REFERENCES

1. J. H. Ferziger and H. G. Kaper, *Mathematical Theory of Transport in Gases* (North-Holland, Amsterdam, 1972; Mir, Moscow, 1976).
2. V. Ya. Rudyak, G. V. Kharlamov, and A. A. Belkin, Preprint No. 2 (12)-98, NGASU (State Architectural Univ., Novosibirsk, 1998).
3. V. Ya. Rudyak, G. V. Kharlamov, and A. A. Belkin, Preprint No. 1 (13)-2000, NGASU (State Architectural Univ., Novosibirsk, 2000).
4. G. A. Mansoori, N. F. Carnahan, K. E. Starling, and T. W. Leland, J. Chem. Phys. **54**, 1523 (1971).
5. B. J. Alder and T. E. Wainwright, Phys. Rev. A **1**, 18 (1970).
6. G. Subramanian, D. Lewitt, and H. Davis, J. Chem. Phys. **60**, 591 (1974).
7. R. Zwanzig and M. Bixon, Phys. Rev. A **2**, 2005 (1970).
8. V. Ya. Rudyak, Zh. Tekh. Fiz. **65** (11), 29 (1995) [Tech. Phys. **40**, 1106 (1995)].

Translated by P. Pozdeev

Technical Physics Letters, Vol. 26, No. 7, 2000, pp. 557–558. Translated from Pis'ma v Zhurnal Tekhnicheskoĭ Fiziki, Vol. 26, No. 13, 2000, pp. 37–40.

Relaxation Time of Radial Oscillations of a Particle in a Condensed Medium

Yu. A. Kartashov and I. V. Popov

Northwest Polytechnical College, St. Petersburg, 190000 Russia

Received July 23, 1999

Abstract—It is proved that, with due regard to an important role of individual properties of the internal electromagnetic field of a medium and its constituent particles, the relaxation time of particle oscillations (determining its magnetic susceptibility in the condensed medium) may differently depend on the Debye relaxation time in different frequency ranges. *© 2000 MAIK "Nauka/Interperiodica".*

One of the central problems related to the susceptibility of condensed media to weak magnetic fields [1] is the problem of determining the relaxation time of particle oscillations in a given medium. It is often assumed that this parameter is close to the Debye relaxation time τ_0. In low-frequency magnetic fields, the cyclotron frequencies are much lower than $1/\tau_0$; therefore, it is usually believed that the effect of a magnetic field on the particle dynamics is negligibly small.

Below, we prove that, in fact, the relaxation time of particle oscillations and the Debye relaxation time are quite different parameters of a medium.

Consider a simple problem of a particle in a homogeneous isotropic condensed medium radially oscillating as a whole under the action of an external homogeneous variable electric field. In this case, the equation of dynamics in the spectral representation has the form

$$\mathbf{F}_\omega(\mathbf{r}) = q\mathbf{e}(\omega, \mathbf{r}), \tag{1}$$

where $\mathbf{F}_\omega(\mathbf{r})$ is the spectral amplitude of the sum of "internal forces" (including the forces of inertia, elasticity, "friction," etc., i.e., the sum of all factors acting upon the total charge q of the particle except for the electric field) and $\mathbf{e}(\omega, \mathbf{r})$ is the spectral amplitude of the electric field intensity at a given point.

According to the fluctuation–dissipation theorem [2], the spectral density of the force $\mathbf{F}_\omega$ is determined by the losses during oscillations:

$$\overline{F_{\omega_s} F^*_{\omega_s}} = \frac{i\theta(\omega, T)}{2\pi\omega}\left(\frac{1}{\alpha_s^*} - \frac{1}{\alpha}\right), \tag{2}$$

where $\theta(\omega, T)$ is the average energy of a quantum oscillator

$$\theta(\omega, T) = (\hbar\omega/2)\coth(\hbar\omega/2kT),$$

$\hbar$ and k are the Planck and Boltzmann constants, respectively, T is the absolute temperature, $1/\alpha_s$ is the spectral representation of the operator transforming translation into force (the asterisk indicating conjugation), and s are the numbers of the coordinate components (s = 1, 2, 3).

Let a particle of a mass m be located in a spherical potential well, with the "friction" forces being of the Stokes nature. Then, the operator $1/\alpha_s$ is equal to

$$1/\alpha_s = m[\omega_0^2 - \omega^2 + (i\omega/\tau)],$$

where ω_0 is the resonance frequency of the particle and τ is its relaxation time.

Formulas (1) and (2) yield

$$\frac{\theta(\omega, T)}{\pi}\frac{m}{\tau} = q^2\overline{e_s(\omega, \mathbf{r}_1)e_s^*(\omega, \mathbf{r}_2)}. \tag{3}$$

In the above expression, $\overline{e_s(\omega, \mathbf{r}_1)e_s^*(\omega, \mathbf{r}_2)}$ is the s-component of the spectral density of the spatial correlation function of the intensity of a random electric field acting upon the particle in the medium under the assumption that the ergodicity theorem is valid for the electric field.

Application of the fluctuation–dissipation theorem to Maxwell's equations for a homogeneous isotropic infinite absorbing medium yields the following expression for the spectral density of the electric field [3]:

$$\left|\overline{\mathbf{e}(\omega, \mathbf{r}_1)\mathbf{e}^*(\omega, \mathbf{r}_2)}\right| = \frac{i\theta(\omega, T)}{8\pi^2\omega\varepsilon_0}\left[\frac{2k_0^2}{r}(e^{-k_0\sqrt{-\varepsilon^*}r} - e^{-k_0\sqrt{-\varepsilon}r}) - \frac{8\pi i\varepsilon''}{|\varepsilon|^2}\delta(\mathbf{r})\right], \tag{4}$$

where $\mathbf{r} = \mathbf{r}_1 - \mathbf{r}_2$, k_0 is the wavenumber in vacuum, ε_0 is the dielectric constant, and ε'' is the imaginary part of the complex dielectric permittivity ε. The first term in (4) is associated with thermal radiation, whereas the second, with a quasistationary field of the oscillating charges, which is concentrated in the medium [4]. The delta function $\delta(\mathbf{r})$ in (4) appears owing to neglect of the medium microstructure. If one considers, for example, the electric field within a vacuum cavity in a homo-

geneous medium, then $\delta(\mathbf{r})$ in (4) can be approximated by the quantity $3/V_0$, where V_0 is the volume of the cavity equal to the particle volume.

Substituting (4) into (3) and ignoring the term taking into account radiation (i.e., assuming that the particle size is much smaller than the wavelength), we obtain

$$\frac{\theta(\omega, T)}{\pi}\frac{m}{\tau} \simeq \frac{q^2\theta(\omega, T)\varepsilon''}{\pi\omega\varepsilon_0|\varepsilon|^2 V_0},$$

whence the relaxation time is

$$1/\tau = q^2\varepsilon''/m\varepsilon_0\omega V_0|\varepsilon|^2. \quad (5)$$

This expression describes a relationship between the particle relaxation time and the dielectric properties of the medium.

As an example, consider the behavior of the function $\tau(\omega)$ for a certain idealized medium where ε has the form

$$\varepsilon = \varepsilon' - i\varepsilon'' = 1 + \frac{\kappa_c}{1 + i\omega_0\tau} - \frac{i\sigma}{\omega\varepsilon_0}. \quad (6)$$

Here, κ_c is the static dielectric susceptibility and σ is the conductivity of the medium. [It should be noted that function (6) approximates behavior of the ε value for distilled water over a wide range of frequencies. For the majority of media (in particular, for solutions), the function $\varepsilon(\omega)$ is more complicated.]

As a result, relationship (5) takes the form

$$\frac{1}{\tau} = \frac{q^2}{mV_0\sigma} \times \frac{[1 + \omega^2\tau_0\tau_\sigma(1 + \tau_0/\tau_\sigma)](1 + \omega^2\tau_0^2)}{[1 + \omega^2\tau_0\tau_\sigma(1 + \tau_0/\tau_\sigma)]^2 + (\varepsilon_c + \omega^2\tau_0^2)^2(\omega\varepsilon_0/\sigma)^2}, \quad (7)$$

where $\tau_\sigma = \kappa_c\varepsilon_0/\sigma$ and ε_c is the static dielectric constant.

Thus, even in the above simple case, the relaxation time of the particle is related to the Debye relaxation time in a rather complicated way. It is seen from (7), that the relaxation time τ depends on τ_0 differently in different frequency ranges.

The above analysis allows adequate evaluation of the frequency dependence of the relaxation time and, in particular, of the magnetic susceptibility in a given medium with due regard to an important role of individual properties of the internal electromagnetic field considered as function of the physical characteristics of the structure of the medium and constituent particles.

REFERENCES

1. M. N. Zhadin, Biofizika **41**, 832 (1996).
2. S. M. Rytov, *Introduction to Statistical Radiophysics* (Nauka, Moscow, 1966).
3. L. D. Landau and E. M. Lifshitz, *Course of Theoretical Physics*, Vol. 8: *Electrodynamics of Continuous Media* (Nauka, Moscow, 1992; Pergamon, New York, 1984).
4. M. L. Levin and S. M. Rytov, *Theory of Equilibrium Thermal Fluctuations in Electrodynamics* (Nauka, Moscow, 1967).

Translated by L. Man

Technical Physics Letters, Vol. 26, No. 7, 2000, pp. 559–560. Translated from Pis'ma v Zhurnal Tekhnicheskoĭ Fiziki, Vol. 26, No. 13, 2000, pp. 41–45.

The Fréedericksz Surface Dynamic Effect

A. V. Koval'chuk

Institute of Physics, National Academy of Sciences of Ukraine, Kiev, Ukraine

e-mail: akova@iop.kiev.ua

Received February 25, 2000

Abstract—It is shown that redistribution of the electric field strength between the bulk and electric double layer and within the electric double layer in a plane-oriented liquid crystal results in a local change of the molecular orientation at an applied voltage below the threshold level. This effect was used to obtain optical modulators by prolonged exposure of the liquid crystal samples to a constant electric field. © *2000 MAIK "Nauka/Interperiodica".*

As was demonstrated previously [1], the onset of the low-frequency dispersion of ε' and ε" can be approximated by the Debye equation. Subsequent investigations showed that dispersion of this type is observed only in the plane-oriented nematic liquid crystals (LCs) and nematic-cholesteric mixtures. These results provided sufficient ground to suggest that the low-frequency dispersion can be due to a change in the orientation of molecules under the action of an external electric field. In order to prove this assumption, it was necessary to find a liquid crystal in which no Debye dispersion was observed in the state of homeotropic orientation and then create the conditions under which a change in the orientation of molecules in the near-surface region would be manifested in the electrooptical response.

The experiments were performed on liquid crystals of the 5TsB type. The cell design, the process of plane-oriented LC preparation, and the method of ε' and ε" measurements were the same as described previously [1]. The homeotropic orientation of 5TsB molecules was provided by special pretreatment of the electrode surface. The electrooptical properties were studied on the samples illuminated with a He–Ne laser beam incident normally to the sample surface. The kinetics of variation of the light transmittance was measured and monitored on screen of an S1-83 oscillograph. The electrooptical phenomena in the LC studied are related to changes in the light scattering. For this reason, the measurements were performed, as in the case of LC dispersed in a polymer matrix [2, 3], using a photodetector with small entrance aperture.

Figure 1 shows typical frequency dependences of ε' (curve *1*) and ε" (curves *2* and *3*) for a 5TsB LC sample with (*1*, *2*) plane and (*3*) homeotropic orientation. An analysis of the Cole–Cole diagrams for the initial portion of the low-frequency dispersion curves for the sample with homeotropic orientation showed that the diagram can be described by a relationship

$$\varepsilon^* = \varepsilon_\infty + \frac{\varepsilon_s - \varepsilon_\infty}{1 + (i\omega\tau)^{1-\alpha}}, \qquad (1)$$

where ε* is the complex dielectric permittivity; $\omega = 2\pi f$ is the circular frequency; ε_∞ and ε_s are the limiting values of permittivity for $f = \infty$ and $f = 0$, respectively; τ is the dielectric relaxation time; and α is a parameter characterizing the spectrum of relaxation times (for the given orientation of molecules, $\tau = 3.45$ s and $\alpha = 0.18$).

In the case of a plane-oriented 5TsB LC sample, the initial portion of the low-frequency dispersion of ε' and ε" is described by the Debye equation, that is, by equation (1) with $\alpha = 0$. The corresponding relaxation time is $\tau = 0.26$ s. It is important to note that, similarly to the case of a plane-oriented liquid crystal of the ZhK1282

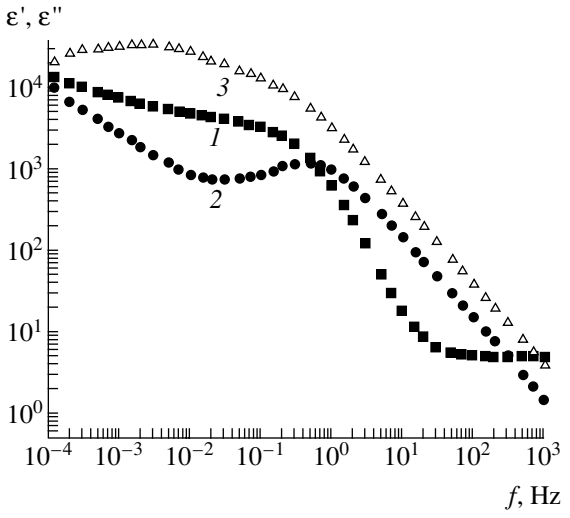

Fig. 1. Frequency dependences of ε' (curve *1*) and ε" (curves *2* and *3*) for a 5TsB LC sample with (*1*, *2*) plane and (*3*) homeotropic orientation. Sample thickness, 40 μm; measuring signal amplitude, 0.25 V; sample temperature, 295 K.

1063-7850/00/2607-0559$20.00 © 2000 MAIK "Nauka/Interperiodica"

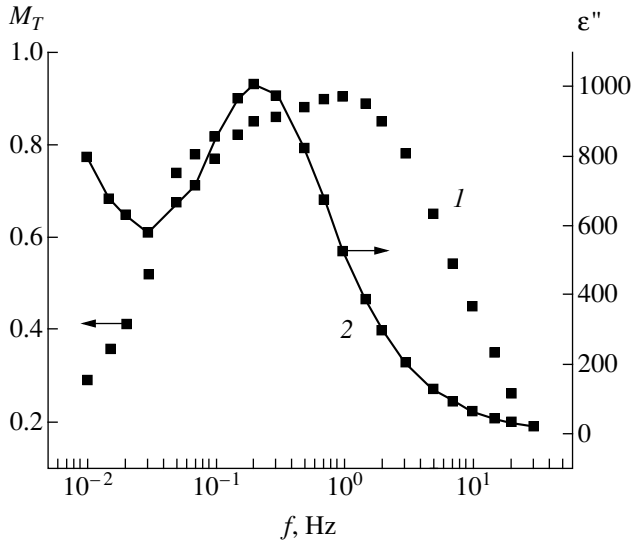

Fig. 2. Frequency dependences of the modulation amplitude M_T (curve *1*) and ε" (curve *2*) for a 40-μm-thick 5TsB LC sample. Measuring signal amplitude: 5 V for M_T and 0.25 V for ε"; sample temperature 295 K.

type [4], the neighboring portion of the dispersion curve (toward decreasing frequencies) also can be described by equation (1) with parameters close to those for the homeotropic 5TsB LC. Thus, we may conclude that a low-frequency dispersion of the Debye type is typical only of the plane-oriented molecules and is related most likely to an electric-field-induced change in the molecular orientation.

Unambiguous evidence for this assumption was obtained from the study of electrooptical properties of a plane-oriented 5TsB LC sample upon a prolonged (more than 4 h) application of constant voltage. It was found that, initially transparent, the sample upon this treatment began to scatter the light. A possible reason for the appearance of a light-scattering structure may be the inhomogeneous adsorption of ions over the electrode surface. This inhomogeneity can be initially preset by the electrode surface roughness, whereby the ions would adsorb predominantly on the "hills" of the electrode surface. The degree of inhomogeneity will increase with the time of sample exposure to the constant electric field. The surface inhomogeneity will induce inhomogeneous orientation of molecules. When the size of regions with different orientations of molecules will become comparable with the light wavelength, the sample will begin to scatter the light.

Figure 2 presents the frequency dependence of the modulation amplitude M_T (curve *1*) and ε" (curve *2*) for a light-scattering (initially plane-oriented) 5TsB LC sample. The M_T value was determined by the formula

$$M_T = \frac{T_{\max} - T_{\min}}{T_{\min}}, \qquad (2)$$

where $T_{\max}$ and $T_{\min}$ are the maximum and minimum light transmittances, respectively, at a given frequency of the applied electric field. A comparison of these curves shows evidence of a clear correlation between the two values, from which we may conclude that initial portion of the low-frequency dispersion of ε' and ε" (described by the Debye equation) is related to a change in the orientation of molecules under the action of applied electric field.

As seen from the results of our calculations, a threshold voltage for the Fréedericksz transition in the 5TsB LC is 0.8 V (for an electric field strength homogeneously distributed over the sample surface). This threshold value being greater than the amplitude of the probing signal (0.25 V), a change in the orientation of molecules is possible only within a local near-electrode region of the sample.

As the frequency decreases under the action of electric double layers, the applied electric field begins to redistribute between the bulk and near-electrode region. This may create conditions for a change in the orientation of molecules in the latter region. With further decrease in the frequency, the electric field redistribution will proceed inside the electric double layer. This will result in decreasing field strength in the region of molecular orientation. Therefore, the electrooptical effect is observed within a narrow frequency interval, which can be controlled by varying the ρ value. Due to the special features of manifestation, the phenomenon descried above can be called the Fréedericksz surface dynamic effect.

The work was supported by the STCU grant no. 637.

REFERENCES

1. O. V. Koval'chuk, Ukr. Fiz. Zh. **41**, 991 (1996).
2. J. W. Doane, N. A. Vaz, B.-C. Wu, and S. Zumer, Appl. Phys. Lett. **48** (4), 269 (1986).
3. A. V. Koval'chuk, M. V. Kurik, and O. D. Lavrentovich, Zarubezh. Radioélektron., No. 6 (1989).
4. O. V. Koval'chuk, Ukr. Fiz. Zh. **41**, 1093 (1996).

Translated by P. Pozdeev

Technical Physics Letters, Vol. 26, No. 7, 2000, pp. 561–562. Translated from Pis'ma v Zhurnal Tekhnicheskoĭ Fiziki, Vol. 26, No. 13, 2000, pp. 46–50.

Fractal Features of Worn Material Particles

Yu. A. Fadin and Yu. P. Kozyrev

Institute of Mechanical Engineering Problems, Russian Academy of Sciences, St. Petersburg, Russia

Received February 4, 2000

Abstract—Fractal characteristics of the worn material particles detached from a polycrystalline copper sample in the course of dry friction on steel were experimentally studied. These data were used to analyze the features of crack formation in copper during friction. © *2000 MAIK "Nauka/Interperiodica".*

Detailed investigations of the wear processes is of both fundamental and practical importance. However, inaccessibility of the contact surface in the course of wear significantly restricts the possibility of studying the surface damage by direct methods. The only objects providing direct evidence of the process of surface fracture in the course of friction are the particles of worn material.

The worn material particles appear as a result of combination of the near-surface cracks of different types. Therefore, a part of the worn particle surface represents the real fracture surface. Investigation of this surface may provide valuable experimental information on the process of fracture development. These data may be extracted by analysis of the amount, size, and shape of the particles detached from a sample in the course of wear [1].

The purpose of this work was to study features of the boundary line in the particles detached from a polycrystalline cooper sample in the course of dry friction on steel.

The dry friction of copper on steel (relative sliding velocity 1 m/s, contact pressure 4 MPa) was studied in the immobile copper sample (M1 grade copper)–rotating steel disk (Grade 35 steel) scheme. The worn material particles were collected and studied as described previously [1].

At present, it is commonly accepted that the fracture surfaces represent fractal objects [2], which implies that the corresponding geometric elements possess fractional dimensionality with respect to surface or length. The friction regime used in our experiments provided for the appearance of flat worn particles. The ratio of maximum size to thickness of the particles studied was in all cases above 5. In literature this phenomenon is usually frequently referred to as the "petal" or "flake" wear mode [3]. Flat particles are convenient to handle and are frequently encountered in practice. Therefore, it was of interest to follow variation of the fractal dimensionality along the boundary line, which must reflect the combined action of compressive and shear stresses participating in the particle formation. The length of a boundary line of the worn material particles obeys the relationship [4]

$$L(\eta) = L_0\eta^{1-D},$$

where η is the unit segment used to measure the boundary line length, L_0 is the length for a nonfractal contour, and D is the fractal dimensionality. The fractal dimensionality of a contour line on the particles studied was determined using photographic images obtained in a microscope in a transmission mode at large magnification. In this work, the coefficient of fractal dimensionality was determined for separate parts of the particle contour rather than for the entire contour length.

In order to provide for the correct comparison between different particles, their contours were separated into parts using a special procedure illustrated in Fig. 1. Each particle, irrespective of its dimensions, can be inscribed into a rectangle. The smoothest part of the particle contour was always arranged in the top part of the rectangle. The parts of the contour against the middle of the corresponding rectangle sides were crossed by straight bars of a fixed length $AB = CD = EF = GH$.

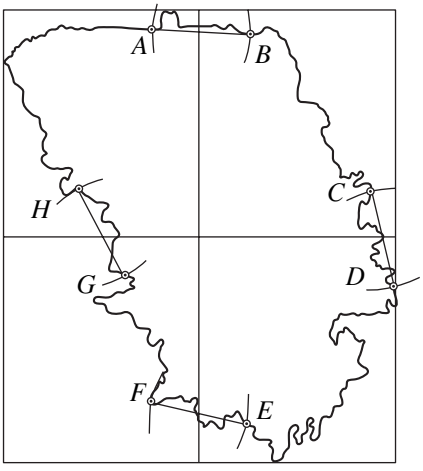

Fig. 1. Subdivision of the particle contour into parts for determining the fractal dimensionality.

1063-7850/00/2607-0561$20.00 © 2000 MAIK "Nauka/Interperiodica"

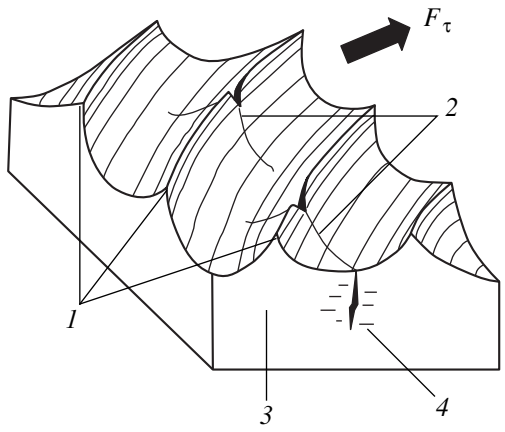

Fig. 2. Schematic diagram illustrating the electron-microscopic observation of cracks near the surface of the friction contact: (*1*) friction grooves; (*2*) cracks perpendicular to the friction force F_τ; (*3*) polished side surface; (*4*) shear bands formed under the action of the friction force.

Then, the fractal dimensionality D was determined for the parts of the contour crossed by these bars.

The D values were calculated by a method described in [5], according to which the length of a particle contour between two points is approximated by a length of a broken line with the ends situated on the contour and the line portions representing the unit segments of length η. As the size of the measuring unit segment decreased, we obtain a series of sequential approximations of the contour length. Dependence of the contour length on the measuring unit size was plotted in a double logarithmic scale. In these coordinates, the plot of $L(\eta)$ is linear and the dimensionality D was determined by the formula $D = 1 - m$, where m is the line slope. The values of the fractal dimensionality determined by averaging the data obtained for 40 particles are given in the table.

It was found that the fractal dimensionality determined on a part of the contour with minimum unevenness was always close to unity ($D \sim 1$), whereas the fractal dimensionality of the parts against the other rectangle sides always exceeded unity. Since the particle surface reflects interaction of the near-surface cracks of different types, we may assume that the particle contour line may reflect to certain extent the features of this interaction.

Fractal dimensionality of the contour segments indicated in Fig. 1 (averaged over 40 particles)

Contour line segment	Fractal dimensionality D
AB	1.02
CD	1.18
EF	1.26
GH	1.25

Let us dwell on this point in more detail. The surface of a friction contact is always very uneven and displays numerous grooves of friction (Fig. 2). It is virtually impossible to reveal cracks on this background (the more so for the ones with a narrow opening) even with the aid of an electron microscope. For this reason, we have studied an electron-microscopic image of a polished side surface of a sample particle in a region very close to the friction contact. Apparently, the friction gives rise to several systems of cracks in the surface layer. One of these systems (Fig. 2) is developed in the plane of the friction contact and is oriented perpendicularly to the friction force (which acts in this case as the tensile force). These cracks propagate and combine to form a highly branched zig-zag fracture surface [6]. We may expect that the corresponding fractal dimensionality of both length and surface on the boundary of such a crack would differ from normal integer values.

Apparently, there exists another system of cracks that are formed under the action of shear stresses also produced by the friction force. The shear regions were clearly pronounced in micrographs of the thoroughly polished and etched side surface (Fig. 2). The shear stresses provide for the formation of a particle contour in the direction of action of the friction force and account for the shear (cleavage) of the whole particle in the plane occurring at certain depth and parallel to the friction surface. The boundaries of the cleavage crack are smooth; hence, the corresponding fractal dimensionality in length in this case differs but little from the Euclidean integer (unity).

Thus, the fractal dimensionality D determined at various points in the boundary contour of worn material particles may provide important information on the mechanisms of crack formation in microscopic regions of the observation sites at the time instants immediately preceding fracture (detachment of the given particle). In addition, this analysis may provide additional information necessary to determine the position of a given particle on the contact surface relative to the friction force direction at the instant of detachment.

REFERENCES

1. Yu. A. Fadin, O. V. Polevaya, and I. N. Popov, Pis'ma Zh. Tekh. Fiz. **19** (22), 62 (1993) [Tech. Phys. Lett. **19**, 725 (1993)].
2. B. B. Mandelbrot, D. E. Passoja, and A. J. Paullay, Nature **308** (5961), 721 (1984).
3. N. P. Suh, Wear **25** (1), 111 (1973).
4. J. Feder, *Fractals* (Plenum Press, New York, 1988; Mir, Moscow, 1991).
5. P. Podsiadlo and G. W. Stachowiak, Wear **217** (1), 24 (1998).
6. I. I. Novikov and V. A. Ermishkin, *Micromechanisms of Metal Fracture* (Nauka, Moscow, 1991).

Translated by P. Pozdeev

Technical Physics Letters, Vol. 26, No. 7, 2000, pp. 563–564. Translated from Pis'ma v Zhurnal Tekhnicheskoĭ Fiziki, Vol. 26, No. 13, 2000, pp. 51–54.

Features of the Ion-Implanted Deuterium Accumulation in Fe–Cr Alloys with Impurities

V. L. Arbuzov, G. A. Raspopova, A. L. Nikolaev, and V. A. Pavlov

Institute of Metal Physics, Ural Division, Russian Academy of Sciences, Yekaterinburg, Russia

e-mail: raspopova@imp.uran.ru

Received February 10, 2000

Abstract—Small additives of silicon and antimony to a Fe–16% Cr alloy differently affect the segregation of ion-implanted deuterium in this material: silicon increases and antimony decreases the degree of deuterium accumulation. The phenomenon is explained by the impurity type influencing the properties of vacancy clusters in the target metal, which serve as traps for the implanted deuterium. *© 2000 MAIK "Nauka/Interperiodica".*

As is known, the structural defects (dislocations, grain boundaries, vacancies, impurity atoms, etc.) in metals may serve as traps for highly mobile hydrogen atoms. However, the resulting hydrogen–defect complexes are in most cases unstable because of small binding energies (0.1–0.2 eV) and readily dissociate even at room temperature (see review [1]). At the same time, we have reported that segregation of the ion-implanted deuterium in metals and alloys related to the trapping of mobile deuterium particles by defects of the vacancy type [2] apparently involves the formation of complexes stable at room temperature.

It is also well known that the structure of vacancy-type defects in alloys depends both on the ion dose and on some other factors. In systems where the vacancies are mobile at room temperature, the related defects frequently represent vacancy clusters. The presence of even small amount of impurities, capable of interacting with vacancies, in metals and alloys may increase the proportion of "survived" vacancies and influence the amount of vacancy clusters. In addition, these impurities can modify the configuration of vacancy clusters. In the presence of impurities, the average cluster size usually decreases. Moreover, the impurity atoms may enter into the cluster configuration. All these factors can alter the pattern of deuterium segregation as compared to that observed in the absence of impurities. Information about these impurity effects is important both from the standpoint of fundamental knowledge of the segregation phenomenon and from the standpoint of solving a practical problem of hydrogen isotope accumulation in the front wall of controlled thermonuclear reactors. Unfortunately, no systematic data concerning the effect of impurities on the hydrogen accumulation are available in literature. The purpose of this work was to study the effect of dopants on the radiation-stimulated segregation of implanted deuterium.

An example of the system featuring stable room-temperature deuterium segregation is offered by the Fe–16% Cr alloy (here and below, at. %) [2]. This is a base material for ferrite steels–candidate front-wall structural materials. Since the properties of vacancies in this alloy are close to those in the pure iron (vacancy migration energy, 0.55 eV [3, 4]), we may estimate the vacancy–impurity interactions in this alloy using the available parameters for iron [5]. According to the published data [5], alloying elements may retard the recovery of positron annihilation parameters in iron in the course of annealing upon a low-temperature electron irradiation. Among the dopants studied, a minimum effect was observed for silicon and a maximum, for antimony. For this reason, we have selected these very elements to study the effect of impurities upon deuterium segregation in the Fe–16% Cr alloy.

The preparation and characterization of the Fe–16% Cr alloy samples were described elsewhere [4, 6]. The main impurities were substitutional Ni (~100 ppm) and interstitial C + N (~200 ppm). The initial (charging) concentrations of silicon and antimony were 0.2 and 0.3 at.%, respectively; the latter value was confirmed by the results of Rutherford backscattering measurements.

The Fe–16% Cr–(Si, Sb) samples were irradiated with 700-keV D^+ ions. This was accompanied by determination of the average deuterium concentration C_D in a 3-μm-thick surface layer. The experimental procedure was described in detail in [2].

The curves of deuterium concentration C_D versus implanted dose Γ for the pure and doped Fe–16% Cr alloys are presented in the figure. As seen, the two impurities differently affect the segregation of ion-implanted deuterium in the target material: silicon increases and antimony decreases the degree of deuterium accumulation.

The impurity-enhanced segregation of deuterium in the Fe–16% Cr–Si alloy is readily explained. Indeed, the presence of silicon increases the number of vacancy

1063-7850/00/2607-0563$20.00 © 2000 MAIK "Nauka/Interperiodica"

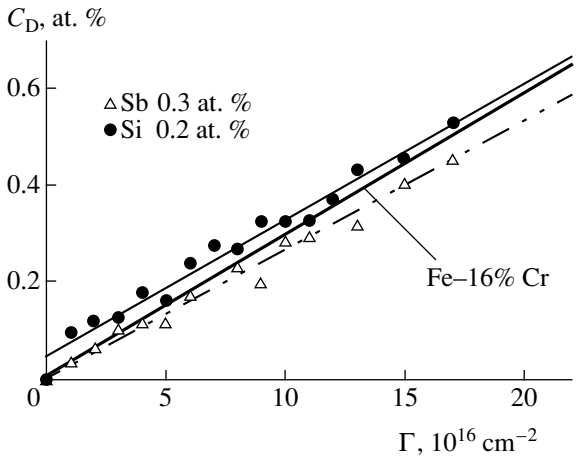

Figure.

clusters formed in the target irradiated with deuterium ions, these clusters being the traps for deuterium. This is a trivial conclusion, according to which any impurity would either enhance the segregation of produce no effect.

The results obtained for the alloy doped with antimony indicates that the effect of impurities on the deuterium segregation has a more complicated character. The binding energy of silicon to vacancy being small, these complexes dissociate already at 260 K [4, 5]. Based on the published data [5], we may expect that the energy of vacancy interaction with dopant atoms in the alloy studied is greater for antimony than for silicon. Accordingly, the number of vacancy clusters formed in the Fe–16% Cr–Sb is greater than that in the pure alloy or in the alloy doped with silicon, while the cluster size distribution is shifted toward smaller values (lower multiplicity). A decrease in the extent of deuterium accumulation with increasing number of the vacancy clusters indicates that the proportion of defects capable of retaining deuterium atoms at room temperature is lower in Fe–16% Cr–Sb than in Fe–16% Cr or Fe–16% Cr–Si alloys.

There are two possible reasons for a decrease in the proportion of vacancy clusters capable of retaining deuterium in the doped alloy: the binding energy of deuterium to the defects may be lower for smaller clusters and in the presence of antimony atoms entering into complex defects. Most probably, the two factors act in phase since the cluster size decreases as a result of vacancy trapping by antimony atoms, with the latter entering into the clusters. More detailed analysis of the process requires additional information that has to be obtained from experiments in progress.

The work was supported by the Russian Foundation for Basic Research, project nos. 98-01-00719 and 96-15-96310.

REFERENCES

1. V. L. Arbuzov, V. B. Vykhodets, and G. A. Raspopova, Metally **4**, 148 (1995).
2. V. L. Arbuzov, G. A. Raspopova, and V. B. Vykhodets, J. Nucl. Mater. **271–272**, 340 (1999).
3. C. Dimitrov, A. Benkaddour, C. Corbel, and P. Moser, Ann. Chim. (Paris) **16**, 319 (1991).
4. A. L. Nikolaev, V. L. Arbuzov, and A. E. Davletshin, J. Phys.: Condens. Matter **9**, 4385 (1997).
5. P. Moser, C. Corbel, P. Lucasson, and P. Hautojarvi, Mater. Sci. Forum **15–18**, 925 (1987).
6. A. L. Nikolaev, J. Phys.: Condens. Matter **11**, 8633 (1999).

Translated by P. Pozdeev

Technical Physics Letters, Vol. 26, No. 7, 2000, pp. 565–566. Translated from Pis'ma v Zhurnal Tekhnicheskoĭ Fiziki, Vol. 26, No. 13, 2000, pp. 55–57.

Bulk Pulsed-Current Magnetostriction of an $YBa_2Cu_3O_{7-x}$ Ceramic Superconductor

E. A. Dul'kin

Institute of Physics, Rostov State University, Rostov-on-Don, Russia

Received January 10, 2000

Abstract—The bulk magnetostriction of an $YBa_2Cu_3O_{7-x}$ ceramic superconductor under the action of dc current pulses was measured at $T = 77$ K with the aid of a differential dilatometer with an error not exceeding 10^{-7}. The magnetostriction in this material is negative and obeys a logarithmic law as function of the current density. It is demonstrated that a considerable contribution to magnetostriction of the $YBa_2Cu_3O_{7-x}$ ceramics is due to the grain boundary layers. © *2000 MAIK "Nauka/Interperiodica".*

As is known, the phenomenon of magnetostriction (MS) in superconductors includes several contributions [1]. In the absence of remagnetization, the main contribution to MS is related to pressure produced by the external magnetic field. This contribution is always negative; that is, it leads to contraction of the samples.

Previously, we have experimentally measured the MS in $YBa_2Cu_3O_{7-x}$ ceramics at $T = 4.2$ K using a capacitive dilatometer [2]. When the magnetic induction was increased, the samples exhibited, in contrast to the theoretical predictions [1], a considerable positive MS. On decreasing the magnetic induction, the MS changed sign. In weak fields (below 1 T), the MS value was of the order of 10^{-7}. The difference in MS values and the change in sign were explained by features of the pinning conditions in $YBa_2Cu_3O_{7-x}$ ceramics.

In order to study the effect of grain boundaries, we have also measured the MS of $YBa_2Cu_3O_{7-x}$ in a magnetic field of the current passed through the samples at $T = 77$ K [3]. The sample response was measured with the aid of a piezoelectric transducer calibrated in the units of pressure. The plot of pressure versus current represented an S-shaped curve with extended linear portion, which attained saturation at a current density of about 200 A/cm^2. The observed nonlinearity was apparently due to the nonlinearity of the piezotransducer. In addition, the acoustic response technique used in [3] is principally incapable of determining the MS sign.

A considerable scatter of data on the MS magnitude and uncertainty of the MS sign stimulated us to perform additional investigation of the MS properties of $YBa_2Cu_3O_{7-x}$ ceramics.

We have studied the samples of $YBa_2Cu_3O_{7-x}$ ceramics in the form of cylinders with a height of 5 mm and a diameter of 2.5 mm. The superconductor ceramics had a density of 4.5–4.8 g/cm^3 and was characterized by $T_c = 92$ K and $\Delta T_c = 2$ K. The MS measurements were performed as described in [4]. The sample was mounted on a polished edge surface of a quartz cylinder in a cryogenic chamber. The differential dilatometry measurements with an error not exceeding 10^{-7} were provided by two rods introduced into the chamber from top. The temperature was measured using a chromel–alumel thermocouple having a junction in direct contact with the sample. The electrical contacts made of copper foil were attached to the sample with a silver paste. The contacts were oriented perpendicularly to the sample and parallel to each other, so as to provide mutual compensation of the currents passing through the contacts. Liquid nitrogen was admitted into the chamber via a special side channel. The MS of the sample at $T = 77$ K was induced by magnetic field of a capacitor discharge current limited by special resistors.

A typical plot of relative MS $\Delta L/L$ versus current density j for a sample of the ceramic composition studied is presented in the figure (part *a*). As seen, the MS is negative and varies as function of the current density according to the logarithmic law. Indeed, the same curve replotted in a logarithmic scale (see figure, part *b*) represents a straight line. Using these data the relative

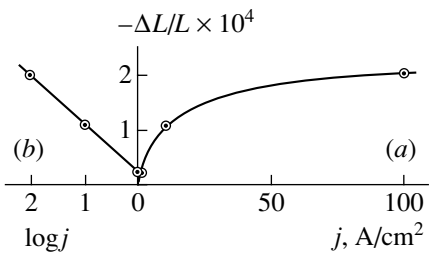

Plots of the relative magnetostriction $\Delta L/L$ versus (*a*) current density j and (*b*) $\log j$ for a $YBa_2Cu_3O_{7-x}$ ceramic sample measured at 77 K.

1063-7850/00/2607-0565$20.00 © 2000 MAIK "Nauka/Interperiodica"

MS variation can be described by the function

$$-\Delta L/L = (0.9\log j)\times 10^{-4}. \quad (1)$$

It should be noted that the MS value obtained in our experiments is greater by three orders of magnitude as compared to the data reported in [2]. The discrepancy can be explained by different temperature conditions (T = 4.2 K in [2] versus 77 K in our work). Another interesting observation is that the samples exhibited partial relaxation toward the initial length upon the capacitor discharge. The relaxation time was of the order of 1 h, which is close to that upon mechanical deformation of the samples of $YBa_2Cu_3O_{7-x}$ ceramics [5]. The inelastic relaxation is usually explained by weak plastic flow in the glassy grain boundary regions during the displacement of ceramic grains [6]. Therefore, the three-order increase in the MS value, accompanying the temperature increase from 4.2 to 77 K, can be attributed to the effect of temperature on the plastic properties of the glassy grain boundary region in the ceramics studied.

REFERENCES

1. G. Brandli, Phys. Condens. Mater. **11** (2), 93 (1970).
2. S. M. Podgornykh, Sverkhprovodimost **2** (10), 93 (1989).
3. A. G. Rozno, V. A. Kozlov, A. S. Lukhin, and V. V. Gromov, Sverkhprovodimost **2** (9), 149 (1989).
4. E. A. Dul'kin, Sverkhprovodimost **6** (2), 314 (1993).
5. I. I. Papirov, V. I. Ivantsov, P. I. Stoev, and V. L. Sobolev, Fiz. Tverd. Tela (Leningrad) **32**, 1540 (1990) [Sov. Phys. Solid State **32**, 901 (1990)].
6. V. S. Bobrov, I. I. Zver'kova, A. P. Ivanov, *et al.*, Fiz. Tverd. Tela (Leningrad) **32**, 826 (1990) [Sov. Phys. Solid State **32**, 487 (1990)].

Translated by P. Pozdeev

Technical Physics Letters, Vol. 26, No. 7, 2000, pp. 567–570. Translated from Pis'ma v Zhurnal Tekhnicheskoĭ Fiziki, Vol. 26, No. 13, 2000, pp. 58–65.

Estimation of the Regular Spike Regime Characteristics of an External-Feedback Injection Laser

V. A. Yurevich

Institute of Applied Optics, Belarussian Academy of Sciences, Mogilev, Belarus

Received January 10, 2000

Abstract—We have theoretically analyzed the conditions of the regular spike generation resulting from the self-phase-modulation of the light field in a cw-pumped external-cavity semiconductor laser. © *2000 MAIK "Nauka/Interperiodica".*

Injection lasers show high sensitivity of the output light field temporal structure with respect to the external feedback level [1]. The output radiation of these lasers exhibits a variety of temporal patterns, from quasi-periodic (leading to a steady-state regime) and regular to chaotic, which is related to the dynamic auto-Q-switching effect [2–5]. The "giant" oscillations of the refractive index in the active layer instantaneously following variations in the concentration of free charge carriers [6] determine the self-phase-modulation of the laser radiation. The cavities consisting of two parts, one of which represents a laser diode with a refractive nonlinearity, may exhibit a phase mismatch. This mismatch initiates a spontaneous (not induced by any external device) Q-switching at the lasing frequencies that may acquire an oscillatory character for a certain relationship between the main parameters of the laser [7].

A practical interest to compact lasers exhibiting a low average level of those oscillations accounts for an intensive development of the computational models of lasers with external feedback in recent years [8–11]. These lasers are capable of producing periodic trains of short pulses without using externally controlled modulators, which makes them suitable for coupling with optical waveguides and integrated optics devices.

In the major part of works (see, e.g., [1–4, 8–11]) the dynamics of external-feedback lasers was analyzed using computational schemes based on modifications of the Kobayashi–Lang equations [12]. This kinetic model uses lumped parameters of a laser and yields an approximate description of its dynamics at the extremely low (about 2–3%) reflectivity of the outcoupling mirror. In this case, we may neglect multiple reflections of the light waves; hence, the amplified frequency cannot correspond to any mode of a complex cavity. Then, it is hardly possible to study the influence of the feedback level on the output radiation dynamics. We inevitably ignore the laser frequency "scanning" over the external cavity modes in the course of the cavity self-tuning [6]. The "giant" nonlinear refraction (NR) in the active layer leads to the light wave frequency scanning over unequally spaced resonances of a feedback laser representing a bistable system. A hysteresis character of the Q-switching determines peculiarities of the output radiation variation with time.

In this work, we propose a system of dynamic equations describing the intensity oscillations in a laser with external feedback (see a schematic diagram in Fig. 1a) and study the stability of solutions. Note that a self-consistent energy exchange between the medium and the transverse mode of the coupled cavity implies a possible self-modulation tuning of the latter. The computational scheme includes equations for the normalized intensity of the mode $I(t)$ and for the inverse population variation $n(t)$ normalized to a threshold inversion value. The former equation takes into account the radiation losses related to the light field phase variation due to nonlinear refraction in the active layer:

$$\begin{cases} \dfrac{dI}{dt} = \dfrac{1}{T_r}\left[n + \ln\left(1 - \dfrac{R_2 \sin^2\Delta\varphi}{1 + R_1 \sin^2\Delta\varphi}\right)\right]I, & (1) \\ \dfrac{dn}{dt} = \dfrac{1}{\tau}[\sigma - (1 + I)(1 + n)]. & (2) \end{cases}$$

Here,

$$R_1 = \frac{4\sqrt{r_0 r}}{(1 + \sqrt{r_0 r})^2}, \quad R_2 = \frac{(1 - r_0)(1 - r)}{(\sqrt{r} + \sqrt{r_0})^2} R_1,$$

$$R = \frac{(1 + r)}{(1 + r_0)}\sqrt{\frac{r_0}{r}}, \quad T_r = \left[\eta l + \frac{(1 - r_0)L}{(1 + r_0)(1 + R)}\right]/(cY)$$

$$Y = \rho + \ln\left(\frac{1 + \sqrt{r_0 r}}{r_0 + \sqrt{r_0 r}}\right)$$

(T_r is the photon lifetime in the coupled cavity and Y represents the cavity losses). The radiation losses (logarithmic term in (1)) are determined by the variable $\Delta\varphi = [\phi(t) - \phi(t - T)]/2(T = 2L/c)$ depending on the difference of the resonance frequencies of the "active"

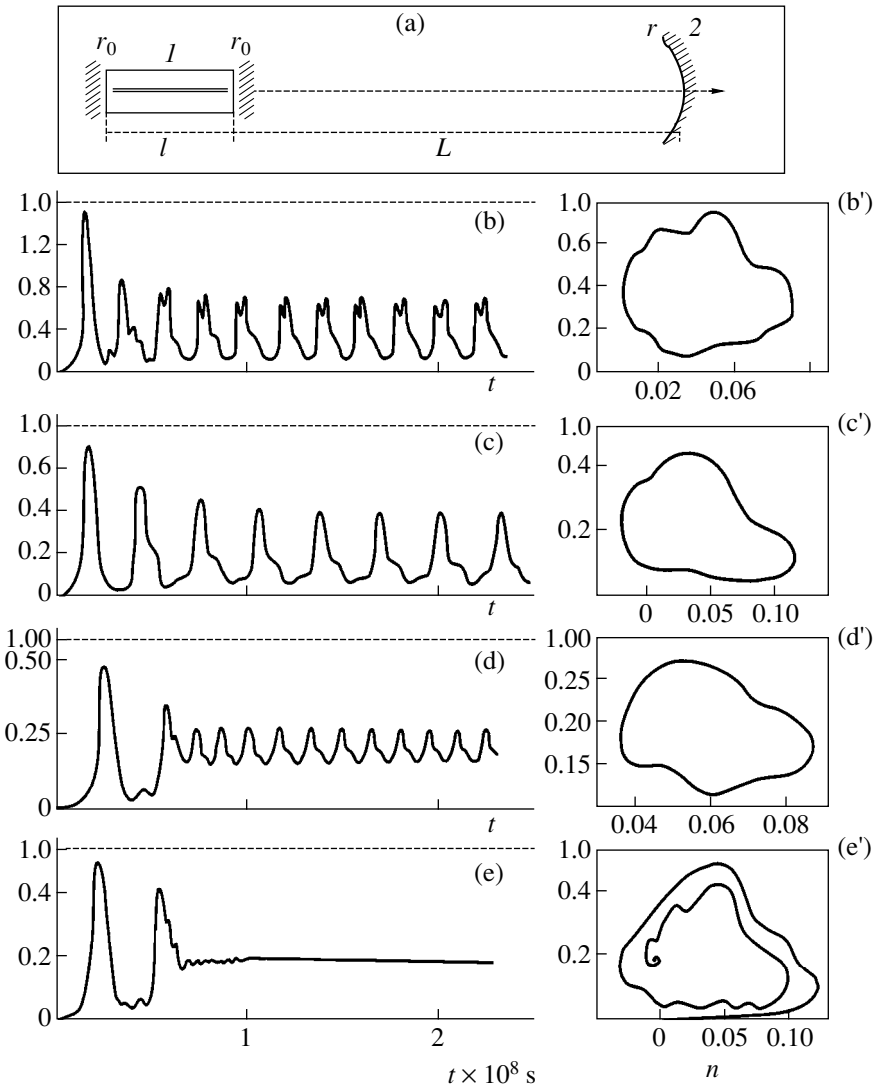

Fig. 1. (a) Schematic diagram of a laser with external cavity: (*1*) amplifying element with the length of the active layer l and the facet reflectivity $r_0 \approx 0.32$, (*2*) an external mirror with the reflectivity r. (b)–(e) Plots of the output intensity versus time for the laser with external mirror and the refraction nonlinearity in the active layer and (b')–(e') the corresponding phase portraits: $\sigma = 1.34$ (b), 1.2 (c–e); $r = 0.57$ (b, c), 0.43 (d), 0.41 (e); L = (b) 0.03, (c–e) 0.04 m; $\alpha = 3$; $\rho = 1.02$; $\tau = 1.5 \times 10^{-9}$ s; $l = 3 \times 10^{-4}$ m.

(containing the active element) and "passive" (external cavity) parts of the laser. The values of the variable $\phi(t)$ are determined from the condition of phase matching between the "active" and "passive" parts:

$$\tan\left\{\left[\frac{\eta\phi}{L} + \beta(n - n_0)\right]l\right\} = -\frac{1 - r_0}{1 + r_0}\frac{\sin\phi}{R + \cos\phi}. \quad (3)$$

In equations (1)–(3), σ/τ is the pumping rate parameter (τ being the longitudinal relaxation time, or the spontaneous recombination time for semiconductors) and η and ρ are the active layer refractive index and the linear absorption coefficient, respectively. To the first approximation, the NR parameter β is a coefficient of proportionality in the expression relating variations of the carrier density and the refractive index [6]. The values of the parameter α representing the ratio of β to the threshold gain coefficient for the field frequencies corresponding to interband transitions were repeatedly and thoroughly measured [13]. In the above notation $\alpha = \beta l/Y \sim 3$–5, which agrees well with the values of this parameter used for estimating the NR effects [1–5, 8–11].

The models of the systems with external feedback used in [14] and, later on, in [5, 15] assume the possible variation of Q at the lasing frequency. The system of equations (1)–(3) is based on a model with distributed parameters [14] and can be used to analyze the behavior of pulsed lasers in a wider range of reflectivities in the external feedback. In the course of Q-switched lasing, such systems evidently pass over a series of equilibrium states with different stabilities. We used the parameters of GaAs-based injection lasers for simula-

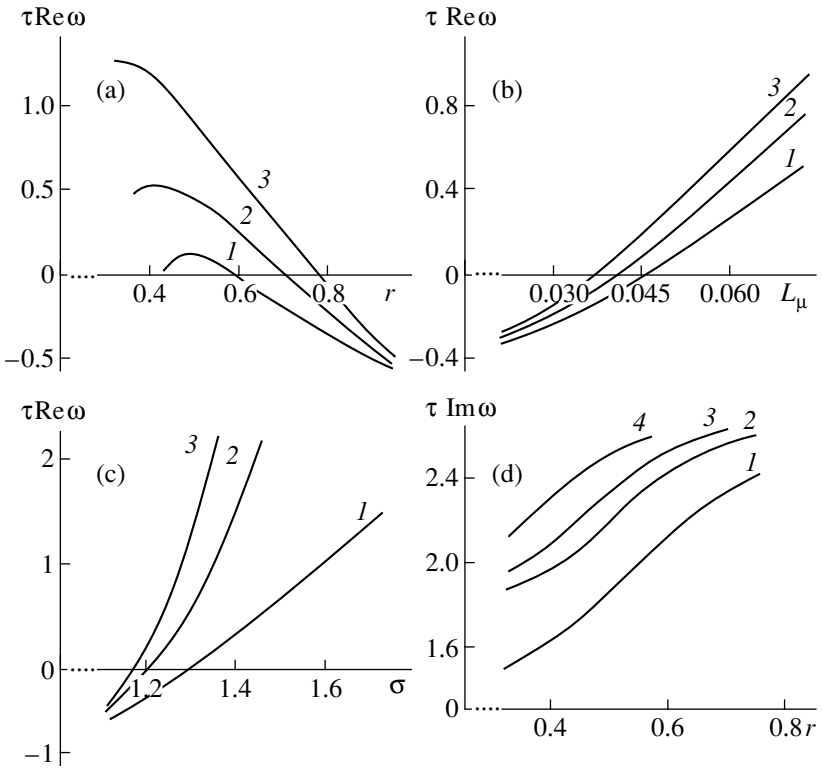

Fig. 2. Plots of the real and imaginary parts of the roots of the characteristic equation versus the parameters of the system of equations (1)–(3): (a) $\sigma = 1.2$ (*1*), 1.25 (*2*), 1.33 (*3*), $L = 0.04$ m; (b) $r = 0.37$ (*1*), 0.57 (*2*), 0.48 (*3*), $\sigma = 1.2$; (c) $L = 0.05$ (*1*), 0.04 (*2*), 0.025 m (*3*), $r = 0.5$; (d) $L = 0.03$ (*1*), 0.04 (*2*), 0.045 (*3*), 0.06 m (*4*), $\sigma = 1.25$; $\alpha = 3$; $\rho = 1.02$; $\tau = 1.5 \times 10^{-9}$ s; $l = 3 \times 10^{-4}$ m.

tion of the output of the lasers with external feedback. Assume that in the initial moment the system amplifies a relatively weak field ($I(t = 0) = I_0 \ll \sigma - 1$, $n(t = 0) = n_0 \geq 0$, $\phi(t = 0) = 0$). The structure of numerical solutions for $I(t)$ (Figs. 1b–1e) exhibit no significant qualitative dependence on I_0 or n_0 and slightly differ from each other only by the amplitude and contrast of pulses in the transition stage before attaining a regular spike regime or passing to the stationary regime. These solutions showed that at certain combinations of the parameters the system of equations (1)–(3) describes the regime of the output power self-modulation oscillations attained for a constant pumping current. Phase portraits of the autooscillations in Figs. 1b'–1c' exhibit attractors representing a limiting cycle that may in fact spontaneously occur in the injection lasers [1]. The main reason of this phenomenon is the laser field self-phase-modulation under the conditions of intracavity interference in the system with external feedback. The above solutions for $I(t)$ admit only relatively slow oscillations in the output radiation (on the nano- or subnanosecond time scale at the given values of parameters). The pulse characteristics (repetition rate, duration, contrast, and peak intensity I) mainly depend on the relationship between the model parameters. The time variation of the laser intensity following from the solution of equations (1)–(3) does not exhibit high-frequency ("fine") field structure predicted by solutions of the refined models [14, 15] and controlled in the general case by chaos [5].

Let us consider the stability of the solutions with respect to small deviations from the initial equilibrium states. Specifically, the solutions of (1)–(3) are stable in the vicinity of the fundamental steady state determined by $n_{S0} = 0$ and $I_{S0} = \sigma - 1$ (output intensity represents a train of pulses decaying to the constant level I_{S0} at the characteristic time τ/σ). At a certain combination of parameters in (1)–(3) the solutions can be unstable near the equilibrium state given by $n_S = -\ln[1 - R_1/(1 + R_2)]$, $I_S = \sigma/(1 + n_S) - 1$, and $\Delta\varphi = \pi$. This state is next to the fundamental one in the frequency scale, where both of them correspond to neighbor modes of the coupled cavity. The instability can easily be demonstrated by performing linear expansion around the solution I_S, n_S. In this case the spectrum of the complex harmonic solutions with small amplitudes represented as $\exp(\omega t)$ emerges from the solution of the characteristic equation:

$$\omega^2 + \frac{\sigma}{(1 + n_S)\tau}\omega + A\{1 + B[1 - \exp(-\omega T)]\} = 0, \quad (4)$$

where

$$A = \frac{(\sigma - 1 - n_S)}{T_r \tau},$$

$$B = \frac{\beta L}{\eta Y} \frac{(1-r)(1-r_0)\sqrt{r_0 r}}{(1 + r_0 r + \pi\sqrt{r_0 r})(r + r_0 + \pi\sqrt{r_0 r})}.$$

In the general case, the quasi-polynomial (4) may have a multitude of the complex roots ω_j. Oscillations with the frequency $\mathrm{Im}(\omega_j)$ decay or grow at the rate $\mathrm{Re}(\omega_j)$. The absolute values of the characteristic frequencies are usually much smaller than the inverse round trip time: $|\omega_j| \ll 1/T$. Under this approximation, the characteristic polynomial (4) can be reduced to a simple relationship:

$$\left(1 - \frac{1}{2}ABT^2\right)\omega^2 - \left[ABT - \frac{\sigma}{(1+n_S)\tau}\right]\omega + A = 0. \quad (5)$$

Equation (5) provides an estimate of the instability interval near the equilibrium state of the fundamental harmonics. Their stability is exclusively determined by the sign of $\mathrm{Re}\,\omega$. It is necessary to meet the instability condition $\mathrm{Re}\,\omega$ to make possible solutions $I(t)$ in the form of output intensity autooscillations. Figures 2a–2c show the combinations of parameters in (1)–(3) corresponding to $\mathrm{Re}\,\omega > 0$. Note a threshold character of the instability development. The solutions of the initial system $I(t)$ corresponding to periodic oscillations apparently exhibit limited amplitudes that correlate with the pumping parameters and the cavity losses. For this reason, it is highly probable that the solutions reach the limiting cycle (corresponding to a regular self-modulation spike regime) if the oscillations develop in the unstable way. The frequency of these self-modulation periodic oscillations roughly equals the imaginary part of the solution of (5) (Fig. 2d) and depends on the relationship between the relaxation constants of the model (1)–(3).

REFERENCES

1. K. Petermann, IEEE J. Sel. Top. Quantum Electron. **1**, 480 (1995).
2. A. Ritter and H. Haug, J. Opt. Soc. Am. B **10**, 145 (1993).
3. A. M. Levine, G. van Tarwijk, D. Lenstra, and T. Erneux, Phys. Rev. A **52**, R3436 (1995).
4. N. Hirono, N. Kurosaki, and M. Fukuda, IEEE J. Quantum Electron. **QE-32**, 829 (1996).
5. V. A. Yurevich, Pis'ma Zh. Tekh. Fiz. **22** (19), 10 (1996) [Tech. Phys. Lett. **22**, 781 (1996)].
6. P. G. Eliseev and A. P. Bogatov, Tr. Fiz. Inst. Akad. Nauk SSSR **166**, 16 (1986).
7. V. I. Borisov, V. I. Lebedev, and V. A. Yurevich, Zh. Prikl. Spektrosk. **51**, 207 (1989).
8. Y. Liu, N. Kikuchi, and J. Ohtsubo, Phys. Rev. E **51**, R2697 (1995).
9. G. van Tarwijk and M. San Miguel, IEEE J. Quantum Electron. **QE-32**, 1191 (1996).
10. K. Wada, T. Umeda, and Y. Cho, Opt. Commun. **109** (2), 93 (1996).
11. C. Masoller, IEEE J. Quantum Electron. **QE-33**, 796 (1997).
12. R. Lang and J. Kobayashi, IEEE J. Quantum Electron. **QE-16**, 347 (1980).
13. M. Osinski and J. Buus, IEEE J. Quantum Electron. **QE-23**, 9 (1987).
14. S. N. Krasovskaya, S. V. Zhestkov, V. I. Lebedev, and V. A. Yurevich, Pis'ma Zh. Tekh. Fiz. **18** (3), 24 (1992) [Sov. Tech. Phys. Lett. **18**, 69 (1992)].
15. V. A. Yurevich, Izv. Vyssh. Uchebn. Zaved., Radiofiz. **38**, 1204 (1995).

Translated by A. Chikishev

Technical Physics Letters, Vol. 26, No. 7, 2000, pp. 571–572. Translated from Pis'ma v Zhurnal Tekhnicheskoĭ Fiziki, Vol. 26, No. 13, 2000, pp. 66–70.

Periodic-Pulse Relativistic Magnetron

L. D. Butakov, I. I. Vintizenko, V. I. Gusel'nikov, M. I. Dvoretskiĭ, P. Ya. Isakov, V. L. Kaminskiĭ, A. I. Mashchenko, V. Yu. Mityushkina, A. I. Ryabchikov, N. M. Filipenko, G. P. Fomenko, É. G. Furman, and V. P. Shiyan

Research Institute of Nuclear Physics, Tomsk Polytechnic University, Tomsk, Russia

Received January 10, 2000

Abstract—We report on the main elements of design of a periodic-pulse relativistic magnetron supplied from an induction linac. Operating in a 10-cm wavelength range, the magnetron provides for a pulse power of 200 MW, an average power of up to 3 kW, and a pulse repetition rate of 320 Hz. © *2000 MAIK "Nauka/Interperiodica".*

The first works on the relativistic magnetrons operating in a periodic-pulse regime date back to the 1980s [1, 2]. The magnetron described in [1] was supplied from an induction linac section with a multichannel spark gap commutator of the stripe forming lines. In the 1990s, new induction linacs with saturation-choke magnetic commutators were developed that allowed the magnetron pulse rate to be increased up to 10^3–10^4 Hz [3, 4]. Figure 1 shows a general view of the new periodic-pulse relativistic magnetron with a magnetic commutator system and a source representing a section of the LIU 0.4/4000 induction linac.

1. Linac section. The main parts of the linac section are the accelerator module and the pulsed power supply unit. A distinguishing feature of the LIU 0.4/4000 induction linac module design [4] is that a common cylindrical case accommodates the main parts (including ferromagnetic induction system, strip lines, magnetic commutator, and inductor core demagnetizing system) together with the magnetic pulse generator. The latter comprises a pulse transformer and the elements of compression stages.

This design minimizes the inductance of chains linking the compression stages and stripe forming lines, thus reducing the energy losses and increasing efficiency of the linac section. In addition, the decrease in inductance allows the stripe lines to be charged from the magnetic pulse generator within several hundreds of nanoseconds, which allows the frequency potential (a few kilohertz) of the magnetic commutator to be effectively employed [4]. Finally, this design decreases the overall module size to virtually a minimum level.

The linac section is power supplied from a unit comprising a three-phase source for oscillatory charging of the primary storage and a thyristor commutator operating in the interval of switching frequencies from 0.4 to 320 Hz.

2. Magnetic system. Continuous operation of the relativistic magnetron is provided by a magnetic system

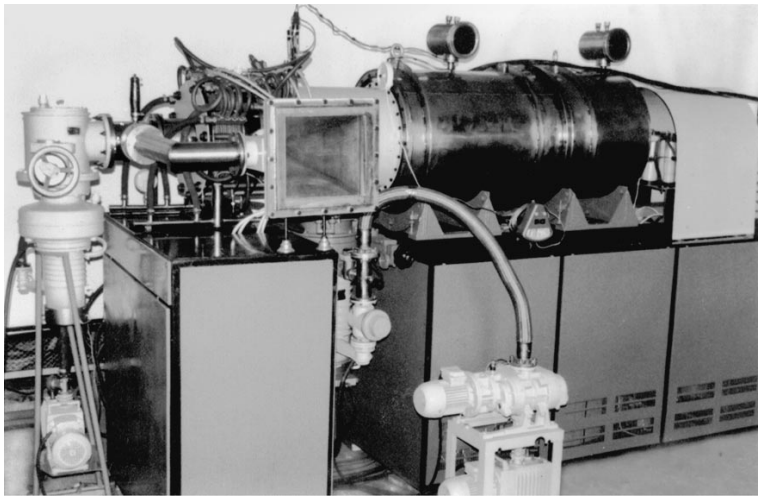

Fig. 1. General view of the periodic-pulse relativistic magnetron.

1063-7850/00/2607-0571$20.00 © 2000 MAIK "Nauka/Interperiodica"

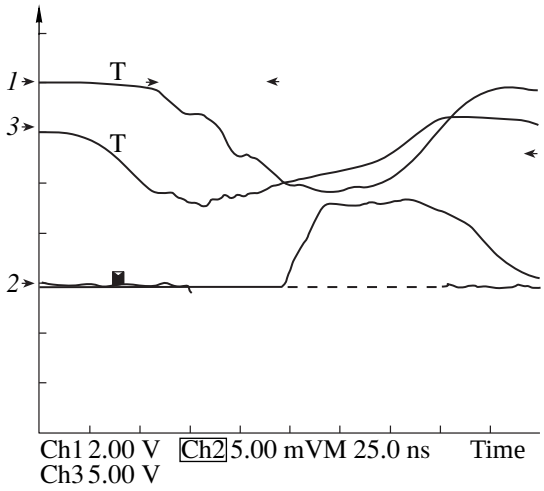

Fig. 2. Oscillograms illustrating operation of the periodic-pulse relativistic magnetron: (*1*) current; (*2*) SHF detector output; (*3*) voltage (time scale: 25 ns per division).

based on the Helmholtz coils made of a hollow copper profile (8.5 × 8.5 mm) with a 5-mm-diam central channel carrying a cooling fluid. Each coil of the magnetic system comprises seven double plane-parallel sections, with a total number of turns in the coil amounting to 196. A magnetic field of 0.4 T is obtained by passing a current of 400 A (at a current density of 8.2 A/mm^2).

The coil sections are connected in series with respect to current, while the coolant channels are connected in parallel. The magnetic system provided for the relativistic magnetron operation at a magnetic field of 0.4 T in the continuous regime and up to 0.5 T in a periodic-pulse mode (3 min work, 10 min pause).

3. Magnetron. The relativistic magnetron is provided, unlike those described previously [1], with water-cooled jacket of the anode unit and a graphite cathode capable of withstanding high temperature. Additional advantages of this cathode are a low threshold for the explosive electron emission and a sufficiently high working resource, which ensures production of a large number of pulses before a significant loss of emissivity.

The resonance system of the magnetron was specially adopted to work with a source of the linac section type. This implies matching a significant difference in impedance between magnetron in the working regime and the linac and taking into account a possible variation of the anode voltage amplitude during the pulse. The magnetron design was improved so that to increase the resistance of commutator segments with respect to damage produced by the incident electrons. The SHF radiation is extracted from magnetron via a coupling slot in one of the anode unit resonators, a smooth waveguide coupler, and a pyramidal antenna.

The magnetron operation in a periodic regime is accompanied by intensive gas evolution because of a large amount of material evaporated from cathode and ion desorption from the anode unit bombarded with electrons. In order to maintain a working vacuum level under these conditions, the setup is equipped with a vacuum system comprising a set of oil diffusion pumps with liquid-nitrogen traps which ensured the magnetron evacuation at a pumping rate of 2000 l/s from the side of the vacuum chamber and 500 l/s from the side of the drift tube. An additional vacuum stage was provided for the evacuation of antenna and interelectrode gap via the SHF waveguide output port. The oil diffusion pumps were selected because, in our opinion, this type is best suited to deal with variable (pulsating) gas ejections and to pump hydrogen that accounts for a considerable part of the total gas evolution.

4. Performance characteristics. Use of the system design elements mentioned above (linac section with magnetic commutator of stripe lines; power supply system with stabilized charging voltage of the primary storage; magnetic system supplied from a dc current source; relativistic magnetron adopted to the linac parameters; high-power pumping stage) allowed the magnetron to be operated in various regimes: continuous (0.4–8 Hz); periodic-pulse (8–80 Hz), and pulse-train (80–320 Hz) with up to 10^3 pulses in the train and high reproducibility of the amplitude and shape of the output pulses. Typical oscillograms are presented in Fig. 2.

The main performance characteristics of the periodic-pulse relativistic magnetron supplied from an injection linac section are as follows:

Voltage (*U*),	400 kV
Current (*I*),	4 kA
Pulse width (FWHM)	110 ns
SHF power (*U* = 360 kV, *I* = 3 kA),	200 MW
Average SHF power,	3 kW
Pulse rate,	0.4–320 Hz
Magnetron frequency,	2840 MHz
Radiation bandwidth,	<2%
SHF pulse width (FWHM),	45 ns
Magnetic induction,	≤0.5 T
Magnetic field inhomogeneity (along anode unit axis),	<4%
Current pulsations in magnetic system,	<0.1%

REFERENCES

1. V. V. Vasil'ev, I. I. Vintizenko, A. N. Didenko, *et al.*, Pis'ma Zh. Tekh. Fiz. **13**, 762 (1987) [Sov. Tech. Phys. Lett. **13**, 317 (1987)].
2. D. A. Phelps, in *Abstracts of the 7th International Conference on High-Power Particle Beams, Karlsruhe, 1988*, p. 321.
3. S. Ashby, R. Smith, N. Aiello, *et al.*, IEEE Trans. Plasma Sci. **20**, 344 (1992).
4. É. G. Furman, V. V. Vasil'ev, O. N. Tomskikh, *et al.*, Prib. Tekh. Éksp., No. 6, 46 (1993).

Translated by P. Pozdeev

Technical Physics Letters, Vol. 26, No. 7, 2000, pp. 573–575. Translated from Pis'ma v Zhurnal Tekhnicheskoĭ Fiziki, Vol. 26, No. 13, 2000, pp. 71–78.

Nonparaxial Gaussian Beams: 1. Vector Fields

A. V. Volyar

Simferopol State University, Simferopol, Ukraine

Received November 25, 1999

Abstract—Rigorous analytical solutions were obtained for the vector field of a propagating nonparaxial Gaussian beam in the vicinity of the beam focus. It is demonstrated that a nonparaxial beam of the lowest order has six modes. Upon the limiting transition $kz_0 \gg 1$, four of these modes exhibit degeneracy and convert into a paraxial Gaussian beam, while the other two modes form the azimuth-symmetric TE and TM fields. A characteristic feature of the nonparaxial modal beam is the absence of symmetry between (still mutually orthogonal) electric and magnetic fields. The deviation from symmetry results in the appearance of negative energy fluxes in the vicinity of the phase singularity manifested by Airy's fringes, "light drops" (special states of the light field), and "singularity islands". The obtained results are in good agreement with other relevant data published.

Description of the evolution of a strongly focused laser beam in the crossover region characterized by interference of homogeneous and evanescent waves [1] requires a vector field representation. Such a vector description, based on the scalar function of a nonparaxial modal beam represented as a superposition of flat waves [2], was developed by Agrawal and Patanyak [3] and refined by Davis [4]. However, an approximate boundary condition introduced in [3], according to which the beam field in the crossover region $z = 0$ must have a Gaussian profile, cuts evanescent waves from the spatial spectrum of beam modes. This, together with integral representation of the scalar field, markedly restricts applicability of the scalar potential method.

The purpose of this work was to study evolution of the vector field of a nonparaxial Gaussian beam based on an analytical representation of the Whittacker potentials [3] and an approximate boundary condition according to Davis [5], requiring that the field would remain Gaussian near the optical axis.

1. According to [6, 7], all components of the vectors of electric $\mathbf{e}(\mathbf{r})$ and magnetic $\mathbf{h}(\mathbf{r})$ fields in the free space and in a homogeneous isotropic medium with a dielectric permittivity ε can be represented in a unified manner provided that rigorous solutions $\Psi_1(\mathbf{r})$ and $\Psi_2(\mathbf{r})$ are obtained for the scalar Helmholtz equation

$$(\nabla^2 + k^2)\Psi(\mathbf{r}) = 0. \qquad (1)$$

Here, $\Psi_1(\mathbf{r})$ and $\Psi_2(\mathbf{r})$ represent the Whittacker potentials, $\mathbf{r} = \{x, y, z\}$, $k = 2\pi/\lambda$, and λ is the wavelength. The scalar potentials $\Psi_1(\mathbf{r})$ and $\Psi_2(\mathbf{r})$ are related to the field vectors by the following relationships:

$$\mathbf{e} = \nabla \times \nabla \times (\hat{\mathbf{n}} \cdot \Psi_1) - ik\nabla \times (\hat{\mathbf{n}} \cdot \Psi_2), \qquad (2)$$

$$\mathbf{h} = -\sqrt{\varepsilon}\nabla \times \nabla \times (\hat{\mathbf{n}} \cdot \Psi_2) - i\varepsilon k_0 \nabla \times (\hat{\mathbf{n}} \cdot \Psi_1), \qquad (3)$$

where $\hat{\mathbf{n}}$ is the constant basis vector and k_0 is the wavenumber in vacuum.

Using the Lorentz gauge, the Whittacker potentials (Ψ_1, Ψ_2) and the vector potential $\mathbf{A}$ can be related as [3]

$$\mathbf{A} = -i\varepsilon k_0(\hat{\mathbf{n}} \cdot \Psi_1) - \sqrt{\varepsilon}\nabla \times (\hat{\mathbf{n}} \cdot \Psi_2).$$

In order to obtain a rigorous analytical solution to equation (1) for a nonparaxial beam, let us place a point source on the optical beam axis z at a point with the imaginary coordinate $z = iz_0$ (z_0 is the beam diameter) [8, 9]. The solution can be found in the form

$$\Psi_1 = A(1/k^2) j_l(kr) P_{ml}(\cos\vartheta)\exp(il\varphi), \qquad (4)$$

where $j_l(kr)$ is the lth-order Bessel spherical function of the first kind, $P_{ml}(\cos\vartheta)$ is the Legendre associated function [10] ($l = 1, 2$; $m = 1, 2, \ldots$), φ is the azimuthal angle, and

$$r^2 = x^2 + y^2 + (z + iz_0)^2. \qquad (5)$$

As was demonstrated in [9], a scalar field of the type (4) can be transformed, for $kz_0 \gg 1$ and $m = 0$, into the field of a paraxial Gaussian beam. This corresponds to the approximated boundary condition according to Davis [5], provided that $z_0 = k\rho^2/2$ (the Rayleigh length), where ρ is the beam radius at $z = 0$ (crossover) and $A = (kz_0)/sh(kz_0)$.

The base vector $\hat{\mathbf{n}}$ entering in relationships (2) and (3) can be selected in three independent ways: (i) {1, 0, 0}, (ii) {0, 1, 0}, or (iii) {0, 0, 1}. In addition, linearity of the medium in which the beam propagates allows us to pose the conditions (iv) $\Psi_1 \neq 0$, $\Psi_2 = 0$ or (v) $\Psi_1 = 0$, $\Psi_2 \neq 0$. These conditions stipulate the existence of six field solutions for a given pair of indexes (l, m). Note that the latter two conditions imply separation of the modes with respect to parity [3], while the former three conditions separate the fields with respect to the polar-

Mode fields of a nonparaxial Gaussian beam of the lowest order ($m = 0$)

Mode	$\mathbf{e}_t$	e_z	$\sqrt{\mu_0/\varepsilon_0}\mathbf{h}_t$	$\sqrt{\mu_0/\varepsilon_0}h_z$
LP(e_y)	$\hat{\mathbf{y}} \cdot ik(z + iz_0)F_1$	$(i/k)\dfrac{\partial F_0}{\partial R}\sin\varphi$	$\cdot\,\hat{\mathbf{x}}G_1 + (\hat{\mathbf{x}}\cos\varphi + \hat{\mathbf{y}}\sin\varphi)F_2k^2R^2\cos\varphi$	$-(z + iz_0)\dfrac{\partial F_0}{\partial R}\cos\varphi$
LP(e_x)	$-\hat{\mathbf{x}} \cdot ik(z + iz_0)F_1$	$-(i/k)\dfrac{\partial F_0}{\partial R}\cos\varphi$	$\cdot\,\hat{\mathbf{y}}G_1 + (\hat{\mathbf{x}}\cos\varphi + \hat{\mathbf{y}}\sin\varphi)F_2k^2R^2\sin\varphi$	$-(z + iz_0)\dfrac{\partial F_0}{\partial R}\sin\varphi$
LP(h_y)	$\cdot\,\hat{\mathbf{x}}G_1 + (\hat{\mathbf{x}}\cos\varphi + \hat{\mathbf{y}}\sin\varphi)F_2k^2R^2\cos\varphi$	$-(z + iz_0)\dfrac{\partial F_1}{\partial R}\cos\varphi$	$-\hat{\mathbf{y}} \cdot ik(z + iz_0)F_1$	$-(i/k)\dfrac{\partial F_0}{\partial R}\sin\varphi$
LP(h_x)	$\cdot\,\hat{\mathbf{y}}G_1 + (\hat{\mathbf{x}}\cos\varphi + \hat{\mathbf{y}}\sin\varphi)F_2k^2R^2\sin\varphi$	$-(z + iz_0)\dfrac{\partial F_1}{\partial R}\sin\varphi$	$\hat{\mathbf{x}} \cdot ik(z + iz_0)F_1$	$(i/k)\dfrac{\partial F_0}{\partial R}\cos\varphi$
TE	$\cdot\,i(\hat{\mathbf{x}}\sin\varphi - \hat{\mathbf{y}}\cos\varphi)F_1kR$	0	$(\hat{\mathbf{x}}\cos\varphi + \hat{\mathbf{y}}\sin\varphi)F_2k^2R(z + iz_0)$	$G_1 + k^2(z + iz_0)^2F_2$
TM	$(\hat{\mathbf{x}}\cos\varphi + \hat{\mathbf{y}}\sin\varphi)F_2k^2R(z + iz_0)$	$G_1 + k^2(z + iz_0)^2F_2$	$\cdot\,-i(\hat{\mathbf{x}}\sin\varphi - \hat{\mathbf{y}}\cos\varphi)F_1kR$	0
$F_0 = j_0(kr)$; $F_1 = j_i(kr)/(kr)$; $F_2 = j_2(kr)/(kr)^2$; $G_1 = F_0 - F_1$			$r = \sqrt{R^2 + (z + iz_0)^2}$, $R^2 = x^2 + y^2$; $i = \sqrt{-1}$	

ization direction. Analytical expressions for the field components of a nonparaxial beam calculated based on equations (2)–(4) are presented in the table.

2. As seen from the table, a nonparaxial beam of the lowest order ($m = 0$) contains six modes. Four of these modes—$LP(e_x)LP(e_y)LP(h_x)LP(h_y)$—exhibit no phase singularity of the transverse components on the optical axis ($R = 0$) and convert at $kz_0 \gg 1$ into a paraxial Gaussian beam. The other two modes, TE and TM, exhibit a polarization disclination on the axis [11]. The notation $LP(e_{x,y})LP(h_{x,y})$, introduced by analogy with that used for the field modes in cylindrical optical fibers [12], indicates the homogeneous linear polarization of the electric or magnetic field along a preset direction (LP = linearly polarized). For the axisymmetric beams, the fields $LP(e_x)LP(h_x)$ can be obtained from $LP(e_y)LP(h_y)$ through rotation by $\pi/2$ and, hence, are degenerate. However, any small deformation of the beam cross section would lift up the degeneracy.

It should be specially noted that the electric and magnetic fields, albeit exhibiting no mutual symmetry in each mode of the nonparaxial beam, are still mutually orthogonal: $(\mathbf{e} \cdot \mathbf{h}) = 0$. The asymmetry of these fields gives rise to a negative energy flux toward the optical axis $P_z = (1/2)\mathrm{Re}(e_xh_y^* - e_yh_x^*)$, which appears during a contour passage of the phase singularity points–Airy's fringes, where $\mathrm{Re}\,\Psi = \mathrm{Im}\,\Psi = 0$ [13, 14]. This behavior of the longitudinal energy flux component P_z is illustrated in Fig. 1. Figure 2 shows a map of the intensity and phase distribution for the $LP(h_y)$ nonparaxial beam mode. The pattern exhibits clearly pronounced Airy's fringes and a "Maltese cross" in the z-component of the field intensity. The phase distribution exhibits singularity points corresponding to intersection of the wave front sheets. Note that the density of the intensity zeros (nodes) displays "singularity islands" rather than a uniform distribution over the ring.

A symmetry in representation of the electric and magnetic fields of a nonparaxial beam can be obtained by taking the superpositions of modes

$$\begin{aligned} LP(eh)_y &= LP(e_y) \pm LP(h_y), \\ LP(eh)_x &= LP(e_x) \pm LP(h_x). \end{aligned} \tag{6}$$

However, this by no means implies that the resulting fields are regular. On the contrary, it can be demonstrated (this is the subject of subsequent publications) that the symmetric fields may give rise to complex wave states: "light drops" in which $\int P_z dS = 0$. It should be noted that the field structure of the nonparaxial Gaussian beam modes is closely similar to the field structure of lowest modes of a cylindrical stepped optical fiber (see, e.g. [12, Table 12.3]) upon replacing the spherical Bessel functions $j_l(x)$ with their cylindrical analogs $J_l(x)$ and $K_l(x)$.

The nonparaxial character of the beam is especially clearly manifested for the TE and TM modes, in which the z-component of the field intensity is greater by the order of magnitude as compared to the corresponding transverse component.

3. In order to provide for the comparison of our results with the published data, it is convenient to write relationships (see table) between the longitudinal and transverse field components of the LP modes:

$$LP(e_y)\text{-mode} \quad e_z/e_y = -i\eta f/(1 + i\zeta), \tag{7}$$

$$LP(h_y)\text{-mode} \quad e_z/e_x \approx -i\xi f/(1 + i\zeta), \tag{8}$$

where $f = \rho/z_0$, $\xi = x/\rho$, $\eta = y/\rho$, and $\zeta = z/z_0$. These

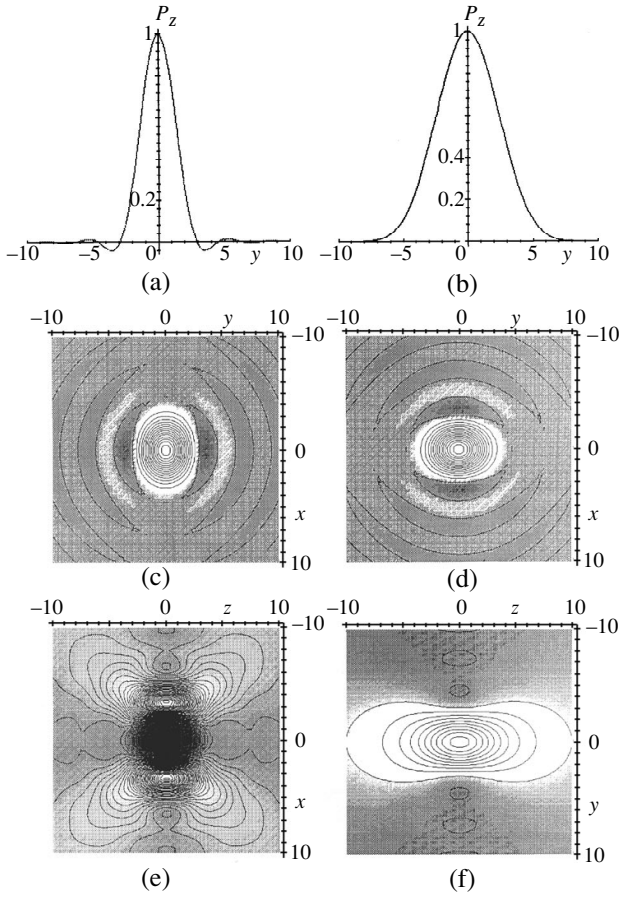

Fig. 1. Plots of the normalized longitudinal energy flux component P_z versus radial coordinate R for the $LP(e_y)$ modes with $\varphi = 0$, $z = 0$, and different Rayleigh lengths $z_0 = 1$ (a) and 10 (b). Maps of the P_z intensity: (c) even $LP(e_y)$ mode ($z_0 = 1$); (d) odd $LP(h_y)$ mode ($z_0 = 1$); (e) $LP(e_y) + LP(h_y)$ combination ($z_0 = 2.6$) with $\int P_z dS = 0$ ("light drop"); (f) $LP(e_y) - LP(h_y)$ combination (quasi-Gaussian beam). All lengths are expressed in the units $k = 2\pi/\lambda$.

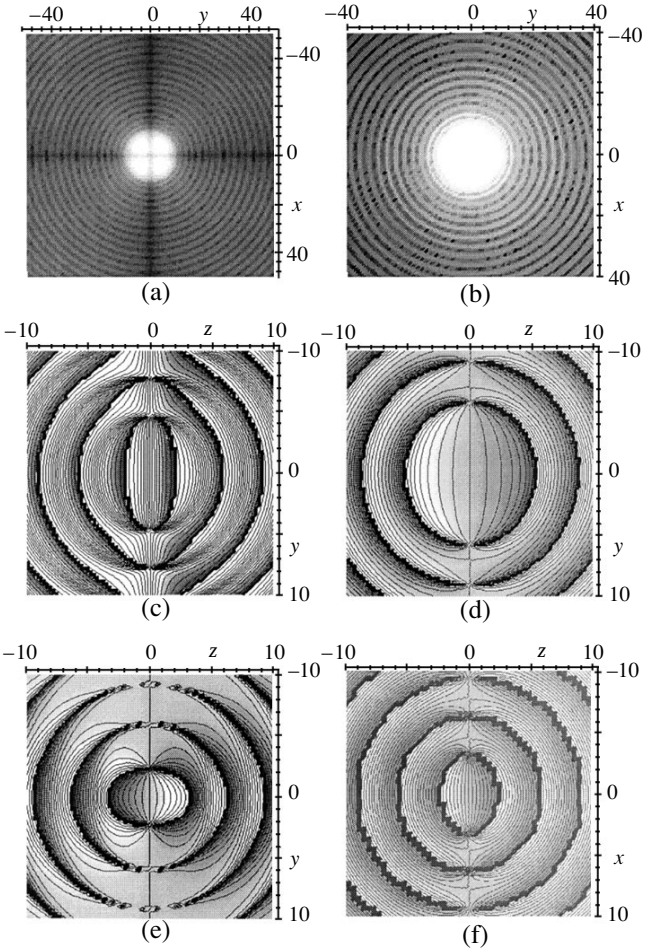

Fig. 2. Intensity maps of the e_y component of (a) $LP(h_y)$ and (b) $LP(e_y)$ modes. Phase level maps for (c) $LP(e_y)$ mode ($z_0 = 1$, $z = 0$); (d) $LP(h_y)$ mode ($z_0 = 1$, $z = 0$); (e) $LP(e_y) + LP(h_y)$ combination ("light drop"); (f) $LP(e_y) - LP(h_y)$ combination (quasi-Gaussian beam). All lengths are expressed in the units $k = 2\pi/\lambda$.

expressions exactly coincide with analogous expressions [3] derived on the basis of different physical prerequisites (e.g., cf. equations (7) and (8) in this work to equations (4.8) and (4.13) in [3]).

The author is grateful to V.G. Shvedov and T.A. Fadeev for the fruitful discussion.

REFERENCES

1. L. B. Felsen, J. Opt. Soc. Am. **66**, 751 (1976).
2. G. P. Agrawal and P. N. Pattanayak, J. Opt. Soc. Am. **69**, 575 (1979).
3. G. P. Agrawal and P. N. Pattanayak, Phys. Rev. A **22**, 1159 (1980).
4. L. W. Davis, Phys. Rev. A **26**, 3702 (1982).
5. L. W. Davis, Phys. Rev. A **19**, 1177 (1979).
6. E. T. Whittaker, Proc. London Math. Soc. **1**, 367 (1904).
7. R. S. Green and E. Wolf, Proc. Phys. Soc. London, Sect. A **66**, 1129 (1953).
8. M. Couture and P. A. Belanger, Phys. Rev. A **24**, 355 (1981).
9. A. V. Volyar, V. G. Shvedov, and T. A. Fadeeva, Pis'ma Zh. Tekh. Fiz. **25** (5), 87 (1999) [Tech. Phys. Lett. **25**, 203 (1999)].
10. *Handbook of Mathematical Functions*, Ed. by M. Abramowitz and I. A. Stegun (Dover, New York, 1971; Nauka, Moscow, 1979).
11. J. F. Nye, Proc. R. Soc. London, Ser. A **387**, 105 (1983).
12. A. V. Snyder and J. D. Love, *Optical Waveguide Theory* (Chapman and Hall, New York, 1983; Radio i Svyaz', Moscow, 1987).
13. J. E. Nye and M. V. Berry, Proc. R. Soc. London, Ser. A **336**, 165 (1973).
14. M. V. Berry, J. Mod. Opt. **45**, 1845 (1998).

Translated by P. Pozdeev

Technical Physics Letters, Vol. 26, No. 7, 2000, pp. 576–578. Translated from Pis'ma v Zhurnal Tekhnicheskoĭ Fiziki, Vol. 26, No. 13, 2000, pp. 79–85.

Dynamic-Cavity Passive Q-Switch Nd-glass Laser

A. V. Fedin*, A. V. Rulev*, and T. T. Basiev**

** Kovrov State Technological Academy, Kovrov, Vladimir oblast, 601910 Russia*

*** Laser Materials and Technology Center, General Physics Institute, Russian Academy of Sciences, Moscow, 117942 Russia*

Received December 24, 1999

Abstract—Lasing regimes in a passive Q-switch Nd-glass laser with self-phase-conjugation in the active medium and LiF : F_2^- crystal were studied. We demonstrate the possibility of single-mode lasing with a pulse train energy above 2 J, peak power up to 0.5 MW, spatial brightness above 1×10^{11} W/(cm^2 sr), and a coherence length of 0.95 m. © *2000 MAIK "Nauka/Interperiodica".*

The output power of the Nd-glass lasers is substantially higher than that of the crystal lasers due to a greater size and higher homogeneity of the active medium of the former case. This advantage is successfully employed in laser technologies such as the laser surface hardening, alloying, cladding, etc. [1, 2]. Use of the single-mode radiation possessing higher spatial brightness substantially increases efficiency of the laser processing [3, 4]. However, multifrequency output of the Nd-glass lasers resulting from a wider amplification band of this active medium compared to that of Nd-containing crystals [5] aggravates the quality and reproducibility of the laser processing [2].

The purpose of this work was to improve the spatial and energy output characteristics by realizing a single-frequency lasing mode in a Nd-glass laser employing a LiF : F_2^- crystal as the passive Q-switch (PQS) and featuring self-phase-conjugation in the active medium and PQS.

Figure 1 shows the optical scheme of our laser based on a Kvant-16 setup. The intracavity loops are formed by terminal (dead-end) mirror *1*, output mirror *2*, and turning mirrors *3–5*. Active element *6* and PQS *7* are placed at the intersections of loops. The active element represents a rod with a diameter of 12 mm and a length of 260 mm made of a GLS-6 Nd-glass. The PQS with the dimensions $8 \times 18 \times 65$ mm exhibits transmittance linearly varying from 60 to 80% perpendicularly to the optical axis.

The initial lasing develops from the terminal (*1*) and output (*2*) mirrors. Four-wave mixing of the intersecting beams induces dynamic holographic gratings in the active (*6*) and passive (*7*) elements which provide for a redistribution of the radiation field and self-phase-conjugation (SPC). Additional amplification of the phase-conjugated radiation creates a positive parametric feedback including mutual enhancement of the gratings and the conjugated radiation. Thus, a dynamic SPC cavity emerges inside the stationary one.

Figure 2 shows plots of the energy and time parameters of the laser radiation versus the initial transmittance of the LiF : F_2^- PQS for the following pumping pulse parameters: energy, 1626 J; duration, 4 ms; repetition rate, 0.1 Hz. The energy parameters were measured using an IKT-1N detector. The time parameters were determined using an LFD-2F avalanche photodiode fitted to an S8-14 memory oscilloscope. The maximum energy of the train of pulses amounts to 2.23 J. A decrease in the initial PQS transmittance from 80 to 60% leads to increasing pulse energy W_i (Fig. 2a, curve *2*), peak power P_i (Fig. 2a, curve *1*), and pulse repetition period T_i (Fig. 2b, curve *4*) in the train. At the same time, we observed a decrease in the total energy W_S of the train of pulses (Fig. 2a, curve *3*) and in the pulse duration τ_i (Fig. 2b, curve *5*). The growth of the single pulse energy parameters is explained by an increase in the radiation losses for the PQS clarification. The resulting increase of the threshold population inversion in the active element (AE) leads to an increase of the peak power (up to 0.5 MW) and the pulse energy (to 127 mJ), a decrease of the pulse duration (down to 250 ns), and an increase of the pulse repetition period in the train.

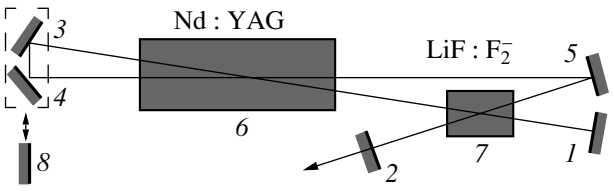

Fig. 1. Schematic diagram of the laser: (*1*) dull-end mirror; (*2*) output mirror; (*3*)–(*5*) turning mirrors; (*6*) active element; (*7*) LiF : F_2^- passive Q-switch; (*8*) dull-end mirror.

1063-7850/00/2607-0576$20.00 © 2000 MAIK "Nauka/Interperiodica"

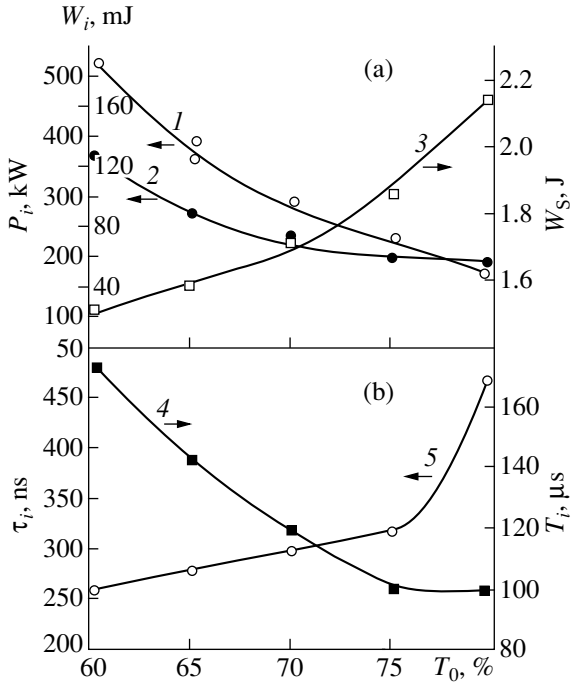

Fig. 2. Plots of the laser output (*1*) peak power, (*2*) pulse energy, (*3*) energy of the train of pulses, (*4*) pulse duration, and (*5*) pulse repetition period in the train versus the initial transmittance of the LiF : F_2^- PQS at a pumping pulse energy of 1626 J, duration of 4 ms, and repetition rate of 0.1 Hz.

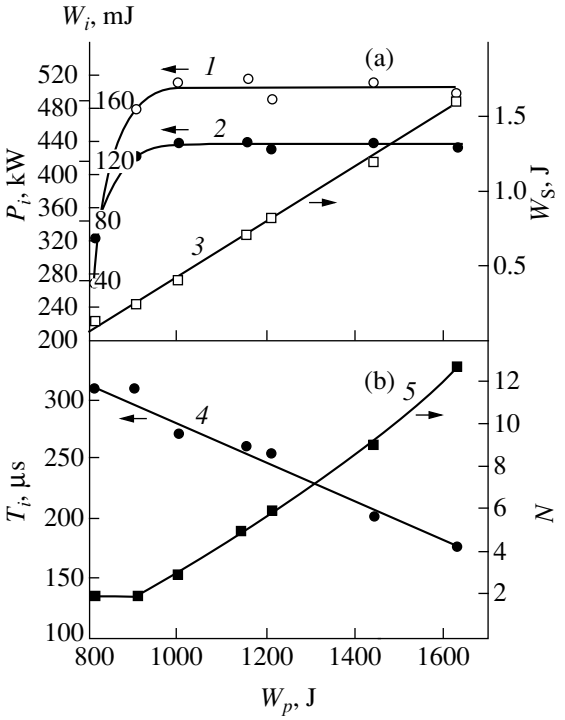

Fig. 3. Plots of the laser output (*1*) peak power, (*2*) pulse energy, (*3*) energy of the train of pulses, (*4*) pulse repetition period in the train, and (*5*) number of pulses in the train versus the pumping pulse energy at an initial passive Q-switch transmittance of 60%, pumping pulse duration of 4 ms, and pumping pulse repetition rate of 0.1 Hz.

Figure 3 shows the plots of the laser radiation parameters versus the pumping pulse energy for the initial PQS transmittance of 60%. It is seen that the increase of the pumping pulse energy W_p leads to decreasing pulse repetition period T_i (Fig. 3b, curve *4*). The latter quantity is determined by the time in which the inverse population reaches a threshold level. As the repetition period decreases, the number of pulses in the train N increases from 2 to 13 (see Fig. 3b, curve *5*) together with the total energy of the train W_S (Fig. 3a, curve *3*). At a maximum pumping pulse energy of 1626 J, the energy of the train of pulses amounts to 1.62 J. In contrast to the cases of lasing with cw [6, 7] and pulse–periodic pumping [8] reported previously, the lasing mode under consideration exhibits increasing peak power P_i and pulse energy W_i only in a narrow interval of the pumping pulse energy ranging from 810 to 1000 J (see Fig. 3a, curves *1* and *2*, respectively). This growth may emerge from better filling of AE by the fundamental mode and from increasing efficiency of the holographic gratings recorded in both AE and LiF : F_2^- crystal. The peak power and pulse energy remain virtually unchanged (P_i = 520 kW and W_i = 127 mJ) with the further increase of the pumping energy from 1000 to 1626 J. This is evidence of the maximum utilization of the pumping energy by its transformation into the output radiation [9] upon the four-wave mixing in the active element.

Figure 4 shows a distribution of the relative radiation intensity for a pumping pulse energy of 1626 J measured in the focal plane of a 1-diopter lens by a photodiode linked to an S1-75 oscilloscope. The estimates of the laser radiation divergence using FWHM and e^{-2} levels yield the values $\theta/2$ = 0.6 and 1.1 mrad, respectively. The radiation quality parameter estimated

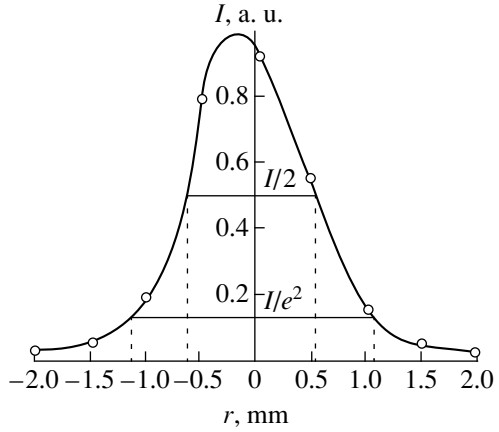

Fig. 4. Relative laser radiation intensity distribution at a pumping pulse energy of 1626 J.

by the formula $M^2 = \pi D\theta/4\lambda$ (where D is the beam diameter in the near zone, θ is the total divergence at the e^{-2} level, and λ is the wavelength) is equal to 8. Spatial brightness of the modulated radiation pulse achieves 1.7×10^{11} W/(cm^2 sr). The coherence length measured by the Michelson interferometer is 95 cm. The radiation spectrum width measured by the Fabry–Perot interferometer did not exceed 0.8×10^{-2} cm^{-1}.

Moving AE or PQS along the optical axis out of the beam intersection leads to decreasing energy parameters and worsening spectral and spatial characteristics of the output radiation. For example, let us place AE near mirror *8* (Fig. 1) and substitute one flat, totally reflecting mirror *8* (optical path *1–8–5–2*) for the system of turning mirrors *3* and *4* (optical path *1–3–4–5–2*). In this configuration, we avoid beam intersection inside AE but maintain the same optical path length and nearly the same reflection angles. Modifying the cavity in such a way results in decreasing train energy [from 1.62 (Fig. 3) to 1.31 J], pulse energy (from 127 to 82 mJ), and spatial brightness [to 1.1×10^{11} W/(cm^2 sr)], while the number of pulses in the train increases from 13 to 16 (for a pumping energy of 1626 J). The divergence and the quality of the laser beam remain virtually unchanged, whereas the coherence length decreases from 95 to 80 cm and the radiation spectral width increases from 0.8×10^{-2} to 1.2×10^{-2} cm^{-1}. Moving LiF : F_2^- crystal to a position immediately adjacent to the output mirror (*2*) (Fig. 1) excluded the beam interaction inside PQS, which sharply decreased the coherence length (down to a few centimeters) and increased the spectral width (by more than one order of magnitude), the divergence (up to 2 mrad), and the quality factor (up to $M^2 = 16$). These results show that a decrease in the interaction length of light beams inside the active element and LiF : F_2^- passive Q-switch substantially aggravates the positive feedback in the self-phase-conjugate loop cavity and worsens the Nd-glass laser output parameters.

Therefore, use of the self-phase-conjugation in the active element and LiF : F_2^- passive Q-switch makes it possible to compensate the wave front phase distortions, to diminish the diffraction losses, and to increase the spatial brightness and the efficiency of lasing. All these benefits are important for technological applications [10, 11] of the solid state lasers with dynamic cavity and passive Q-switching.

REFERENCES

1. T. T. Basiev, A. N. Kravets, S. B. Mirov, and A. V. Fedin, Proc. SPIE **1839**, 2 (1992).
2. T. T. Basiev, A. N. Kravets, and A. V. Fedin, Preprint No. 1, IOF Ross. Akad. Nauk (Institute of General Physics, Moscow, 1993).
3. T. T. Basiev, A. N. Kravets, and A. V. Fedin, Kvantovaya Élektron. (Moscow) **20**, 594 (1993).
4. A. N. Kravets, A. V. Fedin, and A. S. Krinov, Svar. Proizvod., No. 8, 34 (1997).
5. A. A. Mak, L. N. Soms, V. A. Fromzel', and V. E. Yashin, *Neodymium Glass Lasers* (Nauka, Moscow, 1990).
6. T. T. Basiev, A. N. Kravets, S. B. Mirov, and A. V. Fedin, Pis'ma Zh. Tekh. Fiz. **17** (9), 16 (1991) [Sov. Tech. Phys. Lett. **17**, 320 (1991)].
7. T. T. Basiev, A. N. Kravets, S. B. Mirov, and A. V. Fedin, Kvantovaya Élektron. (Moscow) **18**, 822 (1991).
8. T. T. Basiev, A. N. Kravets, and A. V. Fedin, Kvantovaya Élektron. (Moscow) **20**, 594 (1993).
9. S. G. Odulov, M. S. Soskin, and A. I. Khizhnyak, *Dynamic Grating Lasers* (Nauka, Moscow, 1990).
10. A. V. Fedin, A. V. Gavrilov, T. T. Basiev, *et al.*, Laser Phys. **9**, 433 (1999).
11. T. T. Basiev, A. V. Fedin, and A. V. Gavrilov, Kvantovaya Élektron. (Moscow) **27**, 145 (1999).

Translated by A. Chikishev

Technical Physics Letters, Vol. 26, No. 7, 2000, pp. 579–581. Translated from Pis'ma v Zhurnal Tekhnicheskoĭ Fiziki, Vol. 26, No. 13, 2000, pp. 86–92.

Yield Resonances in Electron-Stimulated Desorption of Europium from Tungsten

V. N. Ageev and Yu. A. Kuznetsov

Ioffe Physicotechnical Institute, Russian Academy of Sciences, St. Petersburg, 194021 Russia

Received February 15, 2000

Abstract—The electron-stimulated desorption of europium atoms from layers adsorbed on the surface of tungsten covered with a monolayer of oxygen was observed for the first time. The yield of Eu atoms as function of the energy of bombarding electrons exhibits a pronounced resonance character. The resonances correspond to ionization energies of the core electron levels of Eu and W atoms. © *2000 MAIK "Nauka/Interperiodica".*

Electron-stimulated desorption (ESD) is a phenomenon widely used for the analysis and modification of adsorbed layers [1]. However, the existing ESD models frequently cannot provide for the correct interpretation of experimental data because the underlying assumptions are inadequate to the systems studied. One of the major obstacles hindering development of a complete theory of this phenomenon is the lack of reliably measured values of the fluxes of desorbed neutral particles.

Previously, we studied the ESD of alkali metals [2] and determined the yields and energy distributions of their atoms desorbed from layers on the oxidized surface of tungsten [3] and molybdenum [4]. The experimental results were interpreted using a model according to which the desorption is caused by repulsion between the valence electron shells of the alkali atoms and oxygen ions with electron-excited adsorption bonds. The repulsive forces evidently depend on the structure of the outer electron shells of interacting particles. Therefore, it is important to study the effect of changes in electron configuration of the adsorbed species on the ESD characteristics of neutral particles.

This work opens a cycle of investigations devoted to the ESD of rare-earth metal (REM) atoms from their layers adsorbed on the surface of refractory metal oxides. The selection of REMs as objects for the ESD investigation is explained, on the one hand, by their wide use in electronics, electrical engineering, petroleum industry, automobile and space technologies (permanent magnets, structural and high-temperature semiconductor ceramics, etc.) [5] and, on the other hand, by the fundamental possibility of studying the effect of gradually varying 4*f*-electron structure of REMs on their ESD behavior. The cycle begins with the study of europium (Eu) possessing a comparatively low atomic ionization potential (5.86 eV) [6] and the minimum activation energy (among REMs) for desorption from tungsten (3 eV) [7], which is important for the effective detection of desorbed atomic flux by the surface ionization technique employed.

The experimental setup and the ESD measurement procedure were described in detail elsewhere [8]. The yield of Eu atoms during ESD was measured by the time-of-flight method using a detector based on the surface ionization effect on a tungsten ribbon heated to T = 2000 K. The target had the form of a textured tungsten ribbon sample with the dimensions $70 \times 2 \times 0.01$ mm and the (100)W crystal face predominantly emerging at the surface. The ribbon surface was preliminarily cleaned from carbon-containing contaminations by high-temperature annealing in oxygen at a pressure of 10^{-6} Torr. Then, a monolayer oxygen coverage on tungsten was obtained by a 300-s exposure to oxygen at the same pressure and a lower temperature (1600 K). The sample preparation was accomplished by depositing a europium layer at T = 300 K using a straight-channel evaporator representing a tantalum tube with a hole (charged with metallic europium). The adsorbed europium coating was controlled by varying the deposition time at a preliminarily calibrated constant incident flux. The incident flux was determined by the method of thermodesorption spectroscopy based on the surface ionization current measurements. The surface concentration of europium atoms corresponding to a monolayer coverage was taken equal to 5×10^{14} cm^{-2}. The ESD experiments were performed by irradiating the sample target with electrons in a steady-state regime at an electron beam current density of 5×10^{-6} A/cm^2 and the electron energy ranging from 0 to 300 eV. The electron bombardment in this energy range produced no significant heating of the target surface.

Figure 1 shows the plots of europium yield q versus the energy of bombarding electron E_e for the surface of tungsten bearing a monolayer of oxygen and various initial coverages of Eu atoms. As seen, the yield of Eu atoms depends in a rather complicated manner both on the electron energy and on the initial coverage. At small coverages (Fig. 1, curve *1*), the energy threshold for the appearance of desorbed Eu atoms is close to 25 eV. Above the threshold, the yield first sharply increases

1063-7850/00/2607-0579$20.00

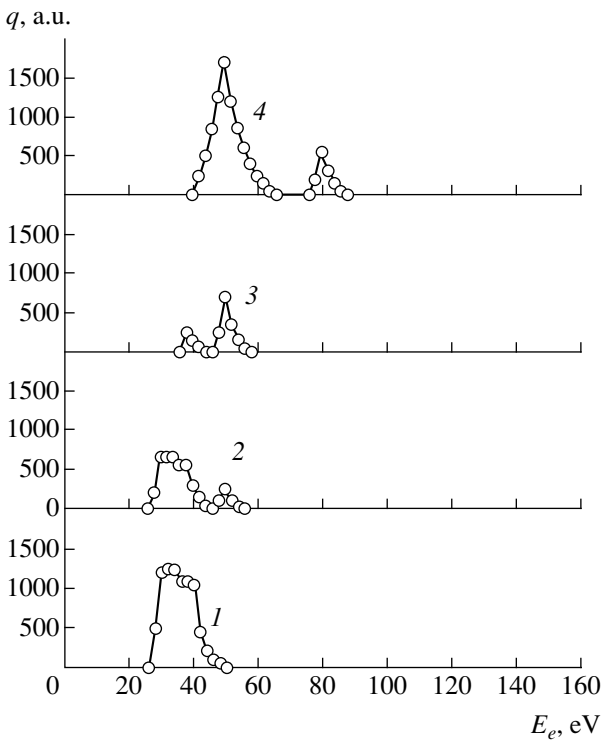

Fig. 1. Plots of the ESD yield of europium atoms q versus the energy of bombarding electron E_e for the surface of tungsten bearing a monolayer of oxygen and various initial europium coverages Θ = 0.07 (*1*), 0.18 (*2*), 0.35 (*3*), 0.70 (*4*).

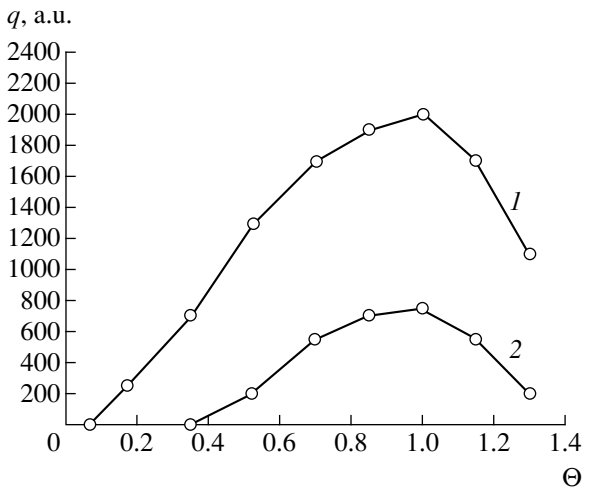

Fig. 2. Plots of the ESD yield of europium atoms q versus the Eu coverage Θ on the tungsten surface with oxygen monolayer for the electron energies E_e = 50 (*1*) and 80 eV (*2*).

with the electron energy to reach a maximum at $E_e \sim$ 33 eV. This peak is followed by a feature (shoulder) situated on the descending branch. As the degree of surface coverage increases, the peak at 33 eV retains the shape but decreases in intensity, and a new peak appears at the electron energy E_e = 50 eV. (Fig. 1, curve *2*). At a surface coverage of Θ = 0.35, the peak at 33 eV disappears to reveal a new peak at about 37 eV followed by still increasing maximum with E_e = 50 eV (Fig. 1, curve *3*). With further growth in the europium coverage, the intensity of the peak keeps growing and an additional peak appears at E_e = 80 eV (Fig. 1, curve *4*). Thus, the peak at 33 eV decreases in intensity with increasing europium coverage, the peaks at 50 and 80 eV continuously grow, and the peak at 37 eV exists within a very narrow interval of coverages.

Figure 2 shows the plots of europium yield q versus Eu coverage Θ on the tungsten surface with oxygen monolayer for the electron energies E_e = 50 and 80 eV. The curves originate at different surface coverages, which reflects the fact that the peaks at 50 and 80 eV appear at approximately $\Theta \cong 0.07$ and 0.35, respectively. The yield increases almost linearly with the coverage to reach the maximum at the same value of Θ, which can be related to a monolayer coverage of the tungsten surface with adsorbed europium.

The peak at E_e = 33 eV disappears on heating the substrate to several tens of degrees, but restores when the sample is cooled down to room temperature. The intensity of ESD peaks at 37, 50, and 80 eV is virtually independent of the substrate temperature up to $T \sim$ 500 K.

When europium is adsorbed on tungsten, the substrate electron work function decreases by more than 1.5 eV [9]. This value may be even greater for the oxidized tungsten surface. Therefore, we may expect that europium occurs on the tungsten surface at low coverages in the form of ions. The observed energy threshold for the appearance of desorbed europium atoms agrees with the analogous value reported for alkali metal atoms (close to 25 eV) [3]. However, the character of variation of the ESD yield of europium with the energy of bombarding electrons significantly differs from the pattern observed for alkali metals. In the latter case, the yield increases with the electron energy to exhibit a single smooth maximum in the energy range of 100–150 eV [3]. In contrast, the ESD curve for adsorbed europium displays several sharp peaks indicative of a resonance character.

Based on the data obtained, we believe that the main channel of excitation for the ESD of alkali metal atoms, related to ionization of the oxygen 2*s* level and neutralization of the adsorbed alkali metal ion (followed by the charge relaxation on the oxygen ion), is not operative in the ESD of europium atoms. Indeed, the presence of two electrons on the 6*s* valence shell of Eu atom results in that the positive europium ion exhibits no any significant change in size upon its neutralization and, hence, no considerable repulsion from the negative oxygen ion. Apparently, the appearance of desorbed europium atoms results from ionization of the europium 5*p* level (ionization energy ~24 eV [10]) and the excited electron transition to a quasibound state. The resulting Eu^{2+} ions will move toward the surface,

driven by the electrostatic image forces, due to the increasing charge and decreasing repulsion between valence shells of the ion and substrate atoms. Upon neutralization (apparently, resonance), the Eu atom is reflected from the surface. In the same way, we may interpret a feature observed at an electron energy of 37 eV (in the descending branch of the 33-eV peak). This feature is assigned to ionization of the europium 5*s* level (ionization energy ~34 eV [10]).

A decrease in the yield of Eu atoms related to ionization of the 5*p* and 5*s* levels at a surface coverage above 0.07 can be explained by changing conditions for the resonance neutralization of Eu^{2+} and re-ionization of Eu atoms leaving the surface [11]. However, we cannot exclude an alternative possibility, whereby increasing europium coverage is accompanied by reconstruction of the oxidized W(100) face leading to a change in the position of adsorbed europium ions relative to the substrate atoms. This rearrangement also affects the measured yield of europium atoms, since the ESD flux is measured within a narrow aperture (take-off) angle. The oxidized W(100) face is subject to reversible temperature-induced rearrangements [12], which can be also related to the observed variation in the ESD yield of europium. Previously, we observed the ESD of cesium [13] and barium [14], chemisorbed on a tungsten surface covered with a monolayer of oxygen, upon the core-level ionization. No evidence of this ionization channel was observed for the ESD of other alkali metal atoms. Thus, we believe that this ESD channel is rather specific and is operative only in systems with atoms of large mass or size.

The peaks of Eu yield for the ESD with 50 and 80 eV electrons can be assigned to ionization of the tungsten core levels (5*p* and 5*s*, with the ionization energies 47 and 77 eV, respectively [10]). The available data are insufficient to unambiguously specify a mechanism responsible for the neutralization of adsorbed Eu^+ ions in this case. However, a neutralization process involving electrons liberated upon the Auger decay of vacancies on the tungsten 5*p* and 5*s* levels is hardly probable because of a comparatively high energy of these electrons. The neutralization via cascade Auger processes involving the 2*s* and 2*p* levels of oxygen also will not lead to the ESD of europium atoms, since the valence shell of europium does not change in size upon neutralization. The need in certain initial coverage for the appearance of desorbed Eu atoms (Fig. 2) is apparently related to the formation of a band of free states to which excited electrons may pass from the core levels.

Thus, we have found and studied for the first time an adsorption system where the ESD yield of adsorbed atoms depends in a resonance manner on the energy of bombarding electrons. The ESD peak energies correspond to ionization energies of the core electron levels of the adsorbate and substrate atoms.

This work was supported by the Russian Foundation for Basic Research (project no. 99-02-17972), by the Federal Program "Surface Atomic Structures" (project no. 4.5.99), and in part by the NATO Research Foundation (grant no. HTECH.LG.973032).

REFERENCES

1. V. N. Ageev, Prog. Surf. Sci. **47** (1–2), 55 (1994).
2. V. N. Ageev, Yu. A. Kuznetsov, and B. V. Yakshinskiĭ, Fiz. Tverd. Tela (Leningrad) **24**, 349 (1982) [Sov. Phys. Solid State **24**, 199 (1982)].
3. V. N. Ageev, Yu. A. Kuznetsov, and N. D. Potekhina, Fiz. Tverd. Tela (St. Petersburg) **38**, 609 (1996) [Phys. Solid State **38**, 335 (1996)].
4. V. N. Ageev and Yu. A. Kuznetsov, Phys. Low-Dimens. Semicond. Struct. **1–2**, 113 (1999).
5. G. V. Tsyganova, N. Yu. Pasechnik, and N. N. Smirnova, Vysokochist. Veshchestva **2** (43) (1991).
6. E. M. Savitskiĭ and V. F. Terekhova, *Physical Metallurgy of Rare-Earth Metals* (Nauka, Moscow, 1975).
7. B. K. Medvedev, Candidate's Dissertation (Leningr. Gos. Univ., Leningrad, 1974).
8. V. N. Ageev, O. P. Burmistrova, and Yu. A. Kuznetsov, Fiz. Tverd. Tela (Leningrad) **29**, 1740 (1987) [Sov. Phys. Solid State **29**, 1000 (1987)].
9. M. V. Loginov and M. A. Mittsev, Fiz. Tverd. Tela (Leningrad) **22**, 1701 (1980) [Sov. Phys. Solid State **22**, 992 (1980)].
10. *Practical Surface Analysis by Auger and X-ray Photoelectron Spectroscopy*, Ed. by D. Briggs and M. Seah (Wiley, New York, 1983; Mir, Moscow, 1987).
11. S. R. Kasi, H. Kang, C. S. Sass, and J. W. Rabalais, Surf. Sci. Rep. **10** (1) (1989).
12. H. M. Kramer and E. Bauer, Surf. Sci. **92**, 53 (1980).
13. V. N. Ageev, Yu. A. Kuznetsov, and N. D. Potekhina, Fiz. Tverd. Tela (St. Petersburg) **35**, 156 (1993) [Phys. Solid State **35**, 82 (1993)].
14. V. N. Ageev, Yu. A. Kuznetsov, and N. D. Potekhina, Fiz. Tverd. Tela (St. Petersburg) **36**, 1444 (1994) [Phys. Solid State **36**, 790 (1994)].

Translated by P. Pozdeev

Technical Physics Letters, Vol. 26, No. 7, 2000, pp. 582–587. Translated from Pis'ma v Zhurnal Tekhnicheskoĭ Fiziki, Vol. 26, No. 13, 2000, pp. 93–105.

On the Possibility of Negative Ion Concentration Growth between Pulses of Discharge Current in Oxygen

A. A. Kudryavtsev* and L. D. Tsendin**

** St. Petersburg State University, St. Petersburg, Russia*

e-mail: akud@ak2138.spb.edu

*** St. Petersburg State Technical University, St. Petersburg, Russia*

Received February 22, 2000

Abstract—We present a critical analysis of data available in literature on the degradation of low-pressure oxygen plasma. Special attention is paid to two effects repeatedly observed in the initial stage of plasma degradation: a sharp growth in the flux of negative ions incident on the wall and an increase in the probing current during the laser-induced photodetachment. Both these phenomena are attributed by various authors to an absolute growth in the negative ion concentration. Our analysis shows that the whole body of experimental data cannot be explained based only on the influence of bulk plasmachemical reactions without taking into account special features of the transport processes in electronegative gases. An alternative mechanism is proposed which involves a two-stage degradation of the electronegative gas plasma accompanied by a change in the diffusion regime. © *2000 MAIK "Nauka/Interperiodica".*

In the past years, there has been increasing interest of researchers in the study of pulsed plasma in electronegative gases. This trend is explained to a considerable extent by the experimental evidence that transition to a pulsed regime can markedly improve the operation of various instruments and devices. Examples are offered by the ion sources [1], plasma etching reactors [2], and some other modern plasma-related devices [3], where variation of the active stage duration, discharge pulse on– off time ratio, supplied power, and other regime parameter provides flexible control of the plasma characteristics.

Investigations of the pulsed plasma behavior under the action of various factors sometimes lead to the observation of rather unusual effects. For example, it was repeatedly reported that the concentration of negative ions N_n exhibits an absolute growth in the initial plasma degradation stage on the background of a monotonic decrease in the concentrations of positive ions N_p and electrons N_e [1–4]. The growth in N_n is manifested by a sharp increase in the flux of negative ions $\Gamma_n(t)$ in the mass spectrometer or by a growth in the photodetachment response $\beta(t) = I_{pd}/I_{es}$ that is proportional to the N_n/N_e ratio (here, I_{pd} is the electron current of photodetachment representing a difference between the electron saturation currents on the probe in the presence and in the absence of laser pulse and I_{es} is the electron saturation current in the unperturbed plasma). Since these effects had been observed for various methods of plasma excitation and in various gases [1–6], it was suggested that the growth of N_n in the initial degradation stage is quite a general phenomenon.

The increase in N_n may be due either to a relative increase in the rate of negative ion production (with respect to the stationary level) or to a decrease in the rate of ion degradation; anyhow, the rate of negative ion formation must exceed the loss rate. Since the characteristic time of electron cooling is usually markedly shorter than the characteristic times of variation in the charged particle concentration, the afterglow stage features a very rapid decrease in the electron gas energy. Therefore, only the rate constants of reactions with high energy thresholds may drop sharply upon switching off the discharge. For this reason, the effects under consideration are usually explained by recourse to one or another bulk threshold process involving the production and loss of negative ions with participation of electrons.

In particular, a sharp switch-off of the electron-impact-induced detachment reaction (characterized by a high energy threshold) in a hydrogen ion source operated in a pulsed regime would slow down the loss of negative ions. Assuming that the electron sticking proceeds predominantly via the highly excited vibrational levels of hydrogen molecules (so that the efficiency of this process only slightly changes in the afterglow), the concentration $N_n(t)$ will increase with time [1].

In contrast, in the case of plasma etching reactors employing chlorine as the plasma-forming medium [2–5], the growth in $N_n(t)$ is usually explained by an increase in the sticking efficiency during the afterglow stage in halogens, related to a decrease in the electron temperature T_e. The loss of negative ions (decreasing N_n) as a result of the ion–ion recombination being independent

1063-7850/00/2607-0582$20.00 © 2000 MAIK "Nauka/Interperiodica"

of T_e, the former circumstance would also lead to a growth in the negative ion concentration.

However, the above reasoning was criticized in [7, 8], where an alternative interpretation was proposed for the experimental observations reported in [1, 2]. The new interpretation was based on the phenomenon of a sharp change in the regime of diffusion upon degradation of the electronegative gas plasma, which was established in [9, 10]. Under these conditions, a rapid growth in the $\Gamma_n(t)$ and $\beta(t)$ signals may take place even despite a monotonic decrease in $N_n(t)$.

The results obtained in a series of experimental investigations [11–14] of the afterglow plasma in oxygen also showed evidence of a sharp increase in the concentration of negative ions in the initial plasma degradation stage. On the one hand, this fact is rather surprising since no such conclusion could be made based on the constants used for the processes of negative ion production and loss in most of the available oxygen plasma models [15–17]. On the other hand, degradation of the electronegative plasma was most thoroughly studied for oxygen [7, 11–14, 18], which is also among the most exhaustively studied electronegative gases.

Below, we present the results of a critical analysis of data reported in literature on the degradation of low-pressure oxygen plasma. It is shown that the whole body of available experimental data cannot be explained based only on the influence of bulk plasma-chemical reactions without taking into account special features of the transport processes in electronegative gases. An alternative mechanism is proposed which involves a two-stage degradation of the electronegative gas plasma accompanied by a change in the diffusion regime.

It should be noted that most of the experiments reported in literature were performed at low gas pressures, when the efficiency of a three-body process of the electron sticking to molecules is negligibly small. For this reason, we will restrict the consideration to the case of negative ion formation as a result of the dissociative sticking process.

The energy threshold for the dissociative sticking of electron to oxygen molecule in the ground state, described by the reaction

$$O_2 + e \longrightarrow O^- + O, \qquad (1)$$

is rather large (~3.6 eV). Because of the rapid electron cooling in the afterglow stage, the constant of this process K_a drops sharply in this stage as compared to the value in the active stage. The same is true for the electron sticking via low excited states of the oxygen molecule ($a^1\Delta$ and $b^1\Sigma$).

The process of dissociative sticking via the highly excited states with the constant K_a^{**} is described by the equation

$$O_2^{**} + e \longrightarrow O^- + O \qquad (2)$$

and has a small energy threshold. Consequently, the Arrhenius exponential dependence of the reaction constant on T_e must be strongly suppressed and, hence, we may expect an even less pronounced (compared to the case of K_a) variation of the K_a^{**} value in the afterglow stage.

It should be noted that the hypothesis [14] concerning the absolute growth in the rate of sticking process (2) in the early stage of the oxygen plasma degradation requires that several unlikely conditions would be simultaneously fulfilled. First, it is necessary that the sticking via highly excited states would dominate both in the active stage and in the afterglow, which implies a large cross section of the process (of the order of values encountered in the gas kinetics [14]). Second, the dissociative sticking cross section must rapidly decrease with increasing electron energy in order to compensate for the inevitable decrease in the concentration of highly excited molecules accompanying degradation of the plasma. Third, the T_e value in the afterglow stage must decay at a sufficiently high rate (within a few microseconds [14]) so that the product of the excited molecule concentration by the rate constant for reaction (2) would increase with time. However, in the range of low pressures (of the order of 5 mTorr) studied in [11–14], cooling of the volume-confined electrons in the course of collisions with molecules proceeds at a rather slow rate [20].

Another point to be noted is that the times characterizing the growth of $\Gamma_n(t)$ and $\beta(t)$ signals observed in [11] were about 10–30 μs, that is, of the order of the characteristic time of collisions of molecules and ions in the gas kinetics, which is smaller than the time constant of plasmachemical reactions). On the other hand, an increase in the rate of negative ion production may result in the growth of $N_n(t)$ (approximately tenfold, as in [11–14]) only with considerable delay.

Thus, it is rather unlikely that the efficiency of electron sticking via the highly excited states of oxygen would increase at a sufficiently high rate.

Once the efficiency of negative ion production in the early afterglow stage is not rapidly growing, the probable fast increase in $N_n(t)$ can be related to a still more pronounced decrease in the loss rate of these ions. This decrease can be provided by electron detachment reactions of the type

$$O^- + e \longrightarrow O + 2e, \qquad (3)$$

since the electron cooling is accompanied by a sharp decrease (switch-off) of the electron detachment from negative ions colliding with fast electrons in the discharge plasma. If this process were the main mechanism decreasing N_n in the active stage of discharge at a weak variation of the sticking coefficient, then the absolute concentration of negative ions might in principle increase. It is this mechanism that was assumed in [1] to account for the growth in the negative ion con-

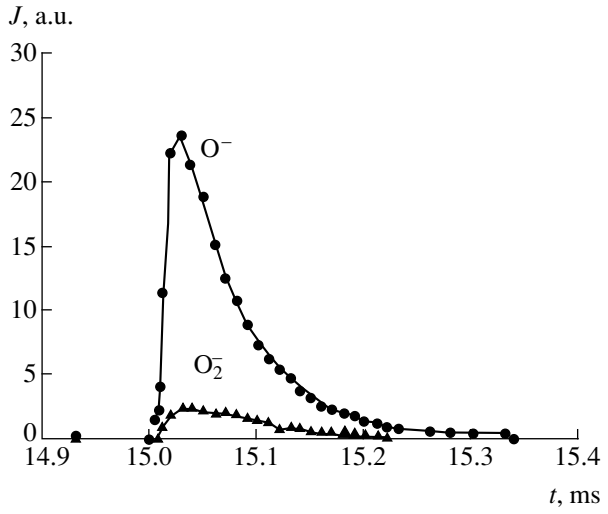

Fig. 1. Time variation of the flux of negative oxygen ions to the wall measured by the time-of-flight mass spectrometer (reproducing Fig. 4 from [11]). Discharge switch-off time t_d = 15 ms.

centration during the hydrogen plasma degradation. However, as noted above, these conclusions were argued against in [4, 5, 11] because the rate K_r (independent of T_e) of the ion–ion recombination process

$$O^- + O_2^+ \longrightarrow O + O_2 \qquad (4)$$

usually exceeds (even in the active stage of discharge) the rate K_{de} of the electron-impact-induced detachment. For oxygen, where $K_r = 10^{-7}$ cm^3/s, we have $K_{de} < K_r$ even in the active discharge stage and even with overstated values of the electron-impact-induced detachment cross section.

Thus, we believe that interpretation of the growth of $\Gamma_n(t)$ and $\beta(t)$ signals in oxygen as due to the increasing efficiency of electron sticking in the afterglow stage [11–13] is rather artificial. Our opinion is based on the fact that the analysis in [11–13] neglected processes of the spatial transport of charged particles, although the loss of these particles at low pressures is determined primarily by their diffusion to toward the walls.

As was demonstrated previously [9, 10], even in the simplest case when plasmachemical processes can be ignored (so that the diffusional degradation of a usual plasma would possess the exponential character), the electronegative gases may exhibit two degradation stages. As long as $N_n/N_e < b_e/b_n$ (b_e and b_n being the mobilities of electrons and ions, respectively), the plasma is depleted of electrons and positive ions, while negative ions are volume-confined by the self-consistent radial field and near-wall potential jump. The second stage of degradation begins at $N_n/N_e > b_e/b_n$ and is determined by the ion–ion ambipolar diffusion (or recombination) in the virtually complete absence of electrons. A sharp change in the regime of plasma degradation, which agrees with this pattern, was experimentally observed by Smith *et al.* [18] at a low initial electronegativity ($\alpha_0 = N_n/N_e \ll 1$). It was established [7] that a transition to the ion–ion plasma is accompanied by a sharpening effect, which implies that the loss of virtually all electrons takes place over a finite time τ_0 determined primarily by the α_0 value. At a greater degree of electronegativity ($\alpha_0 > 1$), the escape of all electrons from the volume is accompanied by relatively small changes in the concentration of positive and negative ions. Therefore, analysis of the degradation processes in a low-pressure plasma must always take into account the transport of electrons toward the walls [7, 18].

Hayashi and Kadota [12, 14] estimated the efficiencies of various plasmachemical processes involved in the production and loss of negative oxygen ions in the afterglow stage (see Table 1 in the papers cited). A complicated experimental geometry and the presence of magnetic field and conducting walls in these experiments makes quantitative analysis of the transport processes in plasma under these conditions a quite complicated task [10]. Nevertheless, we may state that complete neglect of these processes would oversimplify the analysis. Since the electron concentration at the onset of degradation was considerable and the device length was not too large, the electron diffusion flow along the magnetic field was in all probability significant. Under these conditions, a self-consistent electric field will block the escape of electrons and negative ions along the magnetic field **B**. The conducting walls will be negatively charged relative to plasma and the degradation process will retain a two-stage character, with the negative ions confined in the plasma volume as well as in the absence of magnetic field.

Based on the efficiency analysis, it was concluded [12, 14] that the main process responsible for the production of negative oxygen ions (O^-) under the conditions of relatively high degrees of ionization (~10^{-2}–10^{-3}) was reaction (2), while the loss of these species proceeds mainly by the ion–ion recombination reaction (4). The $\Gamma_n(t)$ curve plotted by the ion dynamics data monitored using the time-of-flight mass spectrometer [11, Fig. 4] (reproduced in our Fig. 1) demonstrates a striking similarity with the analogous curve reported by Smith *et al.* [18, Fig. 6]. In both cases, the flux of negative ions $\Gamma_n(t)$ to the wall was virtually absent in the active stage and in the early degradation stage and exhibited a sharp buildup at the time instant t_0 (in Fig. 1, 30 μs after the pulse switch-off) to become comparable with the flux of positive ions. From this fact, it was concluded [11] that no negative ions at all reached the wall in the active stage of discharge and in the initial afterglow stage.

Unfortunately, no probing current–voltage characteristics were reported in [11–14]. We believe that these curves would possess a symmetric shape at $t > t_0$ analogous to that previously observed in [7, 18]. This would be evidence of the transition from the first stage of degradation, where the electric field determined by elec-

trons blocks negative ions within the plasma volume (not admitting them to the wall), to the second stage featuring the ion–ion plasma recombination.

Under the same experimental conditions, the method of photodetachment employed also showed increase in the response $\beta(t)$ [12, Fig. 4]. These results, together with data on the N_p concentration measured by the probing technique, were interpreted as the appearance and growth of $N_n(t)$ in the course of degradation. However, as indicated in [8], the photodetachment data actually indicate only a growth in the N_n/N_e ratio. Since the N_n/N_e value must increase (primarily because of the sharp drop in N_e) in the first stage of plasma degradation, the growth of this ratio cannot be considered as evidence of a sharp increase in the absolute negative ion concentration N_n.

The results of the spectroscopic investigation showing time variation of the intensity $I_\lambda(t)$ of the atomic oxygen emission lines were interpreted [13] assuming that the corresponding levels are occupied due to the ion–ion recombination. Figure 2a (reproduced from [13]) shows the time variation of the intensities of emission at 777 and 845 nm. Using data on the N_p concentration measured by the probing technique (Fig. 2b, reproduced from [13]), we may attempt at reconstructing behavior of the $N_p(t)$ and $N_n(t)$ concentrations during the afterglow. It is seen that for $t > t_0 \approx 20$–30 μs (we believe that this corresponds to the second degradation stage) the $N_p(t)$ and $N_n(t)$ concentrations decay with virtually the same time constant. By the physical meaning, these concentrations must be equal. However, it was stated [13] that $N_p \gg N_n$. We believe that this conclusion is incorrect, which is also indicated by the following fact. The plot of N_e versus time, constructed by the data of Fig. 2b taking into account the electroneutrality condition, exhibits a rather unreasonable and unexplainable behavior: the $N_e(t)$ value remains virtually constant during the afterglow. Note also that, in order to determine the absolute value of $N_n(t)$ from the emission lie intensity, it is necessary to know the value of the partial cross section for the ion–ion recombination with occupation of the upper excited level. These cross sections are still poorly studied, and the values reported by various authors even for the total cross sections differ by more than one order of magnitude. However, increasing the partial recombination cross section employed in [13] only by a factor of three would result in that the $N_p(t)$ and $N_n(t)$ concentrations in the second degradation stage would coincide. Finally, assuming (based on the data of Fig. 2b) that $N_p \approx N_e \gg N_n$, we must conclude that the most effective recombination channel for the charged particles is offered by the dissociative recombination of electron and positive ion:

$$e + O_2^+ \longrightarrow O + O^*. \quad (5)$$

This process has a rate constant close to that for reaction (4) and may also give rise to the recombination

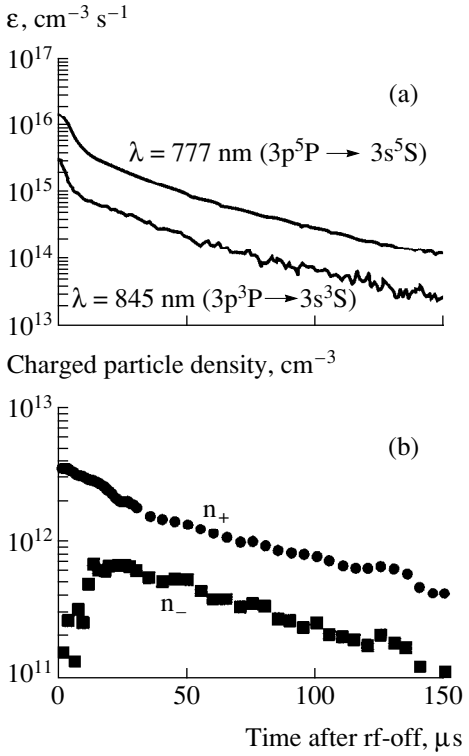

Fig. 2. Time variation of (a) intensity of the 777 and 845 nm emission lines and (b) concentrations of positive and negative ions (reproducing Fig. 2 from [13]).

emission of the atomic oxygen lines. The intensity of this emission cannot be interpreted as resulting from the ion–ion recombination process.

The conclusion made in [13] about a small value of the $N_n(t)$ concentration in the initial degradation stage was based on the following considerations. It was assumed that the sharp initial decay of $I_\lambda(t)$ in Fig. 2a is due to the electron excitation. For this reason, the entire initial part of the $I_\lambda(t)$ curve was approximated by exponent, and this exponent was subtracted from the total signal. This procedure implicitly assumes that no negative ions exist (in accordance with Fig. 1) in the active stage: a which the authors wanted to prove. We believe that it would be a more reasonable procedure to approximate the $I_\lambda(t)$ signal by a sum of two exponents. The $N_n(t)$ curve reconstructed in this way exhibits a slow decrease rather than a sharp growth of N_n with time, which we believe to be a more natural behavior.

Thus, the analysis of data reported in [11–14] shows that many of the conclusions made in those works result from misinterpretation of the experimental data. In our opinion, these data admit an alternative interpretation based on a two-stage character of the electronegative gas plasma degradation [7–10]. This can be illustrated by a simple degradation model [7, 8]. In the range of low pressures under consideration, the electric field corresponds to the Boltzmann distribution of elec-

trons and negative ions [19]. For the time interval $t \ll t_r = K_r^* N_n$, when the recombination can be neglected, we have

$$dN_p/dt = -N_p/t_p \quad (6)$$

and the loss of positive ions obeys the usual exponential law:

$$N_p(t) = N_{p0}\exp(-t/t_p). \quad (7)$$

Here, the characteristic time of the positive ion diffusion determined assuming the Boltzmann distribution of electrons and negative ions is [19]

$$t_p = R^2/(2D_p(2,4)^2). \quad (8)$$

In the first stage of degradation, the negative ions are blocked within the plasma volume by the ambipolar electric field, their flux toward the walls is zero (Fig. 1), and their average concentration remains virtually unchanged in time. Then, equation (7) indicates that, in the absence of plasmachemical processes, the electron concentration varies as

$$N_e(t) = N_{p0}\exp(-t/t_p) - N_{n0}. \quad (9)$$

After the time

$$t_0 = t_p \ln(N_{p0}/N_{e0}), \quad (10)$$

the electron concentration will sharply decrease and the plasma volume will contain predominantly only positive and negative ions ($N_p \sim N_n > N_e$). As a result, the electric potential sharply changes and no longer blocks the negative ions within the plasma volume. For this reason, the onset of the second degradation stage is accompanied by a sharp buildup of the negative ion current toward the walls (Fig. 1). In our opinion, this behavior of the mass spectrometer signal observed in [11] (Fig. 1) is unambiguous evidence of the two-stage character of degradation in the oxygen plasma.

Even if we assume (as in [11–14]) effective electron sticking in the first stage, the pattern of sharpening of the N_e decay would become even more pronounced because of decrease in the characteristic time t_0 determined by the electron sticking:

$$t_{0a} \approx 1/(K_a^{**} N^{**}). \quad (11)$$

Under the experimental conditions studied in [11–14], where the rate of desticking is small compared to that of recombination, a characteristic time of the first degradation stage is determined by minimum of the two values given by (10) and (11).

As the electron concentration N_e decreases to a level such that $N_e b_e < N_p b_p + N_n b_n$, the electrons instantaneously (in the free diffusion regime) escape to the walls and the volume retains only positive and negative ions $N_p = N_n$. For this reason, the degradation of plasma in the second stage ($t > t_0$) is determined by the ion–ion ambipolar diffusion with the characteristic time

$$N_p(t) = N_n(t) = N_p(t_0)\exp(-t/t_i). \quad (12)$$

Should the ion–ion recombination dominate in the second stage [$K_r N_p(t_0) > 1/t_i$], the exponential expression (12) must be replaced by a hyperbolic law describing the ion concentration decay:

$$N_p(t) = N_n(t) = N_p(t_0)/(1 + K_r N_p(t_0)t). \quad (13)$$

Thus, inclusion of the ion–ion recombination and electron sticking into the above scheme of two-stage plasma degradation does not alter the main conclusion concerning sharpening of the electron concentration decay in the first stage and the formation of ion–ion (electron-free) plasma in the second stage. In our opinion, the results of mass-spectrometric measurements reported in [11] (reproduced in Fig. 1) provide unambiguous evidence in favor of this mechanism. In the active stage of discharge (before $t_d = 15$ ms) and in the first stage of degradation, the flux of negative ions to the wall is zero. Then (after $t_0 = 30$ μs upon the discharge switch-off), the flux $\Gamma_n(t)$ sharply increases and then decays at a time constant $t_r = 60$ μs, in agreement with the curves presented in Fig. 2. We may agree with the authors of [11–14] that an effective channel of the negative ion formation in gases such as oxygen, hydrogen, etc. (having an energy threshold for sticking for the ground state of molecules), can be the thresholdless sticking to highly excited molecules. When considering hydrogen, this concept was formulated in [21] and considered in more detail in [22]. However, we believe that the rate of electron sticking in the first stage of afterglow in oxygen increases insufficiently rapidly to provide for a sharp growth in the concentration of negative ions upon the discharge switch-off.

Thus, we have proposed an alternative explanation of the experimental data reported in [11–14] based on a concept of the two-stage character of the electronegative gas plasma degradation. Since this phenomenon is rather general, we believe that special features of the diffusion loss of charged particles must be also taken into account in the analysis of degradation kinetics in other electronegative plasmas.

This work was supported by the Russian Foundation for Basic Research (project nos. 98-02-17778 and 98-02-16000) and by the Ministry of Education of the Russian Federation (project no. 97-0-5.3-33).

REFERENCES

1. M. B. Hopkins, M. Bacal, and W. G. Graham, J. Appl. Phys. **70**, 2009 (1991).
2. S. Samukawa and H. Ohtake, J. Vac. Sci. Technol. A **14** (6), 3049 (1996).
3. M. A. Lieberman and S. Ashida, Plasma Sources Sci. Technol. **5**, 145 (1996).

4. T. H. Ahn, K. Nakamura, and H. Sugai, Plasma Sources Sci. Technol. **5**, 139 (1996).
5. G. A. Hebner, J. Vac. Sci. Technol. A **14** (4), 2158 (1996).
6. L. J. Overzet, B. A. Smith, J. Kleber, and K. Kanakasabapathy, Jpn. J. Appl. Phys. **36**, 2443 (1997).
7. S. A. Gutsev, A. A. Kudryavtsev, and V. A. Romanenko, Zh. Tekh. Fiz. **65** (11), 77 (1995) [Tech. Phys. **40**, 1131 (1995)].
8. A. A. Kudryavtsev, Pis'ma Zh. Tekh. Fiz. **22** (17), 11 (1996) [Tech. Phys. Lett. **22**, 693 (1996)].
9. L. D. Tsendin, Zh. Tekh. Fiz. **55** (12), 2318 (1985) [Sov. Phys. Tech. Phys. **30**, 1377 (1985)].
10. A. V. Rozhanskiĭ and L. D. Tsendin, *Collisional Transport in Partly-Ionized Plasma* (Énergoatomizdat, Moscow, 1988).
11. T. Mieno, T. Kamo, D. Hayashi, *et al.*, Appl. Phys. Lett. **69**, 617 (1996).
12. D. Hayashi and K. Kadota, J. Appl. Phys. **83**, 697 (1998).
13. T. Ishikawa, D. Hayashi, K. Sasaki, *et al.*, Appl. Phys. Lett. **72**, 2391 (1998).
14. D. Hayashi and K. Kadota, Jpn. J. Appl. Phys. **38** (1A), 225 (1999).
15. G. Gousset, C. M. Ferreira, M. Pinheiro, *et al.*, J. Phys. D: Appl. Phys. **24**, 290 (1991).
16. V. A. Feoktistov, A. V. Mukhovatova, A. M. Popov, and T. V. Rakhimova, J. Phys. D: Appl. Phys. **28**, 1346 (1995).
17. C. Lee, D. B. Graves, M. A. Lieberman, and D. W. Hess, J. Electrochem. Soc. **141**, 1546 (1994).
18. D. Smith, A. G. Dean, and N. G. Adams, J. Phys. D: Appl. Phys. **7**, 1944 (1974).
19. H. S. W. Massey, *Negative Ions* (Cambridge University Press, Cambridge, 1976; Mir, Moscow, 1979).
20. R. R. Arslanbekov and A. A. Kudryavtsev, Phys. Rev. E **58**, 7785 (1998).
21. V. V. Kuchinskiĭ, V. G. Mishakov, A. S. Tibilov, and A. M. Shukhtin, Opt. Spektrosk. **39**, 1043 (1975) [Opt. Spectrosc. **39**, 598 (1975)].
22. M. Bacal and G. W. Hamilton, Phys. Rev. Lett. **42**, 1538 (1979).

Translated by P. Pozdeev

Technical Physics Letters, Vol. 26, No. 7, 2000, pp. 588–590. Translated from Pis'ma v Zhurnal Tekhnicheskoĭ Fiziki, Vol. 26, No. 13, 2000, pp. 106–110.

Spatial Distribution of the Electromagnetic Radiation Accompanying Propagation of Magnetostatic Surface Waves in a Ferrite Film Magnetized by a Transversely Nonuniform Field

V. I. Zubkov and V. I. Shcheglov

Institute of Radio Engineering and Electronics (Fryazino Branch), Russian Academy of Sciences, pl. Vvedenskogo 1, Fryazino, Moscow oblast, 141120 Russia

Received January 12, 2000

Abstract—A model is proposed for description of the spatial distribution of electromagnetic waves (EMWs) generated during the propagation of magnetostatic surface waves (MSSWs) in a ferrite film (FF) magnetized by a transversely nonuniform field. The EMW radiation pattern calculated using this model has two lobes mutually symmetric relative to the FF plane. The lobes are tilted in the direction of MSSW propagation, the tilt increasing with the MSSW velocity approaching the velocity of EMW in the film. The calculated results are in good qualitative agreement with experiment. *© 2000 MAIK "Nauka/Interperiodica".*

Previously [1], we reported on the detection of electromagnetic waves (EMWs) emitted from a ferrite film (FF) magnetized by a nonuniform tangent field, with the field intensity H_g varying linearly in the perpendicular direction when magnetostatic surface waves (MSSWs) propagated in the direction of increasing magnetization. The MSSW wavelength gradually increased to approach the EMW wavelength in the free space, which was accompanied by intensive conversion of the MSSW energy into the EMW energy radiated into the free space. The spatial distribution of the EMW radiated into the upper half-space (the bottom half-space was shielded with an absorbing layer) was experimentally investigated [2] and it was found that the EMW radiation pattern relative to the FF plane has the form of a wide lobe strongly (by tens of degrees) tilted in the direction of MSSW propagation. It was also stated [2] that the total radiation pattern is symmetric relative to the film plane and has two lobes tilted in the forward direction. Below, we try to explain the observed pattern, since it is important for the data processing devices utilizing MSSWs [3].

We will use the coordinate system 0*xyz* adopted in [2], where the *y*0*z* plane coincides with the FF plane, the 0*x*-axis is perpendicular to the film plane, and the 0*z*-axis coincides with the direction of constant magnetic field H_g, whose intensity varies along the 0*y*-axis. The MSSW also propagates along the 0*y*-axis. Using well-known concepts of the electrodynamics of gyrotropic media [4] and assuming that the FF permittivity $\varepsilon_f = 1$, we may write an expression for the electric field generated at a large distance from the FF by a unit area of the uniformly magnetized film:

$$\begin{aligned}\mathbf{E}(\mathbf{R}) &= -2\pi G_m v_e^{-2}\lambda^{-2}[\mathbf{R}\times\mathbf{w}_m]\\ &+ 2\pi G_m v_e^{-1}\lambda^{-2}[\mathbf{v}_m\times\operatorname{grad}\lambda],\end{aligned} \quad (1)$$

where

$$\lambda = R - v_e^{-1}\mathbf{v}_m\mathbf{R}, \quad \mathbf{w}_m = \frac{\partial \mathbf{v}_m}{\partial t},$$

$$G_m = M_{x1} - M_{x2} - \left(\frac{\partial M_y}{\partial y}\right)d,$$

R is the distance from the point of EMW generation to the observation point, v_m is the MSSW phase velocity, v_e is the EMW velocity, *d* is the FF thickness, and indices 1 and 2 refer to different surfaces of the film. In formula (1), only the first term proportional to R^{-1} describes radiation (the second term is proportional to R^{-2}). Since the MSSW propagates perpendicularly to the magnetizing field H_g, the vectors $\mathbf{w}_m$ and $\mathbf{v}_m$ are collinear. Denoting the angle between vector **R** and the MSSW propagation direction by α and retaining only the first term in formula (1), we can write

$$E(R) = 2\pi G_m v_e^{-2} R^{-1} w_m (1 - v_m v_e^{-1}\cos\alpha)^{-2}\sin\alpha. \quad (2)$$

Formula (2) shows that the field intensity $E(R)$ is actu-

1063-7850/00/2607-0588$20.00

ally proportional to R^{-1}, which is typical of radiation, and its spatial distribution is determined by two last factors of the product. Since the magnetic field in the EMW is proportional to the electric field, the radiant energy flux is proportional to the squared expression (2). The penultimate factor involves the ratio v_m/v_e that can be close to unity since, when the MSSW propagates in the direction of increasing intensity of the filed H_g, the velocity v_m tends to v_e (in the limit). The attainable value of v_m/v_e is determined by experimental conditions.

As is seen from formula (2), the field of the radiated EMW is proportional to the quantity v_m, which depends on the gradient of the filed H_g along the EMW propagation direction. The radiant energy flux increases with this gradient. Since the oscillations of magnetization in adjacent parts of the FF spaced from each other by half-wavelength are in antiphase, the energy fluxes from theses parts are mutually compensated. Only radiation from a part of the FF in which the field H_g determines the boundary of the MSSW spectrum remains uncompensated. The length of this region being equal to approximately half of the maximum wavelength of the MSSWs, the largest area corresponds to the MSSW wavelength close to half of the EMW wavelength. This means that the field H_g must vary only slightly over a distance equal to the EMW wavelength and its gradient must be sufficiently small. However, for a very small gradient of the field H_g, the path from the exciting transducer to the side of wave emission may increase to an extent such that the MSSW would decay before the EMW is radiated. Thus, to maximize the radiant energy flux, the H_g field gradient must take an intermediate value determined by the joint action of all the aforementioned factors. This value determines only the radiation intensity, whereas, as follows from formula (2), the spatial distribution of the filed H_g remains unchanged upon variation of the field gradient.

Consider the shape of the EMW radiation pattern described by formula (2). Figure 1 presents normalized squared values of a product of two last factors in expression (2), which describe the flux of the EMW energy for different values of v_m/v_e. The drawing plane in Fig. 1 is the $x0y$ plane of Cartesian coordinate system, the $0x$-axis is vertical, and the $0y$-axis is horizontal. The FF plane is perpendicular to the $x0y$ plane and passes through the $0y$-axis. Field lines of the constant field H_g lie in the FF plane. The horizontal arrow in Fig. 1 indicates the direction of MSSW propagation. Curves *1–3* correspond to v_m/v_e = 0.1, 0.5, and 0.9, respectively.

One can see that the pattern has two lobes mutually symmetric relative to the FF plane, and, when the ratio v_m/v_e increases, these lobes tilt forward in the direction of MSSW propagation. These features of the radiation pattern agree with those described previously [2]. According to formula (2), the radiant energy flux in a given direction increases with the ratio v_m/v_e. This dependence is illustrated by Fig. 2, where the product of the last two factors in expression (2) is plotted versus v_m/v_e for different angles α. As is seen, the field of EMWs radiated perpendicularly to the MSSW propagation direction is independent of v_m [and is only deter-

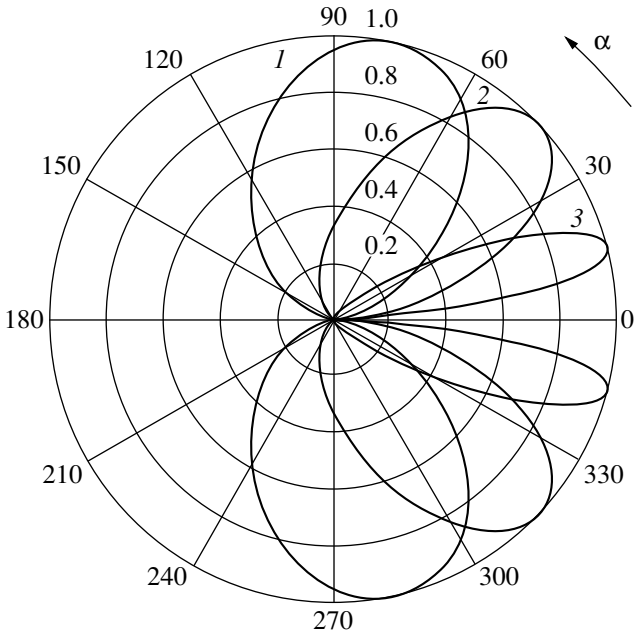

Fig. 1. The EMW radiation pattern calculated for v_m/v_e = 0.1, 0.5, and 0.9 (curves *1–3*, respectively).

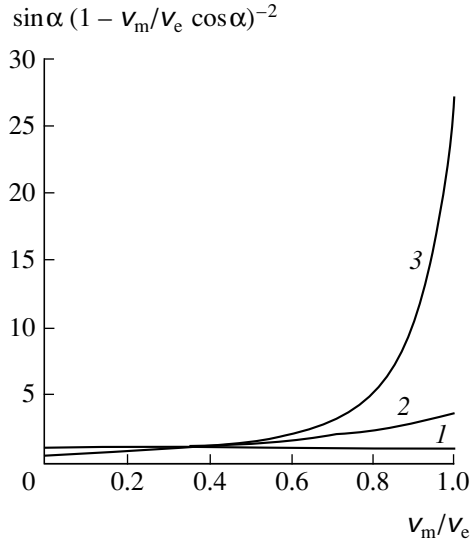

Fig. 2. The product of two last factors in expression (2) versus v_m/v_e for α = 90°, 60°, and 30° (curves *1–3*, respectively).

mined by the factor w_m in formula (2)], whereas the field intensity in the forward direction, that is, in the direction of MSSW propagation, increases with the ratio v_m/v_e. The smaller the angle α, the more pronounced this increase.

Thus, we have proposed a model that provides a good qualitative description for the observed experimental results [2]. We believe that the quantitative agreement can be reached by adequately considering specific parameters of the experiment.

REFERENCES

1. A. V. Vashkovskiĭ, V. I. Zubkov, É. G. Lokk, and V. I. Shcheglov, Radiotekh. Élektron. (Moscow) **38**, 818 (1993).
2. A. V. Vashkovskiĭ and É. A. Lokk, Radiotekh. Élektron. (Moscow) **40**, 1030 (1995).
3. W. S. Ishak, Proc. IEEE **76** (2), 171 (1988).
4. A. G. Gurevich and G. A. Melkov, *Magnetic Oscillations and Waves* (Nauka, Moscow, 1994).

Translated by A. Kondrat'ev

Technical Physics Letters, Vol. 26, No. 7, 2000, pp. 591–593. Translated from Pis'ma v Zhurnal Tekhnicheskoĭ Fiziki, Vol. 26, No. 14, 2000, pp. 1–6.

Light Penetration through a Single-Row Layer of Dielectric Particles

I. L. Volkhin and N. N. Korotaev

Perm State University, Perm, 614600 Russia

e-mail: volkhin@psu.ru

Received February 2, 2000

Abstract—Light penetration through a layer of cubic dielectric particles was studied by the method of microwave physical modeling. The effect of an increase in the layer transmission ("clarification") with increasing particle packing density was observed. Conditions for which the coefficient of directed transmission of a single-row layer turns zero are determined. *© 2000 MAIK "Nauka/Interperiodica".*

Ivanov *et al.* [1, 2] described the physical pattern of light penetrating through a single-row layer of monodisperse weakly absorbing dielectric spherical particles. The description referred to particles with dimensions comparable with the incident light wavelength and was made within the framework of the single scattering approximation. When a parallel light beam is incident onto this layer, one part of the light wave is transmitted via the particles, and another part, via the air gaps between particles. Intensities of the incident (I_0) and transmitted (I) radiation can be experimentally measured to calculate the directed transmission coefficient $T = I/I_0$.

According to the results obtained in [2], the directed transmission coefficient T of a single-row layer of spherical particles can be related to the optical characteristics of these particles

$$T = 1 - Q\eta + LQ^2\eta^2/2, \quad (1)$$

where Q is the particle scattering factor, $\eta = S_p/S$ is the layer overlap parameter, S_p is the sum of projections of all particles onto a plane perpendicular to the direction of light propagation, S is the layer area, $L = 8\pi\Lambda x(0)/Q\rho^2$ is the proton survival probability, $x(0)$ is the indicatrix of scattering in the direction of light propagation, $\rho = \pi a/\lambda$ is the diffraction parameter, a is the particle size, and λ is the light wavelength. For dielectric particles with the size a comparable with the light wavelength λ, the Q and L values can be calculated using the Mie formulas. For $LQ \le 1/\eta_{max}$ (η_{max} is the maximum possible overlap parameter for a single-row layer of spherical particles), the directed transmission coefficient T monotonically decreases with increasing η. For $LQ > 1/\eta_{max}$, the T value exhibits a nonmonotonic variation: as the η value increases, the transmission T first drops to reach a minimum at $\eta_{min} = 1/LQ$ and then begins to increase. At the point of minimum, the transmission coefficient is

$$T_{min} = 1 - 1/2L. \quad (2)$$

Thus, an increase in the number of scattering particles makes the layer less transparent for $\eta < \eta_{min}$ and leads to "clarification" when $\eta > \eta_{min}$. Equation (2) also indicates that the directed transmission coefficient T turns zero for $L = 0.5$, which implies that the waves passing the layer via particles and gaps have equal amplitudes and opposite phases.

For a layer of particles having nonspherical shapes, theoretical calculation of the Q and L values is rather complicated. Moreover, the effects of multiple scattering in a system with a large density of packing of the scattering centers may change the pattern of interference and, hence, the directed transmission coefficient T.

Experimental investigations of the effects of shadowing and clarification in the optical wavelength range are complicated by difficulties in obtaining monodisperse samples, while the results of experiments with polydisperse ensembles of particles are difficult to interpret. To bypass these difficulties, we have passed from measurements in the optical range to experiments with electromagnetic radiations of longer wavelengths. The electromagnetic radiation wavelength and the size of scattering particles were proportionally increased by a factor of about 10^5. Once the radiation fell within the microwave (SHF) range with $\lambda \approx 3$ cm, the particle size increased to several centimeters. The method of physical modeling and the experimental setup were described in detail elsewhere [3].

The weakly absorbing model particles were made of paraffin. In the 3-cm wavelength region, this material is characterized by the magnetic susceptibility $\mu = 1$; the refractive index $n = 1.5$; and the dielectric loss tangent $\tan\delta \approx 10^{-4}$ [4], which corresponds to the absorption coefficient $K \approx 0.029$ m^{-1}. The calculation was per-

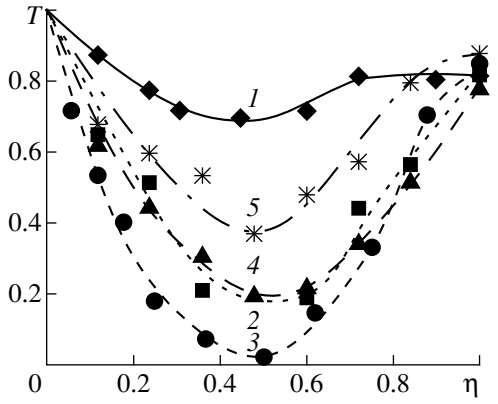

Fig. 1. Plots of the directed transmission coefficient T versus the overlap parameter η for the layer of weakly absorbing ($K \approx 0.029$ m^{-1}) cubic particles with various diffraction parameters ρ = 1.6 (*1*); 2.9 (*2*); 3.6 (*3*); 4.9 (*4*); 5.8 (*5*).

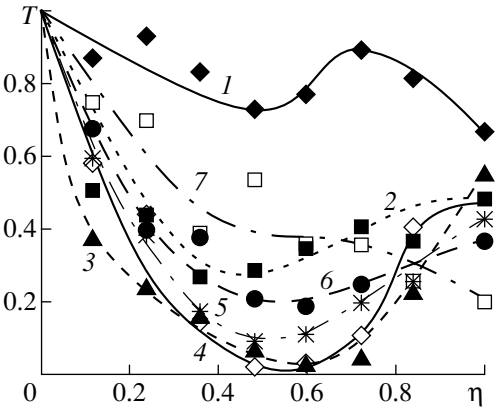

Fig. 2. Plots of the directed transmission coefficient T versus the overlap parameter η for the layer of absorbing ($K \approx 2.9$ m^{-1}) cubic particles with various diffraction parameters ρ = 1.4 (*1*); 1.9 (*2*); 2.9 (*3*); 3.6 (*4*); 4.3 (*5*); 4.9 (*6*); 6.9 (*7*).

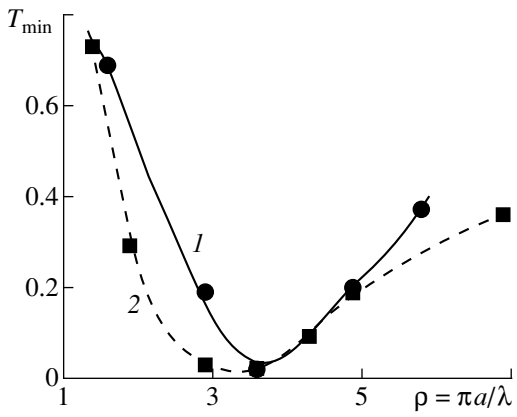

Fig. 3. Plots of the minimum directed transmission coefficient T_{min} (determined at the point of minimum of the $T = f(\eta)$ function) versus the diffraction parameter ρ for the layers of (*1*) weakly absorbing ($K \approx 0.029$ m^{-1}) and absorbing ($K \approx 2.9$ m^{-1}) cubic particles.

formed by the formula $K = 4\pi\{\varepsilon[(1 + \tan^2\delta)^{1/2} - 1]/2\}^{1/2}/\lambda$ [5]. The absorbing particles were made of a paraffin–carbon composition with a carbon concentration of 0.5 wt %. The refractive index of this mixture was virtually the same as that of paraffin, while $\tan\delta$ increased to 0.01 (and, accordingly, K increased to ≈2.9 m^{-1}) [6]. These values of n and K for the model particles studied in the microwave range correspond to the n and K values for an AgBr single crystal studied at λ = 430 nm [7].

The model experiments were performed with particles of a cubic shape. The cube base edge length, expressed in units of the diffraction parameter $\rho = \pi a/\lambda$, was varied from 1.4 to 6.9. The model particles were randomly arranged in the layer, with random orientation of their faces in the plane perpendicular to the direction of radiation propagation. The upper and lower faces of the cubic particles were parallel. In the case of close packing, the presence of neighbors led to increasing order in the spatial orientation of cubic faces. In the limit η = 1, the cubic particles were ultimately ordered by contacting with each other and formed a continuous plane-parallel plate.

The results of experiments represented by plots of $T = f(\eta)$ are shown in Fig. 1 for weakly absorbing model particles and in Fig. 2 for absorbing particles. As seen from these data, the transmission T in all curves initially drops with increasing η, passes through a minimum, and then increases again. The increase of T with η implies clarification of the layer. Thus, the system of cubic particles features the clarification effect theoretically predicted for the spherical particles. For the layer of weakly absorbing particles, the minimum of $T = f(\eta)$ is observed in the vicinity of $\eta_{min} = 0.5$. In the limiting case of η = 1, the transmission increases to $T = 0.78$–0.87. Absorption of the radiation by the particle material leads to a more rapid drop of the transmission in the region of small η, decreases the effect of clarification at large η, and smears the minimum of $T = f(\eta)$. At η = 1, the transmission T decreases with increasing diffraction parameter ρ (i.e., with the layer thickness).

Figure 3 shows the plots of the directed transmission coefficient T_{min} (i.e., the T value at the point of minimum) versus ρ constructed by the data of Figs. 1 and 2. As seen from this plot, the value of T_{min} for weakly absorbing particles (curve *1*) exhibits a minimum at $\rho \approx 3.6$, where $T_{min} = 0.02$ and $\eta_{min} = 0.44$ in satisfactory agreement with the theory [1, 2]. For the absorbing particles (curve *2*), the plot of $T_{min} = f(\rho)$ lies below the curve for the weakly absorbing system.

Thus, we have used the method of microwave modeling of optical phenomena to study the directed transmission coefficient as a function of the overlap parameter η for absorbing and weakly absorbing layers of cubic particles with the edge length $a \sim \lambda$. The system features the phenomenon of clarification calculated previously for a system of spherical particles. Increas-

ing the absorption of the particle material leads to a decrease in the clarification effect.

REFERENCES

1. A. P. Ivanov and V. A. Loĭko, *Optics of Photographic Layers* (Nauka i Tekhnika, Minsk, 1983).
2. A. P. Ivanov, V. A. Loĭko, and V. P. Dik, *Light Propagation in Close-Packed Disperse Media* (Nauka i Tekhnika, Minsk, 1988).
3. I. L. Vol'khin and N. N. Korotaev, Prib. Tekh. Éksp., No. 1, 80 (1999).
4. J. M. Kelly, J. O. Stenoien, and D. E. Isbell, J. Appl. Phys. **24** (3), 258 (1953).
5. A. R. Hippel, *Dielectric Materials and Applications* (Wiley, New York, 1954; Gosénergoizdat, Moscow, 1959).
6. I. L. Vol'khin, N. N. Korotaev, P. V. Meĭklyar, *et al.*, Vestn. Perm. Univ. Fiz. **2**, 203 (1994).
7. *The Theory of the Photographic Process*, Ed. by T. H. James (Macmillan, New York, 1977; Khimiya, Leningrad, 1980).

Translated by P. Pozdeev

Technical Physics Letters, Vol. 26, No. 7, 2000, pp. 594–596. Translated from Pis'ma v Zhurnal Tekhnicheskoĭ Fiziki, Vol. 26, No. 14, 2000, pp. 7–12.

Limiting Geometries and the Dielectric Tensor of Superlattices

A. V. Goncharenko

Institute of Semiconductor Physics, National Academy of Sciences of Ukraine, Kiev, 252028 Ukraine

Received February 2, 2000

Abstract—A one-parameter generalization of the expression for diagonal components of the dielectric tensor of superlattices is derived using the spectral density formalism. The generalization allows for the deviation of a real superlattice geometry from the ideal. *© 2000 MAIK "Nauka/Interperiodica".*

At present, the dielectric and optical properties of superlattices (SLs) are frequently described within the framework of an approach according to which the SL is considered as a uniaxial effective medium [1–5]. In this case, the SL is described by a dielectric tensor

$$\langle \varepsilon \rangle = \begin{pmatrix} \varepsilon_{xx} & 0 & 0 \\ 0 & \varepsilon_{yy} & 0 \\ 0 & 0 & \varepsilon_{zz} \end{pmatrix}. \quad (1)$$

If a superlattice is composed of plane-parallel layers (e.g., quantum wells and barriers) perpendicular to the z-axis, then $\varepsilon_{xx} = \varepsilon_{yy}$ and the diagonal components of the dielectric tensor are determined by the following relationships:

$$\varepsilon_{xx} = f_1\varepsilon_1 + f_2\varepsilon_2 \quad (2)$$

$$\varepsilon_{zz}^{-1} = f_1\varepsilon_1^{-1} + f_2\varepsilon_2^{-1}, \quad (3)$$

where f_1 (f_2) and ε_1 (ε_2) are the volume fraction and dielectric permittivity of the first (second) SL components, respectively. Note that relationship (2) is also valid for the ε_{xx} component in a one-dimensional case of the superlattice formed by a quantum wire, assuming that the x-axis is parallel to the wire. In the general case, $\varepsilon_{xx} \neq \varepsilon_{yy} \neq \varepsilon_{zz}$. The ε_{yy} and ε_{zz} components must depend on the shape of the wire cross section ($\varepsilon_{yy} = \varepsilon_{zz}$ for a circular cross section).

It must be noted that equations (2) and (3) are derived within the framework of geometries that can be considered, in a certain sense, as limiting. The first geometry corresponds to the electric field oriented along the plane-parallel layers (parallel capacitances). The second geometry refers to the electric field oriented perpendicularly to the plane-parallel layers (serial capacitances). It was shown [6–8] that these geometries define the upper and lower Wiener's boundary values of the effective dielectric function (or conductivity) of the system.

In the case of a real 2D (1D) SL, it is hardly possible to expect that all quantum wells (wires) are strictly parallel. For example, 2D SLs usually feature interfacial roughnesses caused by technological factors. These roughnesses may significantly affect the optical spectra even in the long-wavelength approximation (see, e.g., [9–11]). Moreover, the so-called corrugated SLs possess intentionally created interfacial roughnesses. Growing an ideal quantum wire would be an even more difficult task.

Thus, we may ascertain that real SLs exhibit a certain deviation from the ideal geometry. This deviation may affect the $\langle \varepsilon \rangle$ tensor components and, hence, the dielectric and optical properties of SLs. Therefore, once these properties are experimentally measured and the corresponding theoretical model is available, we may find a measure of this deviation and judge on the SL quality. Consequently, we arrive at the following fundamental question having practical significance: how can we formally describe the deviation of a real SL geometry from the ideal? To solve this task, it would be natural to introduce some small phenomenological parameter that could be considered as a measure of this deviation or the SL quality.

Below, we will attempt to solve this task using a formalism of the so-called spectral (Bergman's) representation for the dielectric tensor components [8, 12]. It should be noted that real SLs may also feature the manifestations of other factors affecting their optical properties and restricting direct application of equations (2) and (3). Examples of such factors are offered by mechanical stresses, defects, and composition fluctuations. On the other hand, SLs may also feature factors related to a certain peculiarity of the physics of low-dimensional systems intersubband transitions, electron–phonon interactions, etc. Under certain conditions, this may restrict the applicability of the bulk values of the dielectric permittivity entering into equations (2) and (3). Detailed analysis of these problems falls outside the scope of this work.

1063-7850/00/2607-0594$20.00

In the Bergman representation (see, e.g., [12]), the effective dielectric function of an arbitrary two-component composite can be presented in the following form:

$$\langle\varepsilon\rangle = \varepsilon_1\left(1 + f_2\int_0^1 \frac{g(x)}{s+x}dx\right), \quad (4)$$

where $s = \varepsilon_1/(\varepsilon_2 - \varepsilon_1)$, $g(x)$ is a nonnegative function of the spectral density determined on the segment [0, 1] and satisfying the sum rules

$$\int_0^1 g(x)dx = 1 \quad (5)$$

$$\int_0^1 xg(x)dx = (1 - f_2)/3. \quad (6)$$

Recently [13], we demonstrated that equation (2) corresponds to a spectral density function of the type

$$g_1(x) = \delta(x) \quad (7)$$

and equation (3) corresponds to the function

$$g_2(x) = \delta(x - 1 + f_2) = \delta(x - f_1). \quad (8)$$

In the case of an optical anisotropy, representation (4) is applied to the $\langle\varepsilon\rangle$ tensor components. Our approach to considering real SLs consists in replacing the delta function in equations (7) and (8) by a certain close function Φ possessing a nonzero halfwidth Δ and satisfying the limiting transition $\lim_{\Delta\to 0}\Phi(x) = \delta(x)$ or $\lim_{\Delta\to 0}\Phi(x) = \delta(x - 1 + f_2)$. Then, Δ can be considered as the small parameter ($\Delta \ll 1$) defining a measure of deviation of a real SL geometry from the ideal. The simplest example of this function Φ is a meander function that can be represented as product of two Heaviside's unit functions χ. Then, taking into account the normalization condition (5), the spectral density function (7) can be generalized to

$$g_1^*(x) = \frac{1}{\Delta}\chi(x)\chi(\Delta - x), \quad (9)$$

and the function (8), to

$$g_2^*(x) = \frac{1}{\Delta}\chi\left(x - 1 + f_2 - \frac{\Delta}{2}\right)\chi\left(\frac{\Delta}{2} - x + 1 - f_2\right) \quad (10)$$

(see the figure). Note that the latter relationship must be supplemented by the condition $\Delta < \min(f_1, f_2)$. Upon substituting (9) into (4) and accomplishing a quite simple integration, we obtain

$$\frac{\langle\varepsilon\rangle_1^*}{\varepsilon_1} = 1 + \frac{f_2}{\Delta}\ln\left|1 + \frac{\Delta}{s}\right|. \quad (11)$$

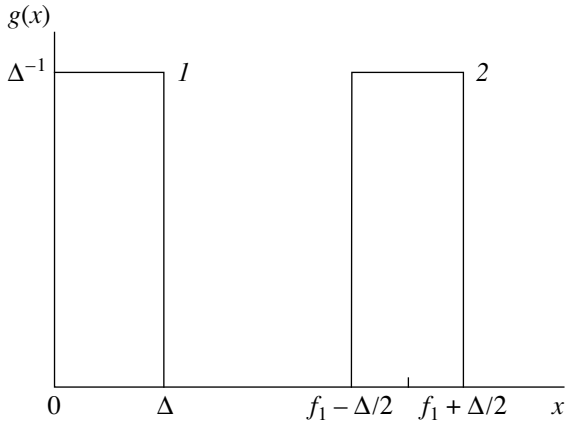

The spectral density function corresponding to equations (9) and (10) (curves *1* and *2*, respectively).

Expansion of equation (11) into a series yields

$$\frac{\langle\varepsilon\rangle_1^*}{\varepsilon_1} = 1 + \frac{f_2}{s} - \frac{1}{2}f_2\frac{\Delta}{s^2} + \frac{1}{3}f_2\frac{\Delta^2}{s^3} + \ldots = \langle\varepsilon\rangle_1 - \frac{1}{2}f_2\frac{\Delta}{s^2} + \frac{1}{3}f_2\frac{\Delta^2}{s^3} + \ldots. \quad (12)$$

By the same token, substituting (10) into (4) we obtain

$$\frac{\langle\varepsilon\rangle_2^*}{\varepsilon_1} = 1 + \frac{f_2}{\Delta}\ln\left|\frac{s + 1 - f_2 + \Delta/2}{s + 1 - f_2 - \Delta/2}\right|. \quad (13)$$

In the expansion of (13) in powers of Δ, the first nonvanishing term is of the order of Δ^2:

$$\frac{\langle\varepsilon\rangle_2^*}{\varepsilon_1} = 1 + \frac{f_2}{p} + \frac{1}{12}f_2\frac{\Delta^2}{|p|^3} + \ldots = \langle\varepsilon\rangle_2 + \frac{1}{12}f_2\frac{\Delta^2}{|p^3|} + \ldots, \quad (14)$$

where $p = s + 1 - f_2 = s + f_1$. This may imply that the ε_{zz} component of the dielectric tensor is less susceptible to changes upon deviation of a real SL geometry from the ideal.

As can be readily checked, in the trivial case $\mathrm{Im}(\varepsilon_1) = \mathrm{Im}(\varepsilon_2) = 0$, a nonideal SL geometry (i.e., $\Delta \neq 0$) leads to a decrease in $\langle\varepsilon\rangle_1$ (or ε_{xx}) according to equation (12) and an increase in ion $\langle\varepsilon\rangle_2$ (or ε_{zz}) according to equation (14), in agreement with the concept of upper and lower Wiener's boundaries.

In conclusion, note that the proposed approach seems to be correct only for the long-period superlattices, because we assume that ε_1 (ε_2) are the bulk dielectric permittivities of the SL components. In the case of short-period SLs, where a considerable role in the IR range may belong to confinement (localization) of the optical phonons (see, e.g., [3]) and/or charge carriers in

the layers, the proposed approach needs certain modifications. However, even in this case we will deal with relationships similar to (2) and (3) with modified ε_1 and ε_2 values. In particular, the phonon localization can be taken into account by replacing ε_1 and ε_2 in (2) by

$$\varepsilon_1 \longrightarrow \varepsilon_1^\infty\left(1 - \sum_{lm}\frac{S_{Tlm}}{\omega^2 - \omega_{Tlm}^2}\right),$$
$$\varepsilon_2 \longrightarrow \varepsilon_2^\infty\left(1 - \sum_{lm}\frac{S_{Tlm}}{\omega^2 - \omega_{Tlm}^2}\right), \quad (15)$$

and in (3), by

$$\varepsilon_1 \longrightarrow \left[\frac{1}{\varepsilon_1^\infty}\left(1 + \sum_{lm}\frac{S_{Llm}}{\omega^2 - \omega_{Llm}^2}\right)\right]^{-1},$$
$$\varepsilon_2 \longrightarrow \left[\frac{1}{\varepsilon_2^\infty}\left(1 + \sum_{lm}\frac{S_{Llm}}{\omega^2 - \omega_{Llm}^2}\right)\right]^{-1}, \quad (16)$$

where $\omega_{Tlm}(\omega_{Llm})$ and $S_{Tlm}(S_{Llm})$ are the frequency and strength of oscillators for the transverse (longitudinal) localized optical phonons, respectively [3].

REFERENCES

1. V. M. Agranovich and V. E. Kravtsov, Solid State Commun. **55** (1), 85 (1985).
2. N. Raj and D. R. Tilley, Solid State Commun. **55** (4), 373 (1985).
3. T. Dumelow, T. J. Parker, S. R. P. Smith, and D. R. Tilley, Surf. Sci. Rep. **17**, 151 (1993).
4. T. Dumelow and D. R. Tilley, J. Opt. Soc. Am. A **10** (4), 633 (1993).
5. E. F. Venger, A. V. Goncharenko, O. S. Gorya, *et al.*, Zh. Prikl. Spektrosk. **66** (4), 460 (1999).
6. O. Wiener, Abh. Leipz. Akad. **32**, 509 (1912).
7. W. R. Smythe, *Static and Dynamic Electricity* (McGraw-Hill, New York, 1950; Inostrannaya Literatura, Moscow, 1954).
8. D. J. Bergman, Phys. Rep. C **43** (9), 377 (1978).
9. E. Molinari, S. Baroni, P. Giannozzi, and S. Gironcoli, Phys. Rev. B **45** (8), 4280 (1992).
10. B. Samson, T. Dumelow, A. A. Hamilton, *et al.*, Phys. Rev. B **46** (4), 2375 (1992).
11. M. M. Dvoynenko, A. V. Goncharenko, V. R. Romaniuk, and E. F. Venger, Superlattices Microstruct. **26** (5), 333 (1999).
12. K. Ghosh and R. Fuchs, Phys. Rev. B **38** (8), 5222 (1988).
13. A. V. Goncharenko, V. Z. Lozovski, and E. F. Venger, Opt. Commun. **174** (1/4), 19 (2000).

Translated by P. Pozdeev

Technical Physics Letters, Vol. 26, No. 7, 2000, pp. 597–599. Translated from Pis'ma v Zhurnal Tekhnicheskoĭ Fiziki, Vol. 26, No. 14, 2000, pp. 13–17.

Resonance Phenomena during Vapor Condensation in a Cooled Tube

N. A. Pribaturin, M. V. Alekseev, and V. A. Fedorov

Institute of Thermal Physics, Siberian Division, Russian Academy of Sciences, Novosibirsk, 630090 Russia

e-mail: pribaturin@etp.nsc.ru

Received January 20, 2000

Abstract—Experiments show evidence of the resonance phenomena during vapor condensation inside a cooled tube. The resonance sharpness depends on the region of application of an external perturbation (vapor or condensed phase). © *2000 MAIK "Nauka/Interperiodica".*

Let us consider the condensation of a water vapor, flowing in a tube, on the inner surface of the tube intensively cooled from outside with a counterflow of cold water (Fig. 1). Under certain conditions, the vapor *1* entering the tube completely condensates so that only a flow of pure liquid phase *2* occurs at the output. Investigations of this process [1–4] showed that vapor condensation under these conditions is accompanied by instability leading to the development of pulsations in the vapor and condensate flow. It was established that the amplitude of pressure pulsations in the system depends on the vapor flow rate and the intensity of heat removal from the outer surface of the tube.

The results of our experiments showed that the nature of pressure pulsations inside the tube is related to periodic oscillations at the vapor–liquid interface. Figure 1 shows a typical cycle of these oscillations. The condensation of water vapor leads to the formation of a ring-shaped film of condensate propagating in the direction opposite to the vapor flow. The relative motion of phases gives rise to surface perturbations at the interface between the annular liquid film and the central vapor core. Moving up along the flow, these perturbations increase in amplitude and block the tube cross section with a continuous liquid plug. The axial velocity of vapor drops along the flow as a result of condensation. Vapor inside the resulting isolated bubble having zero intrinsic velocity, the bubble moves along the flow with the velocity of the condensate. The bubble rapidly condensates and the observed vapor–liquid interface returns back to the preexisting level.

These oscillations at the interface give rise to the synchronous pulsations of pressure in the zone of pure

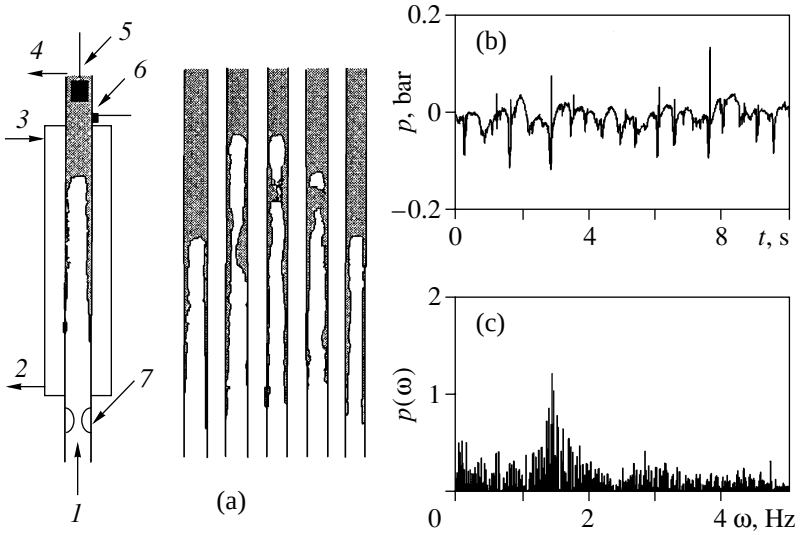

Fig. 1. (a) Schematic diagram of the experimental arrangement: (*1*) vapor inlet; (*2*, *3*) cooling water outlet and inlet; (*4*) condensate outlet; (*5*) piston; (*6*) pressure transducer; (*7*) rubber diaphragm. (b) Typical pressure profile; (c) typical oscillation frequency spectrum.

1063-7850/00/2607-0597$20.00 © 2000 MAIK "Nauka/Interperiodica"

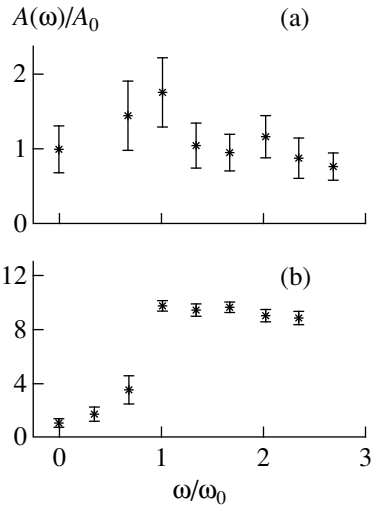

Fig. 2. Plots of the pressure pulsation amplitude versus frequency of the external excitation for the perturbation of (a) condensate and (b) vapor phase.

condensate inside the tube (Fig. 1). The upward motion of the interface leads to increasing pressure and the downward motion is accompanied by decreasing pressure, while the rapid vanishing of the isolated bubble generates on this background a pressure pulse of short duration and large amplitude (exceeding the base pressure variations). The spectrum of oscillations exhibits a region of dominating frequencies featuring the preferred base pulsation frequency. The width of this region with a maximum at the base pulsation frequency well conforms to the Gauss distribution. In our case, the base frequency is 1.5 Hz at a dispersion of 0.38 Hz. These values were obtained for the compete condensation of water vapor flowing at a rate of 6×10^{-4} kg/s, a temperature of 103°C, and a pressure of 0.3 MPa. The vapor was flowing in a glass tube with an internal diameter of 8 mm and a length of 075 m, cooled with water at a temperature of 12°C. The specific dissipated power of this single-tube counterflow vapor condensator was 0.25–0.32 kW/m^2.

Thus, the regime of complete vapor condensation inside the tube can be characterized by the base frequency of pressure pulsations. Since these pressure pulsations are related to the vapor–liquid interface oscillations, this frequency can be considered as an intrinsic frequency of the condensing vapor–liquid system. It was naturally suggested that any external perturbation introduced into this system either on the vapor side or in the condensate at a frequency equal to the intrinsic frequency of the system may give rise to resonance phenomena.

Figure 2 shows the amplitude–frequency characteristic of the pressure pulsations inside the tube measured in the course of induced periodic excitation of the condensed liquid or the vapor flow. The excitation was produced by the translation motion of piston *5* at the tube end or by the oscillations of a rubber diaphragm *7* in the vapor flow (Fig.1). In Fig. 2, A_0 and $\omega_0 = 1.5$ Hz are the average amplitude and the main (intrinsic) frequency of pressure pulsations in the tube in the absence of external excitation. As seen, the coincidence of the frequency of the induced excitation with the intrinsic frequency of the condensing vapor–liquid system is accompanied by an increase in the amplitude of pressure pulsations. As the frequency of the induced excitation increases above or decreases below the intrinsic frequency of the system, the amplitude of the pressure pulsations drops to a level corresponding to unperturbed oscillations. An important factor is the region of application of the external factor. Indeed, when the external excitation at the intrinsic frequency is applied to the vapor, the resonance is more pronounced than in the case of induced excitation of the condensate (the amplitude of pressure pulsations increases by a factor of 10 and 2, respectively).

The induced excitation of the condensate at the resonance frequency not only increases the amplitude of pressure pulsations but also "fills" the oscillation spectrum with frequencies below the intrinsic frequency. The resonance excitation of the vapor leads to an almost sinusoidal pressure pulsation in the tube, with short pressure spikes regularly appearing on top of the pulsations. This shape of the pressure pulsation profile is due to a cyclic motion of the vapor–liquid interface (synchronized with the external factor) reflecting the formation and collapse of the isolated vapor bubble once per cycle. The shape of the oscillation spectrum is characterized by a more clearly pronounced resonance frequency and by the second harmonic generation at 3 Hz.

Thus, we may speak of a differential quality of the (apparently identical) vapor–liquid and liquid–valor oscillatory systems. The difference in behavior of the two systems can be explained by asymmetry in the condensation heat removal through the side surface of the tube, which is always constant, and by variation in the vapor condensation rate upon application of the external factor. An increase in the vapor condensation rate upon excitation is due to a decrease in the dynamic vapor pressure in the phase of depression and by the heat exchange surface in this stage being more developed as compared to the compression stage. This lag is related to inertia of the liquid condensate plug. In the case of induced excitation of the condensate flow, changes in the pressure and velocity of the vapor are rather small because of a small susceptibility of the vapor core to these perturbations.

It is interesting to note that an induced excitation of the system studied at frequencies above the resonance value is also differently manifested depending on the region of application of the external perturbation. In the case of excitation of the condensate flow, the system behaves as a high-frequency filter cutting all frequen-

cies above the intrinsic one. Excitation of the vapor flow above the resonance frequency is accompanied only by an insignificant decrease in the amplitude of oscillations.

The work was supported by the Russian Foundation for Basic Research, project no. 98-02-17812.

REFERENCES

1. T. A. Rabas and P. G. Minard, Heat Transfer Eng. **8** (1), 40 (1987).
2. B. L. Bkhat and G. L. Vedekaind, Trans. ASME, Ser. C: J. Heat Transfer **102** (4), 113 (1980).
3. V. A. Fedorov, Russ. J. Eng. Thermophys., No. 4, 63 (1996).
4. O. O. Milman, V. A. Fedorov, N. A. Pribaturin, and S. I. Lezhnin, in *Proceedings of the 3rd International Conference on Multiphase Flows, ICNF-98, Lyon, France, 1998,* CD No. 630.

Translated by P. Pozdeev

Technical Physics Letters, Vol. 26, No. 7, 2000, pp. 600–602. Translated from Pis'ma v Zhurnal Tekhnicheskoĭ Fiziki, Vol. 26, No. 14, 2000, pp. 18–23.

Increasing the Sensitivity of Ellipsometry for the Study of Nanolayers

A. A. Romanenko

Institute of Applied Optics, National Academy of Sciences of Belarus, Mogilev, Belarus

e-mail: ipo@physics.belpak.mogilev.by

Received January 26, 2000

Abstract—It is shown that the application of a specially prepared dielectric film onto a highly refractive substrate prior to measurements considerably increases the sensitivity of ellipsometry in the study of nanolayers. A solution to the inverse ellipsometry problem is obtained. © *2000 MAIK "Nauka/Interperiodica".*

The task of increasing the sensitivity of ellipsometric measurements and the accuracy of solving the inverse ellipsometry problem are still of great importance for studying the optical properties of nanolayers (e.g., absorbed layers and Langmuir–Blodgett films) by this method [1]. The ellipsometric investigation reduces to analysis of the polarization angles ψ and Δ in the form

$$\rho = R_p(R_s)^{-1} = \tan\psi\exp(i\Delta), \qquad (1)$$

where R_p and R_s are the complex reflection coefficients of the *p*- and *s*-polarized waves. One can readily see from (1) that the relative variations in the angle Δ or in the angles ψ and Δ caused by variations in the R_p and R_s values during the formation of an adlayer can be maximized if one of the initial values of these quantities is close to zero. The traditional approach consists in using the angles of wave incidence close to the Brewster angle for which $R_p \longrightarrow 0$. However, in this case, the relative changes in the angle ψ are too small and fall within the experimental error, which hinders solution of the inverse ellipsometry problem—reconstruction (determination) of the refractive index n and the adlayer thickness d [2, 3]. The situation is considerably improved if one manages to minimize the R_s value, thus providing considerable changes in both ψ and Δ angles. Detailed analysis of this situation is the subject of the present study.

One can provide fulfillment of the condition $R_s = 0$ by applying a dielectric film onto the substrate prior to the experiment so as to obey the conditions that

$$n_2^2 = n_1^2\sin^2\varphi + n_1\cos\varphi\sqrt{n_3^2 - n_1^2\sin^2\varphi},$$

$$k_0 l = \frac{m\pi}{2}\frac{1}{\sqrt{n_2^2 - n_1^2\sin^2\varphi}},$$

which are met in the practically important case where $n_1 = 1.0003$ and $n_2 \geq 1.45$ at $n_3 > 2$. Here, $k_0 = 2\pi/\lambda$, where λ is the light wavelength in vacuum; $m = 1, 2, 3, \ldots$, φ is the angle of incidence; n_1, n_2, and n_3 are the refractive indices of the ambient medium, the film, and the substrate, respectively; and l is the film thickness.

The optical properties of subsurface layers are usually described within the framework of either a simplified model in which a layer is characterized by the effective values of the dielectric constant ε and thickness d (see, e.g., [4, 5]) or a more general model based on the concept of a nonlocal dielectric constant (see, e.g., [6, 7]). Below, the numerical evaluations are made on the basis of the traditional simplest model.

The sensitivity of ellipsometric measurements under the condition that $k_0 d \ll 1$ is usually evaluated by the quantities

$$S_\psi = \frac{\partial\psi}{\partial(k_0 d)} \quad \text{and} \quad S_\Delta = \frac{\partial\Delta}{\partial(k_0 d)},$$

having the sense of the [psi] and [delta] sensitivity coefficients [2]. The quantities S_ψ and S_Δ as functions of the angle of incidence φ are shown in the figure, where curves *1* and *2* refer to the samples with ($l \neq 0$) and without a film ($l = 0$). When calculating S_ψ and S_Δ, we used the following values: $n_1 = 1.0003$, $n_3 = 2.4$, $n_2 = 1.4569$, and $l = l_{opt} = 0.124$ μm ($m = 1$), which provided the zero refractive index for the *s*-polarized wave at $\varphi = \varphi_0 = 45°$. The refractive index of the adsorbed layer was taken to be $n = \sqrt{\varepsilon} = 1.5$ [4]. It is seen from the figure that $S_\psi = 0$ in the case of $l \neq 0$ at $\varphi \cong \varphi_0$, but in the vicinity of φ_0, the function S_ψ has two extrema. The absolute values of S_ψ at these points considerably exceed the absolute value of S_ψ in the vicinity of the Brewster angle ($\varphi = \varphi_B$) for $l = 0$. Similar features are observed in the behavior of S_Δ for the structure under consideration ($l \neq 0$) and for the structure without a film ($l = 0$). It is seen that, at $l = l_{opt}$, high sensitivity is

1063-7850/00/2607-0600$20.00

observed over a wide range of the angles of incidence, which is not characteristic of the case $l = 0$.

Now, consider the inverse ellipsometry problem of determining the ε and d. This problem is usually solved by the method of stepwise minimization of a functional [2, 3, 8] constructed with the use of the rigorous ellipsometry equation. Mathematical difficulties encountered in this approach are well known [3, 8, 9] and are associated with the choice of a zeroth approximation that would be sufficiently close to the true solution, the filtration of the spurious minima of this functional, and the choice of the appropriate criterion of the procedure cessation with an approach to the absolute minimum. Below, we suggest a more efficient method for numerical solution of the inverse ellipsometry problem based on the contour integration technique [10].

We shall use an approximate ellipsometric function obtained by expanding the reflection coefficients for the p- and s-polarized waves in powers of $k_0 d$ and retaining only the linear terms. Then we arrive at the ellipsometric function in the form

$$\rho \cong \rho_0 \frac{1 - 2i\nu\beta_p(k_0 d)}{1 - 2i\nu\beta_s(k_0 d)}, \qquad (2)$$

where $\rho_0 = r_{0p}/r_{0s}$ is the ellipsometric function in a system without the layer studied, $\nu = \sqrt{\varepsilon - n_1^2 \sin^2\varphi}$, $\varepsilon = n^2$, $i = \sqrt{-1}$, $\beta_{p,s} = [(1 - r_1/r_0)/(1 + r_1 r_2)]_{p,s}$, and r_1 and r_2 are the Fresnel coefficients of reflection from the interface between the ambient medium and the adlayer and from two interfaces of the adlayer–film–substrate system. In order to determine the ε and d values, we assumed that the polarization angles (ψ_0 and Δ_0) without the adsorbed layer and the polarization angles (ψ and Δ) with such a layer were measured at two different incidence angles, $\varphi = \varphi_1$ and $\varphi = \varphi_2$. Then, eliminating the quantity $k_0 d$ from (1), we arrive at the following equation for ε:

$$F(\varphi_1) - F(\varphi_2) = 0, \qquad (3)$$

where $F(\varphi) = A[\nu(\beta_s(A + 1) - \beta_p)]^{-1}$ and $A = \tan\psi(\tan\psi_0)^{-1}\exp[i(\Delta - \Delta_0)] - 1$. If this equation is fulfilled, the layer thickness can be obtained from the formula

$$d = \mathrm{Re}[(2ik_0)^{-1} F(\varphi_1)]. \qquad (4)$$

Thus, we reduced our problem to the determination of the roots of equation (3). It is expedient to search for these roots by the method of contour integration with due regard for the fact that, if we consider the branch of the square root $\mathrm{Re}\nu \geq 0$, the left-hand side of (3) is an analytical function of ε in the half-plane $\mathrm{Re}\varepsilon > n_1^2 \sin^2\varphi$. In particular, this method showed that, in the physically important range of $\mathrm{Re}\varepsilon(1.3)^2$, equation (3) has only one root.

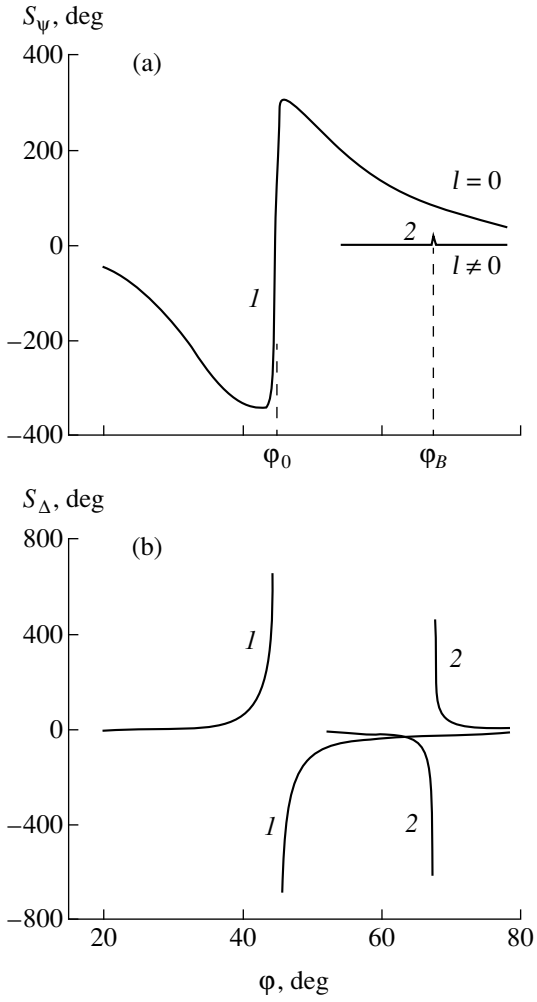

Fig. 1. Sensitivity coefficients S_ψ and S_Δ as functions of the angle of incidence φ.

Now let us evaluate the errors in the determination of ε and d. These errors can be represented as sums of systematic and random errors. The former are associated with the approximate character of (2) and can be evaluated by comparing the exact values of ε and d with the corresponding values obtained from equations (3) and (4) using the rigorously calculated ρ and ρ_0 functions (see below). The random errors are caused by the noise in recording the angles ψ and Δ and can be evaluated using two relationships following from (3) and (4),

$$|\delta\varepsilon| \leq \sum_{i=1}^{2}\left[\left(\left|\frac{\partial\varepsilon}{\partial\psi_{0i}}\right| + \left|\frac{\partial\varepsilon}{\partial\psi_i}\right|\right)|\delta\psi| + \left(\left|\frac{\partial\varepsilon}{\partial\Delta_{0i}}\right| + \left|\frac{\partial\varepsilon}{\partial\Delta_i}\right|\right)|\delta\Delta|\right], \qquad (5)$$

$$|\delta d| \leq \left|\frac{\partial d}{\partial\varepsilon}\right||\delta\varepsilon| + \left(\left|\frac{\partial d}{\partial\psi_{0i}}\right| + \left|\frac{\partial d}{\partial\psi_i}\right|\right)|\delta\psi| + \left(\left|\frac{\partial d}{\partial\Delta_{0i}}\right| + \left|\frac{\partial d}{\partial\Delta_i}\right|\right)|\delta\Delta|, \qquad (6)$$

Table

Angles of incidence φ_1, φ_2, deg	Preset		Reconstructed	
	d, nm	n	d, nm	n
43, 47	1	1.5	0.993	1.5026
41, 49	2	1.5	1.959	1.5066
40, 50	3	1.5	2.885	1.5120
38, 52	5	1.5	4.579	1.5262

where ψ_{0i}, Δ_{0i}, ψ_i, and Δ_i are the values of ψ_0, Δ_0, ψ, and Δ related to the angle of incidence φ_i, whereas $\delta\psi$ and $\delta\Delta$ are the random errors in the measurements of angles ψ and Δ (usually not exceeding 0.02°). The partial derivatives can readily be obtained from (3) and (4).

The table lists the results of the computational experiments on the reconstruction of $n = \sqrt{\varepsilon}$ and d values corresponding to various combinations of the angles φ_1 and φ_2 at various values of d calculated according to the above scheme. An obvious increase in the systematic errors with increasing d indicates the deterioration of the accuracy of approximation (2). Moreover, the approximate character of expression (2) excludes the reconstruction of the imaginary part of n, because it leads to unacceptable errors. The calculations of the $|\delta\varepsilon|$- and $|\delta d|$-values from (5) and (6) for different φ_1 and φ_2 pairs showed that these values reach the minimum in the case $|\varphi_1 - \varphi_0| = |\varphi_2 - \varphi_0|$, where φ_1 and φ_2 refer to the extrema of the function $S_\psi(\varphi)$. Calculations based on the functions $\rho = \tan\psi \exp(i\Delta)$ and $\rho_0 = \tan\psi_0 \exp(i\Delta_0)$, together with their errors $\delta\psi = \delta\Delta = \pm 0.01°$ set in a random way, show that the problem of the determination of ε and d has a stable solution, with the relative random errors $|\delta\varepsilon/\varepsilon|$ and $|\delta d/d|$ not exceeding 2 and 10%, respectively. This corresponds to the ranges of $|\delta\varepsilon|$ and $|\delta d|$ values determined by expressions (5) and (6).

Thus, we have shown that it is possible to increase the sensitivity of ellipsometry in the studies of nanometer layers and to obtain an adequate solution to the inverse problem of ellipsometry. The determination of the ellipsometric function (1) leads to the conclusion that the high sensitivity of the above scheme of ellipsometric measurements is independent of the choice of the electrodynamic model of the layer. This fact provides determination of the integrated parameters characterizing the optical properties of nanolayers using the concept of a nonlocal dielectric constant.

REFERENCES

1. A. Ulman, *Ultrathin Organic Films* (Academic, Boston, 1991), p. 547.
2. R. M. Azzam and N. M. Bashara, *Ellipsometry and Polarized Light* (North-Holland, Amsterdam, 1977; Mir, Moscow, 1981).
3. A. I. Semenenko, V. V. Bobro, and A. S. Mardezhov, Avtometriya, No. 1, 56 (1998).
4. Y. Jiang, S. Zhang, H. Shao, *et al.*, Appl. Opt. **34** (1), 169 (1995).
5. P. V. Adamson, Opt. Spektrosk. **83** (1), 169 (1997) [Opt. Spectrosc. **83**, 154 (1997)].
6. V. A. Kosobukin, Opt. Spektrosk. **59** (2), 370 (1985) [Opt. Spectrosc. **59**, 222 (1985)].
7. G. V. Rozhnov, Zh. Éksp. Teor. Fiz. **103** (3), 740 (1993) [JETP **76**, 364 (1993)].
8. V. A. Aver'yanov, V. A. Fedorov, and S. G. Yastrebov, Zh. Tekh. Fiz. **64** (1), 103 (1994) [Tech. Phys. **39**, 57 (1994)].
9. A. N. Tikhonov and V. Ya. Arsenin, *Solutions of Ill-Posed Problems* (Nauka, Moscow, 1986; Halsted, New York, 1977).
10. A. A. Romanenko and A. B. Sotskiĭ, Zh. Tekh. Fiz. **68** (4), 88 (1998) [Tech. Phys. **43**, 427 (1998)].

Translated by L. Man

Technical Physics Letters, Vol. 26, No. 7, 2000, pp. 603–604. Translated from Pis'ma v Zhurnal Tekhnicheskoĭ Fiziki, Vol. 26, No. 14, 2000, pp. 24–27.

Effect of Thermodynamic Prehistory on the Curie Temperature of Polycrystalline Sodium Lithium Niobate

I. V. Pozdnyakova and L. A. Reznichenko

Institute of Physics, Rostov State University, Rostov-on-Don, Russia

e-mail: klevtsov@ip.rsu.ru

Received January 24, 2000

Abstract—The thermodynamic prehistory of the samples of $Na_{1-x}Li_xNbO_3$ ceramics ($0.015 \le x \le 0.025$) affects the behavior of these solid solutions in applied electric fields. The field-induced shift of the Curie temperature in this system can be minimized by selecting optimum conditions for structure formation. © *2000 MAIK "Nauka/Interperiodica".*

Previously [1], we studied the conditions of the antiferroelectric–ferroelectric (AFE–FE) phase transformation in the $Na_{1-x}Li_xNbO_3$ solid solution system. The temperature-induced shift of the point of transition to the nonpolar phase (the Curie temperature) in the vicinity of the AFE–FE transformation in a composition with $x = 0.02$ was characterized by $\Delta T_c = 35$ K per kV/cm, while Ismailzade *et al.* [2] reported a much smaller value ($\Delta T_c = 1$ K per kV/cm). The discrepancy can be explained either by simple thermodynamic considerations (using the expansion of the thermodynamic potential in powers of the order parameter in the presence of an external electric field) or by the different experimental conditions used in the two works. For example, we measured the electric field strength directly in the sample, which is usually not done in other works.

At the same time, it is well known that the FE ceramics based on alkali metal niobates may possess considerable spatial (in particular, concentrational) inhomogeneity, which is even more pronounced than analogous inhomogeneity in other ceramic materials. This is explained by certain crystallochemical features of the alkali metal niobates. First, by the small size of A-cations and the resulting mismatch with the parameters of structure-forming NbO_6 octahedra, which leads to the formation of large octahedral voids and the free arrangement of cations. Second, by the low atomic weights of alkali metals, which results in the increased mobility of these atoms and susceptibility to exchange with other ions, accumulation of vacancies, and the formation of phases with variable composition. Third, by the inherited Nb_2O_5 block structure, leading to the formation of tetrahedral and octahedral voids [3]. All these features are especially pronounced in the (Na,Li)NbO_3 system, where the aforementioned circumstances are emphasized by the proximity of the ionic radii of Li^+ (0.68 Å) and Nb^{5+} (0.66 Å) making these cations interchangeable and increasing the degree of intrinsic disorder. All these factors result in a strongly nonequilibrium character of this system and, hence, make the system response to external actions significantly dependent on the sample preparation conditions.

In order to elucidate the effects of thermodynamic prehistory (conditions of the ceramic structure formation) on the behavior of solid solutions under the action of an external electric field, we performed the following experiment. Several solid solutions of the $Na_{1-x}Li_xNbO_3$ system with $0.015 \le x \le 0.025$ were prepared by different methods, including the base technique–fast hot pressing (FHP) at a heating rate of 7000–8000 K/h and a total exposure time of 40 min, continued hot pressing (CHP) at the same heating rate and an exposure increased to 4 h, and the conventional ceramic technology (CCT) at a heating rate of 200–300 K/h. Data on the field-induced T_c variation in the samples of (Na,Li)NbO_3 with $0.015 \le x \le 0.025$ prepared by different methods are presented in the figure. Note certain leveling of the ΔT_c maximum in the sam-

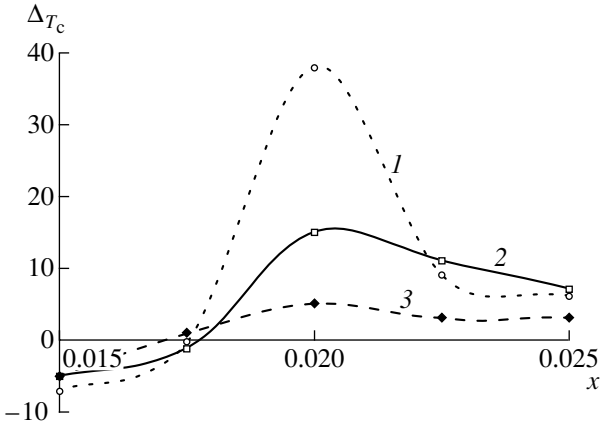

The plot of field-induced T_c variations in the samples of $Na_{1-x}Li_xNbO_3$ ceramics prepared by different methods: (*1*) FHP; (*2*) CHP; (*3*) CCT.

ples obtained by CCT (i.e., under comparatively mild sintering conditions): the change in T_c in the CCT ceramics does not exceed 5–7 K per kV/cm. It should be noted that a minimum scatter of the T_c values was observed in the samples prepared by CHP, while the scatter in CCT and FHP samples was approximately the same.

These results allow us to draw the following conclusions. A change of electric ordering in the (Na,Li)NbO_3 makes the electric-field-induced shift of the Curie temperature (as well as the Curie temperature proper) strongly dependent on the conditions of a solid solution preparation, that is, on the thermodynamic prehistory. This variation can be minimized using the treatment regimes leading to the states close to thermodynamic equilibrium. As is known, the solid-state synthesis does not provide for completeness of the solid solution formation reactions (and, hence, for the homogeneous product composition). Subsequent sintering of the samples in the CCT regime detrimentally affects reproducibility of the material properties, although a comparatively slow temperature increase and prolonged exposure at high temperatures allow the diffusion processes to proceed more completely. The hot pressing method activates the diffusion process (due to applied external pressure), but a very fast temperature rise and comparatively short exposure at high temperatures can hardly allow this process to attain a stationary regime.

Based on the results of our investigation, we may suggest that the best methods for the synthesis of solid solutions of the system studied in the region of the AFE–FE transformation are the hot pressing techniques combining the advantages of hot pressing and conventional ceramic technologies or the hot pressing of large blocks, in which case the rate of temperature rise is sharply reduced and the application of external pressure is accompanied by prolonged exposure to high temperatures.

The work was supported by the Russian Foundation for Basic Research, project no. 99-02-17575.

REFERENCES

1. I. V. Pozdnyakova, L. A. Reznichenko, and V. G. Gavrilyachenko, Pis'ma Zh. Tekh. Fiz. **25** (18), 81 (1999) [Tech. Phys. Lett. **25**, 752 (1999)].
2. I. G. Ismailzade, P. Hagenmuller, O. A. Samedov, *et al.*, Neorg. Mater. **22** (5), 846 (1986).
3. L. A. Reznichenko, O. N. Razumovskaya, and L. A. Shilkina, in *Abstracts of Papers. Intern. Sci.-Pract. Conf. "Piezotechniques-97," Obninsk, 1997*, p. 191.

Translated by P. Pozdeev

Technical Physics Letters, Vol. 26, No. 7, 2000, pp. 605–608. Translated from Pis'ma v Zhurnal Tekhnicheskoĭ Fiziki, Vol. 26, No. 14, 2000, pp. 28–35.

Electromagnetic Wave Propagation in a Plane Dielectric Layer under Critical Conditions

I. P. Kozlov

State Research Institute of Applied Mechanics and Electrodynamics, Moscow, Russia

Received December 7, 1999

Abstract—An exact solution to the problem of a plane wave propagation in a plane-stratified dielectric layer of arbitrary thickness is studied. An approach based on self-consistent finite differences is suggested, replacing the layer by a stack of homogeneous sublayers of variable thickness matched to the local behavior of the permittivity profile. For the region around zero permittivity, it is predicted that small perturbations of the physical parameters of the problem cause qualitative and quantitative changes in the solution. The conditions for the excitation of a surface wave are formulated. Computed data for the wave are presented. © *2000 MAIK "Nauka/Interperiodica".*

Introduction. In solving mathematical problems arising in the design of very-high-speed switching elements for SHF, EHF, or optical integrated circuits, the solutions that have clear physical meaning are the most important. Previously, we studied an exact solution in terms of elementary functions to the problem concerning the propagation of electromagnetic waves in a plane-stratified medium with some of the parameters falling in the vicinity of their critical values, where even small perturbations of these parameters may radically change the solution [1–4]. For example, a wave with a small angle of incidence (state 0) may be transformed into a wave propagating parallel to the surface (state 1). The small parameters were the absorption and the angle of incidence [3] or the reciprocal curvature radius of the surface $\varepsilon = \text{const}$, where ε is the permittivity [4]. A surface *E*-wave in a plane layer was estimated [3].

In this study, our approach is applied to a wave that is normally incident on a nonabsorbing inhomogeneous plane-stratified layer extending from z_1 to z_N. The layer is in a homogeneous environment with $\varepsilon = \varepsilon_1$ for $z < z_1$ and $\varepsilon = \varepsilon_N$ for $z > z_N$, where $\varepsilon > 0$. Only a transmitted wave exists behind the layer. Let us replace the layer by a stack of homogeneous sublayers of variable thickness, $\Delta z_n = z_{n+1} - z_n$, such that $\delta^2 = \varepsilon_n/\varepsilon_{n+1} = \text{const}$. Near the zero of $\varepsilon(z)$, the permittivity is replaced by a nonlinear function:

$$\varepsilon = \beta^2/(b + kz)^2 \quad (gr(\varepsilon_L) = \text{const} \gg 1). \qquad (1)$$

The replacement is done in such a way that $\varepsilon(z)$ remains continuously differentiable at $z = z_L$. Now the problem becomes exactly solvable in elementary functions. In (1), the new variable is $gr(\varepsilon) = -\alpha/\varepsilon^{3/2}$, $\alpha = d\varepsilon/d(kz)$, and $k = 2\pi/\lambda$, λ being the wavelength in free space. Introducing local coordinates with the origin at z_n eliminates the parameter $\sqrt{\varepsilon_n}\, kz_n$ from the recurrent formulas for the reflection coefficient $R_0^n = R_n\{gr(\varepsilon_1), \varepsilon_1/\varepsilon_n, \delta\}$. When $\delta \longrightarrow 1$, the functional equation for R_0^n is reduced to the Riccati equation. According to the principle of layer similarity adopted, such layers have equivalent reflection coefficients $R_0^N = R\{gr(\varepsilon_1), \varepsilon_1/\varepsilon_N\}$ and identical electric fields $E = E\{gr(\varepsilon_1), \varepsilon_1/\varepsilon_N\}$ near the zero of $\varepsilon(z)$. Thus, similar layers have the same $gr(\varepsilon_1) = -\alpha_1/(\varepsilon_1)^{3/2}$ and $\varepsilon_1/\varepsilon_N$ but different α_1 and ε_1 [the layers have equal $gr(\varepsilon_n)$ for each $n = 1, 2, ..., N - 1$].

For a linear-profile layer in the context of model 3 (Fig. 1, see also the next section), the following properties have been established. (1) The solution is unstable

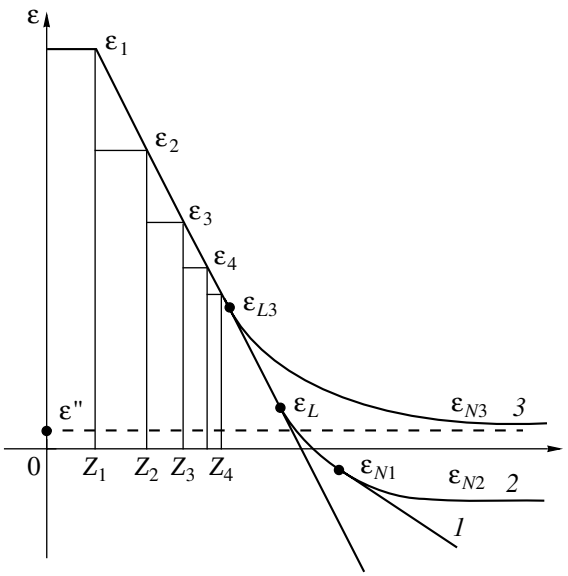

Fig. 1. Linear- and nonlinear-profile layers matched near the zero of $\varepsilon(z)$.

at $\varepsilon = 0$: a small perturbation $\Delta\theta_n$ [or the perturbation $\Delta\varepsilon = \varepsilon_n(\Delta\theta_n)^2$ for a double layer] for $\varepsilon \longrightarrow 0$ results in $\theta \longrightarrow \pi/2$, since $\varepsilon_0 = \varepsilon_n \sin^2(\Delta\theta_n) = \text{const}$ (a plane-layer invariant). (2) When $gr(\varepsilon_N) \longrightarrow 0$, $R \longrightarrow 0$ for any $\varepsilon_N > 0$. (3) $|R| \longrightarrow 1$ for $|\varepsilon_N| \longrightarrow 0$. (4) For a transmitted wave, the energy flux density $S_L/S_1 \longrightarrow 0$ when $\varepsilon_L \longrightarrow 0$. Property 4 and the principle of layer similarity imply that the zero of $\varepsilon(z)$ is a critical point around which the solution is extremely sensitive to small perturbations of physical parameters, especially of the absorption and the incidence angle θ_1.

Problem formulation and solution. The base problem is to describe a plane wave incident at a zero angle on a semi-infinite plane linear-profile layer of a nonabsorbing dielectric ($\varepsilon < \varepsilon_1$). Model 1 refers to a slightly modified base problem with small perturbation in the initial parameters: the absorption $\varepsilon'' = \text{const}$; $\varepsilon' = \varepsilon - i\varepsilon''$; the wave incidence angle θ_1 measured from the z-axis in the zy-plane; or $\varepsilon_0 = \varepsilon_1' \sin^2\theta_1 \ll \varepsilon_1$ (the invariant ε_0 is assumed to be a real quantity). The function $\varepsilon(z)$ is modified near its zero, assuming that $0 < \varepsilon_L, \varepsilon_L > \varepsilon > \varepsilon_N$, $\varepsilon_N < 0$, and $\varepsilon_L \approx \varepsilon_L''$. The linear function $gr(\varepsilon')(\varepsilon')^{3/2} = \text{const}$ is replaced by $gr(\varepsilon') = \text{const}$ such that $gr(\varepsilon_L) > 20$, where $gr(\varepsilon') = -\{d\varepsilon'/d(kz)\}/(\varepsilon')^{3/2}$ and $\varepsilon'' \ll \varepsilon_1$. Model 3 is a degenerate variant of model 1 with $\varepsilon_L''/\varepsilon_L \ll 1$, and model 2 is defined by the condition $d\varepsilon/dz = 0$ at $\varepsilon = \varepsilon_N$. In model 1 with $|\varepsilon_L| \longrightarrow 0$, the nonlinear-profile layer becomes a semi-infinite linear-profile layer that can be approximated by model 3 with infinitesimal absorption: $\varepsilon'' \ll \alpha^{2/3}$. Model 1 allows an exact solution, which is studied below.

According to our approach, the layer with a continuously varying permittivity profile is replaced by a stack of homogeneous sublayers of variable thickness such that $\delta^2 = (\varepsilon_n - \varepsilon_0)/(\varepsilon_{n+1} - \varepsilon_0) = \text{const}$ and $\delta^2 - 1 \ll 1$ ($\varepsilon > \varepsilon_0$ and $\Delta z_n \longrightarrow 0$ as $n \longrightarrow \infty$). Let us denote the amplitudes of transmitted and reflected waves in each sublayer by A^n and C^n, respectively. Then, the electric field E of an H-wave and the magnetic field H of an E-wave (polarized in the plane of incidence) in the sublayers can be expressed in terms of A^n and C^n:

$$E_x^n = A_H^n \exp(-i\sqrt{\varepsilon_n' - \varepsilon_0}kz_n) + C_H^n \exp(i\sqrt{\varepsilon_n' - \varepsilon_0}kz_n),$$

$$H_x^n = A_E^n \exp(-i\sqrt{\varepsilon_N' - \varepsilon_0}kz_n)(1 + R_{0E}^n),$$

where $n = 1, 2, \ldots, L-1$, and A_H^1 and A_E^1 are the given amplitudes. The amplitudes A_E^n and A_H^n refer to the E- and H-waves, respectively. According to [2, 3], $R_{0E}^n = (C_E^n/A_E^n)\exp(2i\rho_n)$, $\rho_n = \sqrt{\varepsilon_n'}\cos\theta_n kz_n$, and A_E^n obey the following equations:

$$R_E^n \exp(2ip_n) = R_{0E}^n = \frac{r_{nE} + R_{0E}^{n+1}\exp(i\Delta\rho_{n+1})}{1 + r_{nE}R_{0E}^{n+1}\exp(i\Delta\rho_{n+1})}, \quad (2)$$

$$A_E^{n+1} = A_E^1 \exp\left\{-i\sum_{p=1}^{n}\left(1 - \frac{1}{\delta_p}\right)\rho_p\right\}P_E^{n+1},$$
$$P_E^n = \prod_{m=1}^{n-1}\left[1 + \frac{\delta_{nE} - 1}{2}(1 - R_{0E}^m)\right], \quad (3)$$

where $n = 1, \ldots, L-1$; $R_{0E}^L = R_{LE}$; $\Delta\rho_L = 0$; $\delta_n = \frac{\sqrt{\varepsilon_n' - \varepsilon_0}}{\sqrt{\varepsilon_{n+1}' - \varepsilon_0}}$; $\delta_{nH} = \delta_n$; $\delta_{nE} = \delta_n\frac{\varepsilon_{n+1}'}{\varepsilon_n'}$; $\xi_n = \frac{\delta^{2n}\varepsilon''}{\varepsilon_1 - \varepsilon_0}$;

$$r_{nH} = \frac{(\delta - 1)(1 + i\xi_n)}{(\delta + 1)(1 + \xi_n^2)},$$

$$r_{nE} \cong -r_{nH}\left[\frac{\varepsilon_0}{\varepsilon_n'} + \frac{\varepsilon_{n+1}'}{\varepsilon_n'}\left(\frac{\varepsilon_0}{\varepsilon_n'} - 1\right)\right],$$

$$\Delta\rho_{n+1} = \frac{\delta^2 - 1}{\delta^{3n} gr(\varepsilon_1)}\sqrt{1 - i\xi_n},$$

and R_{LE} is the reflection coefficient of the layer (z_L, z_N) in the local coordinate system with the origin z_L. Equations for R_{0H}^n and A_H^n can be derived from (2) and (3) by replacing subscripts E with H.

Oblique wave incidence near the zero of $\varepsilon(z)$. For a transmitted E-wave, the direction of the Poynting vector is defined as $\cot\Phi_{nE} = \text{Re}(\gamma_n^*\sqrt{\gamma_n^* - 1})/\text{Re}(\gamma_n^*)$, where $\gamma_n = \varepsilon_n'/\varepsilon_0$ [3]. The Poynting vector coincides with the z-axis if $\varepsilon''/\varepsilon_0 \gg 1$ and with the y-axis if $\varepsilon''/\varepsilon_0 \ll 1$ (a laminar flow). For $\varepsilon'' = 0$, we may consider two limiting cases corresponding to the wave propagation along the z-axis [when $\delta^{2n}(\theta_1)^2 \ll 1$, $r_{nE} \approx -r_{nH} \approx (\delta - 1)/2)$] and along the y-axis [when $\delta^{2n}(\theta_1)^2 \gg 1$, $r_{nE} \approx r_{nH}$]. Since r_{nE} changes its sign when $\varepsilon''/\varepsilon_0 \ll 1$, we suppose $R_{0E} \cong \exp\left\{(i+1)\frac{(\varepsilon'')^{3/2}}{\alpha}\sum_{m=0}^{M} r_{N-m}\right\} \approx 0$ at $\varepsilon = \varepsilon_p$. Then there is no reflected E-wave in this sublayer, the direction of the transmitted E-wave being determined by the relation $\varepsilon_0 = \varepsilon_p \sin^2\theta_p$. If $\varepsilon''/\varepsilon_0 < 0.1$, then the wave energy can be transferred to a surface E-wave [3]. The orders of magnitude estimated for the shortwave approximation are as follows: $\varepsilon_p \approx$

$0.01(\alpha_1)^{2/3}$ at $R = 0.7$ [1]. Furthermore, $\varepsilon'' \approx 10^{-4}(\alpha_1)^{2/3}$ and $\varepsilon_0 \approx 10^{-3}(\alpha_1)^{2/3}$.

Normal incidence near the zero of ε(z). Let $|\varepsilon_L| \longrightarrow 0$. Then model 2 gives $R_L = 0.28 - 0.25i$ for $(\varepsilon''/\varepsilon_L)^2 = 3$ and $R_L = 0.73 - 0.15i$ for $(\varepsilon''/\varepsilon_L)^2 = 1/3$. Furthermore, models 2 and 3 imply

$$S_L/S_1 \longrightarrow 0 \text{ (if } \varepsilon_N > 0 \text{ or } \varepsilon_N < 0).$$

This demonstrates the extreme sensitivity of the solution to the boundary conditions and refines the data obtained previously [1].

In model 3 with $\varepsilon'' = 0$, the solution varies rapidly in response to small variations of z. Upon eliminating uncertainties from the expression for E_x^N, we obtain $\left|E_x^N\right|^2 = S_N\sqrt{\varepsilon_1}/(S_1\sqrt{\varepsilon_N}) \longrightarrow \infty$ for $\varepsilon_N \longrightarrow 0$. Formulas (2) and (3) imply that dE_x^n/dz and dR_0^n/dz grow in magnitude as $\varepsilon_n \longrightarrow 0$, the growth rate for a linear-profile layer being higher than that for a nonlinear profile (see (1)). The possibility of $E \longrightarrow \infty$ was proved in [2] (by expanding the solution into a series) and confirmed in [5] for an E-wave in a semi-infinite linear-profile layer. Figure 1 illustrates the rapid variation of R and E: the sublayer thickness decreases to zero for $\varepsilon \longrightarrow 0$ ($r_n = \text{const}$). The last feature and the solution instability indicate that we face an ill-posed problem in Tikhonov's sense [6]. In the presence of absorption, we deal with a well-posed problem, but computational difficulties do remain because of the resonance character of $E(z)$, the more so that the wave reaches the region $\varepsilon \approx \varepsilon''$ without reflections if $gr(\varepsilon'') \ll 1$. For the base problem, we consider a solution (or, more correctly, a quasi-solution) in terms of the limit $|\varepsilon_L| \longrightarrow 0$ in models 1, 2, and 3 for $\varepsilon''/\varepsilon_0 \gg 1$ (assuming that Snell's law is valid). Physically, the base problem refers to a nearly normal incidence of a wave onto a nearly plane layer with infinitesimal absorption at $\varepsilon''/\varepsilon_0 \gg 1$.

Critical conditions: computing the field near the zero of ε(z). The above-mentioned properties lead to solution branching near the zero of $\varepsilon(x)$. It is the absorption that is responsible for switching from one branch to another. For example, if $\varepsilon''/\varepsilon_0 \ll 1$, then a normally incident ray breaks up near the zero of $\varepsilon(z)$. This may give rise to a surface wave, depending on the polarization of the incident wave, the value of $|\varepsilon'|$, the magnitude and sign of the curvature radius of the surface $\varepsilon = \text{const}$, and the length and shape of the optical path. The surface waves in a plane layer are treated in detail in [8]; however, that analysis rests on an approximate solution of Maxwell's equations. The plane-stratified model is valid for $\chi = \sqrt{\varepsilon''}\,kr \gg 1$. If χ is on the order of unity, one has to consider a diffraction problem. If $\chi \ll 1$ and $gr(\varepsilon'') \ll 1$, the incident power may scatter in all directions, resulting in radiation losses. To allow for the curvature of the surface $\varepsilon = \text{const}$, the proposed approach was extended to the case of spherical coordinates [4]. This entailed description of the diffraction from asymmetrically nested homogeneous balls. The field near the zero of $\varepsilon(z)$ was found by the method of wave amplitude transformation with displacement of the spherical coordinate system [9].

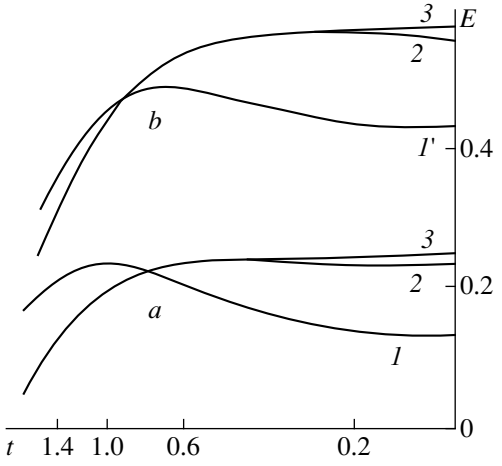

Fig. 2. Electric field vs. $t = \varepsilon/\varepsilon_1[gr(\varepsilon_1)]^{-2/3}$ for $\varepsilon'' = 0$ and $\theta_1 = 0$ for $gr(\varepsilon_1) = 0.4$ (*a*) and 0.5 (*b*) and $\varepsilon_1/\varepsilon_N = 10^2$ (*1*), 0.2×10^5 (*2*), and 0.2×10^9 (*3*). Merging of the curves when $\varepsilon_1/\varepsilon_N \gg 1$ indicates the basic property that $S_L/S_1 \longrightarrow 0$ as $\varepsilon_L \longrightarrow 0$.

Figures 2 and 3 present computed values of the electric field and the reflection coefficient. A solution to the base problem was expressed in terms of the Airy functions. Near the zero of $\varepsilon(z)$, one must allow for absorption and employ both of the Airy functions. Figure 3 demonstrates that the total field $E(t)$ has a resonance character. The computation enabled us to establish a criterion of applicability for the longwave approximation, $gr(\varepsilon_L) > 20$, which can be used for preliminary estimation when designing very-high-speed switches. Also useful are the criterion $\sqrt{|\varepsilon_N'|}\,kr_N \gg 1$ with $\delta^{2N}(\theta_1)^2 \ll 1$ for applicability of the model of a plane wave incident on a plane-stratified medium at a zero angle and the criterion $\varepsilon''/\varepsilon_0 < 0.1$ for the excitation of a surface wave. Finally, we mention a criterion for the shortwave approximation: $gr(\varepsilon_L) \ll 1$ [1]. It was found that 96% of the incident energy can be transferred into a surface wave under nearly normal incidence (for $\varepsilon_1 = 1$), provided that the thickness h of a linear-profile layer is about 2λ. For a nonlinear-profile layer described by equations (2) and (3), the problem can be optimized with respect to h. Sequential run by (2) and (3) enables one to solve the nonlinear problem. The base problem can be solved in terms of model 3 applicable for $\varepsilon'' \ll 0.1\alpha^{2/3}$, which provides a simple solution and allows one to use the principle of layer similarity and the energy conservation law. Physically, the pres-

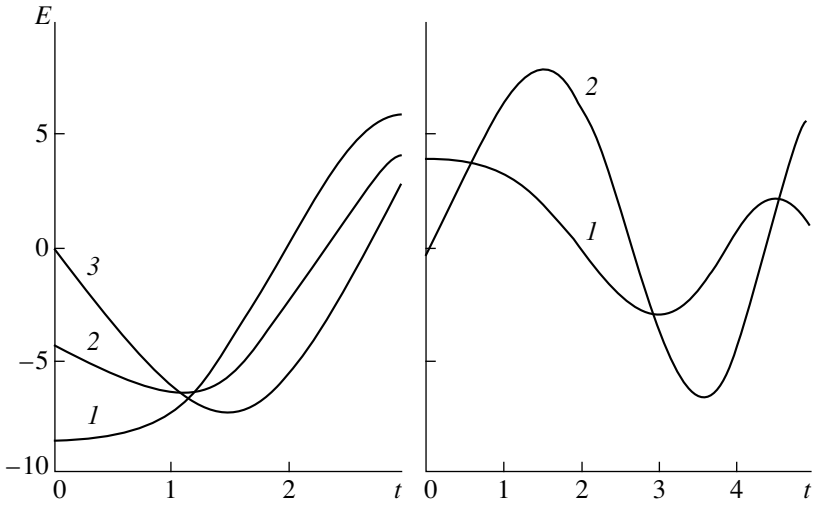

Fig. 3. Resonance behavior of an electric field as a function of $t = \varepsilon/\varepsilon_1[gr(\varepsilon_1)]^{-2/3}$ for $\varepsilon'' = 0$, $\theta_1 = 0$, $gr(\varepsilon_1) = 0.001$, and $\varepsilon_1 = 0.1327355 \pm 10^{-7}$: (*1*) exact solution; (*2*) approximate solution using a single Airy function; (*3*) exact solution for the case of a perfectly conducting plane situated at the zero of $\varepsilon(z)$. The position of the zero of $E(t)$ is sensitive to small perturbations of the layer parameters.

ence of a nonlinear-profile segment (ε_L, ε_N) eliminates the wave reflected from the rear boundary of the linear-profile layer.

Conclusions. This study addressed the problem of electromagnetic propagation in a plane-stratified layer. It has been predicted that small perturbations of the physical parameters, especially of the parameters representing absorption and specifying the propagation direction, may cause qualitative and quantitative changes in the solution near the zero of $\varepsilon(z)$; in particular, a surface wave may arise. The principle of layer similarity allows us to generalize the conclusion to the case of a discontinuity in $\varepsilon(z)$. The approach we suggested has clear physical meaning and may be applied to many engineering problems where the wave equation has to be solved in the presence of discontinuities, such as the design of switching elements and junctions between tiers for very-high-speed integrated circuits when nonlinearity must be taken into account.

REFERENCES

1. I. P. Kozlov, Radiotekh. Élektron. (Moscow) **42** (2), 142 (1997).
2. I. P. Kozlov, Zh. Tekh. Fiz. **69** (8), 5 (1999) [Tech. Phys. **44**, 873 (1999)].
3. I. P. Kozlov, Élektrodin. Tekh. SVCh KVCh **4** (4), 63 (1996).
4. I. P. Kozlov, in *Propagation and Diffraction of Electromagnetic Waves* (Mosk. Fiz. Tekh. Inst., Moscow, 1993), pp. 104–113.
5. L. D. Landau and E. M. Lifshitz, *Course of Theoretical Physics*, Vol. 8: *Electrodynamics of Continuous Media* (Nauka, Moscow, 1973; Pergamon, New York, 1984).
6. A. N. Tikhonov and V. Ya. Arsenin, *Solutions of Ill-Posed Problems* (Nauka, Moscow, 1986; Halsted, New York, 1977).
7. V. L. Ginzburg, *The Propagation of Electromagnetic Waves in Plasmas* (Nauka, Moscow, 1967; Pergamon, Oxford, 1970).
8. *Surface Polaritons*, Ed. by V. M. Agranovich and D. L. Mills (North-Holland, Amsterdam, 1982; Nauka, Moscow, 1985).
9. I. P. Kozlov, Izv. Vyssh. Uchebn. Zaved. Radiofiz. **18** (7), 997 (1975).

Translated by A. Sharshakov

Technical Physics Letters, Vol. 26, No. 7, 2000, pp. 609–611. Translated from Pis'ma v Zhurnal Tekhnicheskoĭ Fiziki, Vol. 26, No. 14, 2000, pp. 36–41.

Critical Current in High-Temperature Superconductors with Disordered Tilt Grain Boundaries

S. A. Kukushkin, I. A. Ovid'ko, and A. V. Osipov

Institute of Problems in Machine Science, Russian Academy of Sciences, St. Petersburg, 199178 Russia

Received February 8, 2000

Abstract—A model is suggested to describe the effect of tilt grain boundaries with partly random dislocation distribution on the critical current value in high-temperature superconductors. Within this model, the field of grain-boundary stresses $\sigma_{\alpha\beta}$ acquires a much more pronounced long-range character than in the case of a periodic dislocation arrangement. At large distances x from a tilt grain boundary, $\sigma_{\alpha\beta} \propto x^{-3/2}$ (which corresponds to the quasi-equidistant dislocation walls), whereas at small x, we have $\sigma_{\alpha\beta} \propto x^{-1/2}$ (which corresponds to randomly arranged dislocation walls). A region with stresses exceeding a certain critical value is treated as the region of normal metal, and, therefore, the critical current passing through this region decreases exponentially. It is shown that the model suggested satisfactorily agrees with experimental data. © *2000 MAIK "Nauka/Interperiodica".*

Almost immediately upon the discovery of high-temperature superconductivity, it was established that grain boundaries strongly reduce the critical current value in high-temperature superconductors (HTSCs) [1]. In particular, the presence of grain boundaries with the misorientation angle $\Theta < 15°$ in $YBa_2Cu_3O_{7-\delta}$ bicrystals results in an exponential decrease in the critical current j_c depending on Θ in accordance with the approximate expression $j_c(\Theta) \sim j_c(0)\exp(-\Theta/8°)$ [1]. With a further increase in the misorientation angle Θ, the critical current exhibits saturation at a level of about $0.02J_c(0)$ [1].

Numerous attempts were made at interpreting this phenomenon [2–6]. In particular, several models were suggested to explain the observed decrease in the critical current in polycrystalline superconductors by various factors, such as a decrease in the free path of electrons in the vicinity of grain boundaries [2], vortex pinning [3], the formation of an antiferromagnetic phase [4], the effect of *d*-electrons [5], inhomogeneous chemical composition, etc. Unfortunately, none of these models can be recognized as satisfactory. However, most of them have one common feature—the stress fields generated by grain-boundary dislocations in HTSCs "suppress" the order in the vicinity of grain boundaries [2–4]. No detailed mechanism of this suppression has been suggested as yet, but it is frequently assumed that there exists a definite critical value of the stress field, σ_c, above which the superconducting phase undergoes transition into a nonsuperconducting state [3, 4, 6]. However, this leads to another problem. The point is that at the periodic arrangement of dislocations forming small-angle grain boundaries, the thickness of the nonsuperconducting phase (which is close to the period of a dislocation ensemble) starts decreasing with an increase in the misorientation angle Θ. This, in turn, should result in an increase in the critical current, which contradicts the known experimental data [1]. Therefore, it was assumed [4] that the nonsuperconducting phase has a dual nature, being partly a normal metal and partly an antiferromagnetic dielectric destroying the Cooper pairs.

Below, we propose a new approach to the problem. Since polycrystalline high-temperature superconductors are obtained under nonequilibrium conditions, the grain-boundary dislocations usually form nonequilibrium (nonperiodical) structures such as partly relaxed disordered walls [7, 8]. In this case, the stress fields have a more pronounced long-range nature. The law describing the stress decrease becomes power rather than exponential. At small distances x from grain boundaries, it has the form $\sigma_{\alpha\beta} \sim x^{-1/2}$, whereas at large distances x it is described as $\sigma_{\alpha\beta} \sim x^{-3/2}$ [7]. This approach provides for a sufficiently adequate description of the known experimental data on the critical current in HTSCs [1].

Consider first an infinite periodic small-angle tilt boundary in the plane yz of a coordinate system with the dislocation ordinates $y_n = nh_0$ ($n = 0, \pm1, \pm2, \ldots$), where $h_0 = b/2\sin(\Theta/2)$ is the dislocation spacing, Θ is the misorientation angle of grain boundaries, and $\mathbf{b} = (b, 0, 0)$ is the Burgers vector. In "nonequilibrium" grain boundaries, dislocations are randomly displaced by the distances $h_0\delta_n$ from their equilibrium positions, where δ_n are random numbers uniformly distributed over a certain interval $(-a, a)$. Then, for a "nonequilib-

rium" small-angle tilt boundary, the ordinates of dislocations are given by the formula

$$y_n = \frac{b}{2\sin(\Theta/2)}(n + \delta_n), \quad (1)$$

where

$$\langle \delta_n \rangle = 0, \quad \langle \delta_n^2 \rangle = a^2/3, \quad \langle \delta_m \delta_n \rangle = 0, \quad (2)$$

and the dispersion of the stress field of the boundary equals the sum of the dispersions of stresses due to individual dislocations:

$$D\sigma_{\alpha,\beta}(x, y) = \sum_{n=-\infty}^{\infty} \{\langle [\sigma_{\alpha,\beta}(x, y)]^2 \rangle - \langle [\sigma_{\alpha,\beta}(x, y)] \rangle^2\}. \quad (3)$$

Here, $\sigma_{\alpha\beta}^{(n)}$ is the stress field of the nth dislocation ($\alpha, \beta = (x, y)$) [9]:

$$\frac{\sigma_{xx}^{(n)}}{G} = \frac{b}{2\pi(1-\mu)} \frac{(y-y_n)[3x^2 + (y-y_n)^2]}{[x^2 + (y-y_n)^2]^2}, \quad (4)$$

$$\frac{\sigma_{yy}^{(n)}}{G} = \frac{b}{2\pi(1-\mu)} \frac{(y-y_n)[x^2 - (y-y_n)^2]}{[x^2 + (y-y_n)^2]^2}, \quad (5)$$

$$\frac{\sigma_{xy}^{(n)}}{G} = \frac{b}{2\pi(1-\mu)} \frac{x[x^2 - (y-y_n)^2]}{[x^2 + (y-y_n)^2]^2}, \quad (6)$$

$$\frac{\sigma_{zz}^{(n)}}{G} = \frac{\mu}{G}(\sigma_{xx}^{(n)} + \sigma_{yy}^{(n)}), \quad (7)$$

where G is the shear modulus and μ is Poisson's ratio.

Following the method suggested in [7], one can readily average $\sigma_{\alpha\beta}$ and $\sigma_{\alpha\beta}^2$ over y in the interval from $-a$ to a and then sum up the corresponding series in (3) to obtain the dispersions of the stress-tensor components averaged over y. The most pronounced dispersion is obtained for σ_{xx}:

$$D\sigma_{xx}(x) = \left(\frac{Gb}{2\pi h_0(1-\mu)}\right)^2 \frac{5\pi a^2}{4(x/h_0)[(x^2/h_0^2) + a^2]}. \quad (8)$$

The values of $D\sigma_{xy}$ and $D\sigma_{yy}$ are five times smaller than the value of $D\sigma_{xx}$, whereas $D\sigma_{zz}$ (at $\mu = 0.2$ [?]) is four times smaller than $D\sigma_{xx}$. Therefore, in what follows, we restrict our consideration to the component $D\sigma_{xx}$. Since $\langle \sigma_{xx} \rangle = 0$, the average value of the σ_{xx} modulus for an infinite grain boundary is

$$\langle |\sigma_{xx}| \rangle = \sqrt{\frac{D\sigma_{xx}}{\pi}}. \quad (9)$$

By a similar method, one can also calculate the dispersion of the stress field of partly relaxed dislocation walls. It was shown [8] that, in this case, dispersion decreases in the same way for all x and attains a value of $\Delta^2 D\sigma_{xx}$ in the range $0 < \Delta < 1$, where Δ is the relaxation coefficient. Thus, the average value of the stress-tensor modulus depends on the distance to the grain boundary in the following way:

$$\sigma(x) \equiv \langle |\sigma_{xx}| \rangle = \Delta \sqrt{\frac{D\sigma_{xx}}{\pi}} = \frac{G\Delta}{2\pi(1-\mu)} \sqrt{\frac{5\sin(\Theta/2)}{2(x/b)\left[1 + 4(x^2/a^2b^2)\sin^2\frac{\Theta}{2}\right]}}. \quad (10)$$

It is seen that the above dependence is determined by two dimensionless parameters a and Δ: $\sigma \sim x^{-3/2}$ for $x \gg ab/2\sin(\Theta/2)$, and $\sigma \sim x^{-1/2}$ for $x \ll ab/2\sin(\Theta/2)$ [7].

Now, assume that the stress field σ suppresses the superconducting order at $\sigma > \sigma_c = \alpha_c G$, where $\alpha_c \ll 1$ is the critical value of the ratio σ/G. According to the estimates [6], $\alpha_c \sim 10^{-2}$ and, if $-x_c < x < x_c$ (where x_c is the root of the equation $\sigma(x)/G = \alpha_c$), the superconducting phase passes into a nonsuperconducting state. In what follows, we will consider this state as a normal metal. The critical current through a $2x_c$-thick layer of a normal metal is known to decrease exponentially [9, 10] as

$$\frac{j_c(\Theta)}{j_{c0}} = \exp(-2x_c(\Theta)/\xi), \quad (11)$$

where ξ is the coherence length of electrons in a normal metal. Thus, once the dependence $x_c(\Theta)$ has been calculated from formula (10), one can also determine the dependence of the critical current on the misorientation angle.

The results calculated for the model suggested in this study were compared with the experiment according to the following scheme. First, the α_c and ξ/b values were set and the a and Δ values providing optimum correspondence to the experimental data were calculated. For example, at $\mu = 0.2$ (which corresponds to the values $\alpha_c = 10^{-2}$ and $\xi/b = 5$ for $YBa_2Cu_3O_{7-\delta}$), we obtain $a_{opt} \approx 4.13$ and $\Delta_{opt} = 0.313$. The theoretical curve $j_c(\Theta)/j_{c0}$ and the experimental data [1] corresponding to the above values are plotted in the figure to demonstrate a satisfactory coincidence. Our studies show that the shape of the calculated curve is almost independent of the choice of ξ/b and α_c, because $a_{opt} \approx 0.83\xi/b$ and, therefore, the value of Δ_{opt} at constant a is proportional

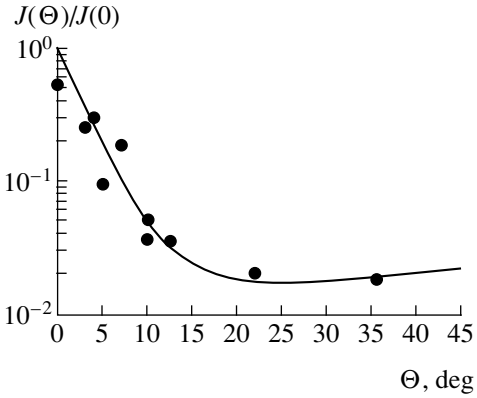

Average critical current as a function of the misorientation angle Θ. The solid line represents the theoretically calculated data and the filled circles represent the experimental data obtained in [1].

to the value of α_c. With an increase in ξ/b, the value of Δ_{opt} also slightly increases. In particular, at $\alpha_c = 0.01$ and $\xi/b = 50$, we obtain $a_{opt} \approx 41.2$ and $\Delta_{opt} = 0.989$.

This, the model of grain boundaries with randomly distributed dislocations in high-temperature superconductors qualitatively agrees with experimental data on the dependence of the critical current on the misorientation angle (see figure).

This study was supported by the US Naval Research Office, project no. 00014-99-1-0896.

REFERENCES

1. D. Dimos, P. Chaudhari, J. Mannhart, and F. K. LeGoues, Phys. Rev. Lett. **61**, 219 (1998).
2. K. E. Bagnall, I. V. Grigirieva, J. W. Steeds, *et al.*, Supercond. Sci. Technol. **8**, 605 (1995).
3. D. Agassi, C. S. Pande, and R. A. Masumura, Phys. Rev. B **52**, 16237 (1995).
4. A. Gurevich and E. A. Pashitskiĭ, Phys. Rev. B **57**, 13878 (1998).
5. H. Hilgenkamp, J. Mannhart, and B. Mayer, Phys. Rev. B **53**, 14586 (1996).
6. M. F. Chisholm and S. J. Pennycook, Nature **351**, 47 (1991).
7. A. A. Nazarov, A. E. Romanov, and B. Baudelet, Philos. Mag. Lett. **68**, 303 (1993).
8. A. A. Nazarov, R. Z. Valiev, and A. E. Romanov, Solid State Phenom. **35**/**36**, 381 (1994).
9. J. P. Hirth and J. Lothe, *Theory of Dislocations* (McGraw-Hill, New York, 1975).
10. P. G. De Gennes, Rev. Mod. Phys. **36**, 225 (1964).

Translated by L. Man

Technical Physics Letters, Vol. 26, No. 7, 2000, pp. 612–614. Translated from Pis'ma v Zhurnal Tekhnicheskoĭ Fiziki, Vol. 26, No. 14, 2000, pp. 42–47.

Microwave Oscillations as an Indicator of the Magnetoplasmadynamic Thruster Operation in a Limiting Regime

V. I. Brukhtiĭ and K. P. Kudryavtsev

Fryazino Department, Institute of Radio Engineering and Electronics, Russian Academy of Sciences, Fryazino, Moscow oblast, Russia

Received January 18, 2000

Abstract—Experimental data indicate a stable relationship between limiting operation modes of a magnetoplasmadynamic engine, the phenomenon of microwave generation, and an increase in the thruster efficiency. © *2000 MAIK "Nauka/Interperiodica".*

Investigation of the limiting parameters of magnetoplasmadynamic (MPD) thrusters is of special importance for constructing engines with increased efficiency and designing high-speed plasma sources. The limiting operation modes are characterized by the discharge current saturation with increasing voltage, electric field localization in the outer (accelerating) discharge region, and instability development in the electron plasma component [1–4]. The concept of microwave oscillations as a factor indicative of the plasma acceleration in an MPD thruster operating in the limiting modes requires experimental verification of a relationship between the intensity of microwave oscillations and the electric propulsion parameters of thrusters.

In this context, we studied the conditions of microwave generation in the course of design refinement and investigation of the limiting operation modes of an MPD thruster. The experiments were performed on a setup based on an applied-field lithium plasma accelerator with coaxial electrode geometry [5]. The experimental plan included the installation of an anode unit with a variable profile of the outer diverging nozzle part and tests with the anode shifted relative to the magnetic system to provide for the formation of discharge structures with variable configuration of the magnetic and electric fields and the discharge current transfer outside the thruster end section. The tests allowed the passage from the electrothermal plasma acceleration mechanism to the acceleration modes based on the Hall current interaction with the applied electric field. The discharge structure was determined to a considerable extent by the position of a neutral insert between the cathode and cylindrical part of the anode, which provided the possibility of forming longitudinal current column configurations near the cathode and the structures with transverse current in the outer discharge region. Various regimes of plasma acceleration and the corresponding characteristics of microwave generation were studied for the following working parameters: discharge voltage, 20–60 V; discharge current, 200–900 A; magnetic field strength, 10^{-2}–10^{-1} T; working substance consumption, 0.001–0.01 g/s. The background pressure in the vacuum chamber of the experimental setup was ~10^{-1} N/m^2.

The microwave oscillations were studied by detecting electromagnetic radiation from the thruster in the spectral range of Langmuir oscillations of the anode discharge region with an electron concentration of 10^{11}–10^{12} cm^{-3}. The method for these measurements [1], based upon comparison with the radiation of a standard gas-discharge source, allowed the intensity of microwaves generated in the vacuum chamber to be measured under arbitrary experimental conditions and provided the evaluation of the intensity of plasma oscillations above the thermal level. The main parameter of the microwaves generated in the system was the spectral density S_f of the electromagnetic radiant energy flux measured in units of W/(m^2 MHz). The S_f values were determined taking into account the size of the radiation source in the MPD thruster, which was determined by the anode configuration in the region of the plasma stream output from the accelerating part of the discharge.

Simultaneously with monitoring the microwave emission, we performed direct measurements of the engine thrust R taking all necessary precautions to exclude the influence of high-frequency interference from the nonequilibrium discharge region and the radiating elements of setup on the thrust-measuring device transducer. This was achieved by shielding the device and by introducing filters into the measuring circuits. These measures proved to be quite sufficient in all the thruster modes studied: a relative variation of the signal from the transducer (within the entire discharge current–voltage characteristic) was within 1.5–2 for the thruster-induced microwave intensity variation over 1.5–2.5 orders of magnitude.

1063-7850/00/2607-0612$20.00

Using the R values measured, we determined the thruster efficiency $\eta = R^2/(2\dot{m} I_0 U_0)$ for the given values of the working substance consumption $\dot{m}$, the discharge current I_0, and the applied voltage U_0. The results of the thrust measurements were used to determine the average ion velocity $v_i = R/\dot{m}$ in the output plasma stream and the transformation coefficient $\mu_i = v_i^2 / v_{i0}^2$, where $v_{i0} = (2eU_0/m_i)^{1/2}$ and m_i is the lithium ion mass.

Based on the analysis of a combination of the microwave generation characteristics and the electric propulsion parameters, we determined the units of the thruster setup featuring an electrothermal regime of plasma acceleration, which corresponded to the electromagnetic radiation intensity on the thermal level. In these regimes, the current–voltage characteristics of discharge exhibit the current growing with the applied voltage for the thruster efficiency $\eta \le 0.1$–0.2 and the transformation coefficient $\mu_i \sim 10^{-2}$.

When a discharge is formed in the region of a diverging magnetic field, the system exhibits a transition to a regime of limited discharge current and, if the discharge voltage exceeds the threshold, the microwaves are generated with an intensity 2–4 orders of magnitude above the thermal level. Excitation of the most intense microwaves is manifested in the high-voltage part of the discharge current–voltage characteristic, where the microwave generation threshold depends on the applied voltage, magnetic field, and working substance consumption.

The results of our measurements of the electric propulsion parameters and the microwave intensity for two models of the MPD thruster differing in the length of the inner cylindrical anode part, the discharge current, and the shape of the current–voltage characteristic are presented in the figure. In the region of the discharge current increasing with applied voltage (see Fig. 1a), the thruster efficiency does not exceed 0.25 and the intensity of microwaves measured in this regime does not exceed the thermal level: 3×10^{-11} W/(m^2 MHz) at 750 MHz and 5×10^{-10} W/(m^2 MHz) at 3000 MHz for an electron temperature of 5 eV. In the limited current mode, the intensity of microwaves generated in a considerable part of the current–voltage characteristic increases by 2–3 orders of magnitude (see Fig. 1b). Under these conditions, for a preset working substance consumption in the high-voltage discharge region, the thrust R markedly increases and the efficiency reaches a level of 0.7. Estimated ion velocity in the output plasma stream amounts to $(1–5) \times 10^4$ m/s for the transformation coefficient $\mu_i \approx 0.2–0.3$ (exceeding the values determined by the gasodynamic and Hall mechanisms of plasma acceleration). In this mode, the effective electric field potential accelerating ions in the plasma stream amounts to a considerable part of the applied voltage.

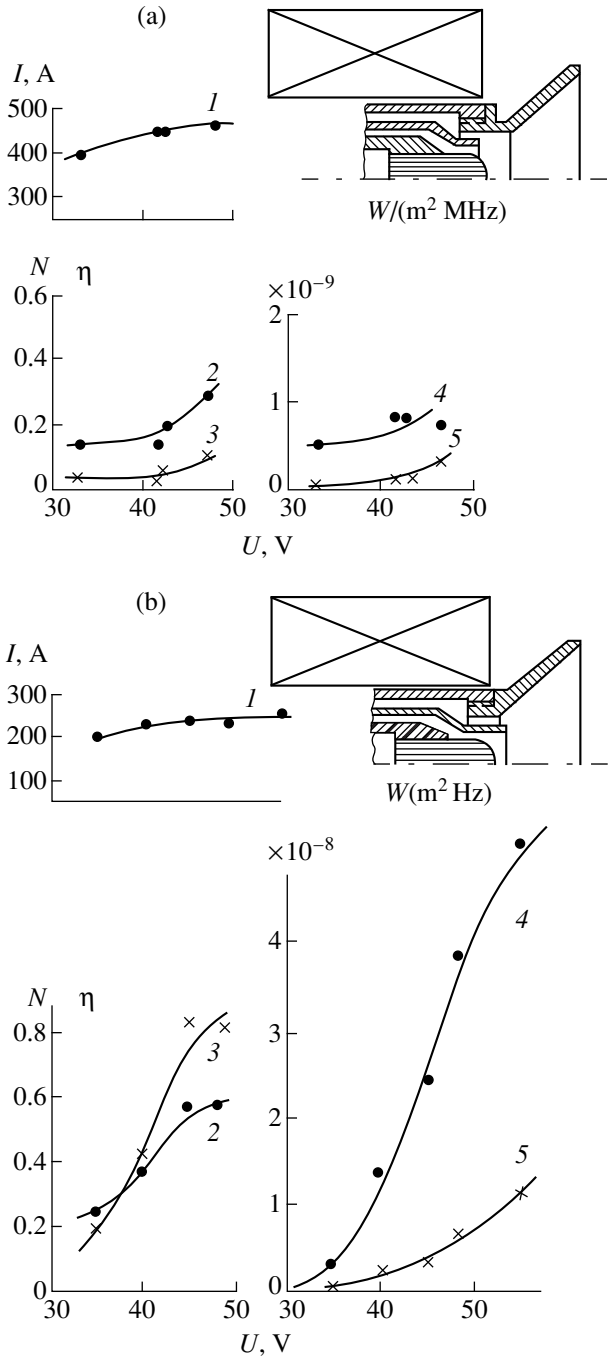

Fig. 1. Relationship between the intensity of microwave radiation at 750 and 3000 MHz, the electric propulsion parameters, and the discharge region design of an MPD thruster: (*1*) discharge current I_0; (*2*) thrust R; (*3*) thruster efficiency η; (*4*) microwave spectral density S_f at 3000 MHz; (*5*) microwave spectral density (a) S_f and (b) $10S_f$ at 750 MHz.

The experimental data are indicative of a determining contribution of the microwave oscillations to the formation of limiting modes of the MPD thruster operation: it is the microwave generation that accounts for the observed increase in the thruster efficiency. Note a

limited realization of the steady-state plasma acceleration in the limiting modes, which is related to an anomalous level of heat evolution at the anode. Under these conditions, the anode temperature reaches 2700–3000°C, which results in local fusion of the anode material (tungsten), leading to anode failure and the whole thruster system malfunction. This suggests a mechanism of turbulent plasma heating in the accelerating anodic region, with manifestations of the turbulent electron–ion friction and nonisothermal plasma acceleration in the outer discharge region. Besides the buildup of anodic losses in the limiting modes, we must also take into account the possible degradation of the accelerating anodic region caused by the scattering of drifting electron fluxes on microwave oscillations.

Thus, the microwave electromagnetic fields generated in the system may provide information about the electron dynamics in the accelerating plasma region. This extends the possibility of using remote probing methods for the plasma diagnostics in magnetoplasmadynamic thrusters [6].

REFERENCES

1. K. P. Kirdyashev, in *High-Frequency Wave Processes in Plasmadynamic Systems* (Énergoatomizdat, Moscow, 1982), p. 142.
2. V. I. Aref'ev and K. P. Kirdyashev, Zh. Tekh. Fiz. **45** (3), 527 (1975) [Sov. Phys. Tech. Phys. **20**, 330 (1975)].
3. N. N. Glotova, K. P. Kirdyashev, E. V. Naumov, *et al.*, Pis'ma Zh. Tekh. Fiz. **1** (10), 474 (1975) [Sov. Tech. Phys. Lett. **1**, 218 (1975)].
4. P. P. Glotova, K. P. Kirdyashev, I. P. Ostretsov, and A. A. Porotnikov, Zh. Tekh. Fiz. **46** (3), 506 (1976) [Sov. Phys. Tech. Phys. **21**, 288 (1976)].
5. N. N. Glotova, V. I. Kazanskiĭ, K. P. Kirdyashev, *et al.*, Zh. Tekh. Fiz. **48** (7), 1381 (1978) [Sov. Phys. Tech. Phys. **23**, 779 (1978)].
6. K. P. Kirdyashev and A. I. Morozov, Fiz. Plazmy **25** (4), 326 (1999) [Plasma Phys. Rep. **25**, 293 (1999)].

Translated by P. Pozdeev

Technical Physics Letters, Vol. 26, No. 7, 2000, pp. 615–616. Translated from Pis'ma v Zhurnal Tekhnicheskoĭ Fiziki, Vol. 26, No. 14, 2000, pp. 48–52.

Electric Resistance Variation during Isothermal Deformation of a Titanium–Nickel Alloy

S. A. Egorov and M. E. Evard

Smirnov Institute of Mathematics and Mechanics, Petrodvorets, Russia

Received March 6, 2000

Abstract—Changes in the electric resistance and strain were simultaneously measured during isothermal torsion of a titanium–nickel alloy specimen. It was established that the inelastic deformation of the specimen in the austenite state is not accompanied by reconstruction of the alloy lattice. © *2000 MAIK "Nauka/Interperiodica".*

Airoldi *et al.* [1, 2] studied the effect of pseudoelasticity in stretched TiNi alloy wire specimens with simultaneous measurements of changes in the strain ε and resistance R. However, because of changes in the geometry of specimens under tension, the features of interest in the $R(\varepsilon)$ curves were pronounced, which hindered the study of the physics of processes occurring in the material studied. We believe that torsion tests would completely realize the potential efficiency of this method *in situ* and elucidate the nature of the physical processes occurring under isothermal deformation of titanium-nickel alloys.

The experiments were performed on a setup described elsewhere [3]. The object was a specimen of the $Ti_{50.5}Ni_{49.5}$ alloy (atomic fractions). Prior to torsion tests, wire specimens with a diameter of 0.5 mm and a working length of 110 mm were subjected to a 40-min annealing at 753 K followed by slow cooling down to 250 K. The temperature T was varied at a rate of about 0.5 K/min and measured by a thermocouple. Changes in the specimen resistance during deformation were measured by a bridge circuit.

Prior to the experiments, we measured the $R(T)$ curve for an unloaded specimen during heating and cooling in the temperature range from 270 to 120 K (Fig. 1). The experiments were performed as follows. An unloaded specimen was first brought into a high-temperature state (an austenite phase with the $B2$ structure), cooled to a certain temperature, and loaded by applying shear stresses τ. Then, the specimen was unloaded, heated to about 400 K, and cooled down to 270 K (a martensite phase with the $B19'$ structure). Three test cycles were performed without intermediate annealing at the following temperatures of isothermal loading: 344 K (point A), 327 K (point B), and 296 K (point C) (Fig. 1). These temperatures corresponded to the austenite phase and the multiphase states at the beginning and at the end of the chain of forward phase transformations, respectively. The results of these experiments are shown in Figs. 2a–2c.

The analysis of the results obtained shows that, irrespective of the test temperatures, the stress–strain curve $\tau(\gamma)$ obtained during loading has a linear and a nonlinear segment (where τ is the shear stress and γ is the torsion strain). Upon unloading, there is some residual strain, but subsequent heating leads to the complete strain recovery. Usually, such a behavior of alloys with the memory effect is explained by stress-induced martensite transformation. The strain recovery on heating is explained by the reverse martensite transformation. However, this was not always the case in our experiments. Figure 2a shows that mechanical loading of the specimen in the austenite state does not change its resistance; in other words, no reconstruction of the crystal lattice is observed at the stages of elastic and inelastic deformation. At the same time, specimen loading at the temperatures at which the material is in the multiphase state (Figs. 2b and 2c) gives rise to considerable changes in the $R(\gamma)$ curves, which indicate the stress-induced martensite transformations. However, Figure 2b shows that loading at the temperature 327 K

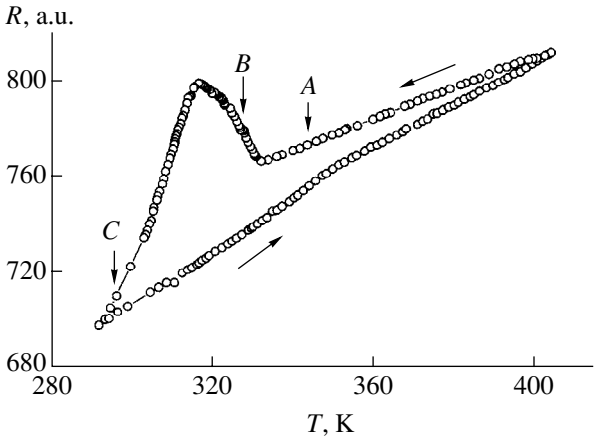

Fig. 1. Resistance R as a function of the temperature during cooling and heating of an unloaded specimen of the TiNi alloy.

1063-7850/00/2607-0615$20.00 © 2000 MAIK "Nauka/Interperiodica"

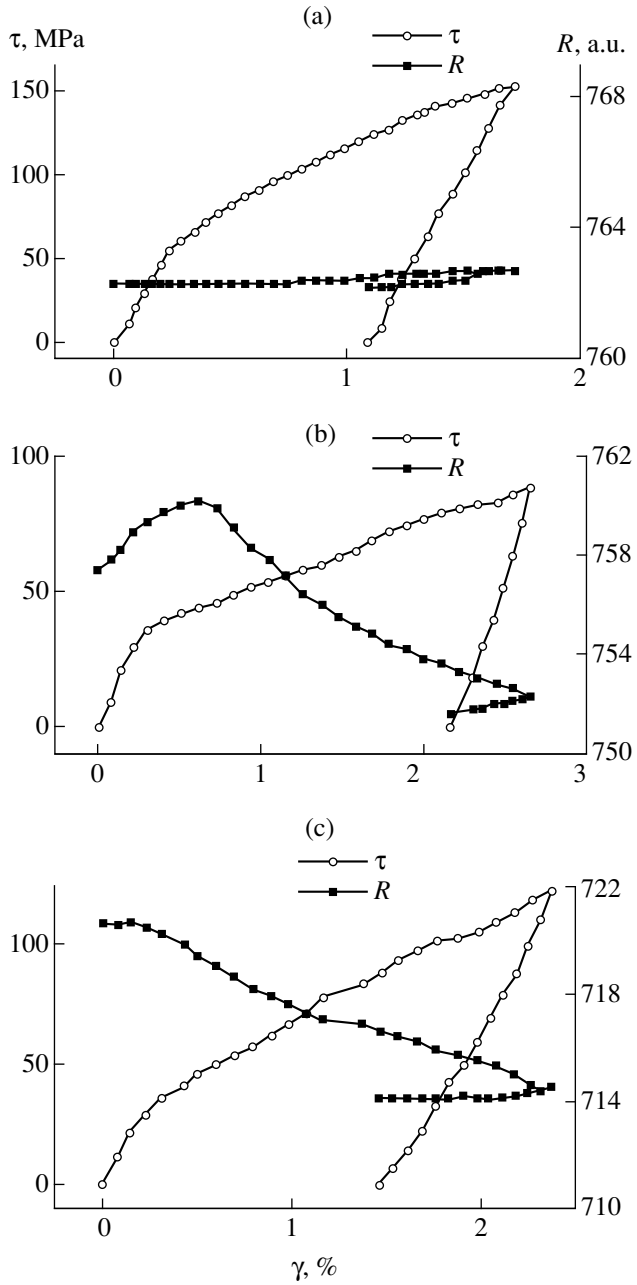

Fig. 2. $R(\gamma)$ and $\tau(\gamma)$ curves obtained during loading and unloading of a TiNi alloy specimen at temperatures of (a) 344, (b) 327, and (c) 296 K.

(the $B2 \longrightarrow R$ transformation) only slightly increases the resistance at the initial stage of inelastic deformation (by 4% of the peak height on the $R(T)$ curve in Fig. 1), whereas at the strains exceeding 0.6%, the resistance decreases rather noticeably (by 23% of the peak height). This indicates that mechanical stresses in the specimen do not promote the initiation of the $B2 \longrightarrow R$ transformation but can induce the $B2 \longrightarrow B19'$, $R \longrightarrow B19'$, or both transformations. An increase in the stresses at 296 K stimulates the $R \longrightarrow B19'$ transformation (Fig. 2c).

Summing up, we can draw the following conclusions:

1. Isothermal loading of a specimen of the alloy under study initiates the $B2 \longrightarrow B19'$ and $R \longrightarrow B19'$ transformations.

2. The stresses applied produce almost no effect on the $B2 \longrightarrow R$ transformation.

3. Loading of a specimen in the austenite state in the vicinity of the onset temperature of the forward martensite transformation does not give rise to any structural rearrangements that can change the specimen resistance. However, the loading leads to the accumulation of inelastic deformation (most probably of the twinning nature), which is fully recovered on heating. This twinning was experimentally observed as reported in [4].

This study was supported by the Russian Foundation for Basic Research, project nos. 99-01-00987 and 96-15-96066 (Program for Support of the Leading Scientific Schools).

REFERENCES

1. G. Airoldi, T. Ranucci, and G. Riva, J. Phys. III **1** (11), C4-439 (1991).
2. G. Airoldi and M. Pozzi, J. Eng. Mater. Technol. **121** (1), 108 (1999).
3. S. A. Egorov and M. E. Evard, Fiz. Met. Metalloved. **88** (5), 78 (1999).
4. E. Goo, T. Duerig, K. Melton, and R. Sinclair, Acta Metall. **33** (9), 1725 (1985).

Translated by L. Man

Technical Physics Letters, Vol. 26, No. 7, 2000, pp. 617–619. Translated from Pis'ma v Zhurnal Tekhnicheskoĭ Fiziki, Vol. 26, No. 14, 2000, pp. 53–59.

Chaotic Tags and Asynchronous Data Transmission

Yu. V. Andreev, A. S. Dmitriev, S. V. Emets, L. V. Kuz'min, A. I. Panas, D. Yu. Puzikov, and S. O. Starkov

Institute of Radio Engineering and Electronics, Russian Academy of Sciences, Moscow, 103907 Russia

Received March 7, 2000

Abstract—A method to identify entities by means of tags is suggested. The tags are represented by sets of unstable periodic orbits that form the framework of a chaotic attractor. The method is applied to asynchronous packet data transmission from a number of users over a shared channel. Experimental transmission of two musical signals is reported. © *2000 MAIK "Nauka/Interperiodica".*

1. A chaotic attractor of a dynamic system is remarkable for possessing a fine structure including two types of unstable trajectories: a countable set of periodic trajectories (cycles) and a set of trajectories along which the system walks from one periodic orbit to another [1–3]. Every chaotic attractor has a unique configuration of unstable cycles, which is uniquely determined by system equations and parameters. The converse is also true: a set of unstable periodic orbits uniquely determines a chaotic attractor and, hence, the corresponding dynamic system. Consequently, if an observer in a certain dynamic system is offered a periodic trajectory (or a set of trajectories) generated by some other dynamic system, then the observer can find out whether the latter system is a replica of the former one. Thus, unstable cycles of dynamic systems can serve as chaotic tags to identify the belonging of an entity (object or system).

Tagging is commonly used to solve a number of problems: letters bear postage stamps; official papers, marks and seals; and various products, bar codes. Tags are also exemplified by electronic signatures, IP addresses, etc. The main goal of tagging is to provide an object with a set of signs so that the object or group to which it belongs can be identified uniquely. Tags are designed for different purposes. Some of them (such as zip codes or telephone numbers) can easily be read or reproduced by any observer. Other tags (such as seals, cash, or credit cards) can be read by anyone but cannot be made without special tools. Finally, there are tags whose structure cannot be readily interpreted by unauthorized observers so as to prevent them from using (and making) the tags without permission. On the other hand, the data conveyed by a tag to an authorized user should be compact and vivid.

In this study, a set of unstable periodic orbits is utilized as a tag for asynchronous packet data transmission from a number of users over a shared channel.

2. The set of unstable periodic orbits of a chaotic attractor consists of cycles with different periods. The total number of orbits with the same period grows exponentially with the period length. For example, consider a dynamic system defined by the Lozi map [4, 5]

$$\begin{aligned} x_{n+1} &= \alpha - 1 - \alpha|x_n| + y_n, \\ y_{n+1} &= \beta x_n. \end{aligned} \tag{1}$$

It can be demonstrated that the chaotic attractors of map (1) have 6–10 orbits of period 7 and from several hundred to about one thousand orbits of period 15, depending on α and β (Fig. 1a). Since the unstable periodic orbits are distinguishable from each other, it was suggested that they should be used as codes for data transmission [6–9], including multiuser access [7–9].

In this study, unstable orbits are employed for tagging rather than coding the data transmitted. In other words, these orbits are used as chaotic tags only designating the owner (a group of users).

3. Consider a communications system where the transmitter serves N senders and the receiver serves N recipients. The channel is assumed to have a capacity sufficient for transmitting the entire amount of data from senders to recipients. It is required that each sender–recipient (SR) pair be able to transmit data within a reasonable time (without considerable delay). It must be taken into account that the SR pairs may considerably differ in the data transmission rate they need.

To meet the requirements, let the transmitter divide every message into fragments (data packets) whose length depends on the data rate requested by the sender and the data rates demanded by other users. In the transmitter, packets belonging to different senders form a common data flow. This flow passes through the channel and comes to the input of the receiver. The receiver sorts the packets according to their recipients and reconstructs the messages. To this end, each SR pair is assigned a pair of chaotic tags representing a pair of unstable periodic trajectories. Every packet is provided with a tag pair corresponding to the given SR pair: one of the tags is used as a "head;" and the other, as a "tail" of the packet. Both of the tags are known to the sender and the recipient. The tags are generated by iterating

1063-7850/00/2607-0617$20.00

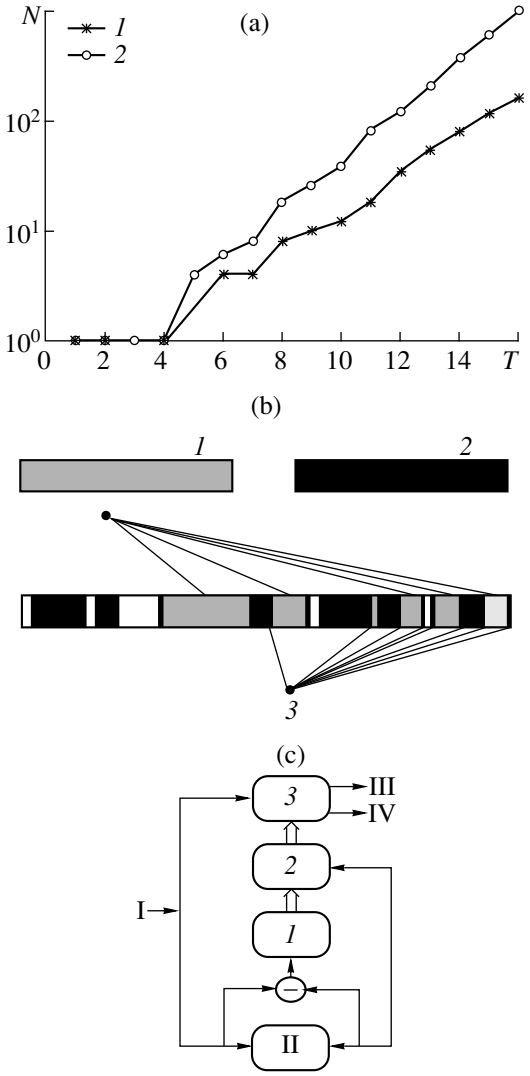

Fig. 1. (a) The total number of unstable periodic orbits N of the Lozi map vs. orbit period T for (*1*) $\alpha = 1.7$, $\beta = 0.5$ and (*2*) $\alpha = 1.7$, $\beta = 0.5$. (b) The structure of an asynchronous packet flow conveying two messages: (*1*) message 1; (*2*) message 2; and (*3*) head and tail tags. (c) The nonlinear filter for packet detection, sorting, and distribution: (I) input data flow; (II) chaotic dynamic system; (III) to recipient 1; (IV) to recipient 2; (*1*) threshold unit; (*2*) tag detector; (*3*) packet distributor.

the same chaotic dynamic systems (CDSs) in the transmitter and the receiver.

Thus, an asynchronous sequence of packets bounded by individual tags comes to the input of the channel. Packets from different senders follow in random order and may be separated by idling intervals of arbitrary length due to, e.g., the absence of data at the transmitter inputs. Figure 1b shows a typical structure of the data flow for two SR pairs.

The receiver uses tags to detect the beginning and the end of each packet and to identify the recipient. The procedures are executed in two stages. In the first stage, the entire data flow is processed by a specially designed nonlinear filter (Fig. 1c) based on the chaotic dynamic system. The filter finds tagged packets in the data flow, identifies and sorts packets, and directs them to the corresponding recipients. In the second stage, the recipients restore messages from packets.

4. To test the scheme described above, we designed an experimental system and carried out experiments with two SR pairs. Two musical signals were transmitted concurrently over a shared channel. A schematic diagram of the system is shown in Fig. 2.

The transmitter and the receiver were built around AD2181 signal processors. The input signals of the transmitter were analog audio signals from a cassette tape recorder and a CD player. In the transmitter, the analog signals were digitized by 16-bit analog-to-digital converters operating at 6 kHz and divided into packets with chaotic terminal tags. A common data flow was formed from the packets (Fig. 1b). The length of each packet, set by a random number generator, ranged from 30 to 300 16-bit words. The tags were unstable trajectories of period 5 from the chaotic attractor of Lozi map (1) with $\alpha = 1.1$ and $\beta = 0.85$.

Each word was converted into a sequence of 16 binary pulses, each pulse representing a bit, so as to transmit them over the channel, which was a wire line.

The receiver performed the following procedures: (1) synchronizing incoming binary pulses; (2) converting the binary data into 16-bit words and performing self-synchronization using tag words; (3) detecting the head and the tail tags of a packet and determining their

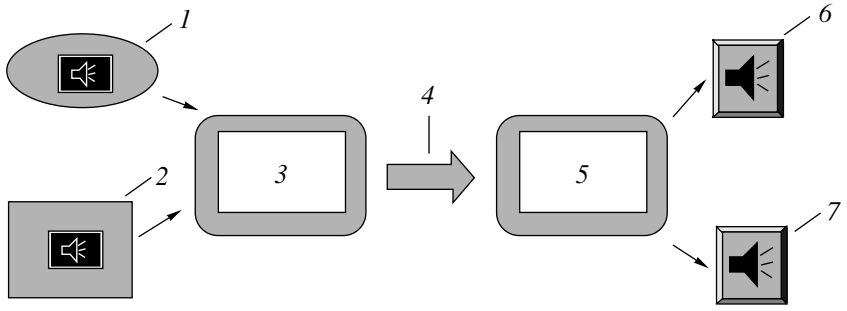

Fig. 2. Schematic diagram of the experimental system for the concurrent asynchronous packet transmission of two musical signals over a shared wire line: (*1*) signal source 1; (*2*) signal source 2; (*3*) transmitter; (*4*) shared wire channel; (*5*) receiver; (*6*) audio system for signal 1; (*7*) the audio system for signal 2. The transmitter and the receiver are built around AD2189 signal processors.

length and position in the data flow; and (4) distributing packets between the two users according to the tags, reconstructing messages from the packets, converting the signals into analog form, and playing them back with audio systems.

5. The experiments demonstrated the high quality of the data transmission, showing that chaotic tags can be used for data identification in multiuser communications systems.

ACKNOWLEDGMENTS

This study was supported by the Russian Foundation for Basic Research (project no. 99-02-18315).

REFERENCES

1. A. N. Sharkovskiĭ, Ukr. Mat. Zh., No. 1, 61 (1964).
2. D. Auerbach, P. Cvitanivic, J.-P. Eckmann, *et al.*, Phys. Rev. Lett. **58**, 2387 (1987).
3. P. Cvitanovic, Phys. Rev. Lett. **61**, 2729 (1988).
4. R. Lozi, J. Phys. (Paris) **39**, 9 (1978).
5. A. S. Dmitriev, S. O. Starkov, and M. E. Shirokov, Radiotekh. Élektron. (Moscow) **39** (9), 1392 (1994).
6. H. D. Abarbanel and P. Linsay, IEEE Trans. Circuits Syst., II: Analog Digital Signal Process **40** (10), 643 (1993).
7. A. S. Dmitriev, A. I. Panas, and S. O. Starkov, Zarubezh. Radioélektron. (Usp. Sovrem. Radioélektron.), No. 10, 4 (1997).
8. Y. Andreev, A. Dmitriev, D. Kuminov, and S. Starkov, in *Proceedings of NDES'97, Moscow, 1997*, pp. 185–190.
9. A. Dmitriev and S. Starkov, in *Proceedings of NDES'99, Bornholm, Denmark, 1999*, pp. 161–164.

Translated by A. Sharshakov

Technical Physics Letters, Vol. 26, No. 7, 2000, pp. 620–622. Translated from Pis'ma v Zhurnal Tekhnicheskoĭ Fiziki, Vol. 26, No. 14, 2000, pp. 60–65.

Shaping and Propagation of the First-Order Guiding-Center Solitons Inherent in Solutions of the Complex Landau–Ginzburg Equation

A. S. Shcherbakov and A. Yu. Kosarskiĭ

St. Petersburg State Technical University, St. Petersburg, 195251 Russia

Received January 28, 2000

Abstract—The results of numerical modeling show that it is possible to considerably increase the region of the first-order guiding-center soliton formation in solutions of the complex Landau–Ginzburg equation. The possibility of using these soliton pulses in solving the tasks of high-precision synchronization in data-processing systems is considered. *© 2000 MAIK "Nauka/Interperiodica".*

Evolution of the solitary waves in a weakly nonlinear medium with anomalous group velocity dispersion and losses γ is described by the complex Landau–Ginzburg equation [1] for the field amplitude A normalized to the fundamental soliton amplitude A_0 at $\gamma = 0$:

$$\frac{\partial A}{\partial z} = -\Gamma A - i\left(\frac{1}{2}\frac{\partial^2 A}{\partial \tau^2} + A|A|^2\right). \qquad (1)$$

Here, $\Gamma = \gamma Z_D$, $z = x/Z_D$, and $\tau = t/\tau_0$ are the normalized variables related to the coordinate x and time t in the comoving frame, $Z_D = \tau_0^2 k_2^{-1}$ is the dispersion length, and τ_0 is the initial length of the solitary wave (determined on the $\sec h(1) \approx 0.65$ level) for the zero initial frequency chirp b. The boundary condition is

$$A(z = 0, \tau) = a_0 \sec h(\tau), \quad b(z = 0) = 0. \qquad (2)$$

Restricting the consideration to first-order solitons [2], we will consider initial normalized amplitudes in the interval $1.0 \le a_0 \le 1.5$ (a_0 determines the initial solitary wave amplitude in A_0 units). Using a_0 and Γ values, we may plot a diagram (Fig. 1) illustrating the domains of existence of various first-order solitary waves satisfying the complex Landau–Ginzburg equation (1) with the boundary condition (2) and the initial amplitudes within the interval $a_0 \in [1.0; 1.5]$.

Analysis of Fig. 1 shows regions I–III corresponding to the previously investigated fundamental solitons [2], adiabatically low-loss-perturbed solitons [3], and asymptotic solitons [4]. In addition, we may distinguish region IV, reflecting the appearance of solutions oscillating in a complicated manner, and region V determined by the limiting value of the parameter $\Gamma = \Gamma_0(a_0)$ corresponding to the formation of guiding-center solitons. The guiding-center soliton pulses were originally considered by Hasegawa and Kodama in [5, 6], where the domain of existence of these solutions was estimated by the condition $\Gamma \gg 1$.

Previously [7, 8], it was established that the formation of guiding-center solitons is possible for $\Gamma \ge \Gamma_0 = 1$. The purpose of this work was to show by numerical modeling methods that the region of formation of the first-order guiding-center solitons inherent in solutions of the complex Landau–Ginzburg equation can be signif-

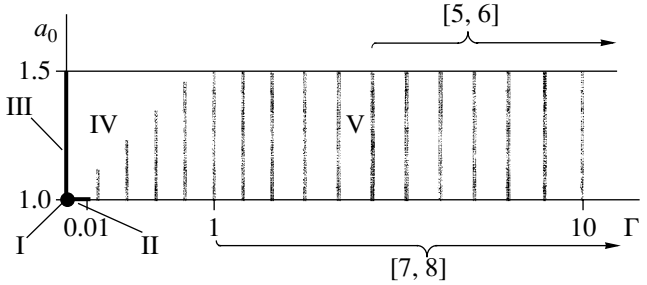

Fig. 1. Schematic diagram illustrating the domains of existence of various first-order solitary waves satisfying the complex Landau–Ginzburg equation.

1063-7850/00/2607-0620$20.00 © 2000 MAIK "Nauka/Interperiodica"

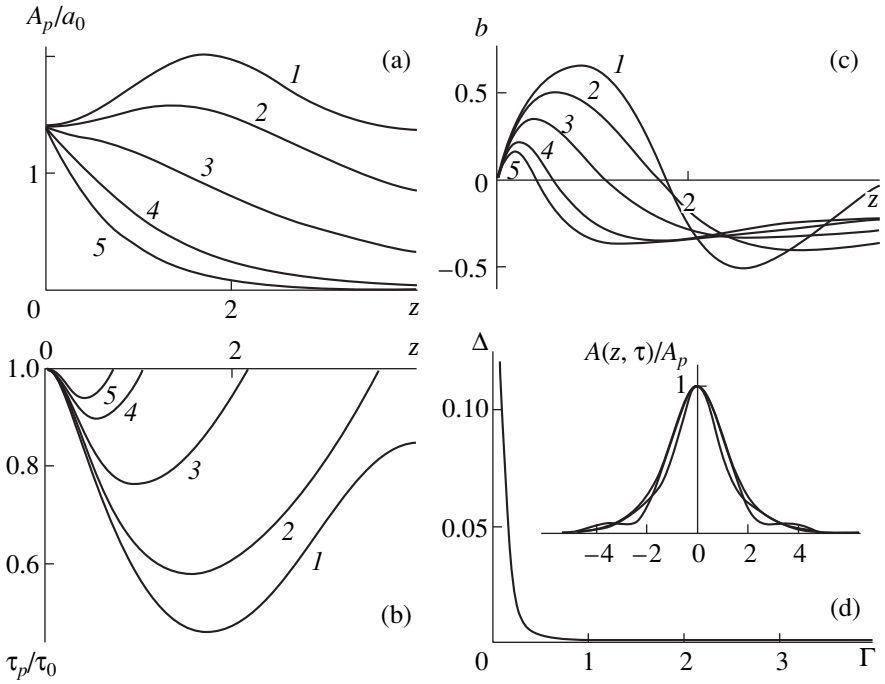

Fig. 2. The results of numerical modeling of the time evolution of parameters of the solitary waves satisfying the complex Landau–Ginzburg equation for $a_0 = 1.4$ and $\Gamma = 0.015$ (*1*), 0.1 (*2*), 0.3 (*3*), 0.8 (*4*), and 1.3 (*5*): (a) normalized amplitude A_p/a_0; (b) normalized duration τ_p/τ_0; (c) frequency chirp b; (d) plot of the mean-square deviation Δ of the guiding-center soliton envelope shape at the point of duration restoration ($z = L_R$) from the hyperbolic-secant envelope at the initial point ($z = 0$) versus parameter Γ. The fiber length is normalized to the dispersion length Z_d.

icantly extended toward $\Gamma_0 < 1$. We also aimed at considering the possibility of using these soliton pulses in solving the tasks of high-precision synchronization in data-processing systems.

In the course of numerical experiments, we modeled the evolution of the amplitude, duration, frequency chirp, and envelope of the first-order guiding-center solitons inherent in solutions of the complex Landau–Ginzburg equation satisfying the boundary condition (2) and the restriction $a_0 \in [1.0; 1.5]$. Analysis of the results of numerical modeling leads to the conclusion that $\Gamma_0(a_0)$ representing a conditional boundary between regions IV and V (see Fig. 1) is an increasing function of a_0. Figures 2a–2c show the results of calculation of the amplitude $A_p = A(z, 0)$, duration τ_p, and frequency chirp of the solitary waves for $a_0 = 1.4$ and various values of Γ. Note that the cases of $\Gamma = 0.015$ and 0.1 (curves *1* and *2*, respectively) correspond to solutions belonging to region IV, $\Gamma = 0.3$ (curve *3*) represents an intermediate case, and the values of Γ for curves *4* and *5* correspond to the guiding-center solitons in region V. The latter curves illustrate the main properties of these solitons, including restoration of the pulse duration to the initial level on traveling over a length $z = L_R$. The curves demonstrate a decrease in the pulse amplitude (which is natural in the dissipative medium) and the appearance of a nonzero frequency chirp for the initially "spectrally pure" pulses. The curves corresponding to $\Gamma = 0.015$ and 0.1 (Figs 2a–2c, curves *1* and *2*) have an oscillating character, while the Γ values corresponding to curves *4* and *5* correspond to monotonic variation of the amplitude as a function of the propagation length and the frequency chirp tends to stabilization.

Figure 2d shows the mean-square deviation Δ of the guiding-center soliton envelope shape at the point of duration restoration ($z = L_R$) from the hyperbolic-secant envelope at the initial point ($z = 0$) plotted as a function of Γ. As seen, the deviation Δ rapidly tends to zero with increasing Γ. However, the soliton envelope rather insignificantly differs from the initial envelope even for $\Gamma \geq 0.1$ because $\Delta \leq 0.1$. This statement is illustrated in the inset to Fig. 2d showing normalized amplitude profiles of a guiding-center soliton at $z = 0$, $z = L_{\min}$; $z = L_R$ for one of the "worst" cases studied ($a_0 = 1.4$; $\Gamma = 0.4$). These amplitude profiles clearly demonstrate the behavior of an envelope that can be interpreted as interference of the central soliton part (having an envelope of the fundamental soliton) and the oscillating part reflecting the nonstationary character of the soliton evolution in the region of $z \in [0, L_R]$. Depending on the current phase of the oscillating part, the interference with the soliton center leads to deformation of the envelope and compression of the pulse at $z = L_{\min}$. It is also seen that a difference in the current envelope from the initial one at $z = L_R$ even in this case is manifested by

the appearance of small (below 10%) wings outside the time interval of $3\tau_0$.

One possible application of the first-order guiding-center solitons inherent in solutions of the complex Landau–Ginzburg equation is related to solving the tasks of high-precision synchronization in high-rate data-processing systems, where the requirements for the parameters of the synchro pulses increase with the information capacity and the data-processing accuracy. Increasing requirements can be satisfied by using picosecond optical pulses, propagating in single-mode fiber guides with losses, for synchronization purposes. In this case, the accuracy of synchronization is limited only by the error of determination of the energy center of a synchro pulse. This error not exceeding the pulse duration, the use of optical first-order guiding-center solitons for the transfer of synchro pulses via a single-mode fiber guide would provide for a synchronization accuracy on the picosecond level. The possibility of using adiabatically low-loss-perturbed fundamental solitons corresponding to the Landau–Ginzburg equation was considered previously [9].

From the standpoint of providing maximum synchronization accuracy related to minimum value of the synchro pulse duration τ_S, there are two possibilities. The first still consists in using adiabatically low-loss-perturbed fundamental solitons with the initial duration $\tau_F = \tau_S \exp(-2\gamma L_0)$ [3] (L_0 is the length of the fiber guide data transfer channel) and the initial energy $E_F = 2k_2\sigma^{-1}\tau_F^{-1}$, where $\sigma = 2.7$ rad/(W km) for a silica fiber [8]. Another possibility is to carry the synchro signal by the first-order guiding-center solitons with the initial duration $\tau_G = \tau_S$ and the energy $E_G = 2a_0^2 k_2\sigma^{-1}\tau_G^{-1}$. Here, an important advantage is that (Fig. 2d) the energy center of the first-order guiding-center solitons exhibits no time shift during propagation in a fiber guide. The main factor in choosing between the adiabatically low-loss-perturbed fundamental solitons and first-order guiding-center solitons is the ratio of their initial energies E_F and E_G (since their durations τ_S become equal upon traveling in the same fiber guide channel L_0). In region V (Fig. 1) where $\Gamma > \Gamma_0$, we have $E_G < E_F$ and, hence, the guiding-center solitons initially possess a lower energy as compared to that of the fundamental soliton energy ($L_0 > L_R = \gamma^{-1}\ln a_0$). For the typical values $a_0 = 1.4$ and $\gamma = 0.5$ dB/km, we obtain $L_R = 5.84$ km. Therefore, for the same synchronization accuracy, the first-order guiding-center soliton is an energetically more favorable synchro signal carrier in a medium-base information system in comparison with the adiabatically low-loss-perturbed fundamental soliton.

REFERENCES

1. R. K. Dodd, J. C. Eilbeck, J. Gibbon, and H. C. Morris, *Solitons and Nonlinear Wave Equations* (Academic, New York, 1982; Mir, Moscow, 1988).
2. A. Hasegawa and F. Tappert, Appl. Phys. Lett. **23** (3), 142 (1973).
3. A. Hasegawa and Y. Kodama, Proc. IEEE **69**, 1145 (1981).
4. J. Satsuma and N. Yajima, Suppl. Prog. Theor. Phys., No. 55, 284 (1974).
5. A. Hasegawa and Y. Kodama, Opt. Lett. **15** (24), 1443 (1990).
6. A. Hasegawa and Y. Kodama, Phys. Rev. Lett. **66** (2), 161 (1991).
7. A. S. Shcherbakov and E. I. Andreeva, Proc. SPIE **2429**, 227 (1994).
8. A. S. Shcherbakov and E. I. Andreeva, Opt. Fiber Technol.: Mater., Devices, Syst., No. 2, 127 (1996).
9. A. S. Shcherbakov, Proc. SPIE **3733**, 306 (1999).

Translated by P. Pozdeev

Technical Physics Letters, Vol. 26, No. 7, 2000, pp. 623–624. Translated from Pis'ma v Zhurnal Tekhnicheskoĭ Fiziki, Vol. 26, No. 14, 2000, pp. 66–70.

IR Spectroscopy of Copper-Intercalated Graphite Nanoclusters in Amorphous Carbon

V. I. Ivanov-Omskiĭ and G. S. Frolova

Ioffe Physicotechnical Institute, Russian Academy of Sciences, St. Petersburg, 194021 Russia

Received March 10, 2000

Abstract—We measured optical absorption coefficients of the metal-induced quasi-Raman absorption bands in hydrogenated carbon films. Parameters of the copper-induced quasi-Raman bands were used to estimate the size of the graphite-like nanoclusters in *a*-C:H(Cu) with various copper concentrations. Preliminary comparative data on Cu-, Er-, and Co-modified *a*-C:H are reported. © *2000 MAIK "Nauka/Interperiodica".*

The atomic structure of hydrogenated amorphous carbon (*a*-C:H) exhibits several types of valence configurations, since carbon is capable of three different variants of hybridization of the valence states. This accounts for a unique adaptability of the *a*-C:H structure to various kinds of inclusions which, in turn, allows the formation of *a*-C:H-based nanocomposites, in particular, with metals. In recent years, these materials have drawn the attention of researchers as low-voltage emitters, one-electron microelectronic devices, and matrices for the encapsulation of metal nanoclusters ensuring their stabilization in data-storage devices. Knowledge of the mechanisms of the metal–carbon interaction and the properties of their interfaces appears to be important for successful application of the carbon-based nanocomposites.

Previously, we demonstrated [1] that the interaction of copper with six-membered graphene rings in graphite-like nanoclusters (GLNs) activates the Raman vibrational modes of graphene rings in IR absorption. In the absence of foreign atoms, these modes are optically inactive (symmetry-forbidden) but contribute to the Raman spectra. The interaction of copper with graphene rings alters the symmetry group so that the vibrations become optically active to give rise to quasi-Raman bands in the IR absorption spectra. In this work,

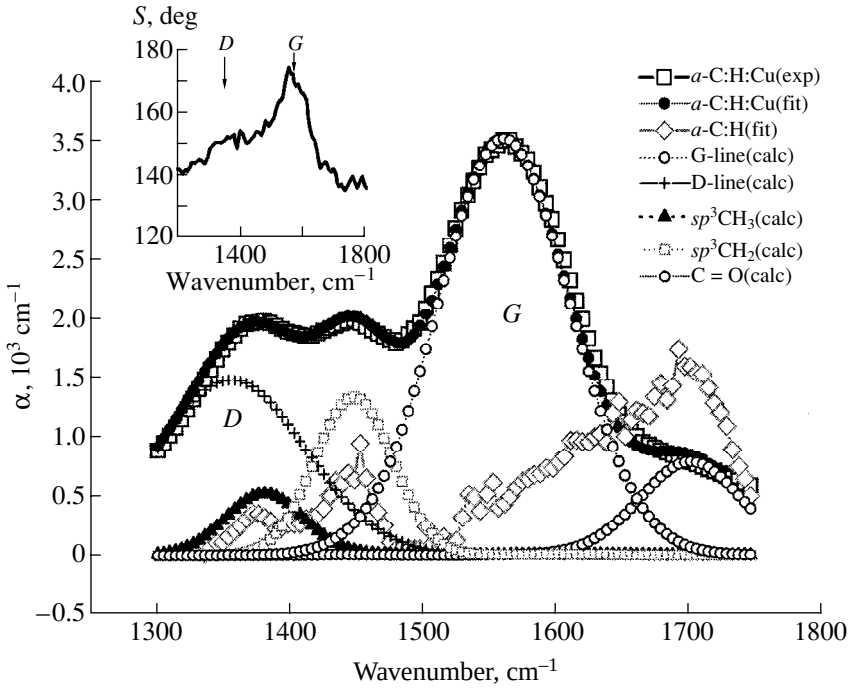

Fig. 1. The region of C–C stretching and C–H bending modes in the IR absorption spectra of *a*-C:H and *a*-C:H(Cu) films with the atomic ratio C : Cu = 0.65 and the results of deconvolution of the *a*-C:H(Cu) spectrum into Gaussian components. The inset shows the corresponding Raman spectrum of *a*-C:H(Cu), with arrows indicating positions of the *G* and *D* graphite bands.

1063-7850/00/2607-0623$20.00 © 2000 MAIK "Nauka/Interperiodica"

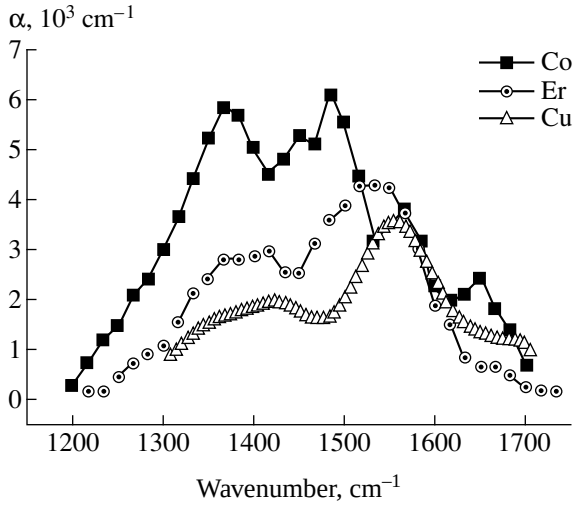

Fig. 2. IR absorption spectra of Cu-, Er-, and Co-modified *a*-C:H in the region of quasi-Raman bands.

we have used this phenomenon to monitor the interaction of metals with graphite-like *a*-C:H fragments. For this purpose, we measured the IR absorption bands assigned to the C–C stretching and C–H bending modes in the spectra of *a*-C:H(Me) films modified by metals Me = Cu, Er, Co.

The *a*-C:H(Me) films were grown by magnetron cosputtering of graphite and metal targets in argon–hydrogen plasma (80% Ar + 20% H) onto a (100) silicon substrate surface at 200°C. Details of the method are described elsewhere [2].

Figure 1 shows the absorption spectra of *a*-C:H and *a*-C:H(Cu) in the region of characteristic Raman frequencies of graphite: *G* band at 1575 cm^{-1} and *D* band at 1355 cm^{-1}. As seen, deconvolution of the experimental *a*-C:H(Cu) spectrum into Gaussian components reveals rather strong absorption bands missing in the *a*-C:H spectrum, which is explained by the modifying influence of the metal [1]. The frequencies of these additional bands are very close to frequencies of the true Raman bands of graphite [3]. For this reason, these bands are denoted with the letters *G* and *D* and referred to as quasi-Raman, despite a small frequency shift. Note that the true Raman bands also exhibit a shift as shown in the inset in Fig. 1. It is also seen that the modification of *a*-C:H by copper leads to enhancement of the C–H and suppression of the C=O and CO vibrational modes. Therefore, the oxygen-containing groups, in contrast to CH_x groups, have no direct coupling with GLN graphene rings.

Parameters of the quasi-Raman absorption bands

[Cu]/[C]*	*G* band frequency, cm^{-1}	*D* band frequency, cm^{-1}	GLN size, nm
0.65	1561	1354	90
0.9	1554	1356	70
0.94	1566	1366	43
1.0	1566	1366	50
1.3	1565	1365	36

* According to the Rutherford proton backscattering data.

Since the quasi-Raman bands emerge due to alteration of the symmetry group of the graphene ring vibrations caused by their interaction with copper atoms, one can estimate the GLN size using the ratio of intensities of the *D* and *G* bands [3]. As seen from the table, the GLN size tends to decrease with increasing copper concentration. A significant spread of the estimates indicates that the copper concentration is not the only factor influencing the nanocluster size. Due to unknown reason, our estimates yield values that are substantially larger than those recently reported in [4].

Figure 2 compares preliminary results on the absorption coefficient in the quasi-Raman bands for the samples activated by erbium, cobalt, and copper. The larger the absorption coefficient, the stronger the interaction of the corresponding metal with the carbon matrix (increasing from Cu to Er and Co). The copper-activated sample shows only a small shift of the well-resolved *G* band relative to the graphite Raman band, which suggests the GLN integrity. Thus, we assume that the copper atoms interact with the graphene rings by intercalating into graphite-like nanoclusters. The simplest mechanism of this interaction in the initial intercalation stage was recently considered in [5] within the framework of the strong coupling theory. It was demonstrated that partial ionization of the copper atom leads to GLN metallization and a substantial charge redistribution. The consequent asymmetry of the charge density in GLNs gives rise to a quasi-Raman band in the absorption spectrum of *a*-C:H(Cu). Significant growth of the absorption coefficient in the *G* band of the cobalt-containing structure implies a more complicated interaction. The erbium-activated sample occupies an intermediate position.

This work was supported in part by the Russian Foundation for Basic Research, project no. 00-02-17004.

REFERENCES

1. V. I. Ivanov-Omskiĭ and G. S. Frolova, Zh. Tekh. Fiz. **65** (9), 186 (1995) [Tech. Phys. **40**, 966 (1995)].
2. V. I. Ivanov-Omskiĭ, T. K. Zvonareva, and G. S. Frolova, Fiz. Tverd. Tela (St. Petersburg) **41** (2), 319 (1999) [Phys. Solid State **41**, 286 (1999)].
3. F. Tuinstra and J. L. Koenig, J. Chem. Phys. **53** (3), 603 (1970).
4. S. G. Yastrebov, V. I. Ivanov-Omskiĭ, V. I. Siklitsky, and A. A. Sitnikova, J. Non-Cryst. Solids **227/230**, 622 (1998).
5. V. I. Ivanov-Omskiĭ and É. A. Smorgonskaya, Fiz. Tekh. Poluprovodn. (St. Petersburg) **32** (8), 931 (1998) [Semiconductors **32**, 831 (1998)].

Translated by A. Chikishev

Technical Physics Letters, Vol. 26, No. 7, 2000, pp. 625–627. Translated from Pis'ma v Zhurnal Tekhnicheskoĭ Fiziki, Vol. 26, No. 14, 2000, pp. 71–77.

Effect of Argon Buffer and the UV Preionization Regime on the Electric-Discharge XeCl Laser Parameters

A. I. Fedorov

Institute of the Optics of Atmosphere, Siberian Division, Russian Academy of Sciences, Tomsk, Russia

Received February 24, 2000

Abstract—The gas discharge and output radiation parameters were studied in XeCl lasers with various buffer gas compositions (argon vs. neon) and different types of excitation regimes (fast vs. quasi-stationary) in the preionization source. The intervals of specific energy for the neon- and argon-based buffer gas mixtures are 10–125 and 45–360 J/(l atm), respectively. The specific parameters of radiation in the neon- and argon-based buffer gas mixtures depend on the energy required for the UV preionization. For high-power UV preionization sources, the output parameters of lasers using argon-based gas mixtures may exceed those obtained with neon-based mixtures. © *2000 MAIK "Nauka/Interperiodica".*

An increase in the reliability and efficiency of wide-aperture high-power excimer lasers is the main prerequisite for the wide use of these devices in novel technologies. Insufficient reliability of excimer lasers is related to a high gas pressure in the discharge chambers and a high charging voltage, whereas low efficiency is explained by the considerable consumption of expensive inert gases. At present, neon—the most expensive inert gas—is usually employed as the buffer, because this medium provides both a sufficiently high homogeneity of the discharge and the maximum output parameters. There have been numerous works [1–7] showing that argon has good prospects as a buffer gas for electric-discharge XeCl lasers. Obviously, the economic efficiency of these lasers would markedly increase if the neon gas mixtures could be replaced by less expensive argon compositions.

Below, we report on the results of investigation of independent gas discharge and the output parameters of lasers using argon gas mixtures and various UV preionization sources [8] operated in two different regimes.

It was suggested [9, 10] that the problem of obtaining volume discharges in argon excimer mixtures, related to the development of ionization instabilities and the formation of current columns, can be markedly simplified by using photoionization processes that may compensate or retard these undesired phenomena. In turn, the gains from the photoionization processes depend on the type and energy of the ionization source employed. The photoionization intensity can be conditionally characterized by the distribution of energies deposited in the preionization (W_1) and main discharge (W_2) stages. The ratio W_1/W_2 can be used as the parameter determining the properties of the excitation source. In this context, we studied the effect of photoionization in argon and neon gas mixtures on the discharge parameters and the generation conditions in XeCl lasers operating in the fast or quasi-stationary excitation regimes.

Fast excitation of a $1.4 \times 0.7 \times 25$ cm^3 active volume was achieved by using a double Blumlain generator. The UV preionization of the laser gap was provided by an additional source of corona discharge bounded by a perforated electrode. The electrical scheme and design features of the experimental setup were reported elsewhere [11]. Variable capacitance of the UV preionization source allowed the energy deposited in this stage to be controlled within 10–15% of the energy supplied to the discharge. This last energy, in turn, did not exceed 50% of the energy stored in the power-supply generator. The UV preionization was automatically maintained only at the initial stage of discharge.

Figure 1 shows the plot of the specific output energy versus the specific energy supplied to the discharge in argon and neon gas mixtures for various intensities of the corona-discharge UV preionization. The specific energy supply was controlled by varying the working gas pressure and discharge voltage. The specific energy supply ranged from 10 to 25 J/(l atm) for neon and from 45 to 100 J/(l atm) for argon. For argon mixtures, an optimum level of the specific energy supply was observed at 90 J/(l atm). Analogous dependences were observed for the higher UV preionization intensities, but the specific output energies were lower. This is related to certain features of the power-supply scheme used in the fast discharge excitation regime. The maximum specific output energies observed in argon did not depend on the UV preionization intensity, which is probably explained by a higher photoionization rate in argon-based gas mixtures as compared to that in the neon mixtures [8].

A quasi-stationary excitation of a $3 \times 1.5 \times 35$ cm^3 active volume was achieved using a double-circuit supply generator with storage (75 nF) and sharpening

1063-7850/00/2607-0625$20.00

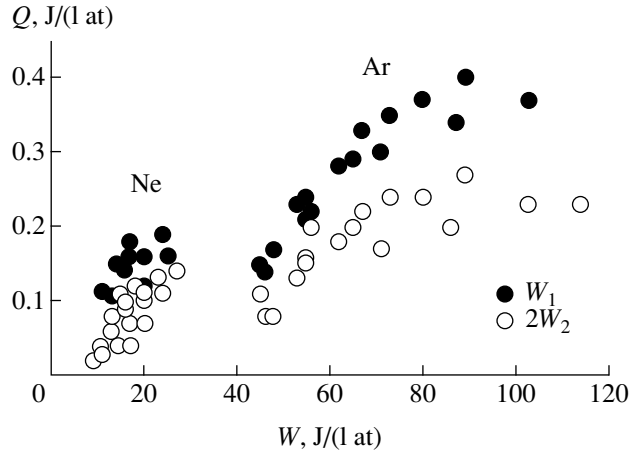

Fig. 1. The plot of the specific output energy Q versus the specific energy W_1 spent for the preionization for argon and neon as buffer gases in a XeCl laser with a Xe–HCl (5 : 1) working gas mixture (4 Torr) and a corona-discharge UV preionization.

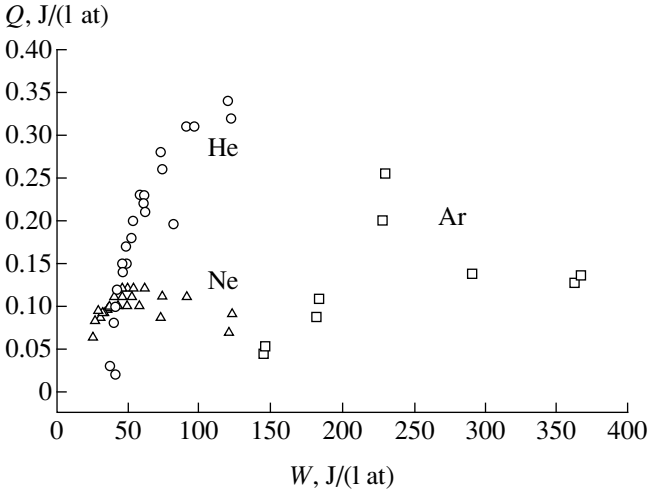

Fig. 2. The plot of the specific output energy Q versus the specific energy W_1 spent for the preionization for helium, neon, and argon as buffer gases in a XeCl laser with a Xe–HCl (10 : 1) working gas mixture (3 Torr) and a spark-gap preionization.

(10 nF) capacitors. Here, the UV preionization in the laser gap was provided by two rows of spark gaps over a dielectric surface bounded by a perforated electrode. Features of the quasi-stationary excitation regime and the power-supply scheme were reported previously [12]. Here, the UV preionization was automatically maintained during the entire discharge time and the energy consumed was approximately equal to the energy supplied to the gas. A maximum energy level was observed for helium at a pressure of 3 atm, argon at 0.8 atm, and neon at 5 atm. All gases exhibited a quasi-stationary discharge stage, the duration of which was maximum in neon (200 ns). However, durations of the generated pulses were different and amounted to 35, 50, and 100 ns for helium, argon, and neon, respectively. This is related to features of the power-supply scheme, which provided high discharge current densities (1–2 kA/cm^2) at the expense of limited pulse duration.

Figure 2 shows the plot of the specific output energy versus the specific energy supplied to the discharge in He, Ne, and Ar. It was found that a maximum specific output energy (0.35 J/(l atm) can be obtained in helium excited in the fast regime. The specific energy supply was controlled in the range from 35 to 125 J/(l atm), with the maximum output parameters corresponding to maximum energy supplied. For neon mixtures, the specific energy supply varied from 25 to 125 J/(l atm), with an optimum level of 50 J/(l atm) corresponding to the specific output of 0.125 J/(l atm). These mixtures featured excitation and generation in the quasi-stationary regime. In argon mixtures, the specific energy supply was controlled in the range from 180 to 360 J/(l atm), with an optimum level at 225 J/(l atm) providing an output energy level of 0.25 J/(l atm) in the fast excitation regime.

Based on the results of our experiments and the data available in the literature, we analyzed the relationship between the specific output energy and the specific energy supplied to discharge for Ar and Ne as the buffer gases preionized in different regimes with various energies. It was assumed that about 50% of the energy stored in the power supply source was supplied to the active medium. An increase in the preionization energy led to a decrease in the practical laser efficiency, and these limiting regimes were mostly rejected. However, an analysis of the published data showed that the energy spent for the preionization varied within a rather broad range, three characteristic cases corresponding to (i) $W_1 < W_2$, (ii) $W_1 = W_2$, and (iii) $W_1 > W_2$.

Figure 3 shows the plot of the specific output energy normalized to the maximum (2 J/(l atm)[6]) versus the specific energy spent for preionization normalized to the energy supplied to discharge constructed by data of [1, 2, 6, 7, 11–17]. The first characteristic case with $W_1 = 0.1$–$0.2W_2$ was most often employed by researchers and enabled them to obtain almost comparable output parameters using both argon and neon. Regimes of the second type ($W_1 = W_2$) allowed the specific output parameters with argon that were two times higher than the values with neon to be reached [6, 7, 12]. The only exception was reported in [13], where the inverse situation was observed with plasma electrodes, probably because of some special features of that system. The third case ($W_1 > W_2$) also allows us to obtain specific output parameters with argon much higher than those with neon [15, 17].

Thus, our analysis of the data for argon and neon buffer gas mixtures showed that the specific output parameters depend on the energy spent for the UV preionization. In addition, we concluded that a growth of the preionization energy for argon is accompanied by a linear increase in the specific output energy, while

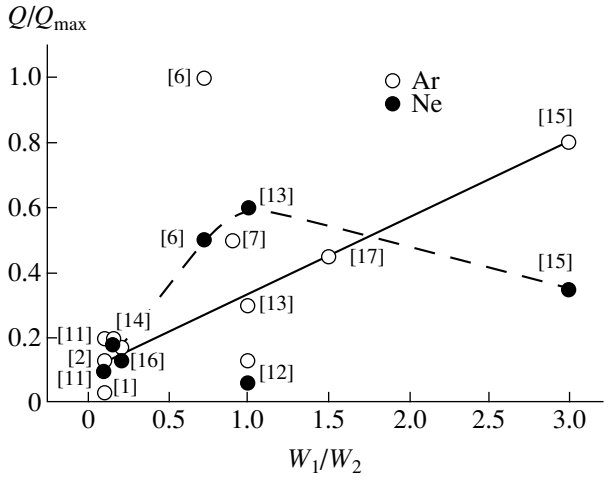

Fig. 3. The plot of the specific output energy Q/Q_{max} (normalized to maximum) versus the specific energy W_1/W_2 spent for the preionization (normalized to the energy supplied to discharge) for argon and neon as buffer gases in XeCl lasers (by data from [1, 2, 6, 7, 11–17]).

the data for neon show the presence of the optimum at $W_1 = W_2$.

Based on the results of investigations described above, we have developed a small-size XeCl laser with an output pulse width of 60 ns and a repetition frequency of 50 Hz. The laser operation with argon mixtures at a pressure of 1 atm provided a maximum average output power of 2.5 W. The same power was obtained with neon mixtures, but at a pressure of 2.5 atm.

REFERENCES

1. A. I. Fedorov, V. F. Tarasenko, and Yu. I. Bychkov, Pis'ma Zh. Tekh. Fiz. **4** (3), 132 (1978) [Sov. Tech. Phys. Lett. **4**, 54 (1978)].
2. Yu. I. Bychkov, I. N. Konovalov, V. F. Losev, *et al.*, Izv. Akad. Nauk SSSR, Ser. Fiz. **42** (12), 2493 (1978).
3. V. F. Tarasenko, V. A. Tel'nov, and A. I. Fedorov, Izv. Vyssh. Uchebn. Zaved. Fiz., No. 6, 91 (1979).
4. M. N. Kostin, V. F. Tarasenko, and A. I. Fedorov, Zh. Tekh. Fiz. **50** (6), 1227 (1980) [Sov. Phys. Tech. Phys. **25**, 704 (1980)].
5. V. F. Tarasenko, A. I. Fedorov, V. V. Gruzinskiĭ, *et al.*, Izv. Vyssh. Uchebn. Zaved. Fiz., No. 8, 121 (1980).
6. R. C. Sze, J. Appl. Phys. **50** (7), 4596 (1979).
7. S. V. Efimovskiĭ, A. K. Zhigalkin, and Yu. L. Sidorov, Pis'ma Zh. Tekh. Fiz. **5** (11), 664 (1979) [Sov. Tech. Phys. Lett. **5**, 273 (1979)].
8. L. B. Loeb, *Fundamental Processes of Electrical Discharges in Gases* (Wiley, New York, 1939; Gostekhizdat, Moscow, 1950).
9. N. G. Basov, E. P. Glotov, V. A. Danilychev, *et al.*, Pis'ma Zh. Tekh. Fiz. **5** (8), 449 (1979) [Sov. Tech. Phys. Lett. **5**, 183 (1979)].
10. V. M. Baginskiĭ, N. G. Basov, P. M. Golovinskiĭ, *et al.*, Pis'ma Zh. Tekh. Fiz. **11**, 627 (1985) [Sov. Tech. Phys. Lett. **11**, 260 (1985)].
11. A. I. Fedorov, Opt. Atmos. Okeana **12** (11), 1020 (1999).
12. A. I. Fedorov, Opt. Atmos. Okeana **10** (11), 1274 (1997).
13. A. I. Fedorov, Author's Abstract of Candidate's Dissertation (Tomsk, 1982).
14. A. I. Fedorov, in *Proceedings of 4th International Conference "Atomic and Molecular Pulsed Lasers," Tomsk, Russia, 1999*, p. 22.
15. M. Steyr and H. Voqes, Appl. Phys. B **42**, 155 (1987).
16. M. Yu. Artem'ev, A. Z. Grasyuk, and V. M. Nesterov, Kvantovaya Élektron. (Moscow) **16** (12), 2374 (1989).
17. I. G. Koprinkov and K. A. Stankov, Printed in the UK, 1986, pp. 907–911.

Translated by P. Pozdeev

Technical Physics Letters, Vol. 26, No. 7, 2000, pp. 628–630. Translated from Pis'ma v Zhurnal Tekhnicheskoĭ Fiziki, Vol. 26, No. 14, 2000, pp. 78–83.

On the Mechanism of Charge Transfer in n^+-CdS–p-InP–p^+-InP Heterostructures

S. V. Slobodchikov, Kh. M. Salikhov, E. V. Russu, and Yu. G. Malinin

Ioffe Physicotechnical Institute, Russian Academy of Sciences, St. Petersburg, 194021 Russia

Received February 26, 2000

Abstract—The mechanisms of charge transfer in n^+-CdS–p-InP– p^+-InP heterostructures were studied in the temperature interval from 100 to 300 K. The forward current is determined either by tunneling via local centers (at low temperatures) or by recombination in the space-charge region. The reverse current is controlled by tunneling via local centers and by direct interband tunneling. Breakdown in these heterojunctions also proceeds by the tunneling mechanism. © *2000 MAIK "Nauka/Interperiodica".*

Being a promising material for photoconverters (solar cells), InP was studied in a number of diode structures, including various homo- and heterojunctions. A wideband component in heterojunctions was represented, among other materials, by CdS [1, 2]. These heterostructures were characterized by high coefficients of the solar energy conversion into electric power. Below, we report on the results of our investigation into the mechanism of charge transfer in InP-based heterostructures of this type, which may be of interest from the standpoint of structure optimization for obtaining the best photoelectric characteristics.

The samples of heterostructures were prepared by the method of n^+-CdS layer deposition from a solid-state source in a hydrogen atmosphere. The deposition was performed in a horizontal reactor onto InP substrates at a temperature of 650°C and a CdS source–substrate temperature gradient of 120°C. The resulting n^+-CdS layer was characterized by the electron concentration $n^+ = (1–3) \times 10^{19}$ cm^{-3} and a mobility of 60–120 cm^2/(V s) at a layer thickness of 3–5 μm. The p-InP substrate had a hole concentration of $p = 2 \times 10^{17}$ cm^{-3} and a mobility of ~250 cm^2/(V s). The samples, having a rectangular shape with an area of ~0.1 cm^2, were characterized by measuring the current–voltage (I–V) characteristics at various temperatures and the effect of magnetic field on the photocurrent through heterostructures under forward and reverse bias conditions.

Figure 1 shows the I–V curves measured under forward and reverse bias conditions for a n^+-CdS–p-InP–p^+-InP sample at T = 300 K (curves *1* and *3*) and 100 K (curves *2* and *4*). Figure 2 shows the temperature variation of the forward current (positive polarity on the p^+-InP side) in the range from 100 to 300 K. Figure 3 shows the pattern of changes in the photocurrent measured with forward and reverse bias at various strengths

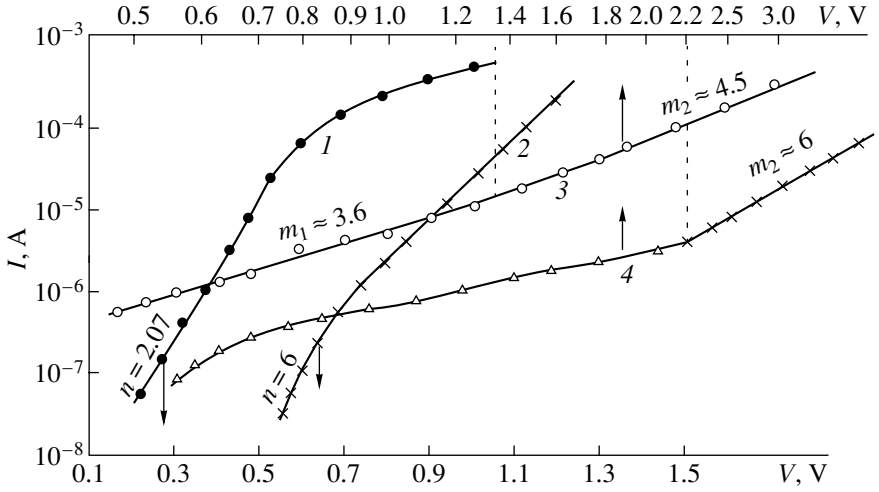

Fig. 1. The I–V curves for a n^+-CdS–p-InP–p^+-InP heterostructure measured under forward (*1*, *2*) and reverse (*3*, *4*) bias conditions at T = 300 K (*1*, *3*) and 100 K (*2*, *4*).

1063-7850/00/2607-0628$20.00 © 2000 MAIK "Nauka/Interperiodica"

of the applied magnetic field. Plotted in the semilogarithmic coordinates, the forward current as a function of the voltage can be described by the relationship $I \sim \exp(qV/nkT)$ with the coefficient n at low bias equal to ~2.07 at room temperature (Fig. 1, curve *1*) and ~6 at $T = 100$°C (Fig. 1, curve *2*); the value of n markedly increases in the region of large bias voltages. The reverse branches (Fig. 1, curves *3* and *4*) can be approximated by the relationship $I \sim V^m$, also featuring two regions depending on the bias voltage: at $T = 300$ K, $m_1 = 3.6$ for $V < 1.4$ V and $m_2 = 4.5$ for high bias; at $T = 100$ K and $V > 2.2$ V, m_2 increases up to about 6.

In the region of low temperatures, the current exhibits weak variation (Fig. 2), but at $T > 150$ K the current increases with temperature as characterized by an activation energy of $E_a \cong 0.08$ eV.

Analysis of the experimental curves leads to the conclusion that the mechanism of charge transfer is not the same in the whole temperature interval studied and must include various components with contributions differing in the regions of low and high temperatures. The value of $n \cong 2$ is evidence of the recombination current dominating in the space-charge region, while $n \gg 2$ is indicative of a process controlled by tunneling. Thus, the total current can be represented as

$$I = I_{g-r} + I_{\text{tun}}. \quad (1)$$

We may suggest that the region of low temperatures, featuring small current variation, is characterized by $I_{\text{tun}} \gg I_{g-r}$.

Since p-InP is not degenerate and n^+-CdS is weakly degenerate, no direct interband tunneling transitions are possible in the heterostructure studied. At the same time, tunneling may proceed by a indirect mechanism, whereby electrons tunnel from the conduction band of n^+-CdS to a local level E_1 and then to the valence band of p-InP (Fig. 2*a*). In this case,

$$I_{\text{tun}} \approx \alpha N_1 T_t, \quad (2)$$

where α is a constant coefficient, N_1 is the density of local centers on the E_1 level, and T_1 is the tunneling probability. The latter parameter is given by the formula

$$T_t = \exp\left(\frac{-4\sqrt{2}m^{*1/2}E^{*3/2}}{3q\hbar E}\right), \quad (3)$$

where E^* is the tunneling activation energy and E is the electric field strength. Evidently, a heterostructure with preset concentrations of doping impurities can be expected to represent a sharp junction. Substituting formula (3) into equation (2) and using the known E value for the sharp transition and the E^* value as function of the barrier height, we eventually obtain an expression for the tunneling current [3]

$$I_{\text{tun}} \cong \alpha N_1 \exp[-\alpha_1(E_g - qV)], \quad (4)$$

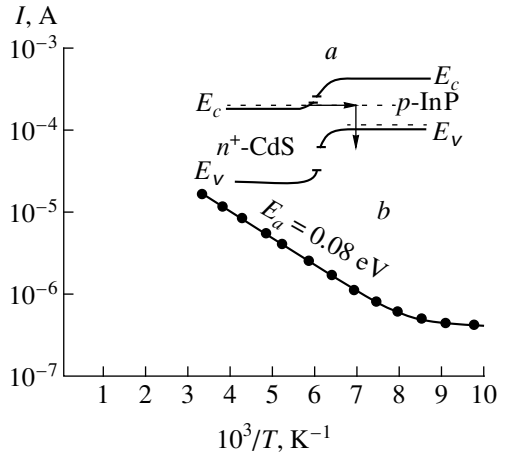

Fig. 2. (*a*) Schematic band diagram of the n^+-CdS–p-InP–p^+-InP heterostructure and (*b*) temperature variation of the forward current (positive polarity on the p^+-InP side).

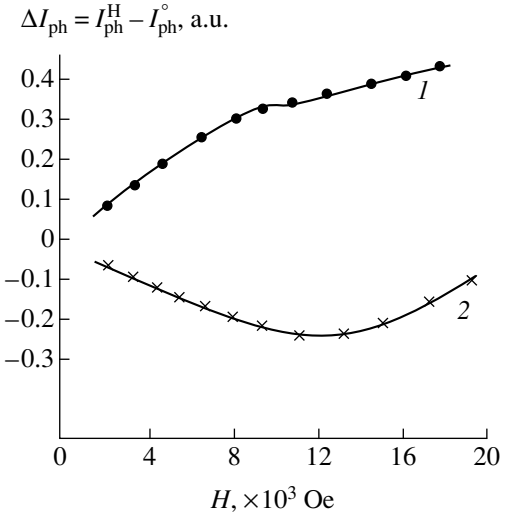

Fig. 3. The plots of photocurrent versus applied magnetic field strengths for the n^+-CdS–p-InP–p^+-InP heterostructure biased in the (*1*) forward and (*2*) reverse directions.

which determines the behavior of the forward current at low temperatures. As the temperature increases, the mechanism of charge transfer is modified and the generation–recombination current component I_{g-r} becomes dominant. This current is determined by the formula

$$I_{g-r} = \frac{qn_iW}{\tau_r}\exp\frac{qV}{2kT}, \quad (5)$$

where n_i is the intrinsic charge-carrier concentration, W is the width of the space-charge region (occurring entirely in p-InP), and τ_r is the carrier lifetime in this region. Since the temperature variation of the forward current at a fixed bias voltage is a process with the activation energy $E_a = 0.08$ eV (for $V = 0.6$ V), we may sug-

gest that the carrier lifetime increases exponentially with the temperature $\tau_r \sim \exp(-E_t/kT)$, where E_t is the depth of the recombination level determining τ_r. According to Eq. (5),

$$I_{g-r} \approx \exp\frac{q(2E_t - E_g + V)}{2kT}. \quad (6)$$

For InP with $E_g = 1.34$ eV ($T = 300$ K) and $E_a = 0.08$ eV, the level depth is $E_t \approx 0.45$ eV.

The reverse current through the heterostructure is predominantly related, in the entire temperature range studied, to the tunneling mechanisms of carrier transfer. In the first region of smaller $m = m_1$, a dominating process is tunneling via local centers, while in the second (high-bias) region with $m = m_2$ the interband tunneling mechanism is operative. In the latter case, the E^* value in equation (3) is replaced by E_g (for *p*-InP) provided that no band breakage takes place. Here, the exponent (at large m_2) can be approximated by the power law in double logarithmic coordinates (Fig. 1, curves *3* and *4*). This region essentially reflects a "soft" breakdown of the heterojunction. The interband tunneling mechanism is confirmed by the negative temperature coefficient of this effect, whereby the breakdown voltage decreases with increasing temperature. The breakdown onset at $T = 100$ and 300 K is observed at $V \sim 2.2$ and 1.3 V, respectively.

The results of an investigation of the magnitude of the photoresponse as a function of the applied magnetic field in the samples biased in the forward and reverse direction (Fig. 3) show an increase in the photocurrent (up to 30% at $H = 16$ kOe) in the former case and a decrease (15 % at $H = 12$ kOe) in the latter. The heterostructure was exposed to a short-wavelength light with $\lambda = 0.63$ μm. The photogeneration of carriers took place in a near-surface layer of *p*-InP containing the space-charge region. We may suggest that the Hall field created by the dark carriers in the space-charge region gives rise to a drift flow of light-induced (minority) carriers. The latter are deflected by a magnetic field toward the heterojunction in the case of forward bias (which increases the photo emf) and outward in the case of reverse bias (which leads to the recombination on deep centers, including those with $E_t = 0.45$ eV, and decreases the photoresponse). Note that the photocurrent exhibits no changes in the absence of a magnetic field.

In conclusion, note that data concerning the mechanism of charge transfer in the n^+-CdS–*p*-InP–p^+-InP heterostructures should be taken into account in applications of the related devices, including photoconverters.

REFERENCES

1. K. Ito and T. Ohsawa, Jpn. J. Appl. Phys. **14**, 1259 (1975).
2. S. Wagner, J. L. Shay, K. J. Bachman, and E. Buehler, Appl. Phys. Lett. **26**, 229 (1975).
3. A. Q. Chynoweth, W. L. Feldmann, and R. A. Loqan, Phys. Rev. **121**, 684 (1961).

Translated by P. Pozdeev

Technical Physics Letters, Vol. 26, No. 7, 2000, pp. 631–633. Translated from Pis'ma v Zhurnal Tekhnicheskoĭ Fiziki, Vol. 26, No. 14, 2000, pp. 84–90.

Photoluminescence from Multilayer InAs/GaAs Structures with Quantum Dots in the 1.3–1.4 μm Wavelength Range

V. A. Egorov, V. N. Petrov, N. K. Polyakov, G. É. Tsyrlin, B. V. Volovik, A. E. Zhukov, and V. M. Ustinov

Institute of Analytical Instrument Engineering, Russian Academy of Sciences, St. Petersburg, 198103 Russia

Ioffe Physicotechnical Institute, Russian Academy of Sciences, Politekhnicheskaya ul. 26, St. Petersburg, 194021 Russia

Received March 10, 2000

Abstract—The optical properties of multilayer heterostructures with quantum dots were studied for InAs/GaAs systems obtained by the combined method of molecular-beam epitaxy and submonolayer migration-stimulated epitaxy. Using these structures, it is possible to obtain the room-temperature photoluminescence with maximum emission in the wavelength range from 1.3 to 1.4 μm. *© 2000 MAIK "Nauka/Interperiodica".*

The design of laser diodes with a wavelength of 1.3 μm is still an urgent problem for the local optical-fiber communication networks. This is explained by the fact that modern optical fiber materials have a minimum signal dispersion at this wavelength. There are several approaches to the solution of this problem: growth of A^3B^5 semiconductors with quantum dots as active regions on InP [1] and GaAs substrates; use of the various molecular-beam epitaxy (MBE) techniques for obtaining an active region of InGaAs quantum dots [2]; incorporation of small amounts of nitrogen into InGaAs quantum dot (QD) layers [3]; growth of an InGaAs solid solution layer over InAs/GaAs-QD layers [4, 5], etc. Recently, we demonstrated that, in principle, it is possible to obtain the photoluminescence at a wavelength of 1.3 μm in multilayer structures with InAs-QD layers grown by combined MBE techniques [6]. For example, a structure consisting of ten 2.5 monolayer (ML) InAs-QD layers (obtained by the scheme 0.5 ML film grown by molecular-beam epitaxy + 2.0 ML film grown by submonolayer migration-stimulated epitaxy, hereafter referred to as 0.5 ML MBE + 2.0 ML SMSE [7]) separated by 8-nm-thick GaAs spacers provides for a room-temperature photoluminescence with the maximum emission at a wavelength of 1.3 μm. Since the generation in these laser structures is possible only via the excited state of quantum dots, it is of interest to grow structures emitting at still longer wavelengths, probably as long as 1.55 μm. Below, we show that the multilayer structures with InAs/GaAs-QD layers obtained by the combined MBE/SMSE method allow an increase in the room-temperature photoluminescence wavelength up to 1.4 μm.

The structures were grown on semi-insulating singular GaAs (100) faces on an ÉP1203 setup. The formation of quantum dots was checked by the reflection high-energy electron diffraction (RHEED) patterns with the use of a special system to record and analyze them [8]. The active QD layers were grown by the following scheme. First, 0.5 ML InAs film was grown by MBE to obtain a corrugated surface [9] providing a higher density of the nucleation centers of three-dimensional islands. Then, 1.7–2.0 ML InAs film was grown by SMSE with the indium and antimony fluxes alternatively directed onto the substrate surface. Each experiment included four deposition cycles. One cycle of indium deposition corresponded to the formation of an 0.4–0.5 ML film and was followed by 10-s-long exposure of the sample to the antimony flux. The RHEED patterns showed that indium deposition resulted in the (4×1) surface reconstruction. When the sample was exposed to the antimony flux, this superstructure changed first to (1×1) and then, upon deposition of a 2 ML InAs film, the bands on RHEED patterns showed the bulk reflections indicative of the formation of three-dimensional islands. The active region between two 6-nm-thick GaAs layers consisted of ten InAs-QD layers separated by 8–10-nm-thick GaAs spacers. The effective thickness of the InAs-QD layer ranged from 2.2 to 2.5 ML in different structures. To prevent the transport of nonequilibrium charge carriers into the subsurface region and the substrate during optical studies, the active region was limited on both sides by short-period $Al_{0.25}Ga_{0.75}As$/GaAs superlattices (five 25 Å/25 Å pairs). Finally, the structure was coated with a 5-nm-thick GaAs layer. The growth temperature was 470–480°C for the active region and 600°C for the remaining part of the structure. The growth rates preliminarily measured on a calibration sample by the method of RHEED intensity oscillation in the zeroth reflection were equal to 0.08–0.10, 0.30, and 0.77 ML/s

1063-7850/00/2607-0631$20.00 © 2000 MAIK "Nauka/Interperiodica"

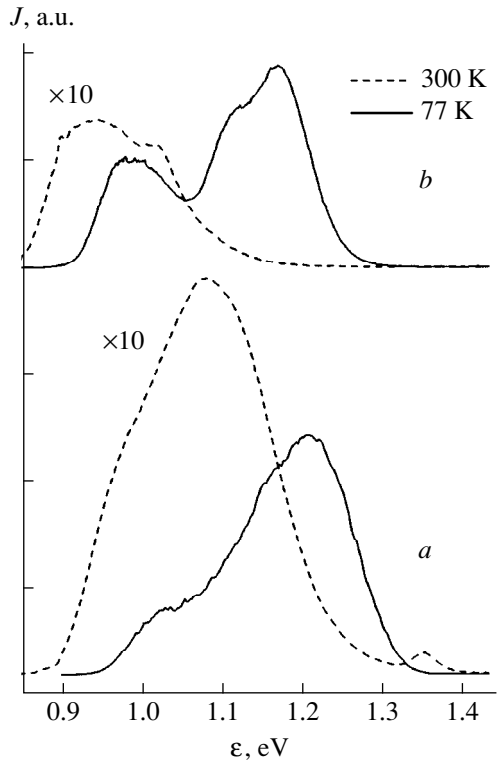

Fig. 1. Photoluminescence spectra of the structure consisting of ten 2.5 ML InAs-QD layers at 77 and 300 K. The GaAs spacer thickness is (*a*) 100 and (*b*) 80 Å.

for InAs, AlAs, and GaAs layers, respectively. The total pressure of antimony vapors in the growth chamber measured by a PMM 46 type transducer was constant in all experiments and amounted to $(1.5–2.1) \times 10^{-6}$ Pa. Photoluminescence was excited by an Ar^+-laser (λ = 514.5 nm) at an excitation density of ~100 W/cm^2 and detected by a cooled Ge photodiode.

To study the effect of various growth parameters on the position of the photoluminescence maximum, we prepared several multilayer structures, the main characteristics of which are listed in the table.

As indicated above, a pronounced photoluminescence with maximum intensity at a wavelength of 1.3 μm was observed for the structure with ten QD layers separated by a 80-Å-thick spacer at room temperature [6]. It is known that an increase in the thickness of the spacer separating QD layers reduces the probability of formation of misfit dislocations, which may increase the photoluminescence efficiency. Figure 1 shows the photoluminescence spectra of sample 1 with a spacer thickness increased up to 100 Å and, for comparison, the spectra of a sample with ten QD layers separated by a 80-Å-thick spacer. It is seen that only the photoluminescence edge reaches the vicinity of 1.3 μm in the spectra from sample 1 with a 100-Å-thick spacer, whereas the photoluminescence maxima fall within the wavelength range of 1.0–1.2 μm (in contrast to the sample with a 80-Å-thick spacer). As was indicated above, the long-wavelength shift in the multilayer structures can be explained by possible lateral merging of neighboring quantum dots and the formation of QD ensembles in the upper layers [6]. It can be suggested that thicker spacers "suppress" the formation of QD ensembles. A relatively weak (approximately fivefold) decrease in the integrated photoluminescence intensity at 77 and 300 K is indicative of a high crystallographic quality of the structure grown.

Samples, their growth parameters, and the positions of room-temperature photoluminescence maxima

Sample	Number of quantum-dot layers	Number of InAs-QD monolayers	Spacer thickness, Å	Photoluminescence peak position, μm
1	10	2.5	100	1.15–1.28
2	15	2.2	80	1.34
3	15	2.5	80	1.39

In order to obtain a long-wavelength shift of the photoluminescence maximum, the number of InAs-QD layers in sample 2 (with a 80-Å-thick spacer) was increased up to fifteen with a simultaneous decrease of their average thickness to 2.2 ML in order to reduce the probability of formation of misfit dislocations. As was indicated in [6], an increase in the average thickness of the InAs layers and/or a decrease in the spacer thickness dramatically decreased the photoluminescence efficiency, which is probably explained by the formation of misfit dislocations. Figure 2*a* shows the photoluminescence spectra of sample 2 measured at the temperatures 77 and 300 K. A rather high photoluminescence maximum occurs at a wavelength of 1.34 μm.

A most pronounced shift of the photoluminescence maximum toward the long-wavelength range was obtained upon increasing the thickness of each InAs-QD layer from 2.2 to 2.5 ML. Figure 2*b* shows the photoluminescence spectra of sample 3 at room and liquid-nitrogen temperatures. In this case, the maximum photoluminescence at 300 K is observed at a wavelength of 1.39 μm. Despite an increase in the average thickness of InAs layers, the photoluminescence efficiency remains rather high, thus indicating that the dislocation density in this case is still rather low.

The long-wavelength shift observed in the spectra of structures with fifteen QD layers can be explained by a higher density of QD ensembles in the upper layers because of more pronounced lateral merging of the neighboring quantum dots [10]. This is also confirmed by theoretical analysis of the behavior of a QD ensembles in multilayer structures [11]. In particular, it was shown that, at a sufficiently small distance between the neighboring quantum dots in the initial layer, the neighboring quantum dots in the upper layers gradually merge together. It is this very situation that was observed in our samples when 0.5 ML InAs-QD layers

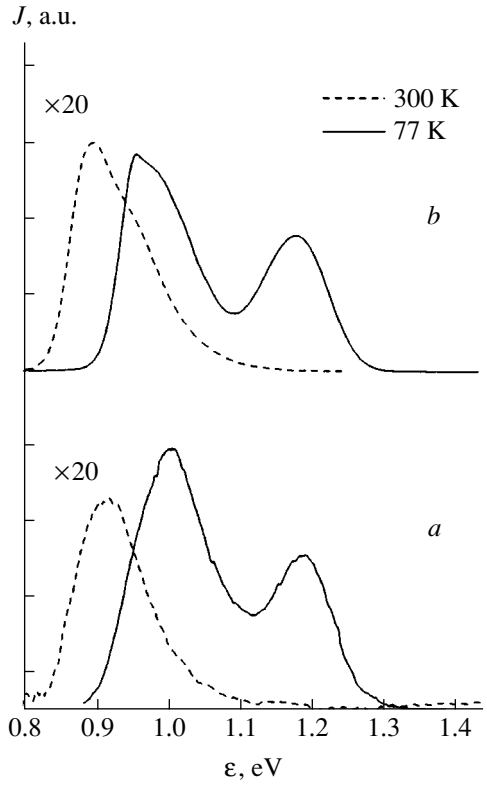

Fig. 2. Photoluminescence spectra of structures consisting of fifteen (*a*) 2.2 ML and (*b*) 2.5 ML InAs-QD layers at 77 and 300 K. The GaAs spacer thickness is 80 Å.

were grown by the MBE method which, as has already been indicated, provided a higher density of nucleation centers of three-dimensional islands and, therefore, a smaller island spacing. If the whole QD layer is grown by the SMSE method, the island density is lower because of a smaller number of the nucleation centers of three-dimensional islands observed in the initial growth stage [6].

In our opinion, the above behavior can hardly be associated with dislocation-induced photoluminescence, since variation of the growth parameters substantially changes the position of the photoluminescence maximum. Nevertheless, reliable interpretation of the above results requires further study of the composition and structure of the grown layers by methods of transmission electron spectroscopy and investigation of the temperature variation of the photoluminescence emission and excitation spectra.

Thus, we have shown that it is possible to obtain room-temperature photoluminescence emission in the wavelength range from 1.3 to 1.4 μm from multilayer InAs/GaAs structures with quantum dots grown by the combined MBE and SMSE methods. The study performed shows a considerable effect of the growth parameters (the number of layers in the multilayer structure, the average thickness of the InAs-QD layer, and the thickness of spacers separating these layers) on the optical properties of the multilayer structures.

ACKNOWLEDGMENTS

The authors are grateful to D.V. Denisov, Yu.B. Samsonenko, D.N. Demidov, and N.P. Korneeva for their help in growth experiments and to A.F. Tsatsul'nikov for fruitful discussions.

This study was partly supported by the Scientific Program *Physics of Solid-State Nanostructures* (project nos. 98-2029 and 99-2014) and the Russian Foundation for Basic Research (project no. 98-02-18317).

REFERENCES

1. S. Seki, H. Oohasi, H. Sugiura, *et al.*, J. Appl. Phys. **79**, 2192 (1996).
2. D. L. Huffaker, G. Park, Z. Zou, *et al.*, Appl. Phys. Lett. **73**, 2564 (1998).
3. M. Sopanen, H. P. Xin, and C. W. Tu, Appl. Phys. Lett. **76**, 994 (2000).
4. B. V. Volovik, A. F. Tsatsul'nikov, D. A. Bedarev, *et al.*, Fiz. Tekh. Poluprovodn. (St. Petersburg) **33**, 990 (1999) [Semiconductors **33**, 901 (1999)].
5. A. R. Kovsh, A. E. Zhukov, N. A. Maleev, *et al.*, Fiz. Tekh. Poluprovodn. (St. Petersburg) **33**, 1020 (1999) [Semiconductors **33**, 929 (1999)].
6. G. É. Tsyrlin, N. K. Polyakov, V. A. Egorov, *et al.*, Pis'ma Zh. Tekh. Fiz. **26** (10), 46 (2000) [Tech. Phys. Lett. **26**, 423 (2000)].
7. G. É. Tsyrlin, A. O. Golubok, S. Ya. Tipisev, *et al.*, Fiz. Tekh. Poluprovodn. (St. Petersburg) **29**, 1697 (1995) [Semiconductors **29**, 884 (1995)].
8. G. M. Gur'yanov, V. N. Demidov, N. P. Korneeva, *et al.*, Zh. Tekh. Fiz. **67** (8), 111 (1997) [Tech. Phys. **42**, 956 (1997)].
9. G. M. Guryanov, G. E. Cirlin, A. O. Golubok, *et al.*, Surf. Sci. **352**/**354**, 646 (1996).
10. A. F. Tsatsul'nikov, A. Yu. Egorov, A. E. Zhukov, *et al.*, Fiz. Tekh. Poluprovodn. (St. Petersburg) **31**, 851 (1997) [Semiconductors **31**, 722 (1997)].
11. V. A. Egorov and G. É. Tsyrlin, Pis'ma Zh. Tekh. Fiz. **26** (5), 86 (2000) [Tech. Phys. Lett. **26**, 220 (2000)].

Translated by L. Man

Technical Physics Letters, Vol. 26, No. 7, 2000, pp. 634–636. Translated from Pis'ma v Zhurnal Tekhnicheskoĭ Fiziki, Vol. 26, No. 14, 2000, pp. 91–96.

Absorption Band Saturation in the Near-IR Spectrum of Molybdenum Blue

A. A. Bugaev and S. E. Nikitin

Ioffe Physicotechnical Institute, Russian Academy of Sciences, St. Petersburg, 194021 Russia

Received March 14, 2000

Abstract—Nonlinear absorption of a picosecond laser pulse in an aqueous solution of a partly reduced heptamolybdate and citric acid was studied. We report on the first observations of the absorption band saturation in the near-IR spectrum of molybdenum blue and its relaxation on a picosecond time scale. A stepwise character of the intensity dependence of the absorption band saturation is demonstrated. Qualitative interpretation of the experimental results is based on the concept of self-defocusing in a three-level system that exhibits two-photon transitions via an intermediate level upon high-power excitation. © *2000 MAIK "Nauka/Interperiodica".*

Analytical chemistry and chemical technology extensively employ molybdenum blues discovered by Bucholz in the XIX century [1–3]. Molybdenum blues fall into two groups, one of which is formed due to the partial reduction of isopolymolybdates. This group includes oxides and hydroxides of penta- or hexavalent molybdenum. The reduction of heteropolymolybdates produces substances of the other group described by the formula $(HtMo_{12}O_{40})^{4+}$ and characterized by the atomic ratio of heteroatoms (Ht) to molybdenum equal to 1 : 12. Although the structure and electronic properties of reduced polymolybdates [2–10, 13] have been extensively studied, the nature of chemical bonds in molybdenum blues remains unclear. Typical absorption spectra of molybdenum blue solutions exhibit one band in the visible region and one band in the near-IR (NIR) range. The former (about 2.5 eV) is assigned to *d–d* transitions in Mo^{5+} centers of the C_{4V} symmetry. The latter absorption (0.9–1.65 eV) is related to transitions with charge transfer between Mo^{5+} and Mo^{6+} via an oxygen bond [4, 7, 8]. In this work, we report on the first observations of NIR absorption band saturation and a picosecond relaxation of the corresponding excited state of the molybdenum blue.

A passively mode-locked solid-state (YAG:Nd^{3+}) laser equipped with a one-path amplifier produced 30-ps pulses with an energy of 7–10 mJ, a wavelength of 1.06 μm, and a repetition rate of 1 Hz. Each pulse was split into two so that the intensity of the delayed and attenuated (by the half-wave retardation plate and the Glan prism) probing pulse was three orders of magnitude (1 : 1000) lower than that of the pumping one. Orthogonally polarized beams were focused at an angle of 15° into the cell with a molybdenum blue solution. A detection system was adjusted to measure only the ratio of energies of the second harmonic and the fundamental radiation, which varied within 5% of the mean value.

The experiments were performed with an aqueous solution of ammonium heptamolybdate tetrahydrate $(NH_4)_6[Mo_7O_{24}] \cdot 4H_2O$ and citric acid $C_6H_8O_7$ with the concentrations 0.027 and 0.071 mol/l, respectively. UV illumination at 365 nm reduces the heptamolybdate $[Mo_7O_{24}]^{6-}$ in solution, which leads to the appearance of blue color. Exposure time variation made it possible to produce samples showing different absorption coefficients at 1.06 μm: 0.7, 1.36, 2.7, and 27 cm^{-1}.

The studies included two types of measurements. Figures 1 and 2 show the corresponding plots of the pumping pulse transmission versus the intensity and

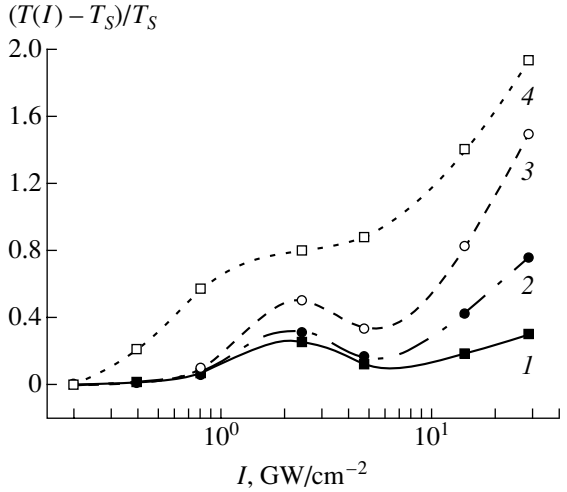

Fig. 1. Plots of the molybdenum blue transmittance $(T(I) - T_S)/T_S$ versus the pumping pulse intensity for the absorption coefficient α_0 = (*1*) 0.7, (*2*) 1.36, (*3*) 2.7, and (*4*) 27 cm^{-1}. The cell thickness was (*1–3*) 10 mm and (*4*) 1 mm. The curves show approximation by the least-squares method.

1063-7850/00/2607-0634$20.00

the probing pulse transmission versus the time delay relative to the pumping pulse at a constant intensity of the latter.

The plots of the relative transmittance $(T(I) - T_S)/T_S$ (Fig. 1) exhibit two characteristic features. The first is the effect of absorption saturation manifested in an increase of the transmittance with increasing pumping pulse intensity. Note that the higher the initial absorption coefficient (or the number of reduced heptamolybdate $[Mo_7O_{24}]^{6-}$ molecules), the larger the change in transmittance at a given pumping intensity. It can be easily demonstrated that the induced change in the absorption coefficient of molybdenum blue amounts to 10 cm^{-1} for the initial value of $\alpha_0 = 27$ cm^{-1}.

A stepwise character is the other feature of the transmittance plots: it is seen that the transmittance first increases, then saturates and even decreases, and finally starts growing again. Measurements in a 10-mm cell (curves *1–3*) show a decrease in the transmittance for intensities in the region of about 5 GW cm^{-2}, which is probably related to the effect of pulse self-defocusing in the nonlinear medium. Shortening the nonlinear interaction length may help to decrease the power density drop caused by self-defocusing. Indeed, curve *4* in Fig. 1 (1-mm cell) shows no decrease in the transmittance, while still retaining the stepwise character.

Let us completely neglect self-defocusing in a thin (1-mm) cell. Then the stepwise character of the transmittance variation unambiguously indicates the existence of at least three energy levels in the molybdenum blue interacting with the photon $\hbar\omega = 1.17$ eV. Theoretical studies [11, 12] of a three-level system ($E_3 > E_2 > E_1$, $E_2 - E_1 < E_3 - E_2$, $E_2 - E_1 = \hbar\omega - \Delta_2$, $E_3 - E_2 = \Delta_2 + \Delta_3 + \hbar\omega$, where Δ_2 and Δ_3 are detunings and $\hbar\omega$ is the photon energy) showed that the increase of the intensity leads to excitation of both one-photon (transition $1 \longrightarrow 2$) and two-photon (transition $1 \longrightarrow 3$) resonances. If the detuning Δ_2 is comparable to the Rabi frequency Ω_{12} of the transition $1 \longrightarrow 2$, then the three-level system is equivalent to a two-level system that exhibits the absorption saturation related to a decrease in the population difference between levels 1 and 2. Since the detuning Δ_3 decreases with increasing field intensity [12], a two-photon resonance occurs at the transition $1 \longrightarrow 3$ and the population density appears to be distributed between three levels. The transition from one-photon resonance to two-photon resonance is just what accounts for the stepwise character of the transmittance variation in Fig. 1. Unfortunately, these heptamolybdate levels have not been identified yet. We can only suggest that these levels are related to two partially overlapping absorption bands (0.77–1 and 0.9–1.3 μm) described in [13], which originate from two types of transitions with charge transfer between Mo^{5+} and Mo^{6+} in the centers differing by the types of terminal and angular Mo–O bonds in the MoO_6 octahedron.

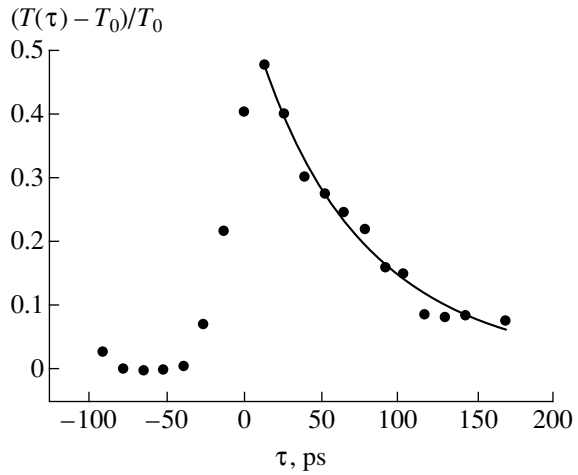

Fig. 2. Plot of the molybdenum blue transmittance versus pump–probe delay showing (filled circles) experimental results and (solid line) fitting curve $0.5\exp[-(\tau - 8\text{ ps})/70\text{ ps}]$.

Further characterization of the absorption saturation in molybdenum blues is based on the results of our measurements of our excited state relaxation kinetics (Fig. 2). It is seen that the leading edge of the nonlinear response roughly follows the integral of the pumping pulse intensity over time. Numerical analysis (fitting curve in Fig. 2) yields a simple exponential decay of the transmittance to the initial level with a characteristic time of 70 ps. This parameter is virtually insensitive to variation of the pumping pulse intensity from 0.2 to 2 GW/cm^2.

Thus, we observed the phenomenon of the absorption band saturation in the NIR spectrum of molybdenum blue (ammonium heptamolybdate tetrahydrate) related to the charge transfer between Mo^{5+} and Mo^{6+} via an oxygen bond. Qualitative description of this phenomenon can be provided within the framework of a three-level scheme with the self-defocusing effect. Based on the results of this work, we anticipate the successful application of nonlinear optics in studying molybdenum and tungsten blues that represent a new type of nonlinear optical materials.

The authors are grateful to B.P. Zakharchenya for interest in this work and support.

REFERENCES

1. Citation from: Gmelin. Molybdän **53** (3), 132 (1935).
2. J. D. H. Strickland, J. Am. Chem. Soc. **74** (4), 862 (1952).
3. C. L. Rollinson, *The Chemistry of Cromium, Molybdenum and Tungsten* (Pergamon, Oxford, 1973).
4. R. I. Buckley and R. J. H. Clark, Coord. Chem. Rev. **65** (2), 167 (1985).
5. M. T. Pope, *Heteropoly and Isopoly Oxometaletes* (Springer-Verlag, Berlin, 1983).

6. M. T. Pope, in *Mixed-Valence Compounds: Theory and Applications in Chemistry, Physics, Geology, and Biology (Proceedings of the NATO Advanced Study Institute, Oxford)*, Ed. by D. B. Brown (D. Reidel, Boston, 1974).
7. K. H. Tytko and O. Glemster, Adv. Inorg. Chem. Radiochem. **24** (3), 239 (1981).
8. T. J. R. Weakly, Struct. Bonding (Berlin) **18** (4), 131 (1974).
9. A. Tokmakoff, R. S. Urdahl, D. Zimdars, *et al.*, J. Chem. Phys. **102** (10), 3919 (1995).
10. F. A. Cotton and G. Wilkinson, *Advanced Inorganic Chemistry* (Willey, New York, 1967).
11. W. Hänsch, Z. Phys. **236** (6), 213 (1970).
12. V. M. Akulin and N. V. Karlov, *Intense Resonance Interactions in Quantum Electronics* (Nauka, Moscow, 1987).
13. J. M. Fruchart, G. Herve, J. P. Lannay, and R. Massart, J. Inorg. Nucl. Chem. **38** (11), 1627 (1976).

Translated by A. Chikishev

Technical Physics Letters, Vol. 26, No. 7, 2000, pp. 637–639. Translated from Pis'ma v Zhurnal Tekhnicheskoĭ Fiziki, Vol. 26, No. 14, 2000, pp. 97–102.

On the Euler Equation Appearing in the Synthesis of Radiating Systems

S. I. Éminov

Novgorod State University, Sankt-Peterburgskaya ul. 41, Novgorod, 173003 Russia

Received January 11, 2000

Abstract—A problem appearing when the Euler equation is used in the theory of antenna synthesis is considered. Behavior of a solution to this equation at the ends of the synthesis interval contradicts the Meixner conditions, according to which this solution must tend to zero as a square root of the distance to the ends. It is shown that this contradiction arises if we seek solutions in the L_2 space and disappears if an L_2 subspace with limited energy norm is selected as the space of solutions. In this case, the Euler equation arises from a variational minimization problem for a functional involving the norm of current determined in the energy space. *© 2000 MAIK "Nauka/Interperiodica".*

1. Formulation of the problem. A relationship between the current $I(\tau)$ of a linear radiator with an electric length $2l$ and a radiation pattern $F(\chi)$ is described by the following equation [1–3]:

$$F = PI \equiv \int_{-1}^{1} \exp(il\chi t) I(t)\,dt, \quad -1 \le \chi \le 1. \qquad (1)$$

Here, operator P is a completely continuous operator specified, for example, in space L_2 of square-summable functions. Inversion of this operator may present a problem. Therefore, equation (1) is replaced with the Euler equation

$$\alpha I + P^*PI = P^*F, \qquad (2)$$

where α is a small parameter,

$$P^*PI = \int_{-1}^{1} I(t) \int_{-1}^{1} \exp(-il\chi(\tau - t))\,d\chi\,dt,$$

and

$$P^*F = \int_{-1}^{1} \exp(-il\chi\tau) F(\chi)\,d\chi.$$

Equation (2) is very attractive, since it is a Fredholm-type equation of the second kind. However, this equation has a serious drawback: a solution to this equation does not vanish at the ends of interval [–1, 1]. At the same time, according to the Meixner conditions [4], the current at the ends of a linear radiator (for example, dipole) must tend to zero as a square root of the distance to the end:

$$I(\tau) \sim (1 - \tau^2)^{1/2}, \quad \tau \longrightarrow \pm 1. \qquad (3)$$

The purpose of this letter is to clarify the cause of this defect appearing in equation (2), namely, to establish whether this defect is related to the method of derivation of this equation or probably stems from incorrect premises. In addition, we will derive an equation whose solution satisfies conditions (3).

2. Energy integral. The theory [1–3] assumes that current $I(\tau)$ belongs to space L_2, that is,

$$\int_{-1}^{1} |I(t)|^2 dt < +\infty \qquad (4)$$

or, taking into account the Parseval equality,

$$\int_{-\infty}^{+\infty} |F(\chi)|^2 d\chi < +\infty. \qquad (5)$$

It should be noted that the choice of the L_2 space was substantiated neither in the works cited nor in other literature known to the author. At the same time, the choice of the space of currents is the key point, because the Euler equation is derived from the condition of the limited norm of the current corresponding to the space chosen.

In our opinion, the space of currents should be chosen based on the physical conditions; namely, the field power must be limited in both far and near zone. It is this condition that ensures the uniqueness of a solution to the Maxwell equations [4].

Let us derive the field power in the near zone of a symmetrically excited dipole with the electric radius a.

1063-7850/00/2607-0637$20.00 © 2000 MAIK "Nauka/Interperiodica"

To do this, we integrate the Poynting vector over the dipole surface [5, p. 74]:

$$P = \frac{1}{2}\iint_S [\mathbf{E}, \mathbf{H}]\mathbf{n}dS = -\frac{1}{2}\iint_S E_z H_\varphi dS = -\frac{\tilde{l}}{2}\int_{-1}^{1} E_z(\tau) I^*(\tau) d\tau, \quad (6)$$

where $2\tilde{l}$ is the length of the dipole and the asterisk denotes the complex conjugate.

Further, we express the electric field E_z in terms of current I using the Fourier integral representation for the Green function in a cylindrical coordinate system [6]:

$$\tilde{l}E_z(\tau) = i\sqrt{\frac{\mu}{\varepsilon}}\frac{l^2}{4\pi^2}\int_{-\infty}^{+\infty}(\chi^2-1)I_0(\sqrt{\chi^2-1}a) \times K_0(\sqrt{\chi^2-1}a)\int_{-1}^{1}\exp(-il\chi(\tau-t))I(t)dtd\chi, \quad (7)$$

where I_0 and K_0 are the modified Bessel functions.

Substituting formula (7) into (6) and taking into account formula (1), we obtain the following final expression for the desired field power:

$$P = -i\sqrt{\frac{\mu}{\varepsilon}}\frac{l^2}{8\pi^2}\int_{-\infty}^{+\infty}(\chi^2-1)I_0(\sqrt{\chi^2-1}a) \times K_0(\sqrt{\chi^2-1}a)|F(\chi)|^2 d\chi. \quad (8)$$

From asymptotics of the modified Bessel functions

$$I_0(\chi)K_0(\chi) = \frac{1}{2\chi} + \frac{1}{16\chi^3} + \ldots, \quad \chi \longrightarrow +\infty,$$

we obtain that the condition of limited power is equivalent to the finite value of the integral

$$\int_{-\infty}^{+\infty}|\chi||F(\chi)|^2 d\chi < +\infty. \quad (9)$$

Comparing expressions (9) and (5), we can deduce the following: the condition that the current belongs to space $L_2[-1, 1]$ is not sufficient to ensure a limited value of the power. This statement can be easily verified.

Thus, in order to limit the power, we must restrict space $L_2[-1, 1]$.

3. Energy space. We define an energy space, in which condition (9) is satisfied, with the help of the operator

$$(AI)(\tau) = \frac{1}{\pi}\int_0^{+\infty} x\int_{-1}^{1}\cos[x(\tau-t)]I(t)dtdx = \frac{1}{2\pi}\int_{-\infty}^{+\infty}|\chi|\int_{-1}^{1}\exp(-i\chi(\tau-t))I(t)dtd\chi, \quad (10)$$

which is a symmetric and positive definite operator with dense domain of definition $D(A)$ in space $L_2[-1, 1]$ [6]. The energy space H_A is defined as a completion of domain $D(A)$ according to the norm

$$[I]^2 = (AI, I), \quad (11)$$

where (I, I) is the inner product in space $L_2[-1, 1]$ and $[I, G] = (AI, G)$ is the inner product in space H_A.

The orthonormal basis in space H_A is given by [6]

$$\varphi_n(\tau) = \sqrt{\frac{2}{\pi n}}\sin[n\arccos(\tau)], \quad n = 1, 2, \ldots, \quad (A\varphi_m, \varphi_n) = \begin{cases} 0, & m \neq n, \\ 1, & m = n. \end{cases} \quad (12)$$

It should be noted that the unit function, having an infinite energy norm, does not belong to space H_A. A smooth function belongs to space H_A only when it vanishes at the ends of interval $[-1, 1]$.

4. Variational problem. The Euler equation. The variational problem consists in minimizing the functional

$$M(I) = \|PI - F\|^2 + \alpha[I]^2. \quad (13)$$

The formulation of this problem is borrowed from [2]. A difference consists in that here the current norm is minimized in space H_A, whereas in [3] this functional is minimized in space $L_2[-1, 1]$. In both approaches, the closeness of patterns is estimated in space $L_2[-1, 1]$. The functional reaches an extremum for a current ensuring zero variation. The variation of this functional is calculated by the formula

$$\delta M(I) = \frac{\partial}{\partial\alpha}M(I + \alpha h)|_{\alpha = 0}. \quad (14)$$

Let us determine the variation of the functional taking into account the definition of the energy norm, the symmetry of operator A, and the definition of the conjugate operator P^*:

$$\delta M(I) = (h, \alpha AI + P^*PI - P^*F) + (\alpha AI + P^*PI - P^*F, h). \quad (15)$$

The variation of this functional must vanish for all variations of parameter h. Whence we obtain the Euler

equation

$$\alpha AI + P^*PI = P^*F. \quad (16)$$

In this equation, the unit operator is replaced with the positive definite operator A. It is this operator that determines the behavior of the current at the ends of the radiator. According to formula (12), the eigenfunctions of operator A satisfy the Meixner conditions (3). The current will also satisfy this condition, since operator P^*P in equation (16) has a smooth kernel and, hence, has no effect on the behavior of the current at the ends of the radiator.

In conclusion, we should point out one more advantage of equation (16). The solution to this equation is sought in the same space as the solution to an integral equation appearing in analysis problem [6]. In the latter case, we find currents induced on the dipole surface by a specified primary field. Thus, the analysis and synthesis problem can be combined into an integrated computational process.

REFERENCES

1. B. M. Minkovich and V. P. Yakovlev, *Theory of Antenna Synthesis* (Sov. Radio, Moscow, 1969).
2. L. D. Bakhrakh and S. D. Kremenetskiĭ, *Synthesis of Radiating Systems: Theory and Practice* (Sov. Radio, Moscow, 1974).
3. V. I. Dmitriev and N. I. Berezina, *Numerical Methods for Solving Problems in the Synthesis of Radiating Systems* (Mosk. Gos. Univ., Moscow, 1986).
4. H. Hönl, A. W. Maue, and K. Westpfahl, in *Handbuch der Physik*, Ed. by S. Flügge (Springer-Verlag, Berlin, 1961; Mir, Moscow, 1964), Vol. 25, Part 1, p. 218.
5. G. T. Markov and D. M. Sazonov, *Antennas* (Énergiya, Moscow, 1975).
6. S. I. Éminov, Radiotekh. Élektron. (Moscow) **38** (12), 2160 (1993).

Translated by A. Kondrat'ev

Technical Physics Letters, Vol. 26, No. 7, 2000, pp. 640–643. Translated from Pis'ma v Zhurnal Tekhnicheskoĭ Fiziki, Vol. 26, No. 14, 2000, pp. 103–110.

A Model of the Hypersensitivity of Compressible Crystal Hydrates in Superlow-Frequency Electric Fields

E. G. Fateev

Institute of Applied Mechanics, Ural Division, Russian Academy of Sciences, Izhevsk, Russia
e-mail: fateev@ipm.uni.udm.ru

Received January 25, 2000

Abstract—A new model is proposed to explain a significant drop in the mechanical stability of highly compressible crystal hydrates in very weak superlow-frequency electric fields. The model is based on the concept of dehydration in a strongly compressed disperse crystal hydrate system, which can be described in terms of the interaction potential of nonpoint electric oscillators with highly variable dipole moments. The results of calculations show that the proposed model concept is quite realistic. © *2000 MAIK "Nauka/Interperiodica".*

Recent experiments [1–5] with the Bridgman effect (explosion-like instability of solid dielectrics subjected to strong uniaxial compressive stresses at high pressures) showed a considerable decrease in the stability threshold of crystal hydrates in response to the very weak action of an electric field in a very narrow range of superlow-frequencies (SLF) ($\omega < 10^3$ Hz). The drop in stability was observed in the SLF electric fields of intensity that was lower by more than one thousand times than the values necessary for the electric breakdown in the media studied. This effect was preceded by a giant increase in the dielectric permittivity in the SLF range, which was probably explained by a short-time appearance of inhomogeneous structures (nonconducting inclusions with thin liquid shells containing mobile ions) in the strongly compressed crystal hydrates [3–5].

The existing models describing these phenomena are based on rather unusual assumptions that may imply, as suggested in [3], the appearance of an SLF peak in the spectrum of energy density supplied to the breakdown and, hence, the appearance of a feature in the SLF hypersensitivity spectrum. This maximum could be manifested [3], provided that the charge relaxation times in the liquid shells surrounding the micron dielectric particles were of the order of $\tau \sim 10^{-2}$ s. However, the real relaxation times in these systems determined from the characteristic frequency of the dielectric loss peak ($\Omega \sim 5 \times 10^4$ Hz) are of the order of $\tau = 1/\Omega \sim 10^{-5}$ s. In order to assess the real possibility of a hypersensitive instability manifestation and the electric excitation localization within a narrow SLF interval (apparently initiating these effects), let us consider a model of a disperse solid system making allowance for the finite size and variable moment of oscillating dipoles in the chain.

In determining the potential energy of a chain of oscillators, we will allow for a possibility of the nonpoint dipoles with variable moment occurring within cells of radius r at a minimum distance of $a \geq 2r$ from each other (Fig. 1). We will consider the interaction between these dipoles in the Coulomb approximation.

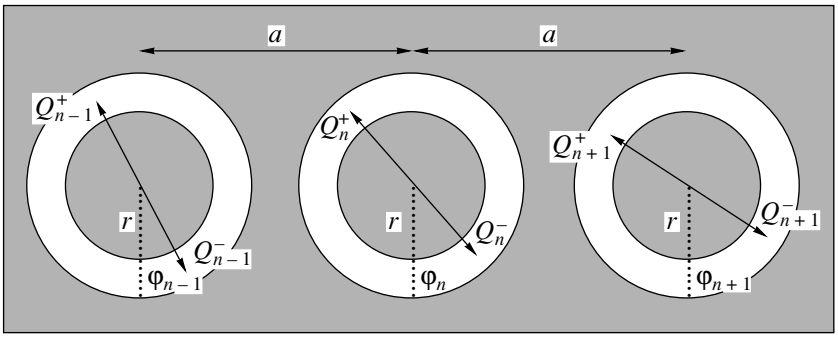

Fig. 1. Schematic diagram showing a model chain of dipole oscillators representing charges oscillating inside the shells (real thicknesses, 30–300 Å) surrounding particles with a diameter $2r$ spaced by a.

1063-7850/00/2607-0640$20.00 © 2000 MAIK "Nauka/Interperiodica"

Let the angles φ_{n-1}, φ_n, φ_{n+1} characterize deviations of the dipole axes in oscillators *1–3*, respectively, from the position of instable equilibrium. Then the general form of the potential energy of the system of oscillators with dipole–dipole interactions can be written in the following form:

$$U_{\text{int}} = \frac{1}{4\pi\varepsilon\varepsilon_0}\sum_n\left\{\left(\frac{Q^+_{n-1}Q^+_n\mathbf{R}^{++}_{n-1,n}}{(R^{++}_{n-1,n})^2} + \frac{Q^-_{n-1}Q^-_n\mathbf{R}^{--}_{n-1,n}}{(R^{--}_{n-1,n})^2}\right.\right.$$
$$\left. - \frac{Q^-_{n-1}Q^+_n\mathbf{R}^{-+}_{n-1,n}}{(R^{-+}_{n-1,n})^2} - \frac{Q^+_{n-1}Q^-_n\mathbf{R}^{+-}_{n-1,n}}{(R^{+-}_{n-1,n})^2}\right)$$
$$+\left(\frac{Q^+_nQ^+_{n+1}\mathbf{R}^{++}_{n,n+1}}{(R^{++}_{n,n+1})^2} + \frac{Q^-_nQ^-_{n+1}\mathbf{R}^{--}_{n,n+1}}{(R^{--}_{n,n+1})^2}\right. \quad (1)$$
$$\left.\left. - \frac{Q^-_nQ^+_{n+1}\mathbf{R}^{-+}_{n,n+1}}{(R^{-+}_{n,n+1})^2} - \frac{Q^+_nQ^-_{n+1}\mathbf{R}^{+-}_{n,n+1}}{(R^{+-}_{n,n+1})^2}\right)\right\},$$

where $\mathbf{R}^{++}_{n-1,n}$, $\mathbf{R}^{--}_{n-1,n}$, $\mathbf{R}^{-+}_{n-1,n}$, $\mathbf{R}^{+-}_{n-1,n}$, $\mathbf{R}^{++}_{n,n+1}$, $\mathbf{R}^{--}_{n,n+1}$, $\mathbf{R}^{-+}_{n,n+1}$, $\mathbf{R}^{+-}_{n,n+1}$ are the vector radii between the corresponding charges in the chain, ε is the dielectric permittivity of the medium between particles, and ε_0 is the dielectric constant.

In constructing the one–dimensional model of the system of nonpoint oscillators with variable dipole moments, it is necessary to take into account that a charge in the *n*th cell must depend on the strengths of both external and internal (local) fields created by moving charges in the neighboring $(n-1)$th and $(n+1)$th cells. Let us assume that interactions of the non-neighboring dipoles are effectively screened and only transferred via the chain. Rather formally considering the phenomenon of polarization in this system of oscillators, we will ignore all other possible physicochemical processes in and around them (see, e.g., [6–8]). We assume that the contributions from external and local fields to the polarization of any of the charges Q^+_n, Q^-_n, Q^+_{n-1}, Q^-_{n-1} obey the principle of superposition, with allowance made for their frequency-dependent effective contributions. Dependence of the polarization on the frequency of local (ω_n) or external (Ω) excitation for a separate particle can be formally described, e.g., using the Debye dispersion equation [6–8]. Then, positive charges (note that $|Q^+_n| = |Q^-_n|$) on the dipole ends in the $(n-1)$th, *n*th, and $(n+1)$th cells can be described as follows:

$$Q^+_n = \beta\left(\frac{c_0e(\varepsilon_s-\varepsilon_\infty)\mathbf{R}^{++}_{n,n-1}}{4\pi\varepsilon\varepsilon_0(1+(\tau\omega_{n-1})^2)(R^{++}_{n,n-1})^3}\right.$$
$$+\frac{c_0e(\varepsilon_s-\varepsilon_\infty)\mathbf{R}^{++}_{n,n+1}}{4\pi\varepsilon\varepsilon_0(1+(\tau\omega_{n+1})^2)(R^{++}_{n,n+1})^3} \quad (2)$$
$$-\frac{c_0e(\varepsilon_s-\varepsilon_\infty)\mathbf{R}^{+-}_{n,n-1}}{4\pi\varepsilon\varepsilon_0(1+(\tau\omega_{n-1})^2)(R^{+-}_{n,n-1})^3}$$
$$\left.-\frac{c_0e(\varepsilon_s-\varepsilon_\infty)\mathbf{R}^{+-}_{n,n+1}}{4\pi\varepsilon\varepsilon_0(1+(\tau\omega_{n+1})^2)(R^{+-}_{n,n+1})^3} + \frac{E^{\text{ext}}_n}{1+(\tau\Omega)^2}\right).$$

Similar expressions can be written for Q^+_{n-1} and Q^+_{n+1} as well. Here, τ is the relaxation time of bound charges in the shells, ε_s and ε_∞ are the maximum SLF permittivity and minimum high-frequency permittivity, respectively, and c_0 is the number of elementary charges *e* on the dipole ends that provides for the permittivity change by unity in the course of polarization. The external harmonic perturbing field (for simplicity, directed along the chain of dipoles) in the vicinity of the *n*th particle can be written as

$$E^{\text{ext}}_n = 2\varepsilon^{-1}E\sin(2\pi\Omega t)\cos(\varphi_n). \quad (3)$$

Similar expressions for the perturbing fields can be written for the $(n-1)$th and $(n+1)$th cells. In calculating the fields E_n, E_{n-1}, and E_{n+1}, we assumed that charges on the ends of the *n*th and $(n-1)$th dipoles may take the value $Q_\infty = c_0e\varepsilon_\infty$ for $\omega_n \longrightarrow \infty$ and $Q_0 = c_0e(\varepsilon_s - \varepsilon_\infty)$ for $\omega_n \longrightarrow 0$. All particles in the chain are characterized by $c_0 = \text{const}$. The proportionality factor β corresponds to a charge induced on the dipole ends in a field of unit strength.

An expression for the kinetic energy of a system of charges with masses $M_n = c_nm$ on the dipole ends is as follows:

$$T_k = \frac{1}{2}\sum_n J_n\dot{\varphi}^2_n, \quad (4)$$

where $J_n = c_nmr^2$ is the moment of inertia and c_n is the number of uncompensated charges (cations or anions) with masses *m* in the shell of the *n*th cell.

Assuming that dissipative forces depend linearly on the angular velocity of charges, the corresponding dissipative function for a chain with the dissipation parameter ξ_n can be written in the following form:

$$D = \frac{1}{2}\sum_n c_n\xi_nr^2\dot{\varphi}^2_n. \quad (5)$$

The force of interaction between the external field and

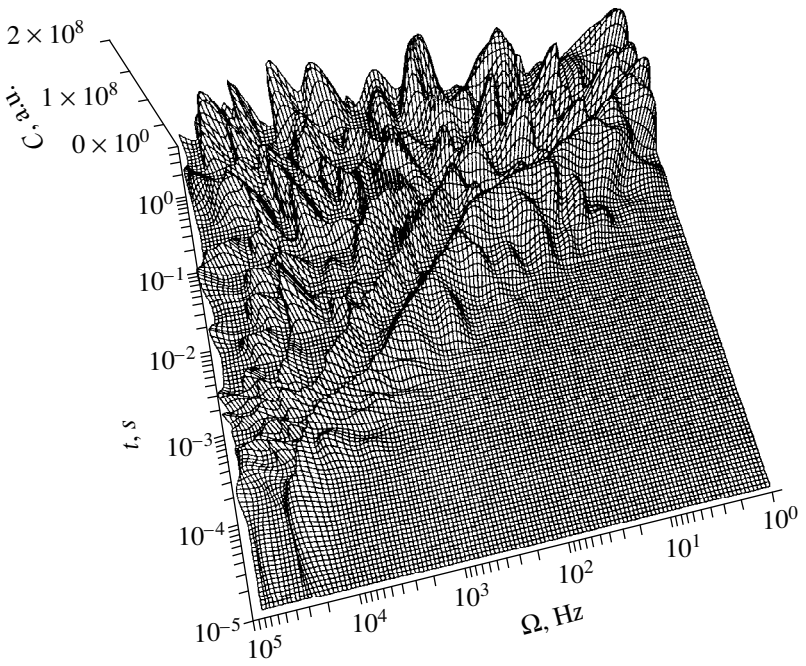

Fig. 2. Time evolution of the SLF spectra of the maximum polarization of charges in a chain of oscillators with the length $l = 10^{-3}$ m under the action of a very weak harmonic electric field ($E_0 = 10^4$–10^5 V/m; $r = 10^{-6}$ m; $a = 2.1 \times 10^{-6}$ m; $\tau = 1.6 \times 10^{-5}$ s; $\varepsilon_\infty = 8$; $\varepsilon_s = 650$, $c_0 = 10^5$; $\beta = 1$; $\xi = 10^{-33}$; $m = 1.6 \times 10^{-27}$ kg).

the chain of oscillators can be expressed as

$$F_n = 2\varepsilon^{-1} E \sin(2\pi\Omega t) \sum_n Q_n \cos(\varphi_n), \qquad (6)$$

where the value of the charge on the dipole end is an additive function of the local and external fields as described by equation (7).

Using the Euler–Lagrange equation, taking into account dissipation (5) and external excitation (6), we will find a Lagrangian in the form

$$L = T_k - U_{\text{int}}. \qquad (7)$$

Assuming that variables φ_n only slightly differ for the neighboring dipoles at the same time instant (which corresponds to the continuum approximation $\varphi_n - \varphi_{n-1} \sim \delta$ with the transition $na \longrightarrow x$, $\varphi_n(t) \longrightarrow \varphi(x, t)$, we obtain the following nonlinear relationship resembling the sine-Gordon equation [9–11]:

$$\frac{\partial^2 \varphi}{\partial t^2} + \nu_0^2 \frac{\partial^2 \varphi}{\partial x^2} - \theta_0^2 \sin(\varphi) - \eta \frac{\partial \varphi}{\partial t} = \gamma(x, t). \qquad (8)$$

Here, ν_0 is the analog of the maximum rate of perturbation spreading in the system studied:

$$\nu_0 = \sqrt{X_1(x, t)/W_1(x, t)}; \qquad (9)$$

coefficient θ_0 is the analog of plasma frequency:

$$\theta_0 = \sqrt{\Gamma_1(x, t)/W_1(x, t)}; \qquad (10)$$

η accounts for the dissipation level:

$$\eta = Dis(x, t)/W_1(x, t); \qquad (11)$$

and γ describes the perturbation:

$$\gamma(x, t) = [F(x, t) - W_2(x, t) - X_2(x, t)]/W_1(x, t). \qquad (12)$$

In these formulas, $X_1(x, t)$, $X_2(x, t)$, $\Gamma_1(x, t)$, $\Gamma_2(x, t)$, $W_1(x, t)$, $W_2(x, t)$, $Dis(x, t)$, and $F(x, t)$ are rather cumbersome expressions written in full elsewhere [12].

To analyze the character of SLF excitations in the system studied and study the possibility of some other effects, taking into account the finite size of the system, we have performed numerical calculations using equation (8). The boundary conditions for a chain of oscillators with the length l were written in the following form:

$$\varphi(0, t) = \varphi(l, t) = 0. \qquad (13)$$

The numerical solution of equation (8) was obtained by the corresponding finite-difference method (see, e.g., [13, 14]). Eventually, using approximations [12] corresponding to equation (8), we obtained a pattern describing the evolution of the frequency spectra of the positive branches of excitation amplitudes (Fig. 2) under the action of a very weak harmonic field on the chain of oscillators (with the parameters indicated in

the legend to the figure). The quantities ε_∞, ε_s, and τ_1 are characteristic of the dispersed systems in which, to our knowledge, the effects induced by SLF electric excitations were observed for the first time [[1– 5]. The *r* and *a* values selected are evidently quite realistic for the crystal hydrate systems studied in [1–5].

An analysis showed that the model system described above exhibits SLF hypersensitivity in a broad range of relaxation times ($\tau \sim 10^{-5}$–10^{-9} s). In the initial time instants ($t < 1$ s) of the SLF pumping, the model system has a region of resonance excitation that transforms with time ($t > 1$ s) into a dispersion dependence of the Debye type. The main resonance peaks and the satellite peaks appearing at $t > 10^{-3}$ s shift ($t \longrightarrow 1$ s) toward superlow frequencies ($\Omega < 10$ Hz). Of course, the particular pattern of evolution of the excitation spectra will change for the other parameters of excitation, cells, etc., but the characteristic features observed in Fig. 2 are retained and reliably localized in the SLF region for other chain lengths and relaxation times τ.

An experimental evidence for the possible existence of this very oscillation dynamics obtained in our numerical model calculations is provided by the effect of hypersensitivity in compressible crystal hydrates with respect to very small electric fields in a rather narrow SLF interval $20 < \Omega < 40$ Hz [1–5]. Additional information on the calculation results and their interpretation will be reported in subsequent publications.

REFERENCES

1. E. G. Fateev, Pis'ma Zh. Tekh. Fiz. **19** (10), 48 (1993) [Tech. Phys. Lett. **19**, 313 (1993)].
2. E. G. Fateev, Pis'ma Zh. Tekh. Fiz. **20** (20), 83 (1994) [Tech. Phys. Lett. **20**, 847 (1994)].
3. E. G. Fateev, Zh. Tekh. Fiz. **66** (6), 93 (1996) [Tech. Phys. **41**, 571 (1996)].
4. E. G. Fateev, Dokl. Ross. Akad. Nauk **354** (2), 252 (1997).
5. E. G. Fateev, Pis'ma Zh. Éksp. Teor. Fiz. **65** (12), 876 (1997) [JETP Lett. **65**, 919 (1997)].
6. P. Debye, *Polar Molecules* (Chemical Catalog Co., New York, 1929; Gostekhizdat, Moscow, 1931).
7. R. Hagedorn, *Preludes in Theoretical Physics in Honor of V. F. Weisskopf* (North Holland, Amsterdam, 1967).
8. T. L. Chelidze, A. I. Derevyanko, and O. D. Kurilenko, *Electrical Spectroscopy of Heterogeneous Systems* (Naukova Dumka, Kiev, 1977).
9. A. S. Davydov, *Solitons in Molecular Systems*, 2nd ed. (Naukova Dumka, Kiev, 1988; Kluwer, Dordrecht, 1991).
10. *Solitons in Action*, Ed. by K. Lonngren and A. Scott (Academic, New York, 1978; Mir, Moscow, 1981).
11. R. K. Dodd, J. C. Eilbeck, J. Gibbon, and H. C. Morris, *Solitons and Nonlinear Wave Equations* (Academic, New York, 1982; Mir, Moscow, 1988).
12. E. G. Fateev, Available from VINITI, No. 1911-V 99 (June 15, 1999).
13. G. I. Marchuk, *Methods of Computational Mathematics* (Nauka, Moscow, 1989).
14. W. F. Ames, *Numerical Methods for Partial Differential Equations* (Academic, New York, 1977).

Translated by P. Pozdeev